Photomanipulation of membrane properties, shape and transport

Inaugural-Dissertation

to obtain the academic degree

Doctor rerum naturalium (Dr. rer. nat.)

submitted to the Department of Biology, Chemistry, Pharmacy

of Freie Universität Berlin

by

Mina Aleksanyan

Berlin, 2024

Disclaimer

I hereby declare that I alone am responsible for the content of my doctoral dissertation and that I have only used the sources or references cited in the dissertation. I have not submitted this document as a doctoral dissertation elsewhere. I have clarified and acknowledged any personal assistance by name.

All the experiments for this dissertation were conducted from October 2019 to July 2024 at the Max Planck Institute of Colloids and Interfaces, as well as Institute for Chemistry and Biochemistry of Free University of Berlin, under the supervision of Dr. habil. PD Rumiana Dimova. This doctoral project is proposed by Dr. habil. PD Rumiana Dimova and Prof. Dr. Joachim Heberle, and funded by the International Max Planck Research School on Multiscale Bio-systems and Germany's Excellence Strategy, EXC 2008/1 (UniSysCat), Grant 390540038.

1st reviewer: Dr. habil. PD Rumiana Dimova
Max Planck Institute of Colloids and Interfaces

2nd reviewer: Prof. Dr. Helge Ewers
Institute for Chemistry and Biochemistry of Free University of Berlin

Date of defense: 06.11.2024

Acknowledgements

Completing this doctoral thesis has been a great journey filled with countless moments of challenge, discovery, and growth. This lovely learning journey would not have been possible without the support and encouragement of many wonderful individuals.

First and foremost, I extend my deepest gratitude to Dr. habil. PD Rumiana Dimova and Professor Dr. Joachim Heberle for proposing this fascinating thesis project and providing the opportunity to conduct my experimental studies in their laboratories within the multidisciplinary research atmosphere of the Max Planck Institute of Colloids and Interfaces (MPIKG) and Free University of Berlin (FUB). Their infinite guidance, generous support, insightful feedback, and constant trust in my potential have been invaluable, I continuously feel very lucky for getting the chance to work with them.

Dr. habil. PD Rumiana Dimova welcomed me into her laboratories during my master thesis studies and has been a constant source of inspiration and guidance ever since. Her leadership and support have been crucial to my scientific development, and I am deeply grateful for her lovely presence in my academic journey.

I would also like to thank Professor Dr. Helge Ewers for greatly supporting my administrative process at the Biochemistry Department of the FUB in very difficult times of COVID by kindly accepting to be my thesis reviewer. I am grateful to him and all my thesis committee members for their valuable insights and time in evaluating my dissertation.

I am thankful to the directors of MPIKG for providing excellent facilities for my experiments. In particular, I appreciate Professor Dr. Reinhard Lipowsky as the director of our department of Theory and Bio-systems of MPIKG between 2019-2022 for accommodating our laboratories, financing and organizing workshops which connected experimental and simulation studies, and for his valuable input. I also thank Professor Dr. Dr. h.c. Peter Fratzl for his support as the director of my graduate program at the International Max Planck Research Schools (IMPRS) on Multiscale Biosystems, and Professor Dr. Dr. h.c. Markus Antonietti and Professor Dr. Silvia Vignolini for accommodating our laboratories in their departments after the retirement of Professor Dr. Reinhard Lipowsky. I thank Prof. Dr. Dr. hc Peter H. Seeberger and Dr. Christian Roth for giving us an access to their laboratories.

I am grateful to Dr. Cécile Bidan for being my lovely, great mentor and generously supporting me whenever I need her insights throughout my graduate program at IMPRS.

During my scientific journey, I have had the privilege of collaborating with many dedicated researchers. I extend my thanks to Dr. Andrea Grafmüller, Fucsia Crea, Dr. Vasil N. Georgiev, Dr.

Naresh Yandrapalli, Dr. Stephan Block, Dr. Agustín Mangiarotti, Dr. Macarena Siri, Tsu-Wang Sun, Dr. Ramona Schlesinger, Antreas Vorkas, Aoife Redlich, Jheng-Liang Chen, Dr. Hammad A. Faizi, Professor Dr. Petia M. Vlahovska, Professor Dr. Karin Riske, Maria-Anna Kirmpaki, Amaury Brisson, Professor Dr. Salvatore Chiantia, Kita Schmidt, Dr. Rafael Lira, Professor Dr. Jan Steinkühler and Öznur Aglar for their collaboration and support during my doctoral studies. I also appreciate Dr. Kayla Sapp, Dr. Alexander Sodt, Anton Joseph, Anna M. Wagner, Professor Dr. César Rodriguez-Emmenegger, Dr. Elias Sabri, Professor Dr. Christian Brosseau, Hazel Erkan-Candag, Denis Krivic, Professor Dr. Klaus Groschner, Dr. Paul Markus Müller, Dr. Oliver Rocks, Professor Dr. Petra Schwille, and Yusuf Qutbuddin for offering additional collaboration projects.

A heartfelt thank you goes to my friends and colleagues at MPIKG and FUB for creating a stimulating and collaborative environment. Their technical assistance and moral support have made my work a joyous experience. Special thanks to Carmen Remde and Dr. Clemens Schmidt for maintaining our well-organized laboratories, and to Susann Weber, Valerie Lecker, Angelina Schneider, Andrea Barnjak, Kerstin Gabbe, and Justyna Powazynska for their administrative support. I also thank the IT support team at MPIKG, particularly Ralf Ditsch, Marco Ehlert, René Genz, Maximilian Briest, Paul Meißner, and Roy Pfitzner, for their assistance with computer and software systems.

I deeply appreciate Isabell Franke and Dr. Alette Winter for their administrative support of my doctoral studies at FUB. I am thankful to Dahlem Research School, Berlin University Alliance, Science Park Golm, Technology Transfer offices, and graduate centers of FUB, Humboldt University, Technical University of Berlin, and Potsdam University for promoting open science policies and offering a wide range of courses that helped me grow as a well-educated and self-aware individual. I also thank the BCP Mentorship platform of FUB, particularly Rafaela Münch, for allowing me to contribute to the academic and cultural integration of international master’s students as a mentor.

My research was funded by IMPRS on Multiscale Biosystems graduate school and Germany's Excellence Strategy, EXC 2008/1 (UniSysCat), Grant 390540038. I am grateful for their financial support.

I am deeply thankful to my family and friends for their endless love and support. Their encouragement and belief in me have been my greatest strength throughout this journey.

This thesis is dedicated to all the amazing people who have played an integral part in my academic and personal growth. Thank you for believing in me and being a part of this wonderful journey.

List of publications and scientific conferences

List of publications during the doctoral work

1. A. Mangiarotti*, **M. Aleksanyan***, M. Siri, T. W. Sun, R. Lipowsky, and R. Dimova. 2024. Photoswitchable Endocytosis of Biomolecular Condensates in Giant Vesicles. *Adv Sci (Weinh)*.e2309864, doi: 10.1002/advs.202309864.

** These authors contributed equally.*

- ***Press Release:*** *https://www.mpikg.mpg.de/6820099/shaping-cells-with-light?c=132305*

2. M. Aleksanyan, A. Grafmüller, F. Crea, V. N. Georgiev, N. Yandrapalli, S. Block, J. Heberle, and R. Dimova. 2023. Photomanipulation of Minimal Synthetic Cells: Area Increase, Softening, and Interleaflet Coupling of Membrane Models Doped with Azobenzene-Lipid Photoswitches. *Adv Sci (Weinh)*. 10(31):e2304336, doi: 10.1002/advs.202304336.

3. K. Sapp, **M. Aleksanyan**, K. Kerr, R. Dimova, and A. Sodt. 2023. Kinetic relaxation of giant vesicles validates diffusional softening in a binary lipid mixture. *Physical Review E*. 107(5):054403, doi: 10.1103/PhysRevE.107.054403.

4. M. Aleksanyan, H. A. Faizi, M. A. Kirmpaki, P. M. Vlahovska, K. A. Riske, and R. Dimova. 2023. Assessing membrane material properties from the response of giant unilamellar vesicles to electric fields. *Adv Phys X*. 8(1), doi: 10.1080/23746149.2022.2125342.

5. A. Joseph, A. M. Wagner, M. Garay-Sarmiento, **M. Aleksanyan**, T. Haraszti, D. Söder, V. N. Georgiev, R. Dimova, V. Percec, and C. Rodriguez-Emmenegger. 2022. Zwitterionic Dendrimersomes: A Closer Xenobiotic Mimic of Cell Membranes. *Advanced Materials*. 34(49):2206288, doi: 10.1002/adma.202206288.

6. E. Sabri, **M. Aleksanyan**, C. Brosseau, and R. Dimova. 2022. Effects of solution conductivity on macropore size dynamics in electroporated lipid vesicle membranes. *Bioelectrochemistry*. 147:108222, doi: 10.1016/j.bioelechem.2022.108222.

7. M. Aleksanyan, R. B. Lira, J. Steinkühler, and R. Dimova. 2022. GM1 asymmetry in the membrane stabilizes pores. *Biophysical Journal*. 121(17):3295-3302, doi: 0.1016/j.bpj.2022.06.011.

- *The article was highlighted as '**New and Notable**': https://doi.org/10.1016/j.bpj.2022.07.037*

8. H. Erkan-Candag, D. Krivic, M. A. F. Gsell, **M. Aleksanyan**, T. Stockner, R. Dimova, O. Tiapko, and K. Groschner. 2022. Characterization of DAG Binding to TRPC Channels by Target-Dependent cis-trans Isomerization of OptoDArG. *Biomolecules*. 12(6), doi: 10.3390/biom12060799.

List of publications before the doctoral work

9. J. S. J. Tang, A. D. Smaczniak, L. Tepper, S. Rosencrantz, **M. Aleksanyan**, L. Dähne, and R. R. Rosencrantz. 2022. Glycopolymer Based LbL Multilayer Thin Films with Embedded Liposomes. *Macromolecular Bioscience*. 22(4), 2100461, doi: 10.1002/mabi.202100461.

10. S. A. Cınar, M. N. Guven, T. N. Eren, B. Cesur, **M. Aleksanyan**, B. Dedeoglu, N. Okte, V. Aviyente, F. Morlet-Savary, J. Lalevée, and D. Avci. 2016. Structure-reactivity relationships of novel monomeric photoinitiators. *Journal of Photochemistry and Photobiology A: Chemistry*. 329:77-87, doi: 10.1016/j.jphotochem.2016.06.015.

11. M. Kieffer, B. S. Pilgrim, T. K. Ronson, D. A. Roberts, **M. Aleksanyan**, and J. R. Nitschke. 2016. Perfluorinated ligands induce meridional metal stereochemistry to generate M8L12, M10L15, and M12L18 prisms. *Journal of the American Chemical Society*. 138(21):6813-6821, doi: 10.1021/jacs.6b02445.

List of presentations at scientific conferences attended during the doctoral studies

1. 3rd International Chemistry Symposium at Potsdam University on 23.10.2019, Potsdam, Germany (**talk**)

2. International Deutsche Gesellschaft fur Biophysik (DGfB) meeting for Membrane Biophysics, on 02.03.2020 – 04.03.2020, Drübeck, Germany (**poster**)

3. German Conference on Synthetic Biology at the 4th German Association for Synthetic Biology Conference on 24.09.2020 – 25.09.2020, virtual (**poster**)

4. Jóvenes Biofísicos – The Young Initiative on Biophysics YouTube contest, 26.10.2020, online at YouTube: https://www.youtube.com/watch?v=jSnBQKn2_HU (**talk**)

- **Received a mention for the most watched video presentation in YouTube**.

5. 65th Annual Meeting of American Biophysical Society, on 22.02.2021 – 26.02.2021, virtual (**talk**)

6. American Chemical Society Spring Meeting 2021, Biomembrane Symposium on 05.04.2021 – 16.04.2021, virtual (**talk**)

7. 7th European Joint Theoretical/Experimental Meeting on Membranes on 07.04.2021 - 09.04.2021, virtual (**poster**)

8. XXVIth International Symposium on Bioelectrochemistry and Bioenergetics of the Bioelectrochemical Society on 'Bioelectrochemistry for improved Life Quality', on 10.05.2021 – 15.05.2021, hybrid event at Cluj-Napoca, Romania (**talk**)

9. 7th School on Pulsed Electric Field Applications in Food and Biotechnology, on 31.05.2021 – 02.06.2021, hybrid event Zaragoza, Spain (**poster**)

10. European Biophysical Societies' Association (EBSA) 13th European Biophysics Congress, on 24.07.2021 – 27.07.2021, Vienna, Austria (**poster**)

- **Received EBSA Bursary - travel award**

11. 20th International Union for Pure and Applied Biophysics (IUPAB) Congress, 45th Annual Meeting of the Brazilian Biophysics Society Meeting, and 50th Annual Meeting of the Brazilian Society for Biochemistry and Molecular Biology Meeting, on 4.10.2021 – 8.10.2021, virtual (**poster**)

- **Received the IUPAB award covering all the conference expenses**

12. American Chemical Society Spring Meeting 2022, Biomembrane Symposium on 20.03.2022 – 24.03.2022, virtual (**talk**)

13. American Chemical Society Spring Meeting 2022, Biomembrane Symposium on 20.03.2022 – 24.03.2022, virtual

14. XXVIIth International Symposium on Bioelectrochemistry and Bioenergetics of the Bioelectrochemical Society, on 3.04.2022 – 7.04.2022, Antwerp, Belgium (**talk**)

15. DGfB meeting for Membrane Biophysics, on 23.05.2022 – 25.05.2022, Drübeck, Germany (**poster**)

- **Received DGfB travel award**

16. CurvoBio Conference 2022, on 24.08.2022 – 26.08.2022, Berlin, Germany (**talk**)

17. Biomembrane Days 2022, on 19.09.2022 – 21.09.2022, Berlin, Germany (**poster**)

18. 2nd Unifying Systems in Catalysis UniSysCat/EC2 SAB Meeting of Technical University of Berlin, on 12.10.2023 – 13.10.2023, Berlin, Germany (**poster**)

Table of contents

List of abbreviations

AC	Alternating current
AFM	Atomic force microscopy
ANOVA	One-way analysis of variance
Atto-647N-DOPE	1,2-Dioleoyl-sn-glycero-3-phosphoethanolamine labeled with Atto 647N
ATP	Adenosine triphosphate
AU	Airy units
Azo-PC	1-Stearoyl-2-[(E)-4-(4-((4-butylphenyl)diazenyl)phenyl)butanoyl]-sn-glycero-3-phosphocholine
BSA	Bovine Serum Albumin
$\boldsymbol{CF}$	Correction factor
cm	Centimeter
CMC	Critical micelle concentration
CSV	Column-separated value
DC	Direct current
DDM	n-Dodecyl-β-D-maltoside
$\boldsymbol{DF}$	Dilution factor
DiLC18	1,1'-Dioctadecyl-3,3,3',3'-Tetramethylindocarbocyanine perchlorate
$\boldsymbol{DL}$	Degree of labelling
DLS	Dynamic light scattering
DMSO	Dimethyl sulfoxide
DOPC	1,2-Dioleoyl-sn-glycero-3-phosphocholine
DOPE	1,2-Dioleoyl-sn-glycero-3-phosphoethanolamine
DSPC	1,2-Distearoyl-sn-glycero-3-phosphocholine
EGTA	Ethyleneglycol- bis(β-aminoethyl)-N,N,N′,N′-tetraacetic Acid
ER	Endoplasmic reticulum
FAAzo-4	4-Butyl-Azo-4:0-Acid-1
FCS	Fluorescence correlation spectroscopy
fps	Frames per second
FRAP	Fluorescence recovery after photobleaching
FTIR-ATR	Fourier-transform infrared attenuated total reflection
FWHM	Full width at half maximum
G22C	Mutant mechanosensitive ion channel of large conductance which is labeled with [2-(triethylammonium)ethyl]methanethiosulfonate bromide
GPMV	Giant plasma membrane vesicles
GUV	Giant unilamellar vesicle
Hist-	Histidine
HyD	Hybrid
ITO	Indium tin oxide
LED	Light emitting diode
LUV	Large unilamellar vesicle
MACH	Methionine-alanine-cysteine-histidine
MD	Molecular dynamics
MscL	Mechanosensitive ion channel of large conductance
MscL-Tb	Mycobacterium tuberculosis MscL
NA	Numerical aperture
OptoDArG	3-Hydroxypropane-1,2-diyl bis(4-(4-((E)-(4-butylphenyl)diazenyl)phenyl)butanoate)
PBS	Phosphate buffered saline
PC	Phosphatidylcholine
PMF	Potential of mean force

POPC	1-Palmitoyl-2-oleoyl-glycero-3-phosphocholine
PS	Phosphatidylserine
Red-azo-PC	Tetra-ortho-chloro azobenzene-substituted phosphatidylcholine
RNA	Ribonucleic acid
ROI	Region of interest
S1	Amphipathic α-helix of MscL situated along the cytoplasmic membrane
SD	Standard deviation
SDS-PAGE	Sodium dodecyl sulfate-polyacrylamide gel electrophoresis
SLB	Supported lipid bilayer
SRB	Sulforhodamine B
SUV	small unilamellar vesicle
TCEP	Tris(2-carboxyethyl)phosphine hydrochloride
TEM	Transmission electron microscopy
TM1	Transmembrane domain of MscL on the pore constriction side
TM2	Transmembrane domain of MscL facing the lipid bilayer
TRPC3	Short transient receptor potential channel 3
UV	Ultraviolet
v-azo-PC	various chain lengths of photoswitchable azobenzene phosphatidylcholine analogs
vol	Volume
Vpp	Peak to peak voltage
v/v	Volume to volume ratio
WHO	World Health Organization
w/v	Weight to volume ratio

List of symbols

A	Absorbance
A_i	Initial vesicle area in the absence of irradiation
A_l	Vesicle area when exposed to light
A^{lip}	Area per lipid
A_0^{lip}	Area per lipid of a bilayer with zero mechanical tension
A_{UV}	UV-induced area increase of the vesicles
A_{li}	Light-induced area change
A_{app}	Apparent area
a	Vesicle semi-axis along to the applied electric field
a/b	Aspect ratio, degree of membrane deformation
b	Vesicle semi-axis perpendicular to the applied electric field
β	Coupling constant between the membrane leaflets
c	Concentration
Ca^{2+}	Calcium ion
C_B	Capacitance of the bare lipid bilayer
$C_{D,in}$	Capacitance of the ionic double layer in the inner solution
$C_{D,out}$	Capacitance of the ionic double layers in the outer solutions
C_m	Specific membrane capacitance
d	Membrane thickness
d	Distance from the estimated outer rim of the vesicle to its interface with the particle
ϵ	ellipticity
ε_0	Vacuum permittivity
$\varepsilon_{r,B}$	Relative (dimensionless) dielectric permittivity of the bilayer
$\varepsilon_{r,W}$	Dielectric constant of water
ε	Molar extinction coefficient
ε_{dye}	Molar extinction coefficient of dye
ε_{MscL}	Molar extinction coefficient of MscL
f_c	Critical field frequency
F_{in}	Fluorescence intensities of GUV interior
F_{out}	Fluorescence intensities of GUV exterior
HeNe	Helium–neon
H_2O_2	Hydrogen peroxide
H_2SO_4	Sulfuric acid
κ	Bending rigidity
K, K_A	Stretching elasticity
k_B	Boltzmann constant
L	Path length of the light
m	Membrane spontaneous curvature
M_{MscL}	Molarity of MscL
N_2	Inert gas
NaCl	Sodium chloride
NaOH	Sodium hydroxide
p	Penetration depth
r_{por}	Pore radius
R	Radius
R_{Cond}	Condensate radius
R_{GUV}	GUV radius
T	Temperature
%	Percentage

Λ	Conductivity ratio
λ_D	Thickness of the Debye length
λ_{in}	Conductivity of the GUV inner solution
λ_{out}	Conductivity of GUV outer solution
Φ	Geometric factor
θ_c	Contact angle facing the condensate interior
θ_e	Contact angle facing the external phase
θ_i	Contact angle facing the vesicle lumen
ΔA	Cylindrical tube of area
ΔE_{ad}	Adhesion energy
ΔE_{be}	Gain of bending energy
Σ_{ce}	Interfacial tension
Σ_{ic}^{m}	Mechanical tension of the membrane segments in contact with the condensate
Σ_{ie}^{m}	Mechanical tension of the membrane segments in contact with the external phase

List of figures

Summary

Cells as the fundamental units of life, exhibit significant complexity, hosting intricate networks of biochemical processes and structural components which enable them to perform a vast array of functions necessary for the survival and adaptation of living organisms. The dynamic and diverse nature of cells causes them to constantly interact and adapt to environmental cues. Cell types and morphologies vary widely among organisms and tissues, reflecting the discrete functions and specialized roles in maintaining the viability of the biosystems involved. Abnormalities in cell size and shape can be associated with pathological conditions, which can be monitored via imaging techniques and used for diagnostic purposes. During the processes of endocytosis and exocytosis, the plasma membrane can form invaginations and exhibit shape remodeling events. The ability of the plasma membrane to undergo dynamic morphological alterations allows cells to control cellular communication, recognition processes, adhesion and immune responses as well as the transport of substances between the cell interior and exterior environment. The plasma membrane composed of a diverse arrangement of lipids, proteins and carbohydrates, plays an important role in maintaining the structural integrity and metabolic activities of cells thus taking part in the regulation of the cellular homeostasis. However, the diverse components of the plasma membrane and their various roles in the extracellular and intracellular activities make them very challenging and complex to characterize.

The structural and functional complexity of the plasma membrane has required the construction of simpler membrane models for the investigation of membrane dynamics. These models can also characterize the individual effects and properties of membrane components during cellular interactions and transport processes. Model membranes can be manipulated with external stimuli. Among them, light irradiation offers several advantages as a non-invasive, reversible, biocompatible and facile tool to provide high spatiotemporal control in biomimicry of cellular events. One of the efficient approaches to utilize light for the manipulation of membrane models is to prepare biomimetic platforms with photoswitchable lipids which can reversibly change their molecular conformation upon light irradiation. In this doctoral thesis, we have developed a light-triggered, multifunctional, and smart biomimetic platform by using phosphatidylcholine (referred as POPC here and in the main text), one of the most abundant phospholipids in animal cells, combined with a photoswitchable azobenzene lipid analog (referred as azo-PC). This platform was designed to provide an optical control of the membrane properties, shape, and molecular transport in the biomimetic system through the photoisomerization of azo-PC under UV and blue light.

First, we comprehensively investigated the reversibility, kinetics and effects of photoswitching on the material properties of varying compositions of azo-PC containing minimalistic membrane models including giant unilamellar vesicles (GUVs) as minimal cell-size models, Langmuir monolayers, large unilamellar vesicles and supported lipid bilayers, and combined the results from a variety of experimental approaches to those obtained from molecular dynamics simulations. These investigations showed that azo-PC photoisomerization induces dynamic alterations in membrane properties, affecting bilayer packing, elasticity, and interleaflet interactions. Using a method based on vesicle electrodeformation and optical microscopy, we revealed how the photolipid, introduced at various fractions, alters the membrane area upon isomerization and found excellent agreement with simulations. UV illumination of azo-PC GUVs triggered *trans*-to-*cis* photoisomerization, resulting in a significant increase in membrane area and a ten-fold decrease in bending rigidity. *Trans* azo-PC bilayers were found to be thicker than POPC bilayers but exhibited higher specific membrane capacitance and dielectric constant. This suggests an enhanced ability to store electrical charges across the membrane. Furthermore, incubation of preformed POPC GUVs with azo-PC rendered them photoresponsive, suggesting therapeutic potential for optical control of cellular activities. By using a wide range of experimental and computational approaches, we collected accurate results about the characterization of the light-induced modifications in azo-PC containing membranes, which also

allowed us to discuss the discrepancies in the previously reported values in the literature and explain the origins of these discrepancies.

Next, we demonstrated the application of photoswitching of azo-PC doped GUVs for the transport of protein-rich droplets by performing light-triggered endocytosis of biomolecular condensates. Protein-rich condensates are phase separated membraneless organelles acting as vessels for biochemical reactions in cells during important cellular processes including signal transduction and gene expression. In our studies, condensates were prepared from the plant protein glycinin, which is a prominent storage protein in soybeans. UV-light-induced *trans*-to-*cis* photoisomerization of azo-PC results in an instantaneous increase in vesicle area, which promotes the wetting of GUVs by condensates and their rapid endocytosis for an appropriate condensate-vesicle size ratio. The process is fully reversible by exposure to blue light, allowing precise spatiotemporal control of the condensate-membrane interaction. The affinity of the protein condensates to the membrane, and the kinetics, reversibility and degree (whether partial or complete) of the engulfment processes were quantified from confocal microscopy images. Theoretical estimations confirmed that the adhesion of protein condensates to azo-PC vesicles in *cis* conformation under UV irradiation is energetically favorable. Experimental results, in good agreement with theoretical estimations, demonstrated that light and azo-PC photoisomerization can be employed as a versatile system to modify membrane-condensate interactions in a fast and reversible manner. To the best of our knowledge, this is the first study in the literature to utilize photoisomerization to control the delivery process of a biomacromolecule across a minimalistic artificial cell, providing a promising approach for further exploration in the control of cellular transport of biomacromolecules.

Lastly, employing azo-PC photoisomerization we established optical control of the activity of mechanosensitive ion channels reconstituted in GUV membrane, which enabled the transport of small molecules across the membrane. These pore-forming transmembrane proteins can open and close in response to changes in membrane properties and tension. As a model protein, we used the bacterial mechanosensitive ion channel of large conductance (MscL) and reconstituted it into azo-PC containing GUVs. Labeling MscL with a dye allowed us to monitor the reconstitution process through confocal microscopy, determine critical parameters of the reconstitution process and develop a protocol for the reconstitution of MscL into azo-PC containing GUVs. In order to understand the initial conformation of the incorporated MscL in the GUV membrane, the vesicles were subjected to a permeability test by adding a water-soluble, membrane-impermeable sulforhodamine dye to the external medium of the GUVs. Most of the GUVs remained impermeable, indicating that the majority pf MscL in the membrane stayed in the closed state after reconstitution. This trend changed when UV/blue illumination was applied to the MscL-reconstituted azo-PC vesicles. UV/blue illumination altered the membrane properties of azo-PC doped GUVs and triggered the opening of the MscL channel, as monitored by the permeation of the sulforhodamine molecules across the GUV membrane. Our preliminary results showed that light can be used as an efficient tool to catalytically activate the MscL channel. Further studies should focus extensively on the optimization and characterization of MscL reconstitution and gating processes.

Overall, our findings in this doctoral thesis provide an essential background for understanding and optimizing light-triggered drug delivery platforms and photoregulation of shape-dependent cellular processes such as endocytosis, exocytosis and intercellular trafficking through azo-PC photoisomerization. Considering our results on the control of membrane shape, mechanics and trafficking by light irradiation, photoisomerization may be used as a promising biomedical alternative for cell repair processes. Photoswitchable biomimetic platforms can be further developed as light-triggered smart activators for high-precision regulation of cellular mechanisms.

Zusammenfassung

Zellen, die grundlegenden Einheiten des Lebens, weisen eine erhebliche Komplexität auf. Sie beherbergen komplizierte Netzwerke biochemischer Prozesse und struktureller Komponenten, die es ihnen ermöglichen, eine Vielzahl von Funktionen auszuführen, die für das Überleben und die Anpassung lebender Organismen notwendig sind. Die dynamische und vielfältige Natur der Zellen führt dazu, dass sie ständig interagieren und sich an Umweltreize anpassen. Zelltypen und -morphologien variieren stark zwischen Organismen und Geweben. Sie spiegeln die unterschiedlichen Funktionen und spezialisierten Rollen bei der Aufrechterhaltung der Lebensfähigkeit der beteiligten Biosysteme wider. Anomalien der Zellgröße und -form können mit pathologischen Zuständen in Verbindung gebracht werden, die durch bildgebende Verfahren überwacht und für diagnostische Zwecke genutzt werden können. Bei den Prozessen der Endozytose und Exozytose kann die Plasmamembran Einstülpungen bilden und ihre Form verändern. Die Fähigkeit der Plasmamembran, dynamische morphologische Veränderungen zu erfahren, ermöglicht es den Zellen, die zelluläre Kommunikation, Erkennungsprozesse, Adhäsion und Immunreaktionen sowie den Transport von Substanzen zwischen dem Zellinneren und der äußeren Umgebung zu steuern. Die Plasmamembran, die aus einer vielfältigen Anordnung von Lipiden, Proteinen und Kohlenhydraten besteht, spielt eine wichtige Rolle bei der Aufrechterhaltung der strukturellen Integrität und der Stoffwechselaktivitäten von Zellen und ist somit an der Regulierung der zellulären Homöostase beteiligt. Die verschiedenen Komponenten der Plasmamembran und ihre unterschiedlichen Rollen bei den extrazellulären und intrazellulären Aktivitäten machen ihre Charakterisierung jedoch sehr schwierig und komplex.

Die strukturelle und funktionelle Komplexität der Plasmamembran hat die Konstruktion von einfacheren Membranmodellen zur Untersuchung der Membrandynamik erforderlich gemacht. Diese Modelle können auch die einzelnen Effekte und Eigenschaften von Membrankomponenten während zellulärer Interaktionen und Transportprozesse charakterisieren. Die Modellmembranen können durch externe Stimuli manipuliert werden. Lichtbestrahlung bietet als nicht-invasives, reversibles, biokompatibles und einfaches Werkzeug mehrere Vorteile, um eine hohe räumliche und zeitliche Kontrolle bei der Biomimikry zellulärer Ereignisse zu ermöglichen. Einer der effizientesten Ansätze zur Nutzung von Licht für die Manipulation von Membranmodellen ist die Herstellung biomimetischer Plattformen mit photoschaltbaren Lipiden, die ihre molekulare Konformation bei Lichteinstrahlung reversibel ändern können. In dieser Doktorarbeit haben wir eine lichtgesteuert, multifunktionale und intelligente biomimetische Plattform entwickelt, indem wir Phosphatidylcholin (hier und im Haupttext als POPC bezeichnet), eines der am häufigsten vorkommenden Phospholipide in tierischen Zellen, mit einem photoschaltbaren Azobenzol-Lipidanalog (als Azo-PC bezeichnet) kombiniert haben. Diese Plattform wurde entwickelt, um eine optische Kontrolle der Membraneigenschaften, der Form und des molekularen Transports im biomimetischen System durch die Photoisomerisierung von Azo-PC unter UV- und blauem Licht zu ermöglichen.

Zunächst untersuchten wir umfassend die Reversibilität, die Kinetik und die Auswirkungen der Photoumschaltung auf die Materialeigenschaften verschiedener Zusammensetzungen von Azo-PC, die minimalistische Membranmodelle enthalten, darunter riesige unilamellare Vesikel (GUVs) als Modelle mit minimaler Zellgröße, Langmuir-Monoschichten, große unilamellare Vesikel und unterstützte Lipiddoppelschichten, und kombinierten die Ergebnisse aus einer Vielzahl experimenteller Ansätze mit denen aus Molekulardynamiksimulationen. Diese Untersuchungen zeigten, dass die Photoisomerisierung von Azo-PC dynamische Veränderungen der Membraneigenschaften hervorruft, die sich auf die Packung der Doppelschicht, die Elastizität und die Interleaflet-Wechselwirkungen auswirken. Mithilfe einer Methode, die auf der Elektrodeformation von Vesikeln und optischer Mikroskopie basiert, konnten wir zeigen, wie das in verschiedenen Anteilen eingebrachte Photolipid die Membranfläche bei der Isomerisierung verändert, und fanden eine hervorragende Übereinstimmung mit den Simulationen. Die UV-Beleuchtung von Azo-PC GUVs löste eine *trans*-zu-*cis*-Photoisomerisierung aus, was zu einer signifikanten Vergrößerung der Membranfläche und einer

zehnfachen Abnahme der Biegesteifigkeit führte. Es wurde festgestellt, dass *trans*-Azo-PC-Doppelschichten dicker sind als POPC-Doppelschichten, aber eine höhere spezifische Membrankapazität und Dielektrizitätskonstante aufweisen. Dies deutet auf eine verbesserte Fähigkeit hin, elektrische Ladungen in der Membran zu speichern. Darüber hinaus machte die Inkubation von vorgeformten POPC-GUVs mit Azo-PC sie lichtempfindlich, was auf ein therapeutisches Potenzial für die optische Kontrolle zellulärer Aktivitäten schließen lässt. Durch den Einsatz einer breiten Palette von experimentellen und rechnerischen Ansätzen haben wir genaue Ergebnisse über die Charakterisierung der lichtinduzierten Veränderungen in Azo-PC-haltigen Membranen gesammelt, die es uns auch ermöglichten, die Diskrepanzen in den zuvor in der Literatur berichteten Werten zu diskutieren und die Ursachen dieser Diskrepanzen zu erklären.

Als Nächstes demonstrierten wir die Anwendung des Photoschaltens von Azo-PC-dotierten GUVs für den Transport proteinreicher Tröpfchen, indem wir eine lichtgesteuerte Endozytose biomolekularer Kondensate durchführten. Proteinreiche Kondensate sind phasengetrennte, membranlose Organellen, die als Gefäße für biochemische Reaktionen in Zellen während wichtiger zellulärer Prozesse wie Signaltransduktion und Genexpression dienen. In unseren Studien wurden Kondensate aus dem Pflanzenprotein Glycinin hergestellt, das ein wichtiges Speicherprotein in Sojabohnen ist. Die durch UV-Licht induzierte *trans*-zu-*cis*-Photoisomerisierung von Azo-PC führt zu einer sofortigen Vergrößerung der Vesikelfläche, was die Benetzung der GUVs durch die Kondensate und ihre schnelle Endozytose bei einem angemessenen Größenverhältnis zwischen Kondensat und Vesikel fördert. Der Prozess ist durch die Bestrahlung mit blauem Licht vollständig reversibel, was eine präzise räumliche und zeitliche Kontrolle der Kondensat-Membran-Interaktion ermöglicht. Die Affinität der Proteinkondensate zur Membran sowie die Kinetik, die Reversibilität und der Grad (ob teilweise oder vollständig) der Engulfment-Prozesse wurden anhand von konfokalen Mikroskopieaufnahmen quantifiziert. Theoretische Abschätzungen bestätigten, dass die Adhäsion von Proteinkondensaten an Azo-PC-Vesikel in *cis*-Konformation unter UV-Bestrahlung energetisch günstig ist. Die experimentellen Ergebnisse, die gut mit den theoretischen Schätzungen übereinstimmen, zeigen, dass Licht und Azo-PC-Photoisomerisierung als vielseitiges System eingesetzt werden können, um Membran-Kondensat-Wechselwirkungen schnell und reversibel zu verändern. Nach unserem Kenntnisstand ist dies die erste Studie in der Literatur, in der die Photoisomerisierung zur Steuerung des Transportprozesses eines Biomakromoleküls durch eine minimalistische künstliche Zelle eingesetzt wird. Dies ist ein vielversprechender Ansatz für die weitere Erforschung der Steuerung des zellulären Transports von Biomakromolekülen.

Mit Hilfe der Azo-PC-Photoisomerisierung gelang es uns schließlich, die Aktivität mechanosensitiver Ionenkanäle, die in der GUV-Membran rekonstituiert sind, optisch zu kontrollieren, wodurch der Transport kleiner Moleküle durch die Membran ermöglicht wurde. Diese porenbildenden Transmembranproteine können sich als Reaktion auf Veränderungen der Membraneigenschaften und -spannung öffnen und schließen. Als Modellprotein verwendeten wir den bakteriellen mechanosensitiven Ionenkanal mit großer Leitfähigkeit (MscL) und rekonstituierten ihn in azo-PC-haltigen GUVs. Die Markierung von MscL mit einem Farbstoff ermöglichte es uns, den Rekonstitutionsprozess mittels konfokaler Mikroskopie zu überwachen, kritische Parameter des Rekonstitutionsprozesses zu bestimmen und ein Protokoll für die Rekonstitution von MscL in Azo-PC-haltige GUVs zu entwickeln. Um die anfängliche Konformation des in die GUV-Membran eingebauten MscL zu verstehen, wurden die Vesikel einem Permeabilitätstest unterzogen, indem ein wasserlöslicher, membranundurchlässiger Sulforhodamin-Farbstoff in das äußere Medium der GUVs gegeben wurde. Die meisten GUVs blieben undurchlässig, was darauf hindeutet, dass die Mehrheit der MscL in der Membran nach der Rekonstitution im geschlossenen Zustand blieb. Dieser Trend änderte sich, als die mit MscL rekonstituierten Azo-PC-Vesikel mit UV/Blau-Beleuchtung bestrahlt wurden. Die UV/Blau-Beleuchtung veränderte die Membraneigenschaften der Azo-PC-dotierten GUVs und löste die Öffnung des MscL-Kanals aus, was durch die Permeation der Sulforhodamin-Moleküle durch die GUV-Membran überwacht wurde. Unsere vorläufigen Ergebnisse zeigen, dass Licht als

effizientes Mittel zur katalytischen Aktivierung des MscL-Kanals eingesetzt werden kann. Weitere Studien sollten sich umfassend auf die Optimierung und Charakterisierung der MscL-Rekonstitution und der Gating-Prozesse konzentrieren.

Insgesamt liefern unsere Ergebnisse in dieser Doktorarbeit einen wesentlichen Hintergrund für das Verständnis und die Optimierung von lichtgesteuerten Wirkstoffverabreichungsplattformen und der Photoregulation von formabhängigen zellulären Prozessen wie Endozytose, Exozytose und interzellulärem Transport durch Azo-PC-Photoisomerisierung. In Anbetracht unserer Ergebnisse zur Kontrolle von Membranform, -mechanik und -transport durch Lichtbestrahlung kann die Photoisomerisierung als vielversprechende biomedizinische Alternative für Zellreparaturprozesse genutzt werden. Photoschaltbare biomimetische Plattformen können als lichtgesteuerte intelligente Aktivatoren zur hochpräzisen Regulierung zellulärer Mechanismen weiterentwickelt werden.

1 General introduction

1.1 Cells, the cellular membrane and its main components

Cells are self-organized fundamental building blocks of all living organisms. They are mainly classified as prokaryotic and eukaryotic cells, each of them posessing a distinct genomic complexity and structural features (Lynch and Conery, 2003; López-García and Moreira, 2015). Eukaryotic cells developed a nucleus, a dynamic cytoskeleton and multi-compartmentalized internal structures called organelles, while prokaryotic cells lack a well-defined nucleus and other compartmentalized structures due to the absence of internal membranes (Vellai and Vida, 1999). What these two fundamental classes of life have in common is their ability to maintain cellular physiology, which includes the coordinated activities and functions of cellular compartments that ensure the survival of the cell. These essential functions are achieved through homeostatic regulation, a process that allows cells to maintain internal stability despite changing external conditions such as temperature, nutrients, osmotic pressure, ion gradients, pH, electric fields, and light (Galluzzi et al., 2018; Billman, 2020).

The cellular membrane (also known as the plasma membrane) serves as a dynamic barrier and separates the cell's internal environment from the external surroundings. It plays a crucial role on cellular homeostasis and viability (Dias and Nylandsted, 2021; Vasconcelos-Cardoso et al., 2022). The main components of the plasma membrane are lipids, proteins and carbohydrates as illustrated in Figure 1.1. Among others, phospholipids are the most predominant molecule of the cellular membrane (van Meer et al., 2008). They are composed of a hydrophilic phosphate head group and a hydrophobic tail containing two fatty acid chains. The functional groups attached to the phosphate head group of the lipid (particularly the presence and relative strength of the acidic and basic functional groups) determines the charge of the phospholipid at physiological pH (around 7.4) (Alberts B, 2002). For instance, phosphatidylcholine (PC) has a zwitterionic head group because it contains both a positively charged quaternary amine group (derived from choline) and a negatively charged phosphate group. At physiological pH, the positive and negative charges cancel each other out, resulting in a net neutral charge for the entire molecule. However, phosphatidylserine (PS) has a charged head group because it contains a negatively charged phosphate group and an uncharged amino acid serine. The lack of a positively charged group on the head group gives PS a net negative charge at physiological pH. Similar to the lipid head group, analyzing the length of the fatty acid chains and the degree of saturation within the lipid tails also gives insights about the physical properties of the lipid molecule (Alberts B, 2002). Two layers of phospholipids form the bilayer structure of the plasma membrane with the arrangement of their hydrophobic tails pointing inward. This double layer structure of phospholipids ensures the unique property of the cellular membrane to act as a semi-

permeable barrier (van Meer et al., 2008). The combination of saturation level and chain length of the lipid determines the overall fluidity of the constructed membrane (Casares et al., 2019). A higher degree of unsaturation and shorter chains lead to a more fluid membrane, which is crucial for various cellular processes such as signal transduction (Casares et al., 2019). The distribution of lipids in the two membrane leaflets is highly asymmetric, and this aspect gains strong interest among researchers in the latter years with the development of various analytical methods and in vitro reconstitution assays (Lorent et al., 2020; Pabst and Keller, 2024). In addition to phospholipids, sterols are another important class of lipids maintaining membrane fluidity and stability of cells at varying temperatures (Yeagle, 1985). Proteins are the second major constituents of the cellular membrane. They are subdivided into integral and peripheral proteins (Yang and Hinner, 2015). Integral proteins are embedded into the phospholipid bilayer. For example, transmembrane proteins belong to this group whereas peripheral proteins are located on the inner or outer surface of the phospholipid bilayer. Membrane proteins are known to speed up chemical reactions, act as receptors for specific molecules, and transport materials across the cell membrane (Yang and Hinner, 2015).

Mechanosensitive ion channels also fall into the class of transmembrane proteins, which respond to mechanical stimuli such as stretch, pressure, and shear force. They alter their conformation to allow the flow of ions across the membrane, thus playing crucial roles in various physiological processes including osmoregulation (Martinac, 2012). For instance, mechanosensitive channel of Large conductance (MscL) as one of the well-studied ion channels in the literature is of particular interest and in the scope of this thesis (see Chapter 5); it has the ability to protect bacterial cells from lysis by rapidly releasing osmolytes in response to sudden increase in membrane tension due to hypoosmotic shock (Kloda et al., 2008). Carbohydrates as third major component of the cellular membrane are located only on the outer surface of the plasma membrane. They are either attached to lipids or proteins forming glycolipids or glycoproteins, respectively. They provide the protective, gel-like lining of glycocalyx and participate in cell recognition processes (Sprovieri and Martino, 2018). The proportions of proteins, lipids, and carbohydrates in the plasma membrane vary between different types of cells (Cooper and Adams, 2022). Similarly, the type and number of membrane-bound organelles also vary between different types of cells (Cooper and Adams, 2022). In addition, a wide range of cells also contain protein condensates which are membraneless dynamic compartments formed through liquid-liquid phase separation of proteins and ribonucleic acid (RNA). They take part in various cellular functions including gene regulation, stress response, and signal transduction (Banani et al., 2017) (in Chapter 4, we discuss one type of protein condensate and its interaction with the

membrane). All of these characteristics of cells and cellular compartments can be related to their functional role in nature and can cause them to exhibit in different morphologies.

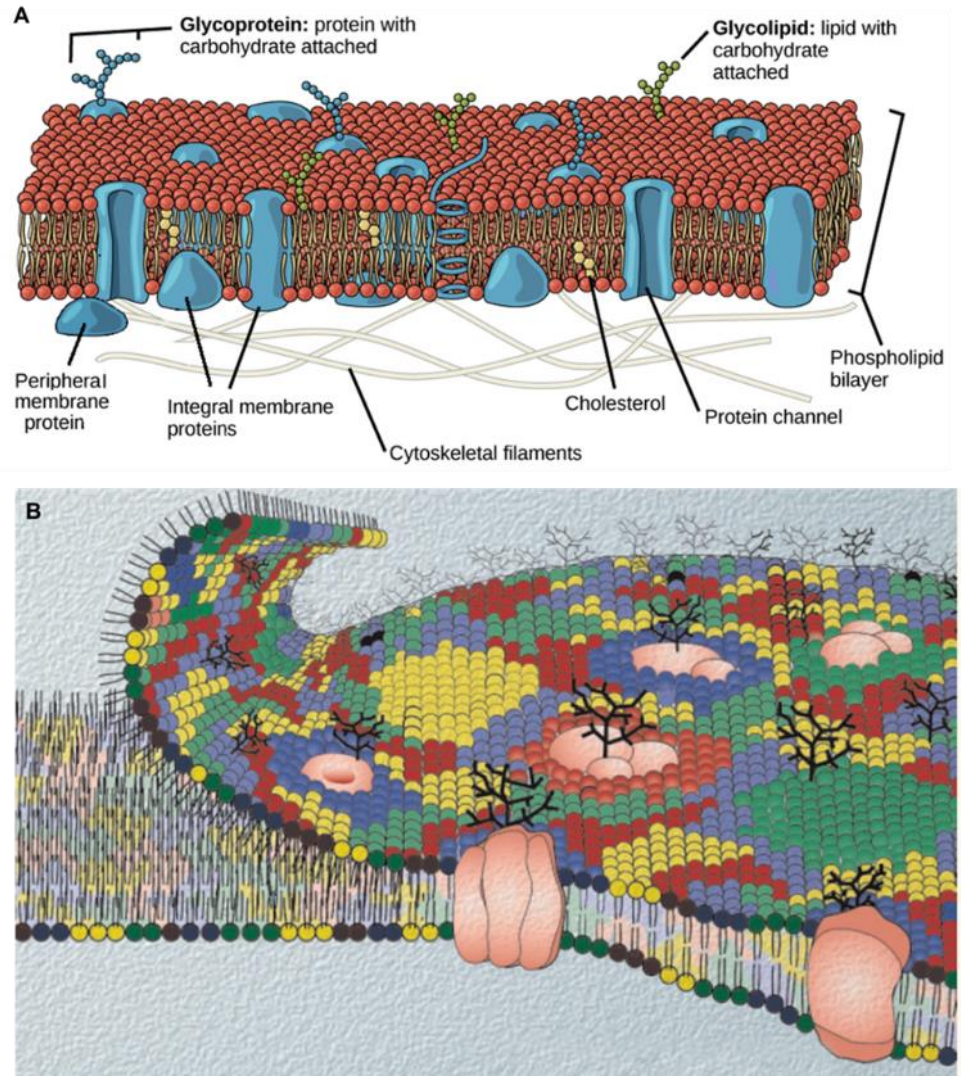

Figure 1.1. Schematic three-dimensional and cross-sectional representation of the plasma membrane illustrating different levels of complexity. (A) A simplified illustration in which the red spheres with two tails represent the lipid molecules forming a matrix. The blue, green and yellow necklace-like arranged spheres indicate glycoproteins, glycolipids and cholesterol, respectively. The solid blue bodies illustrate different types of proteins which are randomly distributed and protrude from or are attached to the membrane. The grey cylindrical lines show the cytoskeletal filaments. The image is reproduced from OpenStax Biology. (B) A more modern view of the plasma membrane. The variety in the colors across the bilayer represents different lipids organized in nano-domains. Their distribution in the membrane leaflet is asymmetric. Membrane proteins are shown as light pink structures while black branched structures on the surface of the bilayer illustrate glycolipids and glycoproteins. The image is reproduced from (Edidin, 2003).

1.2 The importance of shape transformations in cells and plasma membranes for biological functions

Cells and their compartments can adopt diverse morphologies to perform a wide range of biological functions in nature. One of the best examples for the relation between functional role and physiology to a specific morphology of cells is the biconcave disc shape (also termed discocyte) of erythrocytes (red blood cells) (Harvey, 1997). This unique shape of erythrocytes having a larger surface area relative to their volume gives them a flexibility to squeeze through narrow blood capillaries thus allowing them to perform efficient gas diffusion. Erythrocytes lack most organelles (including a nucleus), which leave more space for the production of hemoglobin thus maximizing their oxygen-carrying capacity (Harvey, 1997). Monitoring abnormalities in the shape, size and color of erythrocytes is widely used by hematology professionals in the diagnosis of the pathological conditions of the patients (Ford, 2013). The morphological differences between healthy and unhealthy erythrocytes are demonstrated in Figure 1.2. A recent study of Mesarec et al. (Mesarec et al., 2019) showed that the packing properties and curvature of the plasma membrane have an effect on the stabilization of the discocyte shape of healthy erythrocytes. The curvature of the plasma membrane is also known to affect the performance of pore-forming transmembrane proteins named ion channels (Kluge et al., 2022). Similarly, changes in the size, shape and membrane curvature of the mitochondria is found to influence Ca^{2+} transport, oxidative phosphorylation and adenosine triphosphate (ATP) synthesis mechanisms (Kowaltowski et al., 2019). Lastly, the examples of membrane remodeling events of organelles can be broadened by considering endoplasmic reticulum and Golgi apparatus changing their morphologies in response to metabolic or developmental cues, forming contact cites with plasma membrane and promoting various physiological processes in cells (Henne, 2021; Li et al., 2021; Agliarulo and Parashuraman, 2022).

The plasma membrane takes part in a variety of essential cellular events. It regulates the flow of substances into and out of the cell through chemical interactions, active transport, facilitated diffusion, passive diffusion, phagocytosis, and pinocytosis mechanisms which are crucial for cellular growth and repair (Schultz, 1980; Albers et al., 2012). The selective permeability of the cellular membrane to substances enables the cell to control its internal environment and the occurrence of the various cellular processes (Yang and Hinner, 2015). Among those processes, signal transduction assists cells to communicate with each other and respond to external stimuli (Saiz, 2017). Cellular respiration, on the other hand, generates energy for the cellular events (Lee, 2011). The plasma membrane also takes part in the intercellular communication, recognition processes, adhesion and immune responses (Lee, 2011; Saiz, 2017).

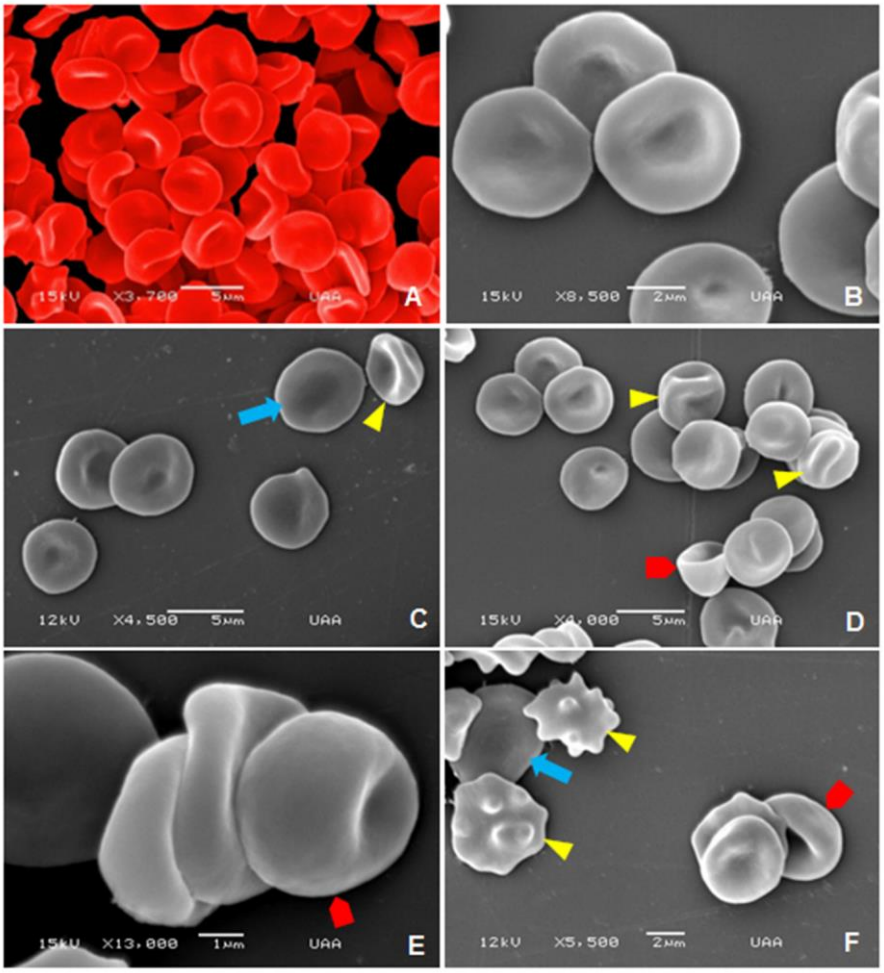

Figure 1.2. Scanning electron microscopy images of healthy and unhealthy erythrocytes in senior dogs. (A,B) The morphology of healthy erythrocytes with a discocyte shape. Unhealthy erythrocyte morphologies: (C) Leptocyte (blue arrow) and knizocyte (yellow arrowhead), (D) stomatocyte (red pentagon arrow) and knizocytes (yellow arrowhead), (E) stomatocyte (red pentagon arrow) and (F) Leptocyte (blue arrow), equinocytes (yellow arrowhead), and stomatocyte (red pentagon arrow) shapes. The scale bars are indicated in the bottom of each image. These images are reproduced from (Montoya-Navarrete et al., 2022).

During cellular events, the plasma membrane exhibits a variety of morphologies in order to maintain the cellular homeostasis and complement cellular functions. The dynamic shape transformations of the plasma membrane can result in the formation of local invaginations (inward folds) and exvaginations (outward bulges) of the membrane to facilitate selective transport of molecules. These modifications locally increase the surface area for the binding of the specific molecules in order to the transport proteins and other substances on the membrane (transmembrane proteins), thus ensuring efficient movement of substances while maintaining homeostasis (Wu et al., 2014). Shape transformations of the plasma membrane facilitate endocytosis and exocytosis processes as demonstrated in Figure 1.3. Next section provides a comprehensive overview of membrane shape transformations and cellular transport processes.

1.3 Membrane shape transformations in cellular transport processes

The dynamic transformations of membrane shapes play a pivotal role in cellular transport processes, enabling cells to efficiently adapt and respond to their ever-changing environments, thus contributing to the regulation of various physiological functions. Cellular transport processes include endocytosis, where cells engulf external materials, and exocytosis, where cells expel their contents to the external environment. The coordination of these mechanisms enables cells to regulate cellular trafficking, which is crucial for maintaining cellular homeostasis, communication, and nutrient uptake, demonstrating the dynamic nature of cellular membranes.

Endocytosis is the ingestion of substances by the cell. In this process, the substances are captured from the external environment of the cell and engulfed (i.e. internalized) into the cell through membrane invaginations and formation of vesicles by pinching off from the plasma membrane into the cell (Marsh and McMahon, 1999). Endocytic pathways can be mainly divided into 4 classes including receptor-mediated endocytosis (also known as clathrin-mediated endocytosis), caveolae, pinocytosis, and phagocytosis.

Among them, receptor-mediated endocytosis is the most common pathway, involving the formation of a protein coat made of clathrin that forms around a pit in the membrane (Kaksonen and Roux, 2018). Specific cargo binds to receptors on the cell surface, triggering the formation of a clathrin-coated vesicle that pinches off to deliver the cargo inside the cell (Kaksonen and Roux, 2018). This pathway can be used in the delivery of various ligands such as low density lipoprotein, transferrin, growth factors and antibodies (Kaksonen and Roux, 2018).

Caveolae-mediated endocytosis, on the other hand, is necessary for the transportation of cholesterol and signaling molecules to the cell (Pelkmans and Helenius, 2002). Caveolae are small invaginations in the membrane enriched with cholesterol, glycolipids and caveolin proteins. Specific cargo molecules bind to caveolar proteins, promoting a vesicle formation and internalization into the cell. Caveolae are known to involve in the internalization of glycosphingolipids; glycosylphosphatidylinositol-anchored proteins; extracellular ligands such as folic acid, albumin and autocrine motility factor; bacterial toxins such as cholera toxin and tetanus toxin; and several nonenveloped viruses such as Simian virus 40 and Polyoma virus (Pelkmans and Helenius, 2002). A recent study (Groza et al., 2024) has revealed that the endocytosis of toxins and pathogens is driven by a purely biophysical mechanism, with the internalization process relying on multivalent protein-lipid interactions between globular particles and the plasma membrane. Virions cause membrane

deformations upon adhesion and these binding-induced membrane deformations facilitate endocytosis (Groza et al., 2024).

Pinocytosis is another form of endocytosis in which cells internalize extracellular fluid and solutes. This pathway contains the formation of large, fluid-filled vesicles through extensive membrane ruffling. The vesicles then travel into the cytosol and fuse with endosomes and lysosomes. (Falcone et al., 2006)

Phagocytosis is another specialized form of endocytosis which is mainly used by immune cells to engulf solid particles larger than 0.5 µm in diameter such as small-sized dust particles, cell debris, microorganisms or dead cells. Pseudopods acting like a temporary arm-like projection of the plasma membrane extend from the cellular membrane, surrounding the target particle and forming a phagosome for the ingestion of the particle. (Rosales and Uribe-Querol, 2017)

Exocytosis has an opposite direction of transport of molecules in comparison to the endocytosis pathways. In this pathway, membrane buds are formed and fused with the cell exterior to release cellular products from the cells. Exocytosis occurs during the secretion of waste product and in the release of signaling molecules such as hormones and neurotransmitters during cell to cell communication, cell repair and growth processes. (Wu et al., 2014)

All these cellular pathways clearly demonstrate the importance of the morphological changes of the plasma membrane on the regulation of cellular viability and homeostasis.

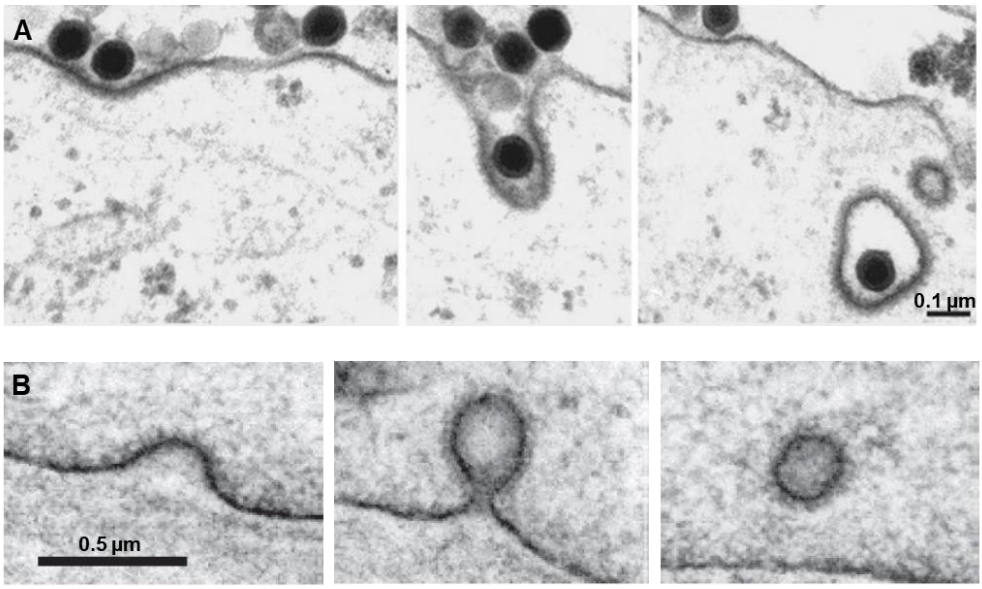

Figure 1.3. Monitoring endocytosis and exocytosis mechanisms in cells through transmission electron microscopy (TEM). (A) Clathrin-mediated endocytosis of *Adenovirus 2* by HeLa cells. TEM micrographs demonstrate the interaction of *Adenovirus 2* with the plasma membrane, formation of clathrin-coated

pit and an internalization of *Adenovirus 2* into the cell through a clathrin-coated vesicle. The scale bar corresponds to 0.1 µm. Images are reproduced from (Meier et al., 2002). (B) Exocytosis steps of the plasma membrane of the fibre cell of young human lens. The scale bar is 0.5 µm. Images are reproduced from (Dahm et al., 2011).

1.4 Building artificial cells for cell and plasma membrane mimetics

Considering the diversity of cell types, the structural complexity of each cell and the plasma membrane, as well as the dynamic interactions between cellular compartments and external cues, we can argue that resolving all the details of the individual function of each cellular component on the cellular events as well as the governing factors and underlying mechanisms of biological processes is still not feasible to address with the current biomedical technology. Understanding the complex organization of cells and cellular compartments is very important for controlling cellular processes and establishing efficient strategies to diagnose and repair dysfunctions in cells. In this respect, synthetic biology is a rapidly growing scientific field which aims to develop a better understanding of the complex biomachinery of cells. It also seeks to design novel, autonomous, cell-like biosystems with desired properties through the research tools and techniques of cell biology and bio-engineering, ultimately using them for the benefit of humanity (Woolfson and Bromley, 2011). One of the fundamental approaches of synthetic biology to overcome the complexity of biological systems is to use simplified bio-mimetic platforms to isolate the interested components of the cell and make the interpretation of their individual roles in cellular processes accessible and easy.

Two main strategies to form simplified artificial cells for characterizing the functions of cellular components are designated as *Top-down* and *Bottom-up* approaches (see Figure 1.4 for the schematic comparison of these two approaches). The *Top-down* approach starts with a living organism and simplifies its components by knocking out the genome to the minimum number of genes which are required for cellular viability or it totally replaces the genome with a synthetic one (Xu et al., 2016). This approach can be occasionally challenging due to high mortality rates of the final biosystem. The modified or inserted genes may create adverse effects and eventually kill the host cell. Additionally, the cost of the gene engineering processes of cells can be expensive (Xu et al., 2016). The *Bottom-up* approach is a cheaper and less-demanding alternative for the generation of simplified artificial cells (Xu et al., 2016). In this approach, artificial cells are created from scratch by using non-living entities as starting material to achieve the targeted molecular complexity. Bottom-up approach also bridges the gap between the non-living matters and living entities, thus it can help us to gain insights about the origin of life (Xu et al., 2016; Szostak, 2017). This approach relies on the self-assembling systems with amphiphilic molecules (such as lipids) having both hydrophobic and hydrophilic residues in their chemical structures. One of the basic requirements for building artificial cells to imitate the natural

cells is to provide a boundary to confine the interior cellular material and area to host various viability activities. The amphiphilic molecules in aqueous interface can spontaneously form monolayer, bilayer or multilayer structures, which can separate inner and outer environment through these self-assembled structures and mimic the plasma membrane (Alberts B, 2002). By diversifying the ingredients of these amphiphilic assemblies, i.e. adding other components of the plasma membrane such as proteins and carbohydrates, the properties and functions of the individual components of the plasma membrane in biological events can be deduced (Xu et al., 2016; Elani et al., 2018).

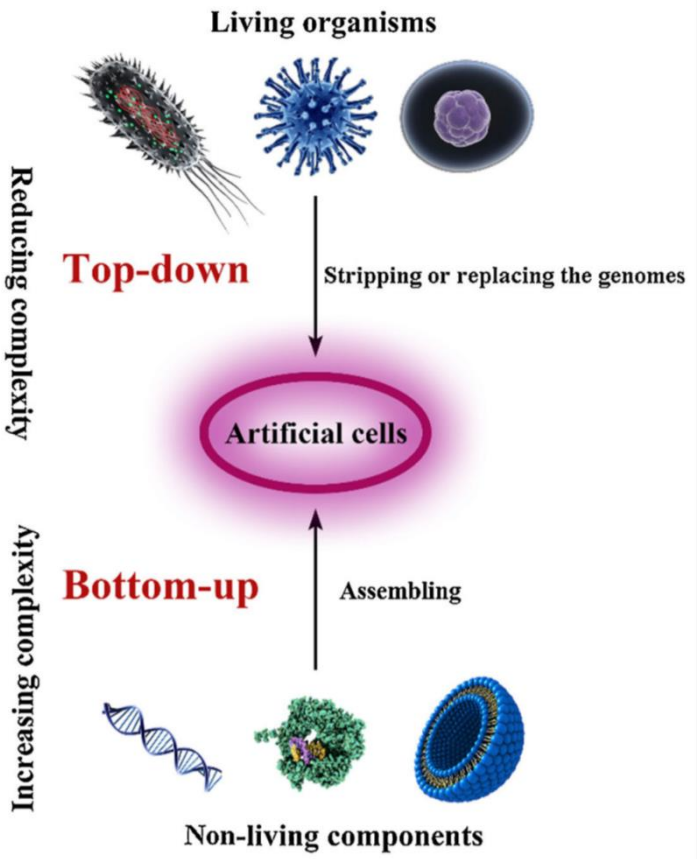

Figure 1.4. Building simplified artificial cells via *Top-down* and *Bottom-up* approaches. In the *Top-down* approach, artificial cells are created by knocking out or replacing the genomes of living organisms and only retaining a minimum number of genes to maintain cellular homeostasis. In the *Bottom-up* approach, artificial cells are created from the self-assembly of non-living components which can imitate the targeted properties or processes of the plasma membrane and cells. This image is reproduced from (Xu et al., 2016).

1.5 Model membranes made of phospholipids

Phospholipids can assemble into various structures, depending on their chemical properties and physical interactions with the water content and other solutions as well as the osmotic pressure and temperature of their environment (van Meer et al., 2008). Phospholipid-containing model membranes are one of the widely applied biomimetic systems for deducing the properties of the plasma membrane in physiological processes. Due to the abundance of phospholipids in the plasma membrane, this thesis also focuses on multicomponent model membrane systems containing phospholipid substances. The main studied multicomponent model membranes throughout the thesis include Langmuir monolayers, supported lipid bilayers (SLBs), large unilamellar vesicles (LUVs) and giant unilamellar vesicles (GUVs) schematically illustrated in Figure 1.5.

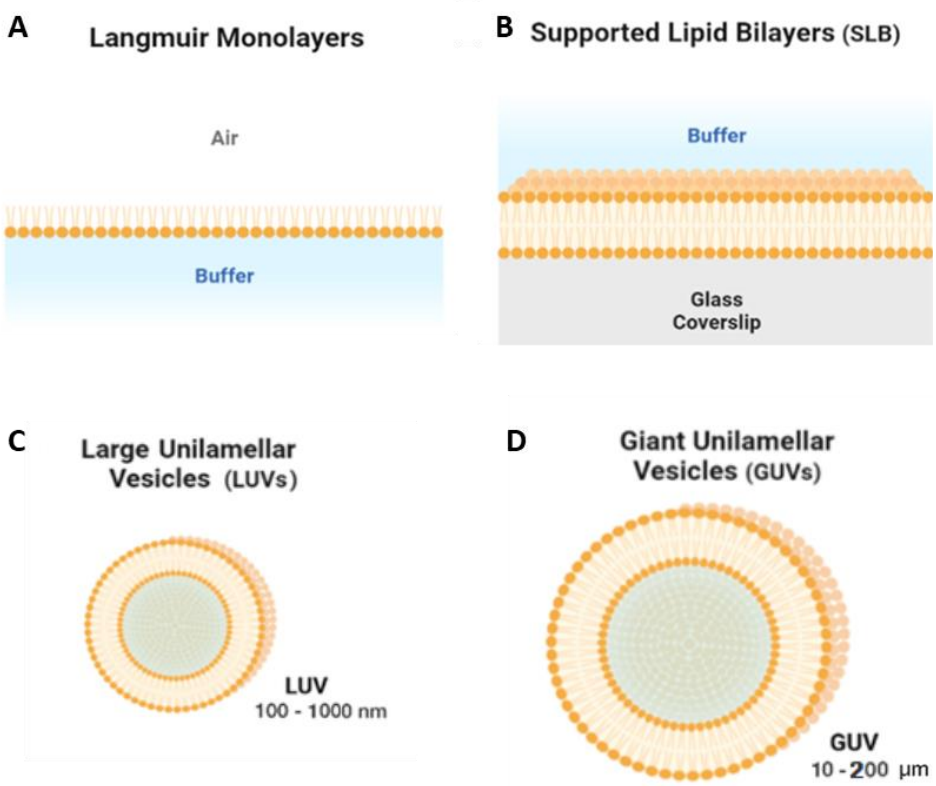

Figure 1.5. Sketches representing the different types of model membranes. (A) Langmuir monolayers are a thin monolayer of lipids at the air/water interface. (B) SLBs represent a single bilayer formed on a solid support. (C) LUVs have diameters ranging between 100 nm and 1000 nm and consist of a closed, single lipid bilayer. (D) GUVs having diameters in the micron-sized range have cell-size dimensions, and thus represent a more realistic model for plasma membrane biomimicry in comparison to the other three membrane models indicated above. This sketch is reproduced from (Brémaud et al., 2022).

Among others, **Langmuir monolayers** are one of the most simplified models for plasma membrane mimicry. They practically represent half a membrane. By forming a two-dimensional arrangement of lipids at a planar air-water interface, in which the lipid heads pointing towards the

water, they can mimic one leaflet of the membrane. This model is good for analyzing the packing properties and fluidity of the monolayer as well as studying the interactions of various molecules with one leaflet of the membrane and cellular processes occurring at the membrane surfaces (Brezesinski and Möhwald, 2003; Stefaniu et al., 2014). In this model, lipid composition as well as thermodynamic parameters such as surface pressure and temperature can easily be controlled. Thus, phase transitions of lipids can also be easily monitored (Stefaniu et al., 2014). However, monolayers lack the bilayer complexity of cell membranes. Insertion of transmembrane proteins or asymmetrical addition of molecules is not feasible. Monolayers cannot represent three-dimensional membrane dynamics. Particularly, the effects of membrane curvature on cellular processes cannot be captured in this membrane model (Sarkis and Vié, 2020).

SLBs provide more complex model membrane systems compared to Langmuir monolayers. They are formed from a lipid layer deposited and stabilized on a solid substrate such as glass, mica or gold. SLBs allow for the creation of well-defined, mechanically stable lipid bilayers with a controlled composition and asymmetry (Castellana and Cremer, 2006; Groves, 2007; Lind and Cárdenas, 2016). This membrane model is suitable for studying lipid-protein interactions, membrane dynamics, and phase transitions. SLBs are compatible with various biophysical techniques including fluorescence microscopy, atomic force microscopy, surface plasmon resonance, and electrophysiology, which makes the probing of the membrane dynamics, protein activity, and transport processes easier compared to some other model membrane systems (Castellana and Cremer, 2006; Groves, 2007; Lind and Cárdenas, 2016). However, the presence of the solid support can alter the fluidity and properties of the bilayer compared to free-standing model membranes, which may also affect certain protein-lipid interactions or membrane processes (Bechinger, 2019). SLBs also lack the full complexity of native cell membranes, particularly a real cytoplasmic environment cannot be captured, which limits the study of processes relying on interactions with cytosolic components (Bechinger, 2019). They also constrain out-of-plane deformations characteristic for curvature-associated processes.

LUVs and GUVs both consist of a closed single lipid bilayer dividing the aqueous environment into inner and outer compartments through the vesicle membrane. However, they differ in their size, which ascribe them with unique advantages for biomimetic studies (Moghimi, 2016). The size of LUVs ranges from 100 to 1000 nanometers (nm) in diameter (smaller vesicles are typically referred to as small unilamellar vesicles), which is close to the size of some viruses and nanoparticles (Rideau et al., 2018). LUV preparation protocols based on extrusion, typically result in a homogeneous size distribution among the produced population, which can lead to the generation of more consistent data during the experiments. LUVs are compatible with a wider range of techniques including

scattering methods, which offer additional insights about the properties of the investigated vesicles (Schwendener, 2007; Akbarzadeh et al., 2013). However, while being a good mimetic of intracellular and extracellular vesicles, LUVs cannot fully capture the actual sizes of cells in nature and the curvature of the plasma membrane. So, they cannot represent a realistic model for the biological processes in which the membrane curvature plays a significant role. GUVs, on the other hand, can provide a more realistic model to study the effects of cellular size and membrane curvature, because they retain cell-size dimensions (Dimova, 2019). GUV radii typically vary between 5-100 µm (Rideau et al., 2018; Dimova, 2019). Due to their larger sizes, GUVs are also accessible with optical microscopy techniques, which enables us to monitor dynamic processes in the membrane (Dimova, 2019). Depending on the preparation protocol, they may involve heterogeneities in lipid composition, shape, mechanical properties, and chemical properties of the produced vesicles (Walde et al., 2010). However, by combining various membrane manipulation approached with optical microscopy techniques, all these above-mentioned heterogeneities can be easily controlled and the vesicles with undesired properties can be easily diagnosed (Walde et al., 2010; Dimova, 2019).

In short, each different alternative of model membrane can play a specific role in the characterization of the plasma membrane components and cellular processes. Elucidation of the functions of cellular components on the various metabolic processes is very important for the control of these mechanisms and elimination of any corresponding abnormalities. Understanding the biological processes through model membrane systems can offer various applications in biotechnology for the development of the efficient and novel treatment approaches to overcome any pathological conditions, metabolic diseases and cellular defects (Stamatialis et al., 2008; Sarkis and Vié, 2020; Brémaud et al., 2022).

1.6 GUV preparation approaches

Throughout the thesis, GUVs represent widely used model membrane systems due to their distinct ability to capture dynamic membrane processes. Since morphological transformations of vesicles are the subject of the interest of this thesis, GUV studies offer a comprehensive framework for gaining insights into the modifications in the properties of the membrane during shape remodeling events. For these reasons, this chapter provides further information about GUV preparation and characterization techniques.

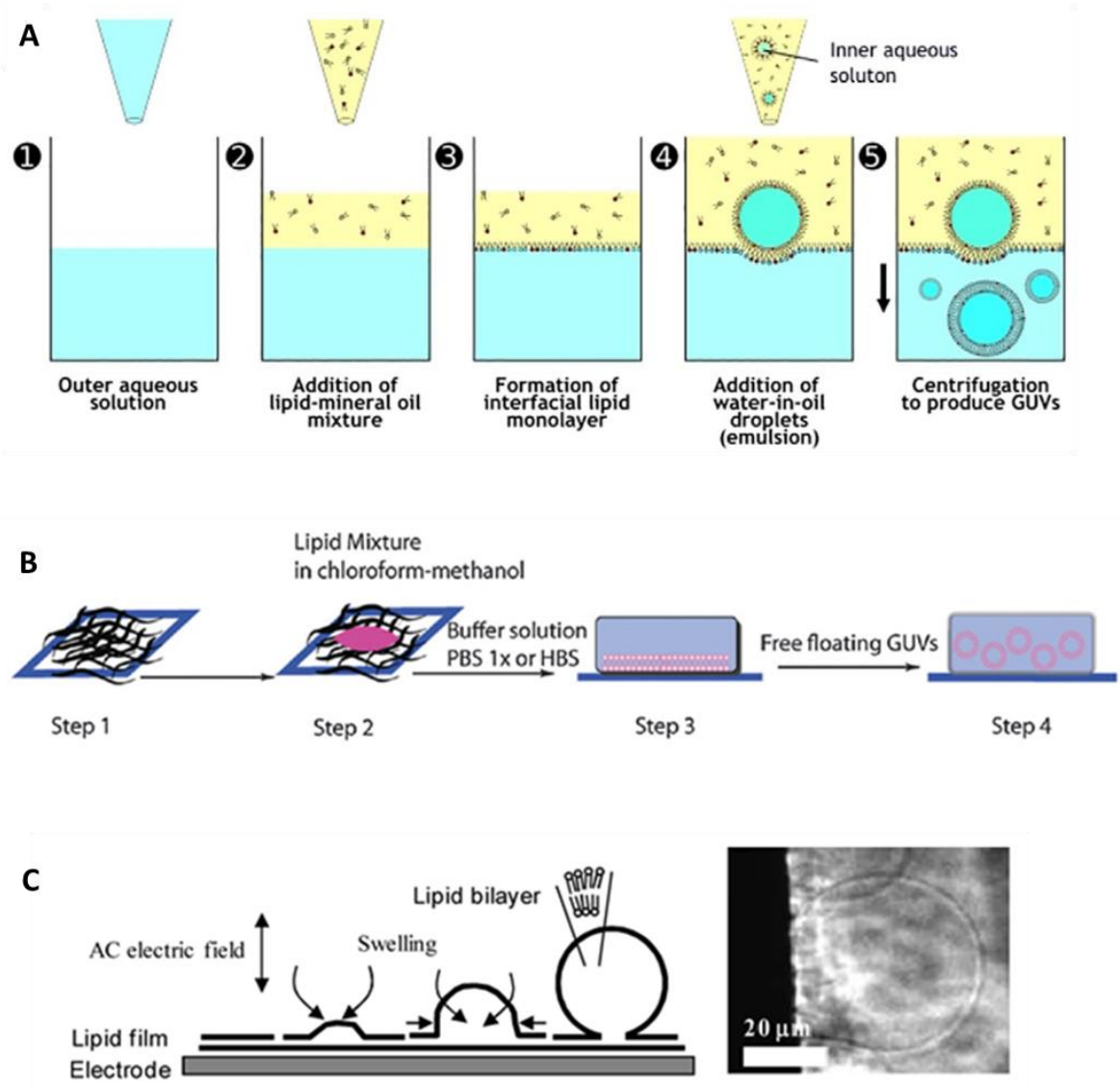

Figure 1.6. Illustration of widely-used strategies for GUV preparation. (A) Emulsion transfer method. Schematics demonstrate five main steps of the emulsion transfer protocol including the addition of lipid-mineral oil mixture to the outer aqueous solution, formation of interfacial lipid monolayer, addition of water-in-oil emulsion droplets and eventually formation of GUVs through a centrifugation step. This figure is reproduced from (Moga et al., 2019). (B) Gel-assisted swelling method. In the first step, polymer-based substrate spread on the glass surface and dried. Then, lipid mixture is spread on top of the dried substrate to form a thin lipid film. In the third step, the thin lipid film is rehydrated by the addition of buffer solution, which also hydrates the polymer forming a hydrogel beneath the lipid that leads to swelling of the bilayer and formation of GUVs. This figure is reproduced from (López Mora et al., 2014) (C) Electroformation method. Here, the lipids are deposited on conductive surfaces (electrodes) and hydrated under the application of an alternate current (AC). Schematic illustration summarizes the mechanism of electroformation of a GUV whereas the light micrograph demonstrates the result of a typical hydration process of a lipid bilayer forming a vesicle. With the application of the AC field, thin lipid film on the surface of the electrode undergoes the process of swelling till the lipid bilayer closes into a vesicle. This figure is reproduced from (Shimanouchi et al., 2009).

Various methodologies have been developed for the preparation of GUVs throughout the literature. The majority of the techniques mainly rely on either the assembly of vesicles from fluid interfaces or swelling of the vesicles on substrates (Walde et al., 2010; Dimova, 2019; Peter Walde, 2019). One widely used example is the emulsion transfer method, which starts with the formation of water droplets suspended in oil (water in oil emulsion) and covered by one monolayer of lipids at the droplet interface which will form the inner leaflet of the vesicles (Träuble and Grell, 1971; Szoka and Papahadjopoulos, 1980). A second lipid monolayer is formed by layering the emulsion at a water phase, whereby the free lipids in the oil phase adsorb at the oil-water to form this monolayer. Upon centrifugation, the droplets cross this oil-water interface and are wrapped by this second monolayer forming the outer leaflet of vesicle (see Figure 1.6A for the schematic overview of the protocol) (Träuble and Grell, 1971; Szoka and Papahadjopoulos, 1980). In this method, the density gradient between the inner and outer aqueous solutions and gravity significantly contribute to the formation of GUVs. In order to facilitate the transfer of the droplets with the inner aqueous solution through the interface and into the outer aqueous solution, both centrifugal force and microfluidic flow can be used (Moga et al., 2019; Ernits et al., 2024). This method is very suitable for the construction of asymmetric vesicles since two leaflets of a vesicle are formed independently. This method is also a good option for forming GUVs with charged lipids, encapsulating nucleic acids or LUVs, incorporating membrane proteins into the GUVs or mimicking the compartmentalization processes in cells. However, the main disadvantages of the emulsion transfer method are the polydispersity of the GUV population (in terms of the lipid content of the leaflets (if asymmetric vesicles are generated) and the size of the vesicles), presence of impurities due to the residual oil in the membrane and low control over the yield and stability of the GUVs. Integrating microfluidic approaches into the emulsion transfer method improves the monodispersity of GUVs and reduces the above-mentioned limitations (Matosevic and Paegel, 2011; Karamdad et al., 2015; Peter Walde, 2019).

Another major category of GUV preparation protocols involves the swelling of a thin lipid film that has been previously dried under vacuum and subsequently rehydrated with an aqueous buffer on the surface of various substrates. The substrate can be a glass or Teflon surface, and the rehydration process takes place slowly. This protocol is referred as the spontaneous swelling method (Reeves and Dowben, 1969; Mueller et al., 1983). Since it does not require any specialized equipment, it is a very simple and inexpensive method. However, it results in a low yield and variable size distribution of GUVs (Peter Walde, 2019). Additionally, rehydration process of lipid film may take several hours to even days with the spontaneous swelling method (Peter Walde, 2019). In order to speed the rehydration process and improve the eventual yield of GUVs, this protocol can be modified

by using polymer-based substrates or by applying mild electric fields through conductive surfaces (Peter Walde, 2019). The polymer-assited swelling employs substrates such as agarose (Horger et al., 2009) and polyvinyl alcohol (Weinberger et al., 2013). The lipids are deposited on a dried layer of polymers. With the addition of the hydration buffer, polymers swell into a hydrogel and form a porous layer. This porosity enhances the influx of the buffer as well as and speeds up the vesicle swelling process (see Figure 1.6B for the schematic overview of this protocol). The vesicles can be formed within a few minutes through gel-assisted swelling. This method is suitable for swelling in the presence of buffers of various salinity, encapsulation of biomolecules and incorporation of membrane proteins into GUVs. However, it has a major drawback of contamination in the GUVs due to the interference of the residual polymers, which may alter the physicochemical properties of the GUVs (Lira et al., 2014; Dao et al., 2017).

The application of AC electric fields to improve the GUV growth, which is named electroformation, results in clean GUVs compared to gel-assisted swelling methods (Peter Walde, 2019). In the mild AC fields, the lipids that have been deposited on an electrically conductive surface can undergo a better controlled hydration process to form a bilayer (see Figure 1.6C for the summary of the protocol and a microscopy image of the electroformed GUVs). In the electroformation method, the electrically conductive surface is typically an indium tin oxide (ITO) coated glass or platinum wire. In comparison to the surface of the platinum wire, the surface area of the ITO-coated glass is larger, which allows more lipids to swell in the larger area and results in a higher yield for GUV growth (Peter Walde, 2019). However, one concern about the electroformation method can be the possibility to produce oxidized products during the formation of GUVs in the presence of the polyunsaturated or charged lipids, which may require an extra caution on the optimization of the electric field parameters (Breton et al., 2015; Steinkühler et al., 2018). Since the electroformation protocol with ITO-coated conductive glasses provides a higher yield and cleaner GUVs, we have preferred to use this method for the preparation of GUVs. The chamber can be assembled by placing a Teflon spacer between the two ITO-glass plates facing their conductive surfaces to each other. The further steps for the used electroformation protocols are indicated in each corresponding chapter with more details.

1.7 Imaging the GUVs

After the preparation of the GUVs, the next important step is the characterization of the material properties and shape of the GUVs in order to assess their functionality in various biology applications. Among the various options, optical microscopy techniques are widely employed in this doctoral thesis to precisely observe the size, morphology, and dynamics of GUVs, both at the single vesicle level and in bulk. Bright field and phase contrast microscopy methods are label-free techniques and rely on the

usage of transmitted light. In bright field imaging, the visible light directly illuminates the sample by using the combination of lenses. Denser or thicker regions within the sample absorb more light and appear darker whereas less dense areas allow more light to pass through thus resulting in a brighter appearance. Since GUVs are transparent, they exhibit low inherent contrast and cannot be distinguished well from the background. So, bright field imaging cannot resolve very fine details within the GUV membrane (Bagatolli, 2019). Phase contrast microscopy offers higher resolution of the images in comparison to bright field microscopy technique. In this method, light undergoes varying degrees of phase shift as it passes through different regions of the sample, which differ in refractive index and thickness (Zernike, 1955). Phase contrast optics transforms the phase shifts into visible differences in the intensity of the transmitted light, thus providing an enhanced contrast for a transparent sample. The intensity of the transmitted light and the contrast of the image of the observed sample in phase contrast microscope depend on the magnitude of the optical path length of the specimen (Zernike, 1955). The regions of the sample with a higher refractive index appear darker than the background whereas the area of a sample having a lower refractive index than its surrounding shows a brighter contrast. In our experiments, growing GUVs in sucrose solution and then diluting them further in glucose solution creates different refractive indices between GUVs interior and exterior thus enabling us to obtain a good contrast and a better monitoring of GUVs in comparison to bright field imaging (Bagatolli, 2019). Phase contrast microscopy is an effective method for studying material properties of GUVs without any usage of dyes. However, resolving finer structural details, such as the presence of tubes or buds, remains challenging with this technique. In this respect, epifluorescence and confocal microscopy offer better resolution for observing these structural details in GUVs. Therefore, we have also used them as complementary approaches to gain additional insights into our biomimetic system.

Epifluorescence and confocal microscopy require the labeling of GUVs with fluorophores that absorb and emit light at specific wavelengths (Lichtman and Conchello, 2005). The excitation of these fluorescent molecules is then captured by the objective lens and directed to a detector to form an image (Lichtman and Conchello, 2005). These fluorophores are incorporated into the lipid bilayer or other components of the vesicle membrane, enabling detailed visualization of their localization, mobility, and interactions with other membrane components. Epifluorescence microscopy illuminates the entire specimen and collects fluorescence signals from all planes and provide a whole projection of the specimen. This technique allows for high sensitivity and specificity in detecting structural details of the vesicle bilayer, such as packing properties, stability, and elasticity, as well as some morphological changes like the formation of tubes and buds (Bagatolli, 2019). Additionally, it

facilitates multicolor imaging, enabling the simultaneous observation of dynamic changes in multiple membrane components at once. However, in order to avoid alterations in the material properties of the membrane due to the addition of fluorophores, their concentration should be kept to a minimum, and the GUV sample should not be exposed to intense light for prolonged periods. Prolonged exposure to intense light can degrade the fluorescent signal and oxidize membrane components, leading to photobleaching. Another limitation of epifluorescence microscopy is out-of-focus fluorescence, which results in high background noise and reduces image contrast and clarity.

In comparison to epifluorescence microscopy, confocal laser scanning microscopy is a more advanced optical imaging technique which enhances the resolution and contrast of the micrographs by eliminating out-of-focus fluorescence. It utilizes a focused laser beam to scan across a sample point by point and incorporates a pinhole aperture which restricts the illumination from outside the focal plane. So, only a specific plane illuminated by the laser is detected and out-of-focus fluorescence is blocked, which results in the generation of higher contrast and resolution images. This technique is particularly useful in detailed analysis of vesicle morphology and internal structures. Another significant benefit of the usage of confocal microscopy is its ability to perform optical sectioning, which provides depth-resolved images and facilitates a detailed three-dimensional reconstruction of vesicle geometry. However, this technique can be slower and more expensive due to the requirement of the specialized equipment and the point-by-point scanning. (Pawley, 2013)

1.8 Assessing membrane material properties using GUVs

Optical microscopy techniques can be combined with quantitative image analysis and various manipulation approaches such as microfluidics, optical tweezers, micropipettes and alternating or direct currents in order to characterize various parameters and deduce material properties and stability of the membrane from the vesicle response.

Microfluidic tools can be effectively used in vesicle formation, sorting and fusion processes (Robinson, 2019). They precisely control the microenvironment of the GUVs and manipulate the vesicles both individually and in bulk with high spatial and temporal resolution (see Figure 1.7A for an example of a microfluidic device). Usage of microfluidic devices enables high-throughput analyses with minimal sample volumes, thus enhancing experimental efficiency and reproducibility (Yandrapalli and Robinson, 2019). However, they require specialized equipment and may be technically challenging to fabricate and operate.

Micropipettes are employed to measure the mechanical properties of GUVs, such as membrane tension, elasticity, and bending rigidity, through techniques like aspiration and

micromanipulation (see Figure 1.7B for an example of micropipette aspiration of a GUV). This method provides direct mechanical measurements and can simulate physiological forces, but it is time-demanding, low-throughput, and requires skilled operation. The limitations include the potential for device-induced perturbations and the difficulty in mimicking in vivo conditions.(Dimova, 2014; Elisa Parra-Ortiz, 2019)

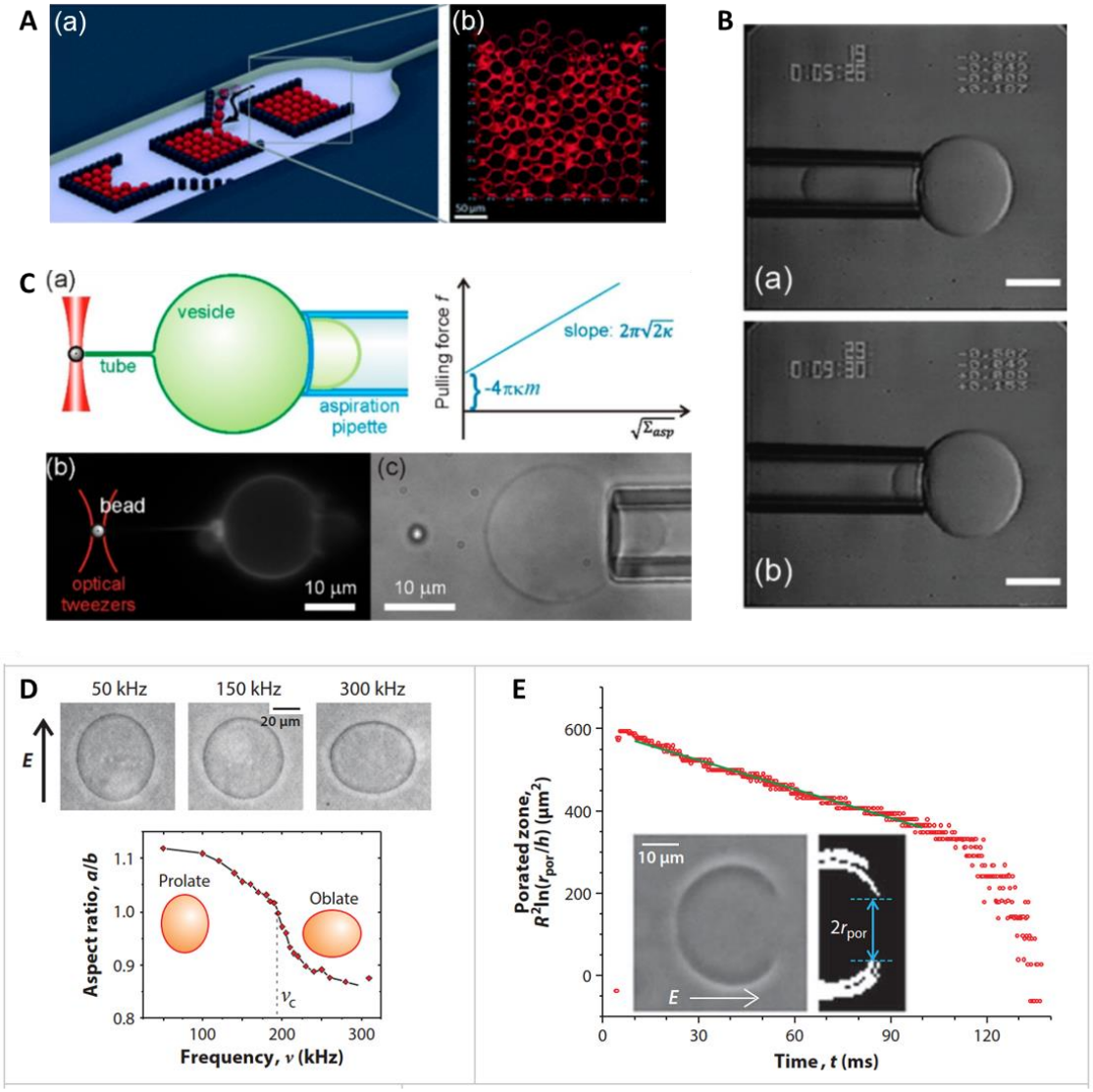

Figure 1.7. Several exemplary experimental approaches for the assessment of membrane material properties based on GUV manipulation. (A) A microfluidic tool to trap GUVs with ultra-high capacity. (A-a) Schematic illustration of the microfluidic channel, (A-b) A confocal cross section of the trapped GUVs in the channel. The scale bar corresponds to 50 µm. This panel is reproduced from (Yandrapalli and Robinson, 2019). (B-a,b) Micropipette aspiration of a GUV at different suction pressures. The scale bars are 10 µm. The images are reproduced from (Bagatolli and Needham, 2014). (C) Experimental assay for pulling out a nanotube from a GUV with optical tweezers. (C-a) sketch of the setup and principle of measurement and (C-b) epifluorescence and (C-c) bright-field images of an aspirated vesicle with a pulled tube. The scale bars are 10 µm. This panel is reproduced from (Karimi et al., 2018). (D) Membrane capacitance measurements from exposing GUVs to AC fields. The shape response of a

vesicle under a frequency sweep is used to determine the critical frequency of prolate-to-oblate transition, which depends solely on the membrane capacitance and the experimentally determined vesicle radius and solution conductivities. The vesicle shape is described in terms of the aspect ratio a/b of the long and short axis of the deformed vesicle. This panel is reproduced from (Vitkova et al., 2018). (E) Electroporation of a GUV and assessment of the membrane edge tension. The porated area of the GUV quantified as $R^2 \ln(\frac{r_{por}}{h})$ is plotted as a function of time (R is the vesicle radius; r_{por} is the pore radius; to avoid plotting a dimensional value in the logarithmic term, $h = 1$ μm). The solid line is a linear fit with slope that yields the edge tension. The inset shows a raw image (left) of a porated vesicle 50 ms after being exposed to a DC pulse with duration of 5 ms and amplitude of 50 kV/m. To the right is a processed image of the vesicle half facing the cathode, showing the pore diameter, $2r_{por}$. This panel is reproduced from (Portet and Dimova, 2010).

Optical tweezers utilize laser beams to trap and manipulate particles and GUVs with high spatial precision, enabling the study of membrane mechanical properties, interactions, and fusion events at the single-vesicle level (Jones et al., 2015) (see Figure 1.7C for an example of pulling out a nanotube from a GUV with optical tweezers). The advantages of optical tweezers include non-invasive manipulation and the ability to apply precise forces, though they are limited by their high cost and the requirement for specialized equipment and expertise (Wang et al., 2021; Cheppali et al., 2022).

In this thesis, we have particularly employed fluctuation spectroscopy and electromanipulation methods for the quantification of the material properties of the GUVs, which require a simpler instrumentation as well as reasonably facile experimental implementation and analysis compared to the above-mentioned techniques. For example, the fluctuation spectrum of a vesicle can be directly obtained from a series of optical microscopy images. In the absence of any external stimuli, the thermal motion of the lipid molecules within the bilayer causes the vesicles to exhibit spontaneous, small-scale undulations and morphological changes in the membrane at a microscopic level (Seifert, 1997). The amplitude and frequency of these thermal fluctuations depend on several factors such as membrane tension, bending rigidity, and the temperature of the surrounding environment (Rawicz et al., 2000).

In **fluctuation spectroscopy** method, the thermal fluctuations of the vesicle membrane are recorded for the analysis of the membrane bending rigidity which describes the ability of the membrane to curve (Dimova, 2014). This method involves capturing high-resolution phase contrast or confocal microscopy images of the GUV over time and extracting the contour of the vesicle membrane (Gracià et al., 2010; Faizi et al., 2020). By examining the amplitude and frequency of the membrane's spontaneous undulations, we can quantify how easily the membrane bends (Gracià et al., 2010). Fitting the observed fluctuation data to theoretical models allows for the estimation of the bending rigidity, which provides insights into the elasticity and stability of the vesicle membrane (Gracià et al., 2010; Dimova, 2014). Recently, in one of my collaboration projects, we have combined the

experimental fluctuation data of GUVs with simulation and theoretical analysis in order to explore how lipid mixtures in the composition of the vesicles affect the bending rigidity of the membrane (Sapp et al., 2023). Our studies about kinetic relaxation of the undulations of GUVs made of phosphatidylcholine-phosphatidylethanolamine mixtures validated the concept of diffusional softening, which describes how the membrane bending rigidity changes due to coupling of the undulations and the diffusion of lipids within the mixture. A vesicle membrane containing 40% phosphatidylethanolamine (while the rest was phosphatidylcholine) was found 25% softer than a single-component phosphatidylcholine vesicle. This work demonstrates that the fluctuation spectroscopy method can also be combined with computational approaches to provide a concise overview about membrane mechanical properties.

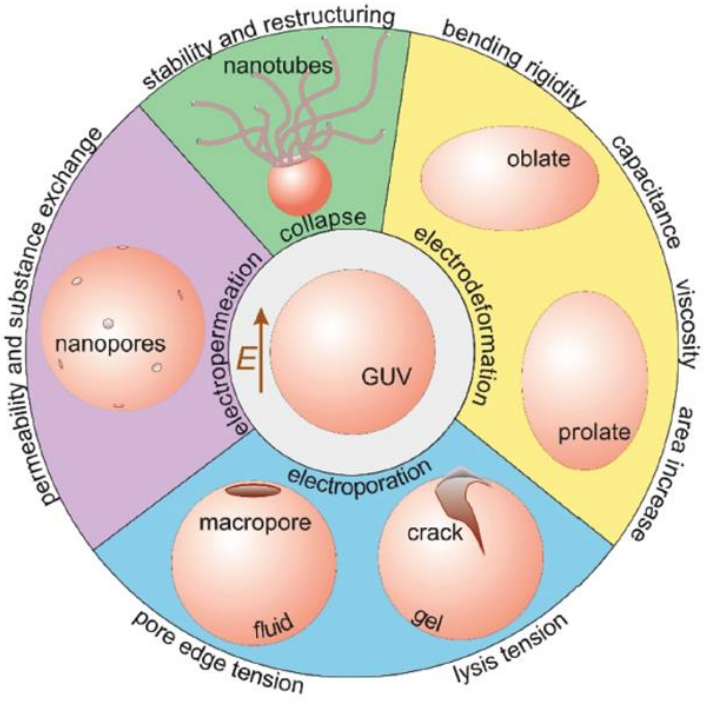

Figure 1.8. Schematics for the possible membrane characterization techniques based on exposing GUVs to electric fields. A broad range of parameters and material properties (including bending rigidity, capacitance, membrane surface shear viscosity, membrane area increase, lysis tension, pore edge tension, permeability and stability after poration) can be obtained from observing the response of GUVs to electric fields. This figure is reproduced from (Aleksanyan et al., 2023a).

Broader range of material properties of the GUV membrane can be studied when GUVs are subjected to **electric fields** (see Figure 1.8 for the overview of the possible approaches). Several electric field based approaches to measure various membrane characteristics are presented in a review with me as a first author (Aleksanyan et al., 2023a). Below, I will give a short overview of some of these approaches, with more emphasis to those relevant to this thesis.

Under **strong direct current (DC) pulses**, transient pores can form in the lipid bilayer; this process is known as electroporation.(Riske and Dimova, 2005) With GUV electroporation, the lysis tension and the pore edge tension values can be deduced respectively from the threshold of electroporation and pore closure dynamics (Riske and Dimova, 2006) (see Figure 1.7E for an example of electroporation and edge tension analysis of a vesicle). Depending on the membrane composition, the application of strong DC pulses can cause irreversible damage to the membrane, leading to vesicle rupture and collapse (Lira et al., 2021). Occasionally, electroporation may also increase the membrane permeability of GUVs due to the formation of long-lasting nanopores or defects in the bilayer after the application of DC pulses. This process is named as electropermeation and it is another measure to compare the stability of the membrane (Perrier et al., 2017).

In comparison to DC pulses, **AC fields** are in general weaker. They represent an oscillating electric field, which alternates the direction of the electric potential across the membrane and only causes vesicle membrane to deform under the influence of the induced electric stresses (Riske and Dimova, 2005). Subjecting a vesicle to AC pulses allows vesicle membrane to pull out the excess area stored in thermal fluctuations and deform into tenser ellipsoidal morphologies (Helfrich, 1974). By calculating the area of an ellipsoidal shape, electrodeformed vesicle from the optical microscopy images, the **excess area of a vesicle stored in thermal fluctuations** can be determined. The type and degree of deformation depends on the electric field strength and frequency as well as the conductivities of the internal and external medium of the GUVs (Dimova et al., 2007). Assessment of the AC field-induced shape deformations of the membrane enables us to deduce a wide range of material, electrical and viscoelastic properties of the vesicles, including the analysis of membrane bending rigidity, capacitance, viscosity and area increase (Aleksanyan et al., 2023a).

At high frequency range (between 1 – 10 MHz) and for arbitrary conductivity condition, GUVs exhibit spherical shapes because the ions in the solution cannot follow the field oscillations and induce any detectable deflection in the membrane to deform the vesicles (Dimova et al., 2007). At intermediate frequencies (between a few KHz and several MHz), the vesicles reveal prolate shapes when the conductivity of the internal solution of the GUVs is higher than the external one (Dimova et al., 2007). For prolate shapes, the long axis of the vesicles is oriented parallel to the field. Conversely, when the conductivity of the internal solution of a GUV is lower than the external one, the higher ion concentration in the external media compresses the vesicle from the outside along the direction of the field and the vesicle adopts an oblate deformation (Dimova et al., 2007). At intermediate frequencies, when the conductivities of the internal and external solution of the GUV are equal, quasispherical shapes can be observed. At low frequencies (below a few MHz), irrespective of the

conductivity conditions, the membrane acts as an insulator and the field deforms the vesicle into a prolate shape. The morphology diagram of the shape transformations of vesicles in various frequency and conductivity conditions is shown in Figure 1.9. In this thesis, by using the vesicle electrodeformation method and analyzing shape transformations of the vesicles at various frequency conditions, we have quantified the membrane area changes, capacitance and dielectric constant of vesicles containing various fractions of photoswitchable lipids (see Chapter 3 for experimental and theoretical details of each analysis).

Membrane capacitance can be determined by performing a frequency sweep, as shown in Figure 1.7D. When the solution conductivity inside the vesicle is less than that outside, the GUV exhibits a prolate to oblate shape transition under AC field with an increasing frequency (Aranda et al., 2008; Vlahovska et al., 2009; Yamamoto et al., 2010). During this morphological transition, the critical frequency at which the GUV becomes spherical is measured (Yamamoto et al., 2010; Salipante et al., 2012). By plotting the aspect ratio, a/b, of the long and short axis of the deformed vesicle, the critical frequency of a vesicle can be experimentally determined. The membrane capacitance can be then deduced from the critical frequency value (Salipante et al., 2012). Experimental and theoretical details of membrane capacitance analysis is further explained in Chapter 3.

In addition to experimental approaches, computational modeling of the lipid bilayer through Molecular Dynamics (MD) simulations is widely used throughout the literature to provide an atomistic level resolution with three-dimensional imaging of the lipid bilayer over time. MD simulations offer deeper insights into the structural organization, dynamics, and interactions of lipids within the bilayer (Moradi et al., 2019). In this thesis, we have also utilized MD simulations to obtain further structural details of our system and assess its key material properties both experimentally and computationally.

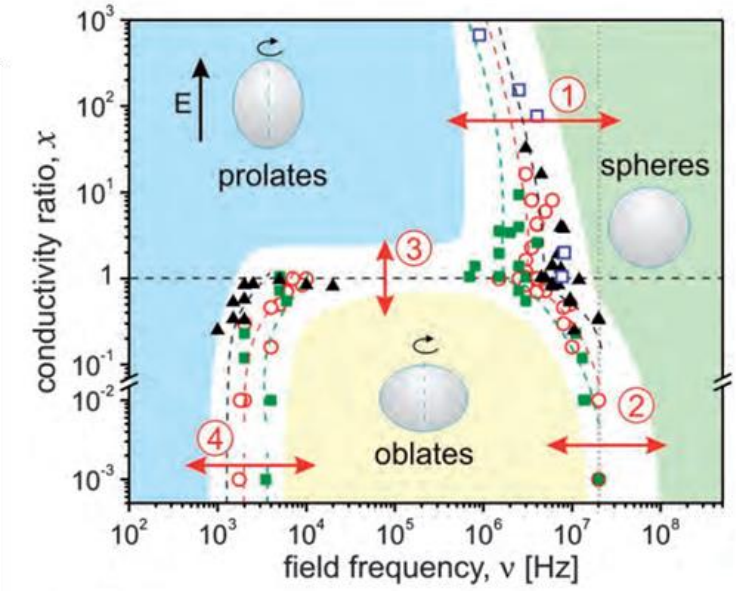

Figure 1.9. Morphology diagram of the shape transformations of vesicles at various frequency and conductivity conditions. Upper part of the diagram demonstrates the conditions in which the conductivity of the internal solution of the vesicles is higher than the external one outside. Then, GUVs transform from prolate to spherical morphologies with increasing field frequency. Lower part of the diagram shows the conditions in which the conductivity of the internal solution of the GUV is lower than the external one. Then, at lower frequencies GUVs undergo prolate-to-oblate transition while at higher frequencies they transform from oblate to spherical morphologies. This figure is reproduced from (Dimova et al., 2009).

1.9 Light and photoswitchable lipids

Light is one of the fundamental components of life on Earth, which plays a crucial role in various biological processes. In the broader context, light is essential for photosynthesis, the process by which green plants, algae, and certain bacteria convert light energy into chemical energy. Light catalyzes the conversion of carbon dioxide and water into glucose and oxygen, providing the primary energy source for these organisms and, indirectly, for heterotrophic organisms that consume them (Nelson and Yocum, 2006). This process not only produces oxygen, which is vital for the survival of aerobic organisms, but also forms the basis of the food chain, supporting life across the planet. In addition to photosynthesis, light affects circadian rhythms in both plants and animals, which regulate various physiological processes such as sleep-wake cycles, hormone release, and metabolism, thus ensuring that cellular activities are synchronized with the day-night cycle (Panda et al., 2002).

Light also facilitates the signaling mechanisms in organisms. In plants, phytochromes which are responsive to red and far-red light, regulate seed germination and flowering time (Li et al., 2011). Cryptochromes, which are responsive to blue and UV-A light, influence circadian rhythms, stem elongation, and leaf expansion (Lin and Todo, 2005). Phototropins are also sensitive to blue light and

they control the growth of plants towards light, stomatal opening, and chloroplast movements in response to changes in light intensity in order to optimize the photosynthetic efficiency of plants (Christie, 2007). In animals, light is detected through specialized photoreceptor cells in the eyes, including rods, cones, and intrinsically photosensitive retinal ganglion cells. These photoreceptor cells contribute to vision and circadian rhythm regulation (Molday and Moritz, 2015). In mammals, light influences the production of vitamin D in the skin, which takes part in calcium homeostasis, bone health and immune function (Bikle et al., 2018). Furthermore, light therapy also has clinical applications in the treatment of Seasonal Affective Disorder (a type of depression that occurs at a specific time of year, usually in the winter when daylight hours are shorter) (Terman and Terman, 2005) and some skin disorders including psoriasis (Elmets et al., 2019), eczema (Musters et al., 2021), vitiligo (Wang and Rodrigues, 2022), and acne (Diogo et al., 2021). Thus, light is a powerful regulator of a wide array of physiological and developmental processes thus enabling organisms to adapt to their environment, optimize energy usage, and maintain homeostasis.

The above-mentioned influence of light as an external trigger for various cellular activities makes it an appealing stimulus for the manipulation of cellular and biomimetic systems. Using light as a biophysical tool for regulating biomimetic systems and biological processes also offers additional advantages in terms of non-invasive control, precision, and flexibility (Deng et al., 2024). Since it is a non-invasive approach, light-induced changes in biomimetic systems are often reversible and tunable. The exposure of light can also be precisely controlled in terms of location, intensity and timing, which allows for targeted and real-time observation of dynamic processes with high spatial and temporal resolution (Boelke and Hecht, 2019). In addition, light can selectively and reversibly activate or deactivate specific components within a biomimetic system, which ensures minimal chemical interference and provides a versatile approach for studying complex cellular interactions (Höglsperger et al., 2022). Since optical manipulation approaches do not require additional reagents, they also eliminate the potential byproducts, side effects and interference with other biochemical processes, offering more accurate and precise investigations (Boelke and Hecht, 2019). Moreover, these approaches are also compatible with a wide range of imaging and analytical techniques, such as fluorescence microscopy and spectroscopy, which enhances the depth and breadth of experimental investigations (Deng et al., 2024). All these beneficial features render light as a powerful manipulation tool for biomimetic systems to perform comprehensive studies in a simple setup.

In order to utilize light efficiently for the control of biomimetic membrane models and cellular processes, a wide variety of photoresponsive (macro)molecules have been synthesized and integrated to the biomimetic platforms over the last decade. Photoresponsive molecules can undergo a rapid

change in their conformation, polarity, electronic state, physical properties, or biological activity upon exposure to specific wavelengths of light (Dube et al., 2019). For example caged ligands have been extensively used in a variety of biological applications, which contain photocleavable protecting groups rendering these molecules inactive without application of light (Höglinger et al., 2014). Active molecules can only be released upon the exposure of the specific wavelength of light when the protection group is cleaved from the ligand (Höglinger et al., 2014). This approach precisely activates the ligand at the targeted region, however uncaging is an irreversible process. Once ligand is activated, it is not possible to control the deactivation process (Lee et al., 2009). Among the photoresponsive molecules, photoswitches can offer a better control over biological processes by changing reversibly upon irradiation at another wavelength of light or undergoing a thermal relaxation to the initial conformational state when the light is switched off (Wang and Zhang, 2012). They often have the ability to remain stable over the repeated cycles of activation and deactivation without any degradation. Molecules containing diarylethene (Irie, 2000), spiropyran (Klajn, 2014) and azobenzene (Beharry and Woolley, 2011) belong to this category. Strategies for integrating these molecules into biomimetic systems include conjugating them to proteins, embedding them in lipid bilayers, and designing responsive hydrogels and nanoparticles.

Among the photoswitches, azobenzenes are reported as one of the most widely used and well-characterized class of photoswitches for the optical control of biomolecules (Beharry and Woolley, 2011). The azobenzene molecule is composed of two phenyl rings linked by a N=N double bond. When it is subjected to UV irradiation, it isomerizes from the thermally more stable *trans* configuration to the higher energy *cis* conformation. However, exposure to blue illumination reverses the isomerization process. It is reported that at equilibrium conditions in the dark, more than 99% of the molecules are in *trans* conformation (Dias et al., 1992). The geometry of *trans* azobenzene is almost planar thus having a dipole moment of nearly zero (Marturano et al., 2017). The *cis* isomer on the other hand exhibits a bent conformation with its phenyl rings twisted $\sim 55°$ out of the plane from the azo group, which has a dipole moment of 3 Debye (Marturano et al., 2017). The values for end-to-end distance for each isomer is different. For example, the distance between the carbons at the *para* positions of the rings is found to change by ~ 3.5 Å from *trans* to *cis* isomers (Marturano et al., 2017). These conformation differences and the fast timescale (few picoseconds) of the isomerization process have increased the interest towards synthesis of azobenzene-conjugated novel macromolecules over the years for further applications in material research and biomimetic studies. Over the years, a diverse range of photolipids has been developed by functionalizing phosphatidylcholine, ceramide, sphingomyelin, cholesterol, diacylglycerol, and phosphatidylserine with azobenzene moieties (Frank

et al., 2016; Pernpeintner et al., 2017; Lichtenegger et al., 2018; Hartrampf et al., 2023). Most of these photolipids are now commercialized on the market due to the high demand in various biochemistry studies. In this thesis, we have used a commercially available azobenzene-phosphatidylcholine (azo-PC) photolipid for the preparation of our biomimetic system with GUVs (see Figure 1.10 for the chemical structure of azo-PC). Since phosphatidylcholine is one of the most abundant lipid of animal cells (Barbour et al., 1999), usage of phosphatidylcholine derived photolipid make our studies biologically more relevant (see Figure 1.10A for the chemical structure of 1-palmitoyl-2-oleoyl-sn-glycero-3-phosphocholine, POPC, and azo-PC used throughout the thesis). Obtaining it commercially ensures consistent purity and accurate composition under the strict production and quality control standards, which is crucial for the reproducibility and reliability of experimental results. Further details about azo-PC photolipid and vesicles are provided in Chapter 3.

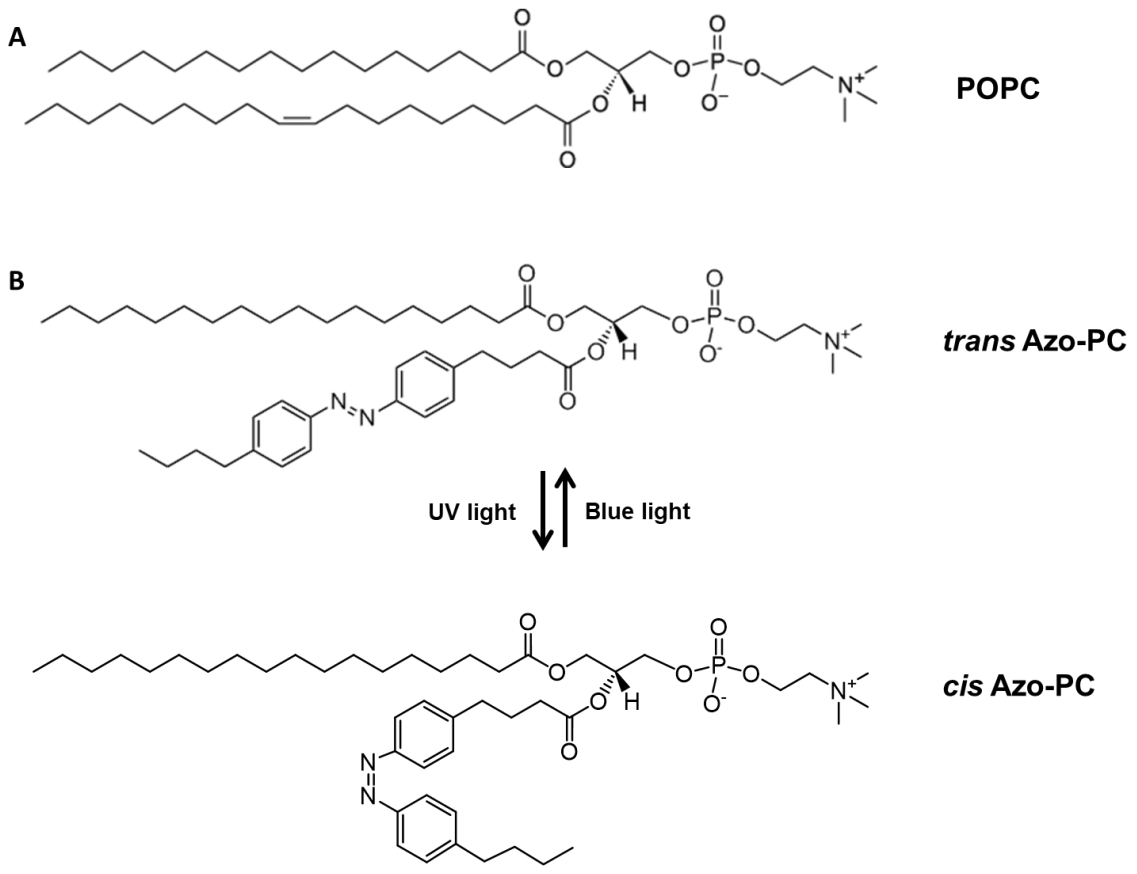

Figure 1.10. Chemical structures of 1-palmitoyl-2-oleoyl-sn-glycero-3-phosphocholine, POPC (A) and 1-stearoyl-2-[(E)-4-(4-((4-butylphenyl)diazenyl)phenyl)butanoyl]-sn-glycero-3-phosphocholine, azo-PC (B). Azo-PC undergoes *cis* and *trans* photoisomerization under UV and blue irradiation, respectively.

2 Objectives and overview of the thesis

During cell life, a wide range of morphological changes occur in the plasma membrane in order to maintain cellular homeostasis and viability. Regulation of membrane morphology is crucial for the control of membrane transport mechanisms and treatment of the corresponding disorders in the cellular and membrane trafficking events. The reversibility, physiological compatibility and high spatiotemporal precision of light-triggered processes render light an efficient external stimulus for the manipulation of biologically relevant events. In this doctoral thesis, we aimed to establish a light-triggered biomimetic platform for the modulation of membrane properties, shape and transport by the usage of azo-PC containing model membranes, particularly GUVs. In the scope of the thesis, photoswitchable GUVs were designed as bio-inspired, minimalistic artificial machinery enabling the transport of molecules between the vesicle interior and the external environment through the light-triggered modifications induced by azo-PC photoisomerization in the membrane. Towards the end of my PhD studies, I also explored the possibility of reconstituting the mechanosensitive channel MscL in them. The overall objectives were as listed below:

- **To characterize the dose dependent effects of azo-PC photoisomerization on the material properties and morphology of the vesicles in order to determine the sufficient amount of azo-PC in the membrane necessary for light-triggered molecular transport.** The mechanism by which azo-PC photoisomerization induces changes in vesicle morphology has been previously explored in the literature, but it remains elusive and insufficiently understood due to inconsistent results among different research groups. We investigated the photoresponse of various membrane models containing different fractions of azo-PC, including GUVs, Langmuir monolayers, LUVs, and SLBs, and linked our experimental results with those from MD simulations of bilayer patches of analogous composition. This approach allowed us to develop a comprehensive understanding of the photoswitchable membrane system at both micro- and nanoscale as well as the leaflet and molecular levels. We quantified light-induced changes in the membrane area and thickness, morphology, elastic and electrical properties, and deduced the effects of azo-PC photoisomerization on the organization and restructuring of the bilayer at the molecular level. We critically addressed existing discrepancies in the literature and proposed potential reasons for inaccurate results in quantifying the effects of azo-PC photoisomerization in the membrane. Furthermore, we tested the applicability of the exogenous addition of azo-PC to pre-formed membranes of artificial cells to observe the photoresponse of

azo-PC incorporated asymmetric vesicles. These findings were summarized in (Aleksanyan et al., 2023b).

- **To employ azo-PC photoisomerization in the membrane to control the endocytosis process in minimalistic artificial cells and allow the transport of protein condensates into cells.** We established a minimalistic biomimetic platform by using azo-PC containing GUVs and glycinin condensates, and explore the potential of this system for light-triggered and reversible endocytosis of protein condensates. The light-induced changes in the affinity of the protein condensate to the membrane were quantified. The kinetics of the light-triggered condensate engulfment and reversibility processes were analyzed. The degree of penetration of the protein condensates into the azo-PC vesicles was calculated. In addition to experimental assessment, theoretical calculations provided a detailed characterization of the photoswitchable engulfment mechanism of protein condensates into azo-PC vesicles. The results of this work were summarized in (Mangiarotti et al., 2024) with shared first author contribution by me.
- **To employ azo-PC photoisomerization to control the gating activity of mechanosensitive ion channels integrated in the membrane and allow the transport of small molecules across the membrane.** MscL was successfully reconstituted into azo-PC containing GUVs. The light-induced gating activity of MscL was tested by monitoring the permeation of the sulforhodamine molecules into the GUV interior after the exposure of the azo-PC containing vesicles to the UV and blue light.

This thesis is structured as a cumulative thesis and divided into six chapters. Chapter 1 introduced relevant concepts and terminology about the cells, plasma membrane and biomimetic membrane models for this doctoral study. It also reviewed the importance of shape transformations of cells in membrane transport processes, explained the strategies to build the artificial cells for the cell and plasma membrane mimetics, compared the advantages and limitations of the most common GUV preparation techniques, summarized the used characterization techniques in this doctoral thesis to assess material properties of the vesicles, and lastly described the motivations and approaches to use light and photoswitchable lipids for the manipulation of membrane properties, shape remodeling events and transport mechanisms. Chapter 2 describes the objectives and overview of the thesis project. Chapters 3, 4 and 5 show the main studies of this research as also outlined in the aims above. Chapters 3 and 4 are published manuscripts in the journal of *Advanced Science*, which contain independent sections of abstract, introduction, materials and methods, results and discussion,

conclusions, supplementary information and the bibliography of the scientific references cited in the main manuscript and supplementary files. Chapter 3 shows our approaches for the characterization of the dose dependent effects of azo-PC photoisomerization on the material properties and morphology of the vesicles and compares the accuracy of our results with the previously published values. It also reports new findings on membrane properties such as capacitance and the response of phospholipid membranes to externally introduced azo-PC. In Chapter 4, we explore the possibility of altering lipid-protein interactions between azo-PC containing GUVs and protein condensates via photoisomerization of azo-PC. The light-induced area change in the membrane allowed us to establish photoswitchable endocytosis of protein condensates. Chapter 5 contains our preliminary studies on the photoactivation of the MscL ion channel in azo-PC containing GUV membranes, facilitated by the photoisomerization of azo-PC within the GUV bilayer. It also contains independent sections of abstract, introduction, materials and methods, results and discussion, conclusions. Chapter 6 provides an extended summary about all the main findings of this doctoral thesis, emphasizing their significance and impact on the field, discusses the current limitations, strategies to overcome the current limitations and the broader implications of the results described in Chapters 3, 4 and 5. Lastly, it proposes future research directions to explore.

3 Photomanipulation of minimal synthetic cells: area increase, softening and interleaflet coupling of membrane models doped with azobenzene-lipid photoswitches

Mina Aleksanyan[1,2], Andrea Grafmüller[1], Fucsia Crea[3], Vasil N. Georgiev[1], Naresh Yandrapalli[1], Stephan Block[2], Joachim Heberle[3], Rumiana Dimova[1]

[1] Max Planck Institute of Colloids and Interfaces, Science Park Golm, 14476 Potsdam, Germany;

[2] Institute for Chemistry and Biochemistry, Freie Universität Berlin, 14195 Berlin, Germany;

[3] Department of Physics, Freie Universität Berlin, 14195 Berlin, Germany

Advanced Science, **2023**, 10(31), e2304336

Contributions

Mina Aleksanyan performed all vesicle-based work. Dr. Andrea Grafmüller performed the simulations. Fucsia Crea performed the experiments on monolayers. Mina Aleksanyan, Dr. Vasil N. Georgiev, Fucsia Crea, Dr. Andrea Grafmüller analyzed data. Dr. Naresh Yandrapalli prepared supported lipid bilayers and generated atomic force microscopy (AFM) data. Dr. Stephan Block analyzed AFM data. Dr. habil. PD Rumiana Dimova and Prof. Dr. Joachim Heberle proposed the project. Mina Aleksanyan wrote the manuscript with contributions from all authors.

The original article including the supporting information is included on the following pages and available online at:

https://doi.org/10.1002/advs.202304336

ADVANCED SCIENCE
Open Access
www.advancedscience.com

Photomanipulation of Minimal Synthetic Cells: Area Increase, Softening, and Interleaflet Coupling of Membrane Models Doped with Azobenzene-Lipid Photoswitches

*Mina Aleksanyan, Andrea Grafmüller, Fucsia Crea, Vasil N. Georgiev, Naresh Yandrapalli, Stephan Block, Joachim Heberle, and Rumiana Dimova**

Light can effectively interrogate biological systems in a reversible and physiologically compatible manner with high spatiotemporal precision. Understanding the biophysics of photo-induced processes in bio-systems is crucial for achieving relevant clinical applications. Employing membranes doped with the photolipid azobenzene-phosphatidylcholine (azo-PC), a holistic picture of light-triggered changes in membrane kinetics, morphology, and material properties obtained from correlative studies on cell-sized vesicles, Langmuir monolayers, supported lipid bilayers, and molecular dynamics simulations is provided. Light-induced membrane area increases as high as ≈25% and a ten-fold decrease in the membrane bending rigidity is observed upon *trans-to-cis* azo-PC isomerization associated with membrane leaflet coupling and molecular curvature changes. Vesicle electrodeformation measurements and atomic force microscopy reveal that *trans* azo-PC bilayers are thicker than palmitoyl-oleoyl phosphatidylcholine (POPC) bilayers but have higher specific membrane capacitance and dielectric constant suggesting an increased ability to store electric charges across the membrane. Lastly, incubating POPC vesicles with azo-PC solutions results in the insertion of azo-PC in the membrane enabling them to become photoresponsive. All these results demonstrate that light can be used to finely manipulate the shape, mechanical and electric properties of photolipid-doped minimal cell models, and liposomal drug carriers, thus, presenting a promising therapeutic alternative for the repair of cellular disorders.

1. Introduction

Conversion of light into mechanical energy as established with photoresponsive molecules provides a clean and renewable source of energy for the fundamental units of life, which offers a potential solution to reducing the demand for rapidly depleting natural resources as well as building a more sustainable world for future generations.[1] Examples include light-driven biocompatible micropumps/microrobots to generate fluid flow[2] as well as transport of macromolecules[3] in biotechnology applications, photoactive micro/nanomotors for wastewater treatment[4] as well as heavy metal removal and sensing,[5] thus providing applications in environmental remediation.[6] One of the advantageous features of light-induced processes is the high spatiotemporal precision allowing control over the targeted system.[7] Adjustment of exposure time, intensity, and wavelength of irradiation also reduces the number and amount of byproducts since light-induced processes generally do not require additional reagents.[7b] Photoprocesses are usually fast and reversible, in which light is used to interconvert photochemically active materials, known as photoswitches, between the low energy, thermodynamically favorable state, and high energy, kinetically favorable metastable states.[8]

Among the myriad of photoresponsive molecules in the literature,[9] azobenzene-derived photoswitches are most commonly studied[10] and the spectrum of applications includes molecular solar thermal energy storage,[1b,11] catalysis of

M. Aleksanyan, A. Grafmüller, V. N. Georgiev, N. Yandrapalli, R. Dimova
Max Planck Institute of Colloids and Interfaces
Science Park Golm
14476 Potsdam, Germany
E-mail: Rumiana.Dimova@mpikg.mpg.de

The ORCID identification number(s) for the author(s) of this article can be found under https://doi.org/10.1002/advs.202304336

DOI: 10.1002/advs.202304336

M. Aleksanyan, S. Block
Institute for Chemistry and Biochemistry
Freie Universität Berlin
14195 Berlin, Germany

F. Crea, J. Heberle
Department of Physics
Freie Universität Berlin
14195 Berlin, Germany

chemical reactions,[12] generation of photostructured polymers,[13] molecular recognition,[14] modulation of neurotransmission,[15] design of photochromic materials,[16] drug delivery systems,[17] optoelectronics[18] and photopharmacological tools.[19] Typically, azobenzene derivatives isomerize from thermodynamically stable *trans* state to metastable *cis* isomer (π–π^* transition) with the effect of ultraviolet type A (UV-A) illumination (365 nm) whereas the irradiation of blue light (465 nm) favors n–π^* transition and reverses the process.[20] Herein, we employ 1-stearoyl-2-[(E)−4-(4-((4-butylphenyl)diazenyl)phenyl)butanoyl]-sn-glycero-3-phosphocholine photoswitch (azo-PC) to build a synthetic photobiomachinery to control membrane shape and mechanical properties of minimal cells for potential biomedical applications.

In biological cells, it is known that cellular morphology plays an important role in regulating cellular activities such as endocytosis,[21] exocytosis,[22] gene expression mechanisms,[23] stem cell differentiation,[24] and proliferation.[25] The abnormal changes in the membrane morphology (e.g., excess membrane area with respect to enclosed volume caused by external triggers) and the incompetency of biological cells to modulate their membrane properties can be associated with accompanying implications in cellular homeostasis,[26] pathological developments,[27] cancer progression[28] or apoptosis.[29] A fast-responding external trigger such as light for controlling membrane area and mechanical properties can facilitate transmembrane transport and exchange of substances across the cell membrane thus reducing the above-mentioned harmful effects stemming from the malfunction of cellular processes.

The response of membranes to external triggers can be visualized in giant unilamellar vesicles (GUVs).[30] GUVs are occasionally referred to as minimal cells, because of their size and features allowing membrane reconstitution and encapsulation of important cellular elements. Because of their large size, GUVs offer the possibility to directly monitor the membrane under a microscope. Light–triggered changes have been investigated on GUVs to interrogate, among others, i) light-sensitive proteins embedded in the membrane such as the photoreceptor bacteriorhodopsin,[31] ii) the photoactivation of channel proteins,[32] iii) membrane-embedded fluorescent dyes which raise the membrane tension and can cause transient poration under irradiation.[33] The effect of azobenzene derivatives has also been studied with giant vesicles. Examples include light-triggered changes in membrane properties[32b,c,34] as well as phase state or fluidity.[34c,d,35] However, some of the studies on membrane mechanical properties, area changes, and thickness lack accurate and consistent characterization (as we discuss in Section 3), while quantitative evaluation of the photoisomerization effects on other characteristics such as the membrane capacitance, dielectric constant, and interleaflet coupling is still missing. Furthermore, to the best of our knowledge, the dose-dependent effect of azobenzene derivatives has been explored only to a very limited extent and mainly with water-soluble light switches, which upon insertion into the GUV membrane induce bursting or morphological transformations.[32c,d] Indeed, understanding the fraction-dependent effect of membrane photoswitches is important when considering the potential implementation of these molecules for the local modulation of membrane characteristics such as thickness, tension, fluidity, and permeability. Water-soluble derivatives are probably less suitable for such applications than more hydrophobic membrane analogs.

In this work, we investigate the dose-dependent function of an azobenzene-derived lipid analog (azobenzene-phosphatidylcholine, azo-PC, see **Figure 1**A) applied to lipid bilayers made of palmitoyl-oleoyl phosphatidylcholine (POPC) and employed giant vesicles to construct artificial photoswitchable cell mimetics from sustainable biomaterials. We subject this system to a thorough investigation for potential biomimetic purposes and applications in biomedical research. In parallel to our minimalistic cell model based on GUVs, we probe the response of Langmuir monolayers, large unilamellar vesicles (LUVs), and supported lipid bilayers (SLBs) with analogous composition and bilayer patches constructed with molecular dynamics (MD) simulations to interrogate the system at the leaflet and molecular level, respectively. Characterizations of light-induced membrane shape transformations of GUVs membranes containing azo-PC have been reported previously,[34a,c,d] however, lacking the quantitative link between material properties and membrane parameters such as changes in area and thickness, morphology, elastic and electrical properties, and their relation to organization and restructuring at the molecular level. Herein, by combining a comprehensive set of experimental methods and model membrane systems with MD simulations, we provide a holistic picture of the photoresponse of membranes containing azo-PC. We first establish an experimentally undemanding approach for direct evaluation of photo-induced area changes based on GUV deformation in electric fields. The method is then employed to characterize the photoswitch isomerization kinetics and reversibility. Comparison across different model systems is also provided. We provide the first measurements on membrane thickness and specific capacitance of azo-PC bilayers and elucidate the interrelation between dynamics of photoswitching, membrane material properties, interleaflet coupling, and changes in membrane area and thickness. Finally, we exogenously introduce azo-PC in preformed vesicles and quantitatively monitor the efficiency of photoswitching to test the potential applicability of this photoswitch in cellular studies. Understanding the underlying photoswitching dynamics on the membrane material properties can elucidate the light-controlled micromanipulation of cellular processes and optimization of light-triggered drug delivery platforms for potential applications of azo-PC containing bio-engineered minimal cells in photopharmacology.

2. Results

2.1. Vesicle Shape Deformation under Light

Electroformation of pure azo-PC vesicles has been previously reported,[34a,c,d,36] using the relatively long swelling time (2–3 h), and harsh conditions of high temperature (70 °C) and high voltage (10 Hz, 3–5 V), note that at such conditions double bonds of lipids may oxidize. Here, we reduced the GUV preparation time (to 1 h) using much milder conditions, namely field strength of up to 1 V and room temperature. Pure azo-PC GUVs have been explored under dark-field and epifluorescence microscopy, to detect effects of illumination.[34a,c] These approaches require intense white light illumination and a substantial fraction of

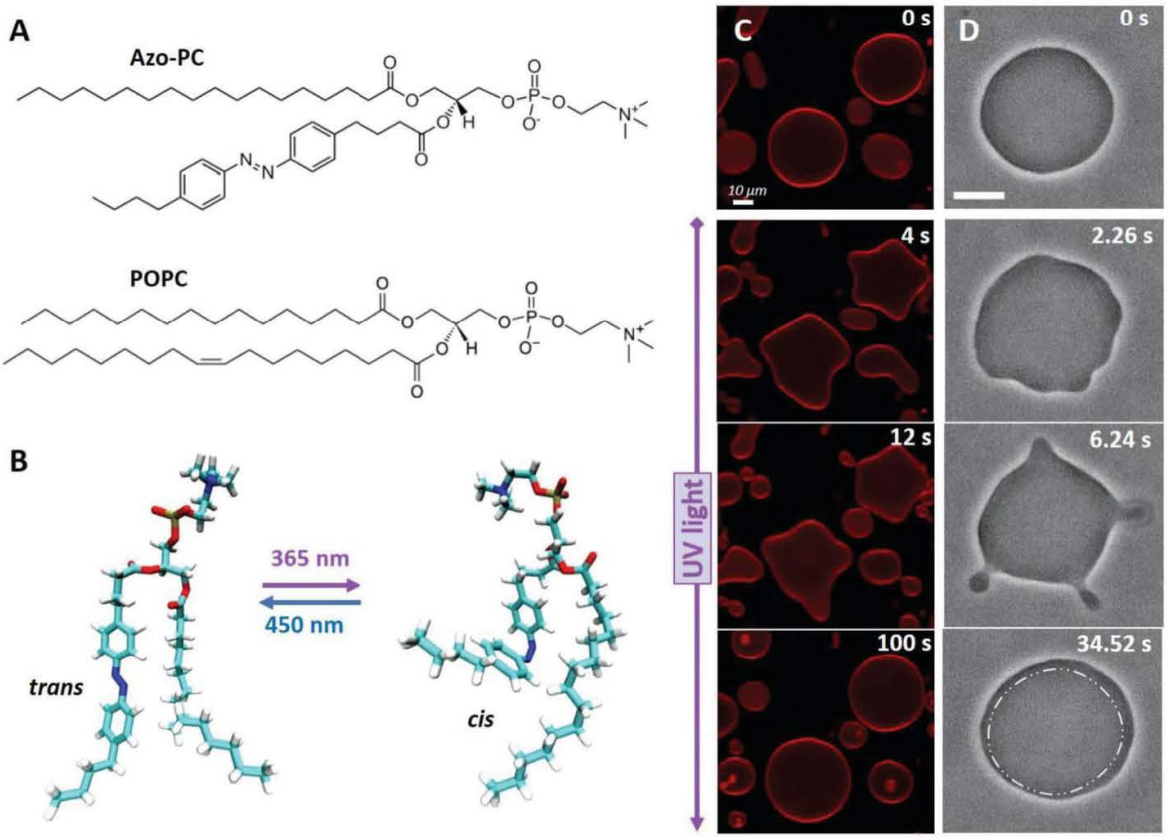

Figure 1. *Trans*-to-*cis* photoisomerization of azo-PC triggers vesicle shape changes and area increase. A) Chemical structures of azo-PC and the POPC. B) Representative snapshots of the molecular conformational changes upon photo isomerization of azo-PC obtained from MD simulations. C) Confocal cross-section images of 100 mol% azo-PC GUVs labeled with 0.1 mol% Atto-647N-DOPE monitored during photoisomerization. Upon UV irradiation (365 nm), the GUVs undergo complex shape transformations of outward budding and bud re-adsorption over time; the time stamps are shown in the upper part of the images. D) Phase contrast microscopy showing a time sequence of the *trans*-to-*cis* photoisomerization response of 50 mol% azo-PC doped vesicles (azo-PC:POPC 50:50) under UV illumination, see also Movie S2 (Supporting Information). Budding and bud re-adsorption occur over time. The area of the vesicle increases: for comparison, the dash-dotted contour in the last image shows the approximate GUV contour before irradiation (first snapshot). Scale bars correspond to 10 µm.

a membrane fluorophore. Here, we implemented confocal microscopy, which offers a higher resolution of the photo-induced membrane deformations and compared to epifluorescence observations, requires only one-tenth of the fraction of the membrane fluorophore (0.1 mol%) for visualization. It is noted that high fractions of fluorophores affect membrane material properties such as bending rigidity[37] and can cause oxidation and changes in membrane composition.[38] In addition, we probed the response of vesicles devoid of fluorescent dye using phase-contrast microscopy to eliminate potential dye effects. The UV irradiation in our confocal setup was implemented with an external source mounted at the microscope condenser (see Experimental Section on Vesicle Imaging and Irradiation). GUVs containing azo-PC and labeled with 0.1 mol% Atto-647N-DOPE were exposed to UV light to initiate *trans*-to-*cis* photoisomerization and observed for a few seconds. Before UV irradiation, GUVs were mostly defect-free (at least 90% of the population) exhibiting thermal fluctuations visible both in confocal and phase-contrast microscopy. Upon UV illumination, GUVs containing substantial fractions of azo-PC (50 or 100 mol%) undergo large shape transformations including complex budding events within a few seconds visible in confocal and phase contrast microscopy (Figure 1C,D; Figure S1 and Movies S1, S2, and S3, Supporting Information). The vesicles increase in size (see the last snapshot in Figure 1D), but a quantitative assessment of the membrane area change is not feasible because of the unknown GUV geometry. Even if the vesicle appears as a sphere in the projected image, it can be flattened due to gravity into an oblate shape which has a similar appearance in the images.

2.2. Assessing the Light-Induced Membrane Area Change by GUVs Electrodeformation, Langmuir Monolayer Isotherms, LUVs, and MD Simulations

To quantitatively characterize the membrane area change associated with photoisomerization, we employed GUV electrodeformation.[39] In this approach, an alternating cur-

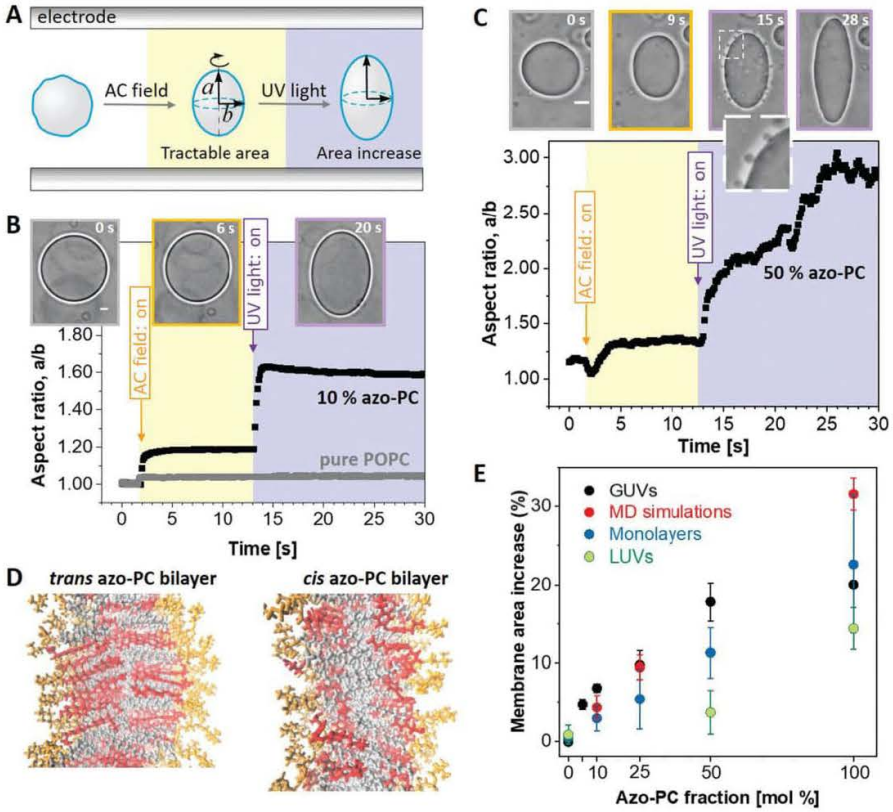

Figure 2. Area increase of membranes and monolayers doped with azo-PC when exposed to UV irradiation. A) Sketch of the approach of GUV electrodeformation to assess the vesicle area change induced by UV light. The vesicles are first exposed to an AC field (5 kV m^{-1} and 1 MHz) to pull out thermal fluctuations and deform them into a prolate ellipsoid with semi-axes a and b. Then, while keeping the AC field on, UV irradiation (365 nm) is initiated. B,C) Electrodeformation and irradiation of GUVs made of pure POPC (gray trace in panel B) and containing 10 and 50 mol% azo-PC, see also Movies S4–S6 (Supporting Information) showing the response of these three vesicles. The snapshots show example images of the vesicles before applying the AC field (gray frame), after the application of the AC field (orange frame), and when exposed to UV light (purple frame). A zoomed-up vesicle segment (dashed region) is given in C, showing the produced vesicle buds right after irradiation. The vesicle semi-axes are used to calculate the vesicle area. Scale bars are 10 µm. D) Snapshots from MD simulations bilayers composed of 100 mol% azo-PC in *trans* and *cis* conformation. The head groups of the lipids are in orange, the azo-benzene moiety in red, and the oleoyl tails in gray. The area of the bilayer increases and tits thickness decreases. E) Membrane area expansion as assessed from GUV electrodeformation (black data show mean and standard deviations, SD; see Figure S3, Supporting Information, for data from individual GUV measurements), MD simulations (red), Langmuir monolayer isotherms (dark blue; see Figure S3, Supporting Information, for data from individual measurements) and LUVs measured with dynamic light scattering (DLS) (green). The LUV data is based on vesicle hydrodynamic radius leading to a systematic underestimate of the area increase as UV-triggered morphological transitions (as those shown in panel C and Figure 1C,D) cannot be accounted for.

rent (AC) field is applied before exposing GUVs to the UV light. Moderate strengths of electric fields are able to pull the excess area stored in thermal fluctuations. The vesicles deform into prolate or oblate shapes depending on the AC field frequency and conductivity ratio between the internal and external GUV solutions.[39b,40] Due to gravity, oblate vesicles lie flat in the observation chamber and appear spherical in the projected images not allowing access to their short semi-axis. On the contrary, prolate deformations, whereby the vesicle elongates along the field direction parallel to the bottom of the observation chamber, allow measuring both semi-axes a and b (**Figure 2**A), and thus, the correct evaluation of the vesicle area. To induce prolate deformation, we prepared the GUVs in solutions containing salt (0.5 mM NaCl and 100 mM sucrose) and diluted the harvested vesicles in salt-free glucose solution (105 mM). These conditions ensure higher conductivity in the GUV interior rendering them prolate under the applied AC field. Additionally, due to the refractive index differences between the interior and exterior sugar solutions, the GUVs appeared with a sharp contour under phase contrast observations (Figure 1D) facilitating image analysis and area measurements.

We explored the area change in POPC vesicles containing 0, 5, 10, 25, 50, and 100 mol% azo-PC. The vesicles were first exposed to an AC field and the area was measured. Then, while keeping the AC field on, they were irradiated with UV light and the changes in vesicle shape were characterized in terms of changes in the vesicle aspect ratio a/b. The morphology change of each GUV was monitored over time under phase-contrast microscopy during the application of electric field and UV-light (see Figure 2A–C; Figure S2 and Movies S4–S6, Supporting

Information). The vesicle response to AC field is fast and completes within less than a second (the dynamics practically depend on the field strength and membrane viscosity[41]). The degree of deformation of the vesicles in the AC field in the absence of UV light showed variations from vesicle to vesicle. These are imposed by the vesicle size (affecting the magnitude of the Maxwell stress tensor deforming the vesicle) and the initial available excess area for deformation (which cannot be controlled as the GUV preparation method yields vesicles with different tensions).

UV illumination was typically applied ≈10 s after applying the AC field. Pure POPC GUVs did not show any response to UV light (see gray trace in Figure 2B; Movie S4, Supporting Information). The response of azo-PC-doped GUVs to UV light was very fast. GUVs containing 5, 10, and 25 mol% azo-PC reached their maximum deformation within a second after switching the UV light on (Figure 2B; Figure S2A and Movie S5, Supporting Information). Increasing fractions of azo-PC resulted in larger membrane deformations in the form of buds (a couple of micrometers in size, see zoomed image in Figure 2C) requiring longer times for the created membrane area to be pulled out into ellipsoidal shape. For GUVs with 50 mol% azo-PC, the buds are pulled back by the electric field within roughly 12–15 s after applying the UV light, contributing to the vesicle elongation. These results indicate that budding and bud re-adsorption slowed down the deformation processes of GUVs containing high fractions of azo-PC (50 mol% and more), (see Figure 2C; Figure S2B and Movie S6, Supporting Information). Indeed, vesicles made of 100 mol% azo-PC often did not reach perfect elliptical shapes affecting our accuracy for assessing the membrane area increase.

The area increase of the cell mimetic vesicles resulting from azo-PC photoswitching was calculated from the ellipsoid surface area of the GUVs at their maximal deformation (Equation 1) and by subtracting the initial electric field-driven deformation in the absence of UV light. This subtraction eliminates the effects associated with the initial membrane tension and the applied electric field. To account for the different vesicle sizes, we normalized the area by the initial one under electrodeformation in the dark. At least 10 vesicles per composition were examined. In the absence of azo-PC (pure POPC membranes), no detectable change in the vesicle area due to UV light was observed suggesting that the illumination conditions (intensity and duration) do not alter the membrane. However, by raising the molar fraction of azo-PC lipids in the membrane, the GUVs area increase could rise up to 20% (gray and black data in Figure 2E). Similar but significantly smaller area change was found from dynamic light scattering (DLS) measurements on LUVs (see green data in Figure 2E; Figure S3, Supporting Information, Experimental Section on LUV Area Change Measurements via Dynamic Light Scattering). It is worthwhile noting that the LUV hydrodynamic radius measured with DLS can be used to obtain only an apparent area change because an assumption for the vesicle shape (typically a sphere) is required. Thus, LUV measurements (as previously used in Ref.[34a]) do not properly represent the vesicle area increase as they do not account for morphological changes as those shown, e.g., in Figure 1C,D. Instead, DLS data leads to systematic underestimates (Figure 2E). Thus, our results emphasize the superiority of GUVs as a minimal cell model over LUVs for measuring area changes.

For higher fractions of azo-PC, the data on GUV area increase under UV exhibit larger scatter (larger standard deviations), and above 50 mol% azo-PC appear to reach saturation (Figure 2E; Figure S3, Supporting Information). This is mostly due to the slow re-adsorption of the light-triggered buds as well as to the strongly elongated GUV shapes (observed for 100 mol% azo-PC) to which the elliptical approximation does not fully apply. Furthermore, the area of the photolipids is expected to be more packed and closely aligned at high azo-PC fractions, which could result in stronger dipole-dipole interactions between the azobenzenes in the lipid tails, potentially leading to photolipid clustering.[34c,42]

In order to test these hypotheses, find out whether they are universal and not constraints to our minimalistic model system, and gain deeper insight at the molecular level into this photoswitchable minimal cellular system, we performed MD simulations of membranes with azo-PC in *cis* and *trans* state (Figure 2D). We also examined Langmuir monolayers with different compositions exposed to UV and blue light, respectively (Figure S4, Supporting Information). Both MD simulations and monolayer isotherms yield excellent agreement with the data from our minimal cell model showing a relatively linear increase in the light-induced area change with increasing azo-PC fractions in the membrane (Figure 2E). Even though linear, the expansion data of the monolayers lie somewhat lower compared to that from the bilayer systems (MD and GUV membranes). This is to be expected as the monolayer lacks all inter-leaflet interactions that are present in the bilayer (and discussed in more detail below) and faces air as a less similar environment compared to that of the lipid chain moieties. The MD simulation, consistent with monolayer data, reveals that the area per lipid decreases with an increasing fraction of *trans* azo-PC in the membrane and the opposite is true for the *cis* azo-PC conformation. The combined effect of these opposite trends yields an increase in the bilayer area by up to ≈30% for the pure azo-PC membrane (Figure 2E). The quantitative match between the GUV model and MD simulations (except for the 100 mol% azo-PC case where the GUV electrodeformation approach lacks high accuracy) also suggests that under the selected irradiation conditions, full photoconversion of the azo-PC molecules occurs.

The simulations offer further insight into the origin of the membrane area changes as a function of photolipid fraction and isomerization state. The fairly rigid planar *trans* tails tend to orient along the membrane normally and can stack flatly against each other. The bent *cis* tails on the other hand orient more along the membrane plane and localize predominantly close to the headgroup-tail interface. As a result, the palmitoyl tails fill the region near the bilayer center, as clearly visible in the density profiles (Figure S5, Supporting Information).

2.3. Reversibility and Kinetics of Membrane Response

To further examine the photoswitching efficiency on the bilayer, we investigated the reversibility and relaxation kinetics of the membrane response of azo-PC-containing GUVs. Establishing a fully reversible and reproducible photoswitching process is an important criterion for the efficient regulation of membrane shape and material properties. In order to fully reverse the photoswitching from *cis*-to-*trans* isomerization, we applied blue

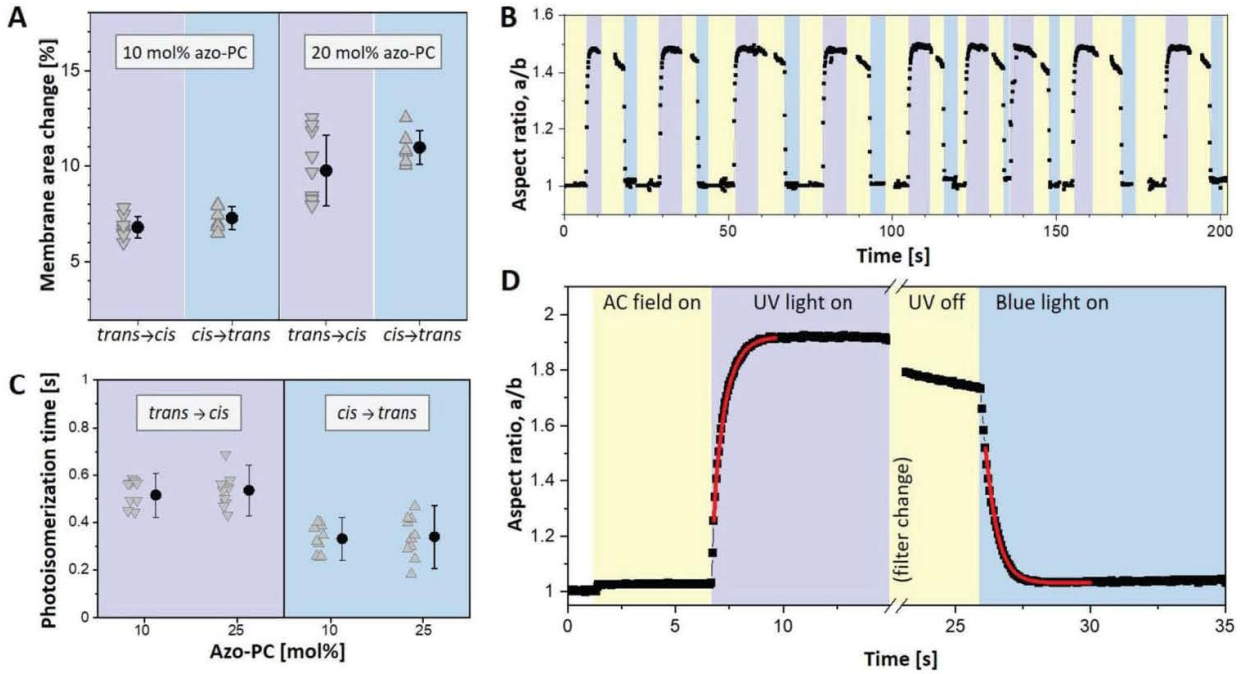

Figure 3. Photoswitching reversibility and kinetics assessed from the response of azo-PC GUVs exposed to UV and blue light. A) Membrane area change measured on vesicles containing 10 and 25 mol% of azo-PC. *Trans*-to-*cis* isomerization upon UV illumination leads to area changes similar to that observed upon *cis*-to-*trans* isomerization under blue light. Each triangle indicates a measurement of an individual GUV. Mean and standard deviation values are also shown on the right. ANOVA test for null hypothesis testing for 10 and 25 mol% azo-PC GUVs gives, respectively, $p = 0.136$ and $p = 0.065$, indicating statistically insignificant difference for the *trans*-to-*cis* versus *cis*-to-*trans* area change of membranes of a fixed fraction of azo-PC. B) Multiple photoswitching cycles of 10 mol% azo-PC vesicle shown in terms of the degree of deformation (a/b, aspect ratio) under UV light (purple regions) and blue light (blue regions) sequentially switched on and off; the same vesicle is shown in Movie S7 (Supporting Information). Throughout the experiment, the GUV is continuously exposed to AC-field (5 kV m^{-1} and 1 MHz; yellow). Purple and blue regions in the graph schematically illustrate the time intervals when UV and blue light are switched on. C) Photoisomerization kinetics of 10 and 25 mol% azo-PC containing GUVs. Data from individual GUVs are shown with triangles (10 vesicles per composition and condition were measured). Solid circles and line bars show means and standard deviations. D) Kinetic trace of the aspect ratio response to UV and blue light irradiation of a GUV containing 25 mol% azo-PC. The exponential fits (red curves) yield the respective time constants as plotted in panel C. A short period of time is needed to mechanically change the filter at the microscope turret, during which the recording of the vesicle is paused.

irradiation after exposing azo-PC GUVs to UV light. Upon reversible and complete photoswitching, the area expansion of the vesicle due to *trans*-to-*cis* isomerization under UV light should be fully recovered and equal to the area shrinkage resulting from the *cis*-to-*trans* isomerization under the blue light. We compared the area changes under these two illumination conditions for GUVs containing 10 and 25 mol% azo-PC, where no complex budding events are observed and the area changes can be measured at high precision. The data are presented in **Figure 3**A. Based on the results of the statistical tests, no significant differences were observed between the means of vesicle area changes for *trans*-to-*cis* and *cis*-to-*trans* isomerization for fixed membrane composition, indicating that light-induced morphological changes of azo-PC GUVs are reversible.

Similarly, the reversibility of swelling and shrinkage of GUVs due to photoswitching under UV and blue light were monitored several times (Figure 3B; Movie S7, Supporting Information). Vesicle deformation was fully reversible and could be switched back and forth over multiple cycles. Furthermore, we observed that the sharp contrast resulting from sugar asymmetry between GUV interior and exterior solutions was preserved, suggesting that during the multiple photoswitching cycles, the membrane remains intact, i.e., the photoisomerization process did not generate any permeation or leakage over time. All these data illustrate that photoswitching under the selected irradiation conditions can be repeated without any sign of decomposition (of either azo-PC and POPC) or membrane leakage.

Based on the area swelling and shrinkage of electrode-formed GUVs under UV and blue light, we assessed the rates of isomerization from the response of GUVs containing 10 and 25 mol% azo-PC over the course of photoswitching. An example kinetic trace and the rates of photoswitching obtained from exponential fits to the data for *trans*-to-*cis* and *cis*-to-*trans* isomerization are shown in Figure 3C,D. Our results demonstrated that the *cis*-to-*trans* exponential time constant (with a mean value of 335 ms) is shorter than the *trans*-to-*cis* response time (525 ms). This faster *cis*-to-*trans* photoswitching kinetics is understandable considering that the *trans* isomer is thermodynamically more stable. We note that these rates depend not on the molecular isomerization kinetics which are in the femtosecond to picosecond time range[43] but are determined by the vesicle hydrodynamics and membrane viscosity. Photoisomerization kinetics did not

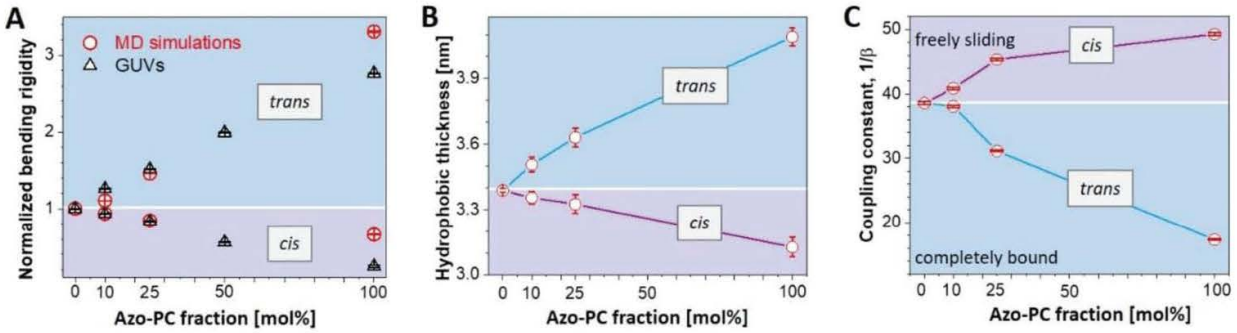

Figure 4. Bending rigidity, thickness, and interleaflet coupling in membranes with various fractions of azo-PC in the *cis* and *trans* states. A) Bending rigidity obtained from fluctuation spectroscopy (open triangles) and MD simulations (open circles). The results are normalized by the bending rigidity value of pure POPC (see non-normalized data in Figure S6, Supporting Information). Blue and purple data correspond to *trans* and *cis* azo-PC, respectively. For each composition, 10 GUVs are analyzed. Standard deviations are illustrated with line bars, smaller than the sizes of the symbols. B) Bilayer thickness data at various fractions of azo-PC in *trans* and *cis* conformation obtained from MD simulations. C) Interleaflet coupling in *cis* and *trans* azo-PC containing bilayers. The coupling constant is deduced from simulation data by using the formula based on polymer brush model,[47] in which the elasticity ratio scales quadratically with a hydrophobic thickness of the bilayer ($\kappa/K = \beta d^2$) and $1/\beta$ describes the coupling between the bilayer leaflets. Purple and blue trends demonstrate the coupling constants for *cis* and *trans* bilayers, respectively. Line bars are standard deviations and smaller than the size of the symbols.

show any difference between 10 and 25 mol% azo-PC containing vesicles.

2.4. Membrane Mechanical Properties

Considering the differences detected in the bilayer area, structure, and photoisomerization kinetics of *cis* and *trans* azo-PC GUVs, we hypothesized that membrane mechanical properties should also show differences depending on the isomerization state and photoswitch fraction. We employed fluctuation spectroscopy[44] as a contactless approach to characterize the bending rigidity of POPC membranes with various fractions of azo-PC in different isomerization states (Figure S6A, Supporting Information). In parallel, computational studies have been performed to calculate the bending rigidity of the simulated membranes from the real space fluctuations of the tilt and splay of lipid tails.[45] The absolute values obtained from the experiment and simulations are expected to differ (as we find, see Figure S6B, Supporting Information), because the bending rigidity is sensitive to the composition of solutes in the bathing medium[46] (pure water in simulations and sugar solutions in the experiment). To allow comparison, the results were normalized by the mean value of the bending rigidity measured for pure POPC membranes, **Figure 4**A.

We find excellent agreement between experiments and simulations demonstrating the adeptness of the used force fields. Membranes doped with azo-PC in the *cis* conformation have lower bending rigidity compared to pure POPC and *trans* azo-PC GUVs, therefore, *cis*-photoisomerization of azo-PC softens the membrane. On the one hand, as the *cis* azo-PC fraction in the membrane increased from 0 to 100 mol%, the bending rigidity decreased fourfold dropping down to values as low as 5 k_BT (Figure S6A, Supporting Information); similar bending rigidity decrease has been observed upon the insertion of fusion peptides[48] pointing to the destabilizing potential of azo-PC. On the other hand, equivalently increasing *trans* azo-PC fractions in the membrane stiffens the membrane threefold reaching bending rigidity values ≈70 k_BT (Figure 4A; Figure S6A, Supporting Information); such bending rigidities are characteristic of membranes in the liquid-ordered phase.[44a,49] This is indeed consistent with the strong alignment of the azo-PC tails structurally resembling liquid-ordered phases.

A simplistic reason for the changes in the bending rigidity could be sought in changes in the membrane thickness due to photoisomerization. X-ray scattering studies on pure azo-PC vesicles have shown thinning of the bilayer by ≈4–5 Å resulting from *trans*-to-*cis* isomerization.[36] Thinner membranes are generally softer and vice versa but such a small thickness change cannot account for the large bending rigidity changes we observe. We thus questioned the reported data and measured the thickness of POPC and azo-PC membranes from AFM on supported lipid bilayer patches (see Figure S7, Supporting Information, Experimental Section on Preparation of Supported Lipid Bilayers and Measurement of Bilayer Thickness through Atomic Force Microscopy). The thickness of POPC bilayers was measured as 4.7 ± 0.3 nm, which is in very good agreement with the literature data.[50] In the case of 100 mol% azo-PC containing bilayer, thickness values of 6.2 ± 0.4 and 4.7 ± 0.4 nm were measured for the *trans* and *cis* conformations, respectively. This thickness change is more consistent with the membrane softening as shown from the bending rigidity measurements.

Considering that the MD simulations correctly represent the experimental findings on the area and bending rigidity changes, we also explored how the membrane hydrophobic thickness varies with azo-PC fraction and isomerization. MD simulations show that isomerization and increasing azo-PC fractions can alter membrane thickness by almost 1 nm (Figure 4B), consistent with the whole-bilayer thickness changes measured with AFM. The thickness of membranes containing azo-PC in the *trans*-state is more influenced by the photolipid fraction.

In addition to thickness changes as a reason for softening the membrane, the bending rigidity behavior in Figure 4A could also be related to dipole-dipole coupling between azobenzene groups

in the acyl chains of the photolipids.[34c,42] Stronger molecular interactions between photolipids might lead to a more densely packed bilayer giving less flexibility to the membrane for bending. Another factor modulating the membrane mechanical properties is the interleaflet coupling, which relates the bending rigidity, κ, the stretching elasticity, K, and the membrane thickness, d. The relation of the two elastic moduli κ and K has been theoretically considered[47,51] and experimentally explored for pure lipid membranes.[51a] Their ratio scales quadratically with the membrane thickness: $\kappa/K = \beta d^2$, where the proportionality constant β described the coupling of the monolayers constituting the membrane. For $1/\beta = 12$, the leaflets are completely bound,[51a] for $1/\beta = 48$, they are unbound and freely sliding,[51b] while the polymer brush model[47] predicts the intermediate value of $1/\beta = 24$ for lipid bilayers. To resolve the leaflet coupling in our azo-PC membranes, we first assessed the stretching elasticity modulus K from MD simulations. This was achieved by fitting the tension versus area curves (see Experimental Section on MD Simulations), which did not show any systematic dependence on the azo-PC fraction in the bilayer. A combined fit to all data points resulted in a value of $K = 221.8 \pm 6.8$ mN m^{-1} which we kept constant for all calculations. The coupling constant values were then estimated for the corresponding fractions of *cis* and *trans* azo-PC in the bilayer using the simulation data for the bending rigidity and the membrane thickness, see Figure 4C. Increasing the *trans* azo-PC fraction in the membrane from 0 to 100 mol% causes a decrease in $1/\beta$ from 35.6 ± 0.2 to 17.3 ± 0.1. These results indicate stronger interleaflet interactions in the *trans* azo-PC bilayer. The opposite is true for increasing fractions of *cis*-azo-PC, which result in $1/\beta$ values corresponding to freely sliding monolayers, i.e., interleaflet interactions become weaker. All these results clearly demonstrate that the membrane elasticity of azo-PC vesicles and monolayer interactions can be conveniently regulated by light.

2.5. Specific Membrane Capacitance and Dielectric Constant of Lipid versus azo-PC Bilayers

The observed changes in the membrane thickness between *cis* and *trans* azo-PC GUVs prompted us to explore differences in the electrical properties of these membranes, which are thickness dependent such as the membrane capacitance. This property quantifies the ability of a membrane to store electrical charge and determines the propagation velocity of action potentials. The membrane capacitance of a vesicle or cell is proportional to its surface area while the specific membrane capacitance is normalized by the surface area. Thus, the specific membrane capacitance allows accurate comparison of vesicles and cells irrespective of their size and shape.[52] We utilized an approach introduced by Salipante et al.[53] based on GUV electrodeformation, to deduce the specific membrane capacitance of POPC and azo-PC membranes and subsequently interrogate the membrane dielectric constant (see Experimental Section on Specific Membrane Capacitance Measurements and Evaluation of the Membrane Dielectric Constant). To the best of our knowledge, this is the first study addressing the specific membrane capacitance and dielectric constant of azo-PC membranes.

Phase contrast micrographs of vesicles were recorded under a frequency sweep of the applied electric field (see **Figure 5**A) and used to obtain the GUV aspect ratio (Figure 5B). The critical frequency at which GUVs undergo prolate-to-oblate transition is used to obtain the specific membrane capacitance (see Equation 2 and Experimental Section on Specific Membrane Capacitance Measurements and Evaluation of the Membrane Dielectric Constant).

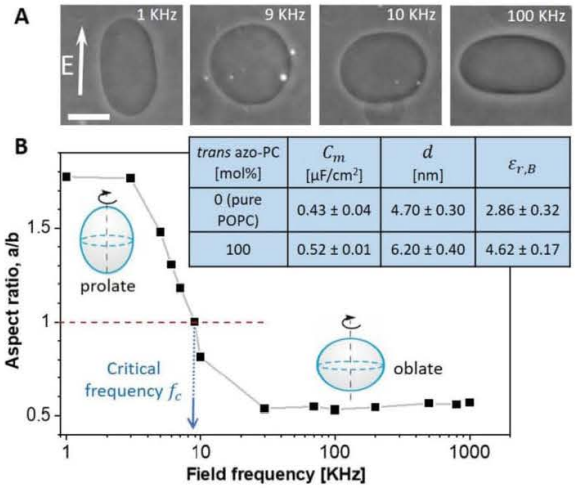

trans azo-PC [mol%]	C_m [μF/cm^2]	d [nm]	$\varepsilon_{r,B}$
0 (pure POPC)	0.43 ± 0.04	4.70 ± 0.30	2.86 ± 0.32
100	0.52 ± 0.01	6.20 ± 0.40	4.62 ± 0.17

Figure 5. Specific membrane capacitance measurements and estimates of the dielectric permittivity of 100 mol% *trans* azo-PC and pure POPC membranes. A) Phase-contrast images of a GUV exhibiting morphological prolate-sphere-oblate transitions under a frequency sweep at a field strength of 10 kV m^{-1}. The scale bar is 10 μm. B) Aspect ratio versus frequency plot of the same GUV shown in (A). The critical field frequency (≈9 KHz) of the prolate-oblate transition point with an aspect ratio $a/b = 1$ is indicated with an arrow. The table in the inset summarizes the specific membrane capacitance (averaged over 10 vesicles per composition), results for the mean bilayer thickness obtained from AFM (see also Figure S7, Supporting Information), and the estimated dielectric constant for pure POPC membrane and pure azo-PC bilayer in the *trans* state.

The method was applied to measure pure POPC and 100 mol% azo-PC vesicles. We intended to explore the effect of azo-PC isomerization, but because the frequency sweep of a single GUV takes ≈15–20 min, the long-term exposure of the GUVs to UV illumination led to membrane tubulation and complex morphological transitions, which we believe are related to photooxidation of the bilayer components. Furthermore, the deformations prevented us from reliably detecting the transition frequency. Thus, data for membranes in the *cis* state are not included. The table in Figure 5D summarizes the specific membrane capacitance values of pure POPC and 100 mol% *trans* azo-PC bilayers. The specific membrane capacitance of pure POPC GUVs, 0.43 ± 0.04 μF cm^{-2}, is consistent with literature values.[54] However, for GUVs composed of pure *trans* azo-PC, the specific membrane capacitance significantly increased to 0.52 ± 0.01 μF cm^{-2}.

The specific membrane capacitance is the resultant capacitance of a series of three capacitors: the bare lipid membrane and the adjacent space charge regions in the solution on both sides of the bilayer, see Experimental Section Specific Membrane Capacitance Measurements and Evaluation of the Membrane Dielectric Constant. The bare lipid capacitance scales inversely with its thickness (Equation 4), which is why the larger thick-

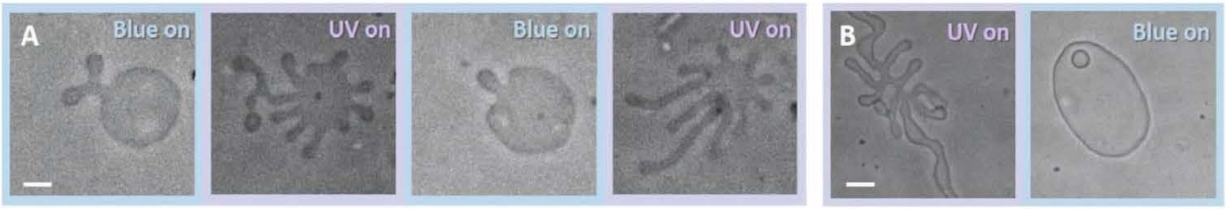

Figure 6. Two examples (a) and (b) of the photoresponse of POPC vesicles exogenously doped with azo-PC and irradiated with UV and blue light. The vesicles were exposed to a solution of azo-PC at 15.56 μM bulk concentration (equivalent to the total lipid concentration in the GUV suspension). The GUVs adopt highly tubulated morphologies under exposure to UV light (365 nm). Under blue light irradiation (450 nm), most of the tubules are re-adsorbed and the vesicles adopt their initial non-tubulated morphology, see also Movie S8 (Supporting Information). Illumination conditions are indicated on the upper-right side of each snapshot. The scale bars correspond to 10 μm.

ness and capacitance of *trans* azo-PC bilayers compared to pure POPC ones is counterintuitive unless the membrane dielectric constant changes as well. Using the obtained values for the specific membrane capacitance from vesicle electrodeformation and bilayer thickness from AFM, we deduced the dielectric constants of each membrane. The dielectric constant of the *trans* azo-PC bilayer was found to be 4.62 ± 0.17, almost twice higher than that of POPC, which was found to be 2.86 ± 0.32 (see the table in Figure 5D).

2.6. Photoresponse of Minimal Cells to Exogenous Addition of azo-PC

Above we provided a detailed characterization of photo-triggered membrane remodeling events on vesicle bilayers prepared from POPC and varying fractions of azo-PC. In view of the potential application of the photoswitch to modulate the area, morphology, material, and electric properties of cellular membranes, we raise the question whether it is possible to observe similar membrane dynamics and photoresponse upon incubating pure POPC membranes in solutions containing the azo-PC photoswitch. Such exogenous incorporation of azo-PC into the already established membrane bilayers is a prerequisite for the direct manipulation of cells. We hypothesized that the amphiphilic nature of azo-PC molecule may enable the membrane to adsorb this photoswitch from the external media to the outer leaflet of the bilayer asymmetrically thus rendering the membrane photoresponsive.

POPC GUVs were prepared and incubated in a solution of azo-PC at a concentration equal to that of the total lipid concentration in the GUV suspension (see Experimental Section on Exogenous Addition of azo-PC). In this way, we aimed at obtaining vesicles with 50 mol% azo-PC. After 20 min incubation in the azo-PC solution, and prior to UV illumination, most GUVs appeared to exhibit thick outward protrusions (see first snapshot in **Figure 6**A). Controls based on the addition of the same amounts of azo-PC-free solution resulted in no detectable changes in the GUV morphology.

Upon UV illumination, quasi-spherical GUVs with a few outer protrusions transform into tubular networks or highly tubulated morphologies. This process occurs within a couple of seconds of irradiation (see Movie S8, Supporting Information). The protrusions retract back under blue light (Figure 6). These morphological transformations could be reversed back and forth over multiple photoswitching cycles (Figure 6A). This result demonstrates the reversibility of the light-induced manipulation of exogenously doped azo-PC vesicles. Thus, we conclude that it is feasible to achieve light-triggered membrane remodeling events on cells exogenously exposed to azo-PC, similarly to exposing GUVs as artificial cells.

2.7. Molecular Shape and Flip-Flop Free Energy of azo-PC

The asymmetric distribution of amphiphilic molecules in the membrane is known to induce membrane tubulation stabilized by spontaneous curvature[55] of the bilayer. The outward formation of relatively thick tubes of micron-sized diameters that we observe (Figure 6) indicates that the bilayer has only small positive spontaneous curvature, which implies that the final distribution of azo-PC in the GUVs upon exogenous addition is only slightly asymmetric. We speculate that the externally added azo-PC translocates to the inner membrane leaflet either via defects or flip-flop to equilibrate the surface coverage in both leaflets. Azo-PC was introduced in the GUV sample as a solution of dichloromethane/methanol. Before evaporation, the organic solvents could create temporary defects in the membrane allowing material exchange between the leaflets thus balancing the asymmetric distribution of azo-PC.

To explore flip-flop as a possible mechanism, we estimated the energy barrier for translocating azo-PC across the membrane by performing PMF calculations (see Experimental Section on MD Simulations). Analyzing a bilayer made of 25 mol% azo-PC and 75 mol% POPC allowed us to directly compare the PMF of interleaflet translocation of POPC and of azo-PC when the photoswitch is in *trans* and in *cis* conformation (**Figure 7**A,B,D,E). The translocation of POPC in pure POPC bilayer was also examined (see Figure S8, Supporting Information). All PMFs for POPC and different conformations of azo-PC showed a similar energy barrier of 47–50 kJ mol^{-1} for the flip-flop of both molecules across the bilayer. Considering that typical flip-flop times of lipids are on the order of an hour,[56] we find that azo-PC flip-flops at a similar time scale and we can thus exclude flip-flop as a possible mechanism of azo-PC translocating to the inner leaflet upon exogenous addition to GUVs.

We also explored the molecular curvature of azo-PC, comparing the *trans* and *cis* states. For this, we generated MD simulation snapshots from 100 azo-PC molecules aligned at the C2 carbon (the atom where the two tails come together) rotating

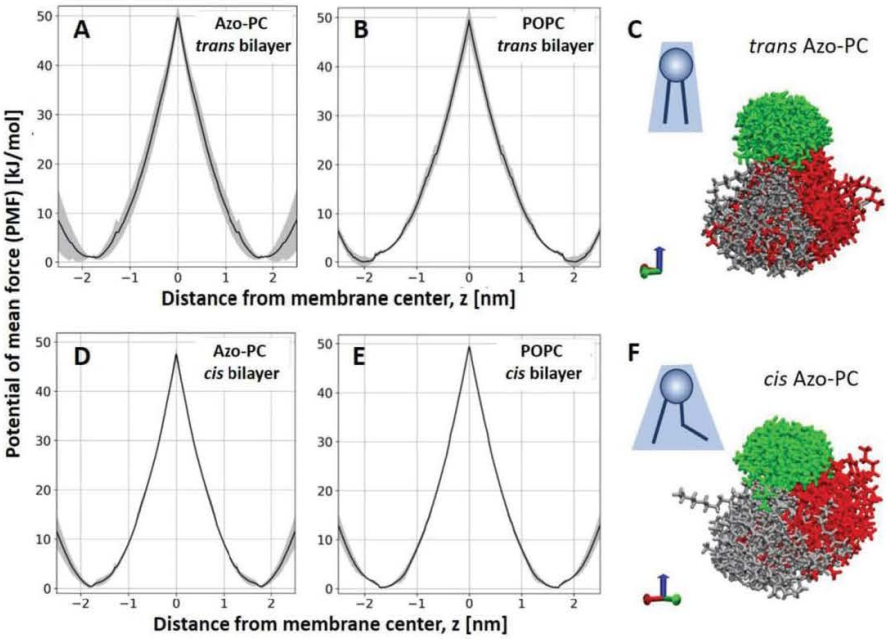

Figure 7. Free energy of flip-flop of azo-PC and molecular curvature. A,B,D,E) PMF calculation plots for the flip-flop energy of azo-PC (A,D) and POPC (B,E) in a bilayer containing 25 mol% azo-PC and 75 mol% POPC when the photoswitch is in the *trans* (A,B) or in the *cis* state (D,E). The maxima of the plots illustrate the energy barrier for the flip-flop. The standard error of each calculation is shown in gray. C,F) Snapshots of 100 aligned and centered azo-PC molecules (see text for details) in *trans* (C) and *cis* (F) state. Green, gray, and red corresponded to PC head groups, hydrocarbon tails, and azobenzene tails, respectively. The blue arrow on the bottom right indicates the direction of the membrane normal.

the molecules around the *z*-axis to align the first two bonds along each chain (see Figure 7C,F). This presentation produces an apparent spatial cloud explored by an azo-PC molecule in the bilayer, giving a rough idea of the molecular curvature of azo-PC in POPC environment. The results illustrate that in the *cis* state, the azo-PC hydrophobic tails explore or occupy a larger volume (similarly to phosphatidylethanolamine lipids) compared to the molecular arrangements of the molecule in the *trans* state, suggesting that *cis* azo-PC may generate higher curvature compared to *trans* azo-PC.

3. Discussion

Our results demonstrate that light can be employed as a facile, fast, and sustainable tool for the micromanipulation of artificial minimal cells in combination with the photoswitch azo-PC as an efficient converter of light to mechanical energy. As mentioned in the introduction, several other studies have investigated the response of azo-PC membranes to light. As we will discuss below, we find that some of the previously published data are inconsistent among themselves (even though reported from the same group) and partly with ours and will propose reasons to explain these inconsistencies.

3.1. Membrane Area Changes Upon Isomerization

Our results reveal that photoisomerization of azo-PC under UV and blue light triggers complex shape transformations and budding events in the membrane (Figure 1C,D) also reported in Refs.[32c, 34a-c] for various photoswitches. Here, using several model membranes, we show that an area increase of as much as 20-30% can be obtained for pure azo-PC membranes (Figure 2E). Our results clearly demonstrate the deficiencies of measuring area changes using DLS on LUVs for this purpose. Indeed, previous measurements suggested very small changes in the diameter of pure azo-PC LUVs of the order of 3%[34a] implying area change of only ≈6% which is obviously unrealistic considering the directly observed area change seen with microscopy of GUVs and accompanying simulations. Similarly, photoinduced size changes of SUVs made of an azo-PC derivative showed a tiny increase of 1%,[36,57] which could be due to the fact that the measurement is model dependent (X-ray scattering) but also because the SUV membrane is highly curved.

We also showed that the membrane area can be finely tuned by altering the molar fraction of azo-PC in the membrane thus modulating shape-dependent cellular processes such as endo/exocytosis and intra/intercellular trafficking. The potential phototoxicity of UV and blue light can be remedied by shifting the excitation wavelength of azobenzene derivatives into the lower energy range as recently demonstrated.[57] Coupling optical microscopy and GUV electrodeformation allowed us to precisely quantify the reversibility and kinetics of the photoisomerization process over the whole membrane. These measurements are also direct (not model dependent) and just like seeing is believing, we consider them reliable. Among previously published data, this is also the first report to directly and

accurately quantify the dose-dependent, reversible area changes of membranes containing azo-PC photolipids.

3.2. Membrane Bending Rigidity and Leaflet Coupling

We find inconsistencies in the literature also regarding the membrane's mechanical properties, in particular, the bending rigidity. Using optical tweezers and a model for the deformation of GUV trapped locally and deformed by a flow, Pernpentier et al.[34a] reported example bending rigidity values for *cis* and *trans* azo-PC GUVs, $\kappa_{cis} = (5.4 \pm 1.8) \times 10^{-19}$ J and $\kappa_{trans} = (1 \pm 0.6) \times 10^{-17}$ J corresponding to 131 and 2433 k_BT, respectively. These measurements correctly point to lower bending rigidity of the membrane in the *cis* state but with the following caveats. First, such bending rigidities, and especially that of *trans* azo-PC would correspond to very stiff membranes (like gel phase),[58] which is inconsistent with the fact that these membranes are liquid in nature. Second, at such high bending rigidity, the membrane should not fluctuate, which is also not the case in their study, suggesting that the model used to calculate the values[34a] is incorrect (presumably, the assumption for ellipsoidal deformation affects the calculation).

Another study by the same research group,[34c] reports the following values for *cis* and *trans* azo-PC membranes measured micropipette aspiration of GUVs, $\kappa_{cis} = 6.4 \times 10^{-21}$ J and $\kappa_{trans} = 3.1 \times 10^{-20}$ J (respectively corresponding to 1.6 and 7.5 k_BT), largely contradicting their own previous result. The reason for these extremely low values could be that micropipette aspiration measurements rely on the mechanical deformation of the membrane and are known to suffer from stretching elasticity contributions[46] as demonstrated in more detail by Henriksen and Ipsen.[59] In this respect, fluctuation spectroscopy, not relying on mechanical perturbation of the membrane is the gold standard, providing us with more reliable results; this is supported also by the agreement with literature data for the bending rigidity of pure POPC bilayers.[46]

Our experimental results for azo-PC dose-dependent bending rigidity and area increase are fully consistent with MD simulations (Figures 2E and 4A), especially for azo-PC fractions smaller or equal to 50%. Using this as evidence, we explored additional elastic parameters, not accessed experimentally, namely the intermonolayer coupling which hasn't been characterized previously.

The coupling constant $1/\beta$ of *trans* azo-PC membrane is close to values reported for 1,2-dioleoyl-sn-glycero-3-phosphocholine (DOPC), $1/\beta_{DOPC} \approx 18$.[48a] For POPC we find $1/\beta \approx 36$. DOPC with its two unsaturated long chains of (18:1) oleic acid, must form a relatively tightly coupled bilayer compared to POPC with only one unsaturated chain. *Trans* azo-PC significantly increases the interleaflet interactions monolayers compared to *cis* azo-PC, which decreases the coupling, showing a similar trend as that reported for a fusion peptide[48a] that was shown to shift the coupling towards freely sliding monolayers. The weaker interleaflet interactions for *cis* azo-PC-containing membranes may be caused by the reorientation of the azobenzene tail somewhat parallel to the membrane plane reducing the coupling and facilitating interleaflet slip. This idea is corroborated by the spatial distribution and molecular occupancy that we find from MD simulations for the *cis* state, as shown in Figure 7F.

3.3. Electrical Properties and Membrane Thickness

We characterized the electrical properties of the azo-PC membranes providing the first values for the specific membrane capacitance and the dielectric constant of azo-PC bilayers. In our studies, the specific membrane capacitance, and the thickness of azo-PC and POPC bilayers obtained from separate experiments (GUV electrodeformation and AFM on membrane patches, respectively) presented higher values for membranes with *trans* azo-PC compared to pure POPC bilayers. Previously, results on increasing membrane capacitance have been reported for an amphiphilic photoswitch (Ziapin2) in neuronal membranes,[60] but have been attributed to membrane thinning. We refrain from comparing these data to ours on specific membrane capacitance (which is the area-rescales capacitance) as the area changes related to the insertion of Ziapin2 in the membrane are not known. We interpret our observations for the larger specific capacitance and thickness of the *trans* azo-PC membrane compared to POPC (table in Figure 5) as resulting from a higher dielectric constant signifying a higher ability to store electrical energy and to polarize in electric fields.

Our AFM measurements showed a dramatic thickness decrease of ≈1.5 ± 0.6 nm of the azo-PC bilayer upon *trans*-to-*cis* isomerization (Figure SB). This is consistent with the decrease in the hydrophobic thickness as observed with MD simulations (Figure 4B). Membrane thickness data for azo-PC membranes from X-ray scattering on azo-PC SUV suspensions reported only a 0.4 nm decrease in the membrane thickness associated with the *trans–cis* isomerization. Considering that the membrane as an elastic sheet should preserve its volume (equal to the area times the thickness) upon thinning, we believe that our results are much more realistic as an area increase by 20–30% (Figure 2E) would roughly correspond to 17–24% decrease in the membrane thickness, which is of the order of 1.1-1.5 nm as seen by the AFM measurements.

From a structural point of view, we note that azo-PC in the trans conformation partly resembles the lipid DSPC (1,2-distearoyl-sn-glycero-3-phosphocholine), having the same fatty acid tail. The DSPC bilayer thickness is ≈5.8 and 5.5 ± 0.5 nm.[61]

In conclusion, through careful integration of accurate experimental and computational methodologies, we addressed an existing knowledge gap by delivering a comprehensive depiction of the membrane response to the photoisomerization of azo-PC across a range of model membrane systems. We critically evaluated current reports and existing discrepancies providing an encompassing understanding of membrane expansion, thinning, softening, interleaflet coupling, capacitance, and dielectric constant. We should also mention that we cannot exclude that some of the above-mentioned issues with discrepancies in the literature could be associated with the specific source of azo-PC lipids used in the different studies (commercial as here versus synthesized by other authors) and, potentially, the different fraction of impurities.

Overall, our studies with GUVs, LUVs, SLBs, Langmuir monolayers, and MD simulations consistently illustrated that light-induced membrane deformations due to photoisomerization of azo-PC cause dynamic alterations in the membrane. These include changes in bilayer packing, membrane elasticity as well as interleaflet interactions thus leading to dramatic changes in

the material and electric properties of membranes, which scale with azo-PC fraction. Lastly, the reproducible photoresponse of already formed vesicles after the exogenous insertion of azo-PC in the membrane provides a promising background for intercalating this photoswitch in more complex cell systems to optically control cellular activities.

4. Experimental Section

Vesicle Preparation: GUVs were prepared by the electro-formation method[30a] at room temperature (23 °C). Varying molar fractions of azo-PC (0, 5, 10, 25, 50, and 100 mol%) and 1-palmitoyl-2-oleoyl-sn-glycero-3-phosphocholine (POPC) (both purchased as chloroform solutions from Avanti Polar Lipids, Alabaster, AL) were dissolved in chloroform to a concentration of 4 mM. Then, 8 µL of this lipid solution was spread as a thin film on a pair of indium-tin-oxide (ITO)-coated glass plates (PGO GmbH, Iserlohn, Germany), which are electrically conductive. A stream of N_2 was applied to evaporate most of the chloroform, and the plates were subsequently placed under a vacuum for 2 h to remove traces of the solvent. For chamber assembly, a Teflon spacer of 2 mm thickness was placed between the ITO-glass plates, and the chamber was filled with a solution of 100 mM sucrose (Sigma Aldrich, St. Louis, USA) to hydrate the lipid film. For the GUV electrodeformation studies, the sucrose solution was also supplemented with 0.5 mM NaCl to ensure higher conductivity of the internal solution and thus prolate deformation of the GUVs.[40] Electroswelling was initiated by applying a sinusoidal AC electric field at 10 Hz frequency with a 1.6 V_{pp} (peak to peak) amplitude for 1 h in the dark. GUVs were then transferred to light-protective glass vials for storage at room temperature and used the same day. For microscopy observations during electrodeformation studies, GUV solutions were diluted eightfold with 105 mM glucose. The osmolarity was adjusted with an osmometer (Osmomat 3000, Gonotec GmbH, Germany). For bending rigidity measurements, GUV solutions were diluted 1:1 in 85 mM sucrose and 20 mM glucose to avoid gravity effects affecting the fluctuation spectra.[44c] For confocal microscopy observations, GUVs were prepared from 100 mol% azo-PC further doped with 0.1 mol% 1,2-Dioleoyl-sn-glycero-3-phosphoethanolamine labeled with Atto 647N (Atto-647N-DOPE) (Avanti Polar Lipids).

For membrane capacitance measurements, following previously established protocols,[53,62] the GUVs were electroformed in 40 mM sucrose solution containing 0.3 mM NaCl at 50 Hz and 1.5 V_{pp} for 1 h. Then, they were harvested and ninefold diluted in a 45 mM glucose solution containing 0.6 mM NaCl. The resulting conductivities of the GUV inner (42.70 µS cm^{-1}) and outer (81.67 µS cm^{-1}) solutions measured via Seven-Compact Conductivity Meter (Mettler Toledo, Ohio, USA) were thus adjusted to result in the conductivity ratio of inner to outer solution $\Lambda = 0.52$.

LUVs were prepared via extrusion at room temperature. Azo-PC (0, 50, and 100 mol%) and POPC (Avanti Polar Lipids, Alabaster, AL) were dissolved in chloroform to a concentration of 10 mg mL^{-1}. An aliquot of 100 µL of the lipid solution was dried under a gentle stream of nitrogen until the formation of a film on the walls of a glass vial. The vial was placed in a desiccator under vacuum overnight for the complete evaporation of the chloroform. The dried lipid film was hydrated with 1 mL Milli-Q water and agitated with a vortex mixer. The suspension was extruded 31 times through a polycarbonate membrane (Whatman Nuclepore Track-Etched Membranes, Merck, Germany) with a pore size of 200 nm using a mini-extruder (Avanti Polar Lipids).

Preparation of Langmuir Monolayers and Area Change Measurements in a Langmuir–Blodgett Trough: Azo-PC and POPC lipids were diluted to 1 mg mL^{-1} in chloroform. The two solutions were mixed in the desired ratios: 0%, 10%, 25%, 50%, and 100% azo-PC molar fraction in POPC. An aliquot of lipid chloroform solution was deposited on the water surface of a commercial Langmuir–Blodgett trough (Kibron MicroTroughX, Kibron, Finland) with an available surface of 80 × 350 mm^2, in the correct amount (≈16 µL) to yield an initial lipid density at the air-water interface of 100 Å^2/lipid. A UV rod lamp (365 nm, Camag, Switzerland) and an array of blue LEDs (450 nm, Luxeonstar, Canada) placed above the film illuminated the trough surface with a power density of 30 µW cm^{-2} and 10 mW cm^{-2}, respectively. The power density was measured at the sample position with a handheld power meter (LaserCheck, Coherent, USA). The film was first illuminated for 10 min with blue or UV light, respectively, to obtain either the *trans* or the *cis* isomer of the azo-PC component of the deposited lipids, and then compressed to a lateral pressure of 30 mN m^{-1} reducing the available area by compression with Teflon barriers at a speed of 35 mm min^{-1}.

Compression isotherms during illuminations with both light sources and for all azo-PC molar fractions were recorded with a sampling rate of 0.25 s^{-1}. To calculate the area expansion as a percentage of the footprint of azo-PC in the *trans* state, the area per lipid at 30 mN m^{-1} occupied under blue-light illumination (azo-PC in the *trans* state) was subtracted by the value obtained under UV light illumination (azo-PC in the *cis* state) and divided by the first value. A subsequent new *trans* isotherm was recorded to then calculate the area reduction in analogy. For each azo-PC fraction, the results from four or five illumination cycles on different films were calculated.

Vesicle Electrodeformation and Area Change Measurements: Electrodeformation experiments to measure vesicle area changes[39a,63] were conducted in a commercial Eppendorf electrofusion chamber (Eppendorf, Germany) described previously. The chamber has two parallel cylindrical platinum electrodes (92 mm in radius) spaced 500 µm apart. GUVs between the electrodes were exposed to a sinusoidal AC field at 1 MHz with a 5 V (peak-to-peak) amplitude. In the absence of an electric field, the vesicles are quasi-spherical and exhibit visual fluctuations. The membrane area stored in these fluctuations is not possible to assess directly from the microscopy images. The mild AC field deforms the GUVs and the type of the deformation depends on the field frequency and conductivity ratio between the internal and external GUV solutions.[39b,64] At the conditions employed here, the GUVs adopt prolate ellipsoidal shapes, allowing for the precise measure of the total vesicle area from the vesicle geometry:

$$A = 2\pi b\left(b + a\,\frac{sin^{-1}\,\epsilon}{\epsilon}\right) \tag{1}$$

where a and b are the vesicle semi-axes along and perpendicular to the applied electric field, respectively, and ϵ is the ellipticity defined as $\epsilon^2 = 1 - (b/a)^2$. Subsequently, the GUVs were irradiated with UV and blue light while the AC field was still on and vesicles were recorded for 25–30 s at an acquisition speed of 8 frames per second (fps). Subtracting the initial vesicle area in the absence of irradiation (but with applied field), A_i, from the vesicle area when exposed to light with a specific wavelength, A_l, yields the percentage of relative area increase as $\frac{A_l - A_i}{A_i} \times 100\%$ associated only with the photoisomerization of the azo-PC molecules.

The length of the semi-axes was measured from the recorded vesicle images either manually or using a home-developed software for GUV contour detection.[44a] Data and statistics for GUVs with varying azo-PC fractions were plotted and analyzed using Origin Pro software. At least 10 GUVs from three separate sets of experiments for each investigated azo-PC fraction were used to plot the graphs. The statistical significance of the vesicle area changes due to photoswitching was tested with the one-way analysis of variance (ANOVA).

Vesicle Imaging and Irradiation: UV-induced shape transformations of 100 mol% azo-PC GUV were monitored through Leica TCS SP8 scanning confocal microscope (Wetzlar, Germany) using an HC PL FLUOTAR 40×/ Numerical Aperture (NA) 0.6 (air) objective. The pinhole size during the experiment was set to 1 AU (Airy units) and the scanning speed was 400 Hz in unidirectional mode. The Atto-647N-DOPE dye was excited with a HeNe 633 nm laser with 3% (laser intensity) and the emission signal was collected with a HyD (hybrid) detector in the range of 645–705 nm. In order to observe the photoisomerization response of GUVs, the external 365 nm UV-LED was attached to the condenser of the confocal microscope. The observation chamber was made of two coverslips (22 × 40 mm^2 and 22 × 22 mm^2, Knittel Glass, Germany) sandwiching a spacer with a thickness of 1 mm.

Electrodeformation measurements were performed under phase contrast mode of an inverted microscope Axio Observer D1 (Zeiss, Germany), equipped with a Ph2 20× (NA 0.5) objective. Images were taken with an ORCA R2 CCD camera (Hamamatsu, Japan); see also Experimental Section on Bending Rigidity Measurements for the Setup used for Bending Rigidity Measurements. The GUVs were placed in an Eppendorf electrofusion chamber with an approximate thickness of 8 mm (other specifications are indicated in Experimental Section on Vesicle Electrodeformation and Area Change Measurements). For UV and blue irradiation of the samples, the light from the microscope mercury lamp (HBO 100 W) mounted in epi-illumination mode passed through 365 and 470/40 nm filters, respectively. The irradiation power of the HBO lamp was 60 mW cm^{-2} for the UV filter set (365 nm) and 26 mW cm^{-2} for the blue filter. Power intensities were measured with a LaserCheck power meter after the objective and at the position of the sample.

Bending Rigidity Measurements: The membrane bending rigidity was measured with fluctuation spectroscopy of the thermal undulations of quasi-spherical vesicles as reported previously.[44a,c] Membrane fluctuations were observed under phase contrast of an inverted microscope Axio Observer D1 (Zeiss, Germany) equipped with a PH2 40 x (0.6 NA) objective. Sequences of 3000 images recorded with Pco.Edge sCMOS camera (PCO AG, Kelheim, Germany) at an acquisition rate of 25 fps and exposure time of 200 µs (the same camera was used also for imaging kinetics of vesicle deformation under photoisomerization imaged at 100 fps). The vesicle contour was detected and analyzed with home-developed software.[44a] Low crossover modes were selected as 3–5 for eliminating the effects of vesicle tensions. Only defect-free, quasi-spherical vesicles with low tension values in the range of 10^{-7}–10^{-9} N m^{-1} and 10–25 µm in radius were analyzed.

MD Simulations: POPC lipids were modeled using the amber Lipid14 force field;[65] parameters for the azo tail of azo-PC were taken from the optimized parameters for azobenzene from Ref. [66] based on the general AMBER force field.[67] Figure 1B shows the simulated structures of azo-PC and the respective conformations under UV and blue light. The partial charges for the tails were derived following the methodology used in the Lipid14 force field[65] using 50 conformations from a 50 ns MD trajectory and the R.E.D. tool scripts.[68] The topologies for azo-PC and POPC lipids were converted using the glycam2gmx.pl, script.[69]

The initial topology of the POPC bilayer structure with 400 lipids was generated using the CHARMM-GUI[70] and charmmlipid2amber.py script;[71] coordinates for the azo-PC bilayers were created from the POPC bilayer by fitting and replacing the required number of oleoyl tails with azo tails using VMD.[72] The bilayer systems were then solvated with 24 467 TIP3P water molecules.[73] The GROMACS simulation topologies as well as coordinate files for equilibrated structures of all bilayer systems are included as part of the Supporting Information.

All simulations were performed using GROMACS version 5.1.2.[74] Systems were energy minimized with the steepest descent and equilibrated with and without position restraints on the lipids for a total of 21 ns using the weak coupling scheme[75] to relax the size of the simulation box. Production runs were performed for 100 ns at 303 K, applying the Nose–Hoover thermostat[76] and Parrinello–Rahman barostat[77] to keep the pressure and temperature constant.

The bilayer hydrophobic thickness was defined from the distance between the maxima in the phosphate atom distribution along the bilayer normal. Error estimates were calculated as the standard deviations from 8 subsets of the time frames from the trajectory. Bilayer elastic properties were calculated as follows: The bilayer stretching modulus K_A was obtained from simulations of all bilayer compositions at lateral pressures of −2, −4, −8, −12, and −16 bar. K_A is found from a linear fit of $\Sigma(A) = K_A \frac{A^{lip} - A_0^{lip}}{A_0^{lip}}$, where Σ is the mechanical tension, A^{lip} the area per lipid and A_0^{lip} the area per lipid of a bilayer with zero mechanical tension. The standard deviation was calculated overall systems. The bending modulus κ was calculated from the lipid splay distribution as described in Ref.[45] using the Python modules available at https://github.com/njohner/ost_pymodules/.[78]

The potential of mean force (PMF) for displacing phospholipid headgroups along the reaction coordinate z perpendicular to the lipid bilayer, was calculated by using umbrella sampling. For each lipid displaced across the membrane, 7 evenly spaced umbrella windows were created between $z = 0$ and $z = 3$ nm, with a harmonic umbrella potential with force constant 200 kJ mol^{-1} centered at that position. Two lipids, one from each monolayer, were restrained with an offset of 3 nm between their potentials. In this way, at $z = 0$ for one lipid, the second lipid had $z = 3$ nm. Each umbrella window was simulated for a total of 200 ns, where the first 50 ns were discarded as equilibration time. The PMF profiles were then constructed using the weighted histogram analysis method.[79] Error bars reflect the differences between the PMFs of the separate lipids.

LUV Area Change Measurements via DLS: The average diameter of the LUVs was measured through Zetasizer Nano ZS90 DLS (Malvern Instruments, Malvern, United Kingdom) equipped with a 632.8 nm 4 mW HeNe laser and measuring the scattered light at 173°. In order to detect the UV-induced area change of the LUVs, the UV LED (used also for the measurements with GUVs) was mounted inside the measuring compartment of the Zetasizer. Three replicates were produced for each light condition for each sample. The average size distribution of the LUVs was plotted and the area of LUVs was calculated from the formula of a sphere, $4\pi R^2$, in which R is the LUV radius. Area increase is defined similarly to that for the GUV measurements, namely as $\frac{A_L - A_i}{A_i} \times 100$ where A_L here is the LUV area after the UV exposure and A_i is the initial area of the vesicle before the UV irradiation.

Preparation of Supported Lipid Bilayers (SLBs) and Measurement of Bilayer Thickness through Atomic Force Microscopy (AFM): SLBs were prepared based on a previously reported protocol[80] with some modifications. Briefly, a chloroform solution of POPC or azo-PC lipids was dried in a clean glass vial under nitrogen flow and in a desiccator for 45 min. A 1 mg mL^{-1} final concentration (≈1 mM) of multilamellar vesicle suspension was produced by adding buffer (10 mM sodium citrate, 100 mM NaCl, and 0.5 mM Ethyleneglycol- bis(β-aminoethyl)-N,N,N′,N′-tetraacetic Acid (EGTA), pH 4.5, 45 °C; all materials from Merck, Germany) to the dried lipid layer after overnight incubation at room temperature. The lipid suspension was subjected to bath sonication for 30 min before performing 21 extrusions through a 50 nm membrane using the mini extruder at 45 °C. Thus obtained small unilamellar vesicles (SUVs) were used to produce SLBs on a freshly cleaned (first with 5% sodium dodecyl sulfate solution, then subjected for 1 h and 20 min with freshly prepared piranha solution (H_2SO_4:H_2O_2 ratio of 3:1) under bath sonication) petri dish with glass bottom (µ-Dish, ibidi GmbH). After thoroughly rinsing with deionized water, 400 µL of SUV suspension (2 µM) was pipetted into the petri dish and incubated for 20 min at 45 °C. After a rinsing step (to remove excess SUVs), the SLBs were used for AFM measurements at room temperature.

SLB thickness measurements were performed using a JPK NanoWizard 3 (Bruker Nano GmbH, Berlin, Germany) atomic force microscope mounted on an inverted microscope (model IX3-CBH, Olympus Corp., Japan). The AFM was equipped with an SNL-10 cantilever (Bruker AFM probes; spring constant: 0.35 N m^{-1}, tip height: 7 µm, nominal tip radius: 2 nm; resonance frequency: ≈89 kHz in air). AFM measurements were performed using QI mode, yielding images of 256 pixels × 256 pixels. The images were taken at a vertical speed of 89 µm s^{-1}, z-length of 300 nm, and a cycle period of 3.4 ms per pixel. The SLBs produced in the petri dish were directly used for measurement without further sample treatment. In the case of SLBs containing azo-PC lipids, *trans*-to-*cis* transition was achieved using the DAPI filter (350/50 nm wavelength) from the source SOLA light engine (Lumencore, USA) of the inverted microscope (with a typical output of ≈5 mW cm^{-2}) under dark conditions.

The preparation conditions described above typically resulted in samples, in which patches of SLBs were distributed across the glass substrate. The corresponding AFM images were analyzed using home-written scripts implemented in MatLab (MathWorks, Natick, MA).[81] The open-source software Gwyddion[82] was used to store the height channel of the raw AFM data files as column-separated value (CSV) files, which can be directly loaded into MatLab. In each height map, the substrate (i.e., the glass surface) was assigned to a height value of 0 by fitting and subtracting a poly-

nomial of first order to and from each line of the height map. Pixels, which are not related to the substrate (e.g., SLB-related pixels), were automatically rejected from this process using the following iterative procedure: i) line-wise linear fit to all pixels, ii) rejecting all pixels being higher than 1 nm from the result of the first fit, followed by a line-wise linear fit to all remaining pixels, iii) rejecting all pixels being higher than 0.5 nm from the result of the second fit, followed by a line-wise linear fit to all remaining pixels. Afterward, the height maps were smoothed using a 10 × 10 pixel^2 moving average. The thickness of SLB patches was determined by cropping patch-containing areas from the AFM height map and by generating histograms of the height values of all pixels from such crops. These histograms typically exhibited two prominent peaks, which correspond to pixels of the substrate (centered around a height value of 0) and of the SLB patch, respectively; see, e.g., Figure S7B, Supporting Information, left column). The height distance of these peaks measures the thickness of the corresponding SLB patch.

Specific Membrane Capacitance Measurements and Evaluation of the Membrane Dielectric Constant: Membrane capacitance of pure POPC and 100 mol% *trans* azo-PC GUVs were deduced using an established protocol based on vesicle electrodeformation.[53–54] The field frequency is gradually varied between 500 Hz and 1 MHz at 10 kV m^{-1} field strength. In this frequency range, the GUVs can adopt different morphologies (prolate, oblate, or spherical) depending on the conductivity ratio $\Lambda = \frac{\lambda_{in}}{\lambda_{out}}$ between the inner and outer GUV solutions.[40,64] For $\Lambda < 1$, the GUVs adopt prolate shapes at low field frequencies. With increasing frequency, the aspect ratio a/b decreases and at a critical frequency f_c, the vesicle shape is a sphere, i.e. $\frac{a}{b} = 1$. Further increase in the frequency leads to oblate morphologies, $\frac{a}{b} < 1$. Critical frequency depends on the specific membrane capacitance, C_m[83]:

$$f_c = \frac{\lambda_{in}}{2\pi R C_m} \frac{1}{\sqrt{(1-\Lambda)(3+\Lambda)}} \quad (2)$$

where R is the GUV radius. The critical frequency can be obtained from frequency-sweep experiments in the AC field. The GUV solution (see Section 2.1 for preparation) was transferred into the commercially available Eppendorf electrofusion chamber described in Section Vesicle Electrodeformation and Area Change Measurements and exposed to the AC field. GUVs were monitored via Axio Observer D1 Phase contrast microscope equipped with Ph2 20× (NA 0.5) objective. Images were acquired with an ORCA R2 CCD camera (Hamamatsu, Japan) and the aspect ratio changes of GUVs were analyzed from the contour of the vesicles via lab-owned software.[44a] For the statistics, 10 GUVs were analyzed with radii varying between 3 and 10 µm for each composition. The specific membrane capacitance was deduced from the slope of a linear fit to the critical frequency as a function of $1/R$ using Equation 2.

The experimentally measured capacitance C_m is the resultant of the capacitances of the bare lipid bilayer, C_B and of the ionic double layers in the inner and outer solutions $C_{D,in}$ and $C_{D,out}$ so that

$$C_m = \left(1/C_B + 1/C_{D,in} + 1/C_{D,out}\right)^{-1} \quad (3)$$

The membrane can be considered a 2D surface with dielectric permittivity $\epsilon_{r,B}\epsilon_0$, where $\epsilon_{r,B}$ is the relative (dimensionless) dielectric permittivity of the bilayer and ϵ_0 is the vacuum permittivity, $\epsilon_0 \approx 8.85 \times 10^{-12}$ F m^{-1}. The dielectric permittivity of the bilayer relates to its capacitance and thickness d as:

$$C_B = \frac{\epsilon_{r,B}\,\epsilon_0}{d} \quad (4)$$

The capacitive contributions $C_{D,in}$ and $C_{D,out}$ can be estimated from the dielectric constant of the water solution $\epsilon_{r,W} \approx 80$ and the thickness of the Debye length, λ_D. For the inner and outer vesicle solutions used here λ_D is 17.5 and 12.4 nm, respectively, yielding $C_{D,in} = 4.05$ µF cm^{-2} and $C_{D,out} = 5.72$ µF cm^{-2}. These values and C_m were used in Equation 3 to estimate the specific bilayer capacitance C_B for pure POPC and 100 mol% *trans* azo-PC membrane. Then, the bilayer dielectric constant $\epsilon_{r,B}$ was deduced from Equation 4 by using membrane thickness values from the AFM studies in Experimental Section on Preparation of Supported Lipid Bilayers (SLBs) and Measurement of Bilayer Thickness through Atomic Force Microscopy.

Exogenous Addition of azo-PC: For exposing preformed GUVs to exogenous azo-PC, pure POPC GUVs prepared in 100 mM sucrose solution were diluted 1:1 in 105 mM glucose solution to a final volume of 174 µL, which was then mixed with 1 µL of 2.72 mM azo-PC dissolved in 2:1 (vol) dichloromethane/methanol solution. The final concentration of azo-PC in the GUV suspension was 15.56 µM being close to the total amount of POPC lipids forming the vesicles, i.e., the final azo-PC-to-POPC ratio was ≈1:1. After 20 min of incubation allowing the evaporation of the organic solvents, POPC GUVs enriched with azo-PC were placed in an observation chamber and exposed to UV and blue irradiation, respectively, and monitored by phase-contrast imaging.

Supporting Information

Supporting Information is available from the Wiley Online Library or from the author.

Acknowledgements

M.A. acknowledges funding from the International Max Planck Research School on Multiscale BioSystems. R.D. and M.A. thank M. Miettinen for the fruitful discussions on the stability and flip-flop in asymmetric membranes. M.A. thanks V. Vitkova for the feedback on the calculations of the dielectric constant of vesicles. This work was supported by Germany's Excellence Strategy, EXC 2008/1 (UniSysCat), Grant 390540038.

Open access funding enabled and organized by Projekt DEAL.

Correction added on November 3, 2023, after first online publication: Projekt Deal funding statement has been added.

Conflict of Interest

The authors declare no conflict of interest.

Data Availability Statement

The data that support the findings of this study are available from the corresponding author upon reasonable request. The simulation files which are use in this study are openly available at: https://doi.org/10.17617/3.CWOZQO.

Keywords

atomic force microscopy (AFM), azo-PC, bending rigidity, giant vesicles, membrane capacitance, molecular dynamics simulations, photoswitchable lipids

Received: June 28, 2023
Revised: July 24, 2023
Published online: August 31, 2023

[1] a) S. Masiero, S. Lena, S. Pieraccini, G. P. Spada, *Angew. Chem., Int. Ed.* **2008**, *47*, 3184; b) Z. Wang, P. Erhart, T. Li, Z.-Y. Zhang, D. Sampedro, Z. Hu, H. A. Wegner, O. Brummel, J. Libuda, M. B. Nielsen, K. Moth-Poulsen, *Joule* **2021**, *5*, 3116.
[2] D. Baigl, *Lab Chip* **2012**, *12*, 3637.
[3] J. Palacci, S. Sacanna, A. Vatchinsky, P. M. Chaikin, D. J. Pine, *J. Am. Chem. Soc.* **2013**, *135*, 15978.

[4] A. Mallick, S. Roy, *Nanoscale* **2018**, *10*, 12713.
[5] M. Pacheco, B. Jurado-Sánchez, A. Escarpa, *Angew. Chem., Int. Ed.* **2019**, *58*, 18017.
[6] a) D. Zhou, R. Zhuang, X. Chang, L. Li, *Research* **2020**, *2020*, 6821595; b) J. Parmar, D. Vilela, K. Villa, J. Wang, S. Sánchez, *J. Am. Chem. Soc.* **2018**, *140*, 9317.
[7] a) F. Höglsperger, T. Betz, B. J. Ravoo, *ACS Macro Lett.* **2022**, *11*, 537; b) J. Boelke, S. Hecht, *Adv. Opt. Mater.* **2019**, *7*, 1900404.
[8] P. Klán, J. Wirz, in *Molecular Photoswitches*, Wiley, Weinheim **2022**.
[9] a) H. A. Wegner, *Angew. Chem., Int. Ed.* **2012**, *51*, 2281; b) V. Balzani, M. Clemente-León, A. Credi, B. Ferrer, M. Venturi, A. H. Flood, J. F. Stoddart, *Proc. Natl. Acad. Sci. U. S. A.* **2006**, *103*, 1178; c) N. Katsonis, M. Lubomska, M. M. Pollard, B. L. Feringa, P. Rudolf, *Prog. Surf. Sci.* **2007**, *82*, 407.
[10] a) H. M. D. Bandara, S. C. Burdette, *Chem. Soc. Rev.* **2012**, *41*, 1809; b) A. A. Beharry, G. A. Woolley, *Chem. Soc. Rev.* **2011**, *40*, 4422; c) J. Morstein, A. C. Impastato, D. Trauner, *ChemBioChem* **2021**, *22*, 73.
[11] L. Dong, Y. Feng, L. Wang, W. Feng, *Chem. Soc. Rev.* **2018**, *47*, 7339.
[12] R. S. Stoll, M. V. Peters, A. Kuhn, S. Heiles, R. Goddard, M. Bühl, C. M. Thiele, S. Hecht, *J. Am. Chem. Soc.* **2009**, *131*, 357.
[13] A. Kopyshev, K. Kanevche, N. Lomadze, E. Pfitzner, S. Loebner, R. R. Patil, J. Genzer, J. Heberle, S. Santer, *ACS Appl. Polym. Mater.* **2019**, *1*, 3017.
[14] a) I. A. Banerjee, L. Yu, H. Matsui, *J. Am. Chem. Soc.* **2003**, *125*, 9542; b) M. Liu, X. Yan, M. Hu, X. Chen, M. Zhang, B. Zheng, X. Hu, S. Shao, F. Huang, *Org. Lett.* **2010**, *12*, 2558.
[15] P. Leippe, J. A. Frank, *Curr. Opin. Struct. Biol.* **2019**, *57*, 23.
[16] H. Nakano, T. Takahashi, T. Kadota, Y. Shirota, *Adv. Mater.* **2002**, *14*, 1157.
[17] a) J. Liu, W. Bu, L. Pan, J. Shi, *Angew. Chem., Int. Ed.* **2013**, *52*, 4375; b) W. A. Velema, W. Szymanski, B. L. Feringa, *J. Am. Chem. Soc.* **2014**, *136*, 2178; c) N. Chander, J. Morstein, J. S. Bolten, A. Shemet, P. R. Cullis, D. Trauner, D. Witzigmann, *Small* **2021**, *17*, 2008198.
[18] J. Morstein, D. Trauner, *Curr. Opin. Chem. Biol.* **2019**, *50*, 145.
[19] a) S. Kellner, S. Berlin, *Appl. Sci.* **2020**, *10*, 805; b) K. Hüll, J. Morstein, D. Trauner, *Chem. Rev.* **2018**, *118*, 10710.
[20] N. Tamai, H. Miyasaka, *Chem. Rev.* **2000**, *100*, 1875.
[21] A. Yoshida, N. Sakai, Y. Uekusa, Y. Imaoka, Y. Itagaki, Y. Suzuki, S. H. Yoshimura, *PLoS Biol.* **2018**, *16*, e2004786.
[22] F. L. Urbina, S. M. Gomez, S. L. Gupton, *J. Cell Biol.* **2018**, *217*, 1113.
[23] a) S. Maharana, K. V. Iyer, N. Jain, M. Nagarajan, Y. Wang, G. V. Shivashankar, *Nucleic Acids Res.* **2016**, *44*, 5148; b) C. Cadart, E. Zlotek-Zlotkiewicz, M. Le Berre, M. Piel, Helen K. Matthews, *Dev. Cell* **2014**, *29*, 159.
[24] S. B. Khatau, S. Kusuma, D. Hanjaya-Putra, P. Mali, L. Cheng, J. S. Lee, S. Gerecht, D. Wirtz, *PLoS One* **2012**, *7*, e36689.
[25] J. Tong, Y. Qi, X. Wang, L. Yu, C. Su, W. Xie, J. Zhang, *Biochim. Biophys. Acta, Mol. Cell Res.* **2017**, *1864*, 2389.
[26] J. V. Shah, *J. Cell Biol.* **2010**, *191*, 233.
[27] F. L. Au-Kriegel, R. Au-Köhler, J. Au-Bayat-Sarmadi, S. Au-Bayerl, A. E. Au-Hauser, R. Au-Niesner, A. Au-Luch, Z. Au-Cseresnyes, *JoVE* **2018**, *140*, e58543.
[28] a) P. Pascual-Vargas, S. Cooper, J. Sero, V. Bousgouni, M. Arias-Garcia, C. Bakal, *Sci. Data* **2017**, *4*, 170018; b) S. M. Lyons, E. Alizadeh, J. Mannheimer, K. Schuamberg, J. Castle, B. Schroder, P. Turk, D. Thamm, A. Prasad, *Biol. Open* **2016**, *5*, 289; c) A. Pasqualato, A. Palombo, A. Cucina, M. A. Mariggiò, L. Galli, D. Passaro, S. Dinicola, S. Proietti, F. D'Anselmi, P. Coluccia, M. Bizzarri, *Exp. Cell Res.* **2012**, *318*, 835.
[29] a) A. Saraste, K. Pulkki, *Cardiovasc. Res.* **2000**, *45*, 528; b) G. Häcker, *Cell Tissue Res.* **2000**, *301*, 5; c) U. Ziegler, P. Groscurth, *Physiology* **2004**, *19*, 124.
[30] a) R. Dimova, *Ann. Rev. Biophys.* **2019**, *48*, 93; b) R. Dimova, C. Marques, in *The Giant Vesicle Book*, Taylor & Francis Group, LLC, Boca Raton **2019**.
[31] J. B. Manneville, P. Bassereau, D. Levy, J. Prost, *Phys. Rev. Lett.* **1999**, *82*, 4356.
[32] a) H. Erkan-Candag, D. Krivic, M. A. F. Gsell, M. Aleksanyan, T. Stockner, R. Dimova, O. Tiapko, K. Groschner, *Biomolecules* **2022**, *12*, 799; b) J. Pfeffermann, B. Eicher, D. Boytsov, C. Hannesschlaeger, T. R. Galimzyanov, T. N. Glasnov, G. Pabst, S. A. Akimov, P. Pohl, *J. Photochem. Photobiol. B* **2021**, *224*, 112320; c) V. N. Georgiev, A. Grafmüller, D. Bléger, S. Hecht, S. Kunstmann, S. Barbirz, R. Lipowsky, R. Dimova, *Adv. Sci.* **2018**, *5*, 1800432; d) A. Diguet, M. Yanagisawa, Y.-J. Liu, E. Brun, S. Abadie, S. Rudiuk, D. Baigl, *J. Am. Chem. Soc.* **2012**, *134*, 4898; e) F. Crea, A. Vorkas, A. Redlich, R. Cruz, C. Shi, D. Trauner, A. Lange, R. Schlesinger, J. Heberle, *Front. Mol. Biosci.* **2022**, *9*, 905306.
[33] a) E. Karatekin, O. Sandre, H. Guitouni, N. Borghi, P. H. Puech, F. Brochard-Wyart, *Biophys. J.* **2003**, *84*, 1734; b) O. Sandre, L. Moreaux, F. Brochard-Wyart, *Proc. Natl. Acad. Sci. U. S. A.* **1999**, *96*, 10591.
[34] a) C. Pernpeintner, J. A. Frank, P. Urban, C. R. Roeske, S. D. Pritzl, D. Trauner, T. Lohmüller, *Langmuir* **2017**, *33*, 4083; b) P. Albanese, S. Cataldini, C. Z. J. Ren, N. Valletti, J. Brunetti, J. L. Y. Chen, F. Rossi, *Pharmaceutics* **2022**, *14*, 2777; c) P. Urban, S. D. Pritzl, D. B. Konrad, J. A. Frank, C. Pernpeintner, C. R. Roeske, D. Trauner, T. Lohmüller, *Langmuir* **2018**, *34*, 13368; d) S. D. Pritzl, P. Urban, A. Prasselsperger, D. B. Konrad, J. A. Frank, D. Trauner, T. Lohmüller, *Langmuir* **2020**, *36*, 13509.
[35] N. Hartrampf, S. M. Leitao, N. Winter, H. Toombs-Ruane, J. A. Frank, P. Schwille, D. Trauner, H. G. Franquelim, *Biophys. J.* **2023**, *122*, 2325.
[36] P. Urban, S. D. Pritzl, M. F. Ober, C. F. Dirscherl, C. Pernpeintner, D. B. Konrad, J. A. Frank, D. Trauner, B. Nickel, T. Lohmueller, *Langmuir* **2020**, *36*, 2629.
[37] H. Bouvrais, T. Pott, L. A. Bagatolli, J. H. Ipsen, P. Meleard, *Biochim. Biophys. Acta Biomembr.* **2010**, *1798*, 1333.
[38] N. F. Morales-Penningston, J. Wu, E. R. Farkas, S. L. Goh, T. M. Konyakhina, J. Y. Zheng, W. W. Webb, G. W. Feigenson, *Biochim. Biophys. Acta* **2010**, *1798*, 1324.
[39] a) K. A. Riske, T. P. Sudbrack, N. L. Archilha, A. F. Uchoa, A. P. Schroder, C. M. Marques, M. S. Baptista, R. Itri, *Biophys. J.* **2009**, *97*, 1362; b) M. Aleksanyan, H. A. Faizi, M.-A. Kirmpaki, P. M. Vlahovska, K. A. Riske, R. Dimova, *Adv. Phys.: X* **2023**, *8*, 2125342.
[40] S. Aranda, K. A. Riske, R. Lipowsky, R. Dimova, *Biophys. J.* **2008**, *95*, L19.
[41] H. A. Faizi, R. Dimova, P. M. Vlahovska, *Biophys. J.* **2022**, *121*, 910.
[42] a) V. Czikklely, H. D. Forsterling, H. Kuhn, *Chem. Phys. Lett.* **1970**, *6*, 207; b) A. Eisfeld, J. S. Briggs, *Chem. Phys.* **2006**, *324*, 376.
[43] T. Nägele, R. Hoche, W. Zinth, J. Wachtveitl, *Chem. Phys. Lett.* **1997**, *272*, 489.
[44] a) R. S. Gracià, N. Bezlyepkina, R. L. Knorr, R. Lipowsky, R. Dimova, *Soft Matter* **2010**, *6*, 1472; b) H. A. Faizi, S. L. Frey, J. Steinkühler, R. Dimova, P. M. Vlahovska, *Soft Matter* **2019**, *15*, 6006; c) H. A. Faizi, C. J. Reeves, V. N. Georgiev, P. M. Vlahovska, R. Dimova, *Soft Matter* **2020**, *16*, 8996.
[45] M. Doktorova, D. Harries, G. Khelashvili, *Phys. Chem. Chem. Phys.* **2017**, *19*, 16806.
[46] R. Dimova, *Adv. Colloid Interface Sci.* **2014**, *208*, 225.
[47] E. A. Evans, *Biophys. J.* **1974**, *14*, 923.
[48] a) P. Shchelokovskyy, S. Tristram-Nagle, R. Dimova, *New J Phys* **2011**, *13*, 025004; b) S. Tristram-Nagle, R. Chan, E. Kooijman, P. Uppamoochikkal, W. Qiang, D. P. Weliky, J. F. Nagle, *J. Mol. Biol.* **2010**, *402*, 139.
[49] A. W. Tian, B. R. Capraro, C. Esposito, T. Baumgart, *Biophys. J.* **2009**, *97*, 1636.

[50] a) M. Azouz, C. Cullin, S. Lecomte, M. Lafleur, *Nanoscale* **2019**, *11*, 20857; b) O. Domènech, L. Redondo, L. Picas, A. Morros, M. T. Montero, J. Hernández-Borrell, *J. Mol. Recognit.* **2007**, *20*, 546.
[51] a) W. Rawicz, K. C. Olbrich, T. McIntosh, D. Needham, E. Evans, *Biophys. J.* **2000**, *79*, 328; b) R. Goetz, G. Gompper, R. Lipowsky, *Phys. Rev. Lett.* **1999**, *82*, 221.
[52] J. Golowasch, F. Nadim, in *Encyclopedia of Computational Neuroscience*, (Eds.: D. Jaeger, R. Jung), Springer, Manhattan, New York **2014**.
[53] P. F. Salipante, R. L. Knorr, R. Dimova, P. M. Vlahovska, *Soft Matter* **2012**, *8*, 3810.
[54] a) V. Vitkova, V. Yordanova, G. Staneva, O. Petkov, A. Stoyanova-Ivanova, K. Antonova, G. Popkirov, *Membranes* **2021**, *11*, 847; b) H. A. Faizi, A. Tsui, R. Dimova, P. M. Vlahovska, *Langmuir* **2022**, *38*, 10548.
[55] a) R. Dasgupta, M. S. Miettinen, N. Fricke, R. Lipowsky, R. Dimova, *Proc. Natl. Acad. Sci. U. S. A.* **2018**, *115*, 5756; b) M. Aleksanyan, R. B. Lira, J. Steinkühler, R. Dimova, *Biophys. J.* **2022**, *121*, 3295; c) S. A. Gandhi, C. V. Kelly, *Biophys. J.* **2022**, *121*, 3173; d) P. Bassereau, R. Jin, T. Baumgart, M. Deserno, R. Dimova, V. A. Frolov, P. V. Bashkirov, H. Grubmüller, R. Jahn, H. J. Risselada, L. Johannes, M. M. Kozlov, R. Lipowsky, T. J. Pucadyil, W. F. Zeno, J. C. Stachowiak, D. Stamou, A. Breuer, L. Lauritsen, C. Simon, C. Sykes, G. A. Voth, T. R. Weikl, *J. Phys. D: Appl. Phys.* **2018**, *51*, 343001.
[56] a) V. T. Armstrong, M. R. Brzustowicz, S. R. Wassall, L. J. Jenski, W. Stillwell, *Arch. Biochem. Biophys.* **2003**, *414*, 74; b) W. F. D. Bennett, J. L. MacCallum, M. J. Hinner, S. J. Marrink, D. P. Tieleman, *J. Am. Chem. Soc.* **2009**, *131*, 12714.
[57] S. D. Pritzl, D. B. Konrad, M. F. Ober, A. F. Richter, J. A. Frank, B. Nickel, D. Trauner, T. Lohmüller, *Langmuir* **2022**, *38*, 385.
[58] a) R. Dimova, B. Pouligny, C. Dietrich, *Biophys. J.* **2000**, *79*, 340; b) E. Evans, D. Needham, *J. Phys. Chem.* **1987**, *91*, 4219.
[59] J. R. Henriksen, J. H. Ipsen, *Eur. Phys. J. E Soft Matter* **2004**, *14*, 149.
[60] M. L. DiFrancesco, F. Lodola, E. Colombo, L. Maragliano, M. Bramini, G. M. Paternò, P. Baldelli, M. D. Serra, L. Lunelli, M. Marchioretto, G. Grasselli, S. Cimò, L. Colella, D. Fazzi, F. Ortica, V. Vurro, C. G. Eleftheriou, D. Shmal, J. F. Maya-Vetencourt, C. Bertarelli, G. Lanzani, F. Benfenati, *Nat. Nanotechnol.* **2020**, *15*, 296.
[61] a) T. V. Ratto, M. L. Longo, *Biophys. J.* **2002**, *83*, 3380; b) M. C. Giocondi, L. Pacheco, P. E. Milhiet, C. Le Grimellec, *Ultramicroscopy* **2001**, *86*, 151.
[62] V. Vitkova, D. Mitkova, K. Antonova, G. Popkirov, R. Dimova, *Colloids Surf. Physicochem. Eng. Aspects* **2018**, *557*, 51.
[63] R. B. Lira, T. Robinson, R. Dimova, K. A. Riske, *Biophys. J.* **2019**, *116*, 79.
[64] R. Dimova, K. A. Riske, in *Handbook of Electroporation*, (Ed.: D. Miklavčič), Springer International Publishing, Cham **2016**.
[65] C. J. Dickson, B. D. Madej, Å. A. Skjevik, R. M. Betz, K. Teigen, I. R. Gould, R. C. Walker, *J. Chem. Theory Comput.* **2014**, *10*, 865.
[66] P. Duchstein, C. Neiss, A. Görling, D. Zahn, *J. Mol. Model* **2012**, *18*, 2479.
[67] J. Wang, R. M. Wolf, J. W. Caldwell, P. A. Kollman, D. A. Case, *J. Comput. Chem.* **2004**, *25*, 1157.
[68] F. Y. Dupradeau, A. Pigache, T. Zaffran, C. Savineau, R. Lelong, N. Grivel, D. Lelong, W. Rosanski, P. Cieplak, *Phys. Chem. Chem. Phys.* **2010**, *12*, 7821.
[69] M. Wehle, I. Vilotijevic, R. Lipowsky, P. H. Seeberger, D. Varon Silva, M. Santer, *J. Am. Chem. Soc.* **2012**, *134*, 18964.
[70] a) S. Jo, T. Kim, V. G. Iyer, W. Im, *J. Comput. Chem.* **2008**, *29*, 1859; b) S. Jo, J. B. Lim, J. B. Klauda, W. Im, *Biophys. J.* **2009**, *97*, 50; c) E. L. Wu, X. Cheng, S. Jo, H. Rui, K. C. Song, E. M. Dávila-Contreras, Y. Qi, J. Lee, V. Monje-Galvan, R. M. Venable, J. B. Klauda, W. Im, *J. Comput. Chem.* **2014**, *35*, 1997.
[71] D. A. Case, T. A. Darden, T. E. Cheatham III, C. L. Simmerling, J. Wang, R. E. Duke, R. Luo, R. C. Walker, W. Zhang, K. M Merz, B. Roberts, S. Hayik, A. Roitberg, G. Seabra, J. Swails, A. W. Götz, I. Kolossváry, K. F. Wong, F. Paesani, J. Vanicek, R. M. Wolf, J. Liu, X. Wu, S. R. Brozell, T. Steinbrecher, H. Gohlke, Q. Cai, X. Ye, J. Wang, M.-J. Hsieh, et al., AMBER 12, University of California, San Francisco, **2012**.
[72] W. Humphrey, A. Dalke, K. Schulten, *J. Mol. Graph.* **1996**, *14*, 33.
[73] W. L. Jorgensen, J. Chandrasekhar, J. D. Madura, R. W. Impey, M. L. Klein, *J. Chem. Phys.* **1983**, *79*, 926.
[74] a) M. J. Abraham, T. Murtola, R. Schulz, S. Páll, J. C. Smith, B. Hess, E. Lindahl, *SoftwareX* **2015**, *1–2*, 19; b) D. Van Der Spoel, E. Lindahl, B. Hess, G. Groenhof, A. E. Mark, H. J. C. Berendsen, *J. Comput. Chem.* **2005**, *26*, 1701.
[75] H. J. Berendsen, J. v. Postma, W. F. van Gunsteren, A. DiNola, J. R. Haak, *J. Chem. Phys.* **1984**, *81*, 3684.
[76] a) S. Nosé, *Mol. Phys.* **1984**, *52*, 255; b) W. G. Hoover, *Phys. Rev. A* **1985**, *31*, 1695.
[77] a) M. Parrinello, A. Rahman, *J. Appl. Phys.* **1981**, *52*, 7182; b) S. Nosé, M. L. Klein, *Mol. Phys.* **1983**, *50*, 1055.
[78] N. Johner, D. Harries, G. Khelashvili, *BMC Bioinformatics* **2016**, *17*, 161.
[79] S. Kumar, J. M. Rosenberg, D. Bouzida, R. H. Swendsen, P. A. Kollman, *J. Comput. Chem.* **1992**, *13*, 1011.
[80] N. Yandrapalli, Q. Lubart, H. S. Tanwar, C. Picart, J. Mak, D. Muriaux, C. Favard, *Sci. Rep.* **2016**, *6*, 39332.
[81] S. Block, G. Glöckl, W. Weitschies, C. A. Helm, *Nano Lett.* **2011**, *11*, 3587.
[82] D. Nečas, P. Klapetek, *Open Phys.* **2012**, *10*, 181.
[83] a) T. Yamamoto, S. Aranda-Espinoza, R. Dimova, R. Lipowsky, *Langmuir* **2010**, *26*, 12390; b) P. M. Vlahovska, R. S. Gracia, S. Aranda-Espinoza, R. Dimova, *Biophys. J.* **2009**, *96*, 4789.

Open Access

Supporting Information

for *Adv. Sci.*, DOI 10.1002/advs.202304336

Photomanipulation of Minimal Synthetic Cells: Area Increase, Softening, and Interleaflet Coupling of Membrane Models Doped with Azobenzene-Lipid Photoswitches

*Mina Aleksanyan, Andrea Grafmüller, Fucsia Crea, Vasil N. Georgiev, Naresh Yandrapalli, Stephan Block, Joachim Heberle and Rumiana Dimova**

SUPPORTING INFORMATION

Photomanipulation of minimal synthetic cells: area increase, softening, and interleaflet coupling of membrane models doped with azobenzene-lipid photoswitches

Mina Aleksanyan[1,2], Andrea Grafmüller[1], Fucsia Crea[3], Vasil N. Georgiev[1], Naresh Yandrapalli[1], Stephan Block[2], Joachim Heberle[3], Rumiana Dimova[1]*

[1] Max Planck Institute of Colloids and Interfaces, Science Park Golm, 14476 Potsdam, Germany

[2] Institute for Chemistry and Biochemistry, Freie Universität Berlin, 14195 Berlin, Germany;

[3] Department of Physics, Freie Universität Berlin, 14195 Berlin, Germany

* Address for correspondence: Rumiana.Dimova@mpikg.mpg.de

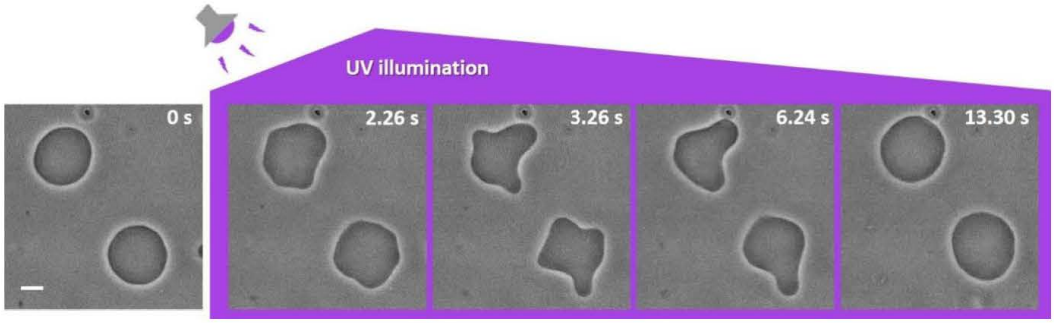

Figure S1: Time sequence of the response of GUVs made of azo-PC:POPC 50:50 mol% to *trans*-to-*cis* photoisomerization under UV illumination, see also Movie S3. The GUVs were grown in 100 mM sucrose solution and 1:1 diluted in 105 mM glucose solution. The time stamps show the time after starting the UV irradiation. The scale bar corresponds to 10 µm. UV illumination triggers complex shape transformations in GUVs over time.

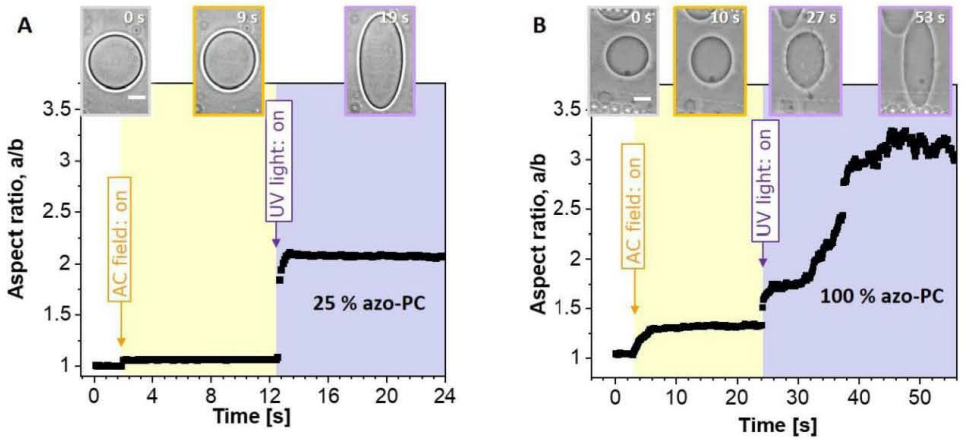

Figure S2: Deformation of vesicles composed of 25 mol% (A) and 100 mol% azo-PC (B) under the influence of UV light. The graph shows the vesicle degree of deformation (a/b, aspect ratio) over time. The snapshots illustrate vesicle shape changes over time. The color code is as follows: Gray frames correspond to the vesicles in the absence of AC-field and UV-light, orange frames correspond to the vesicles exposed to AC-field (5kV m^{-1} and 1 MHz), purple frames correspond to vesicles exposed to both AC-field (5kV m^{-1} and 1 MHz) and UV illumination (365 nm). The scale bar corresponds to 20 µm. As azo-PC fraction in the membrane increases from 25 to 100 mol %, GUVs undergo larger membrane deformations through complex shape transformations and budding events slowing down vesicle response and increasing the time for the GUV to reach to the maximum degree of deformation.

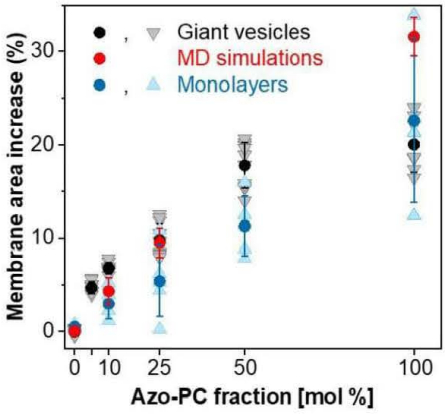

Figure S3: Individual measurement data points for membrane area expansion associated with photoisomerization as assessed from GUV electrodeformation (gray symbols show data on individual GUVs; black data given as mean values +/-SD are as in Fig. 2E in the main text) and monolayers (light blue triangles show measurement of individual Langmuir monolayers, dark blue – mean +/- SD as in Fig. 3E). The MD simulations data (red, as in Fig. 3E) are also included.

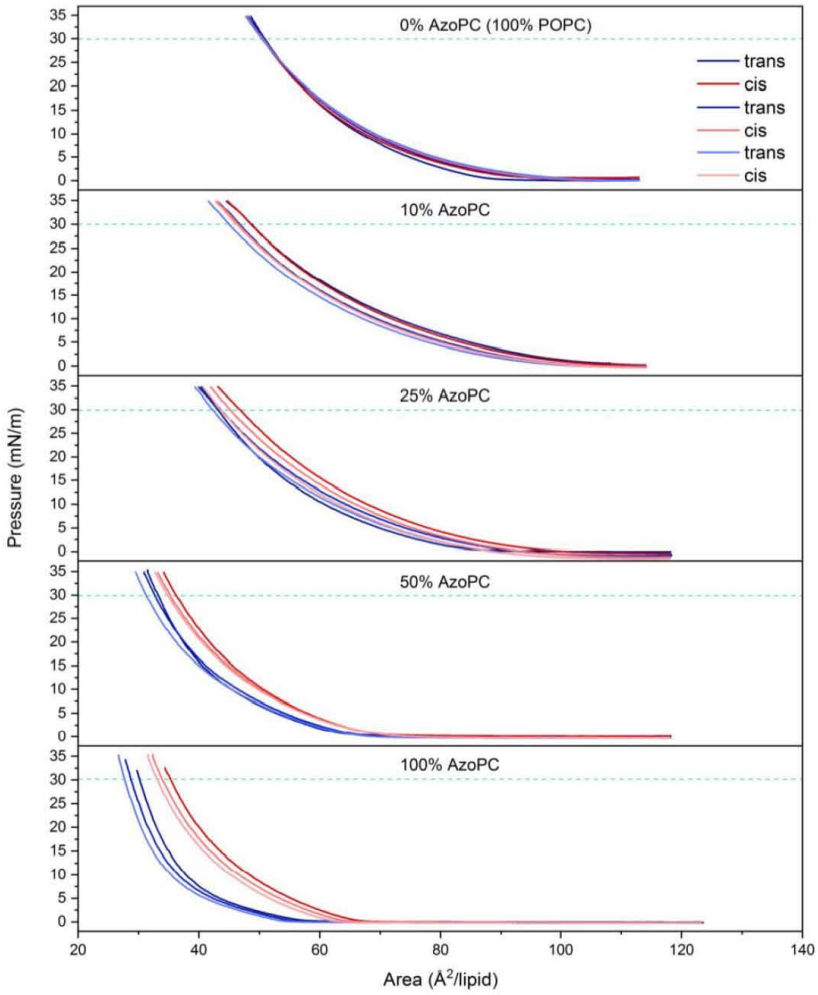

Figure S4: Example pressure-area isotherms of lipid monolayers containing different fractions of azo-PC measured consecutively. The area values at 30 mN/m pressure (indicated with a green dashed line in all panels) were used for calculating the monolayer area expansion reported in Fig. 2E in the main text. The small drift towards smaller area between consecutive isotherms of monolayers with the same composition are due to lipid loss occurring in cycles of compression isotherms. The pairs of isotherms considered for the calculation of the area expansion are always two consecutive ones, one *trans* and one *cis*. For visual clarity, only one set of isotherms per film composition is shown. The area increase of the films containing 10 % (mol) Azo-PC was on average 1.3 ± 1.1 % (standard deviation); for the 25 % film it was 5.0 ± 2.2 %; for the 50 % film it was 10.9 ± 3.8 %; for the 100 % it was 19.5 ± 6.4 %. The control experiment with a pure POPC monolayer showed no expansion (-0.20 ± 0.38 %). With increasing Azo-PC fraction in the lipid monolayers the pressure-area isotherms show larger expansion.

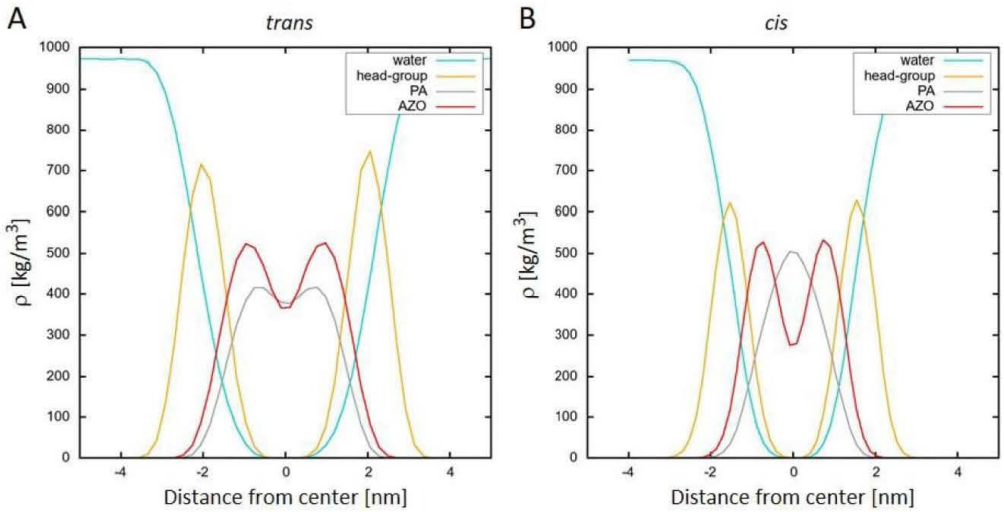

Figure S5: Radial density profiles from MD simulations of 100 mol% azo-PC in (A) *trans* and (B) *cis* conformation. The conformational change from *trans* to *cis* of azo-PC (AZO, red) leads to relocation of the palmitoyl chains (PA, gray) deeper in the bilayer and the headgroup region becomes better hydrated.

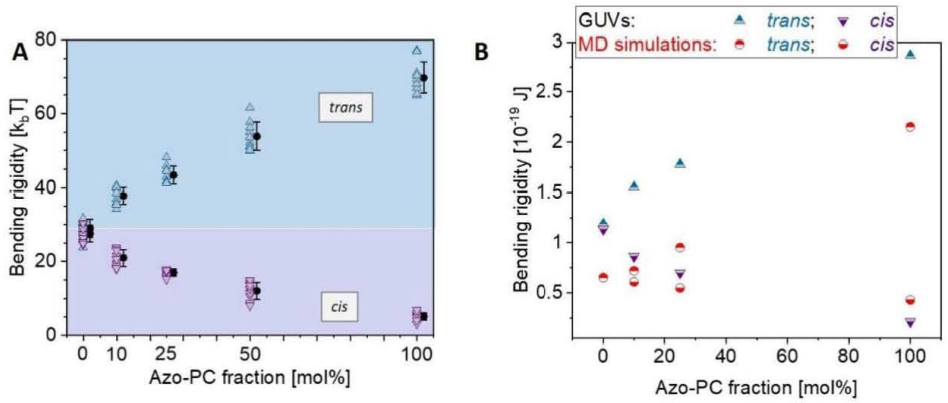

Figure S6: Raw data for the values of bending rigidity of POPC membranes with various azo-PC fractions obtained from experiments and simulations. (A) Experimental data obtained from fluctuation spectroscopy: open triangles show measurements on individual vesicles; solid circles and error bars indicate mean and standard deviations. (B) Mean values of the bending rigidity (in Joules) obtained from experiment (triangles – same mean data +/-SD as in B) and MD simulations (circles). As *trans* azo-PC fraction in the membrane increases, GUVs become stiffer. As *cis* azo-PC fraction in the membrane increases, GUVs become softer.

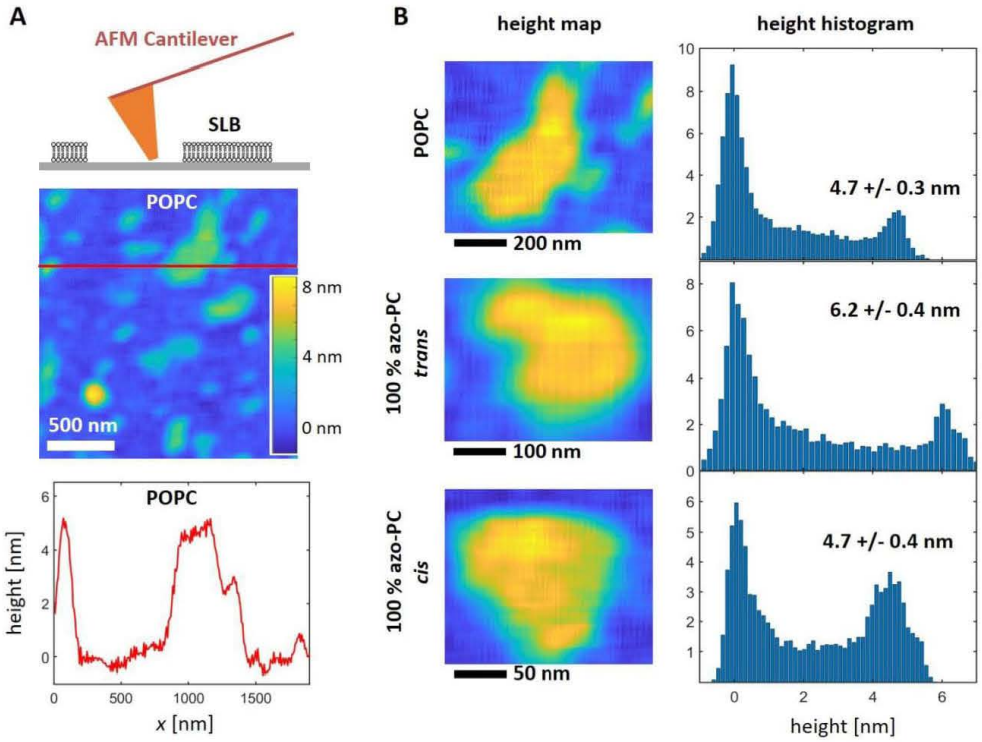

Figure S7: Thickness measurements of POPC and 100 % azo-PC supported lipid bilayers (SLBs) using atomic force microscopy (AFM). (A, top) Schematic representation of the measurement geometry, in which SLB patches were formed on glass surfaces and imaged using liquid phase AFM. (A, middle) Representative height map of a sample containing POPC patches and (A, bottom) a typical cross section in the height map. (B, left) AFM screenshots of example patches of pure POPC (top) and azo-PC SLBs in *trans* (middle) and *cis* state (bottom), and (B, right) the corresponding height histograms. The thickness of the bilayers made of POPC, 100 mol % *cis* and *trans* azo-PC measured as 4.7 ± 0.3, 4.7 ± 0.4 and 6.2 ± 0.4 nm, respectively.

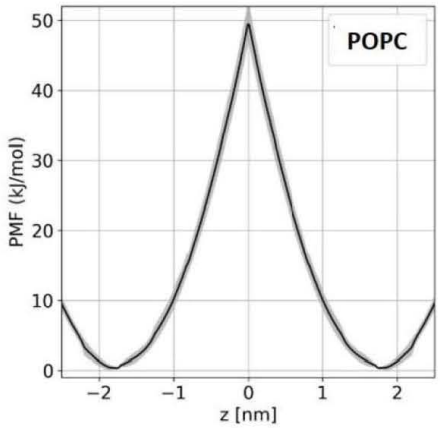

Figure S8: Potential mean force calculations (PMF) of interleaflet translocation of a POPC lipid in POPC bilayer. The potential maximum of the plot illustrates the energy barrier for flip flop while 'z' is the displacement coordinate being perpendicular to the lipid bilayer. Standard error of the calculation is

shown in grey. PMF profiles of POPC, *cis* and *trans* azo-PC lipids showed the same trend indicating the absence of flip-flop in the experimental time scales for all these lipid compositions.

Simulation files

Coordinate files, simulation topologies and force field parameters for simulating the azo-PC systems in GROMACS are available at: https://doi.org/10.17617/3.CWOZQO

Movie captions

Movie S1: A sequence of confocal images of a sample of GUVs made of 100 mol% azo-PC labelled with 0.1 mol% Atto-647N-DOPE monitored during photoisomerization (images are acquired roughly every 1.3 s). Time stamps show time after initiating acquisition. The initial radius of the larger vesicle is approximately 20 µm. The frames in which UV irradiation is applied are marked in the upper part of the images. The video was processed with LAS X, Fiji and HandBrake software.

Movie S2: Real time video of 50 mol% azo-PC GUV acquired under phase contrast at 50 frames per second (fps); same vesicle as in Fig. 1D in the main text. The initial radius of the GUV is approximately 12 µm. The time stamps and the period of UV irradiation are indicated in the upper part of the images. The video was processed with FiJi and HandBrake software.

Movie S3: Real time video (50 fps) of two 50 mol% azo-PC GUVs shown also in Fig. S1. The radii of GUVs are approximately 10 and 12 µm. The time stamps and the period of UV irradiation are indicated in the upper part of the images. The video was processed with FiJi and HandBrake software.

Movie S4: Phase contrast video (8 fps) of a POPC GUV during electrodeformation and UV irradiation; the data from this vesicle is plotted in Fig. 2B. The AC-field amplitude is 5 kV m^{-1} at a frequency of 1 MHz. The initial GUV radius is approximately 14 µm. The time stamps, electric field application and UV illumination are indicated in the upper part of the images. The video was processed with FiJi and HandBrake software.

Movie S5: Phase contrast video (8 fps) of a 10 mol% azo-PC GUV during electrodeformation (5kV m^{-1}, 1 MHz) and UV irradiation; the data from this vesicle is plotted in Fig. 2B. The initial GUV radius is approximately 25 µm. The time stamps, electric field application and UV illumination are indicated in the upper part of the images. The video was processed with FiJi and HandBrake software.

Movie S6: Phase contrast video (8 fps) of a 50 mol% azo-PC GUV during electrodeformation (5kV m^{-1}, 1 MHz) and UV irradiation; the data from this vesicle is plotted in Fig. 2C. The initial GUV radius is approximately 15 µm. The time stamps, electric field application and UV illumination are indicated in the upper part of the images. The video was processed with FiJi and HandBrake software.

Movie S7: Phase contrast video (16 fps) of a 10 mol% azo-PC GUV under AC field (5kV m^{-1} and 1 MHz) and UV and blue-light illumination, illustrating reversible photoswitching over multiple cycles; data from this vesicle is plotted in Fig. 3B. The initial GUV radius is approximately 11 µm. The time stamps, electric field application, UV and blue light illumination are indicated in the upper part of the images. The video was processed with FiJi and HandBrake software.

Movie S8: Phase contrast video (acquired at 100 fps) of POPC vesicles exogenously doped with azo-PC and irradiated with UV and blue light; the larger vesicle is shown in Fig. 7A. The time stamps, UV and blue light illumination are indicated in the upper part of the images. The video was processed with FiJi and HandBrake software.

4 Photoswitchable Endocytosis of Biomolecular Condensates in Giant Vesicles

Agustín Mangiarotti[1*], **Mina Aleksanyan[1,2*],** Macarena Siri[1,3], Tsu-Wang Sun[1], Reinhard Lipowsky[1], Rumiana Dimova[1]

[1] Max Planck Institute of Colloids and Interfaces, Science Park Golm, 14476 Potsdam, Germany;

[2] Institute for Chemistry and Biochemistry, Freie Universität Berlin, 14195 Berlin, Germany;

[3] Max Planck Queensland Centre, Science Park Golm, 14476 Potsdam, Germany

* These authors contributed equally to this work.

Advanced Science, **2024**, e2309864

Contributions

Dr Agustin Mangiarotti and Mina Aleksanyan contributed equally to this work. Dr. habil. PD Rumiana Dimova proposed the project. Dr. Agustin Mangiarotti and Mina Aleksanyan performed all protein condensate and giant vesicle-based experiments and analyzed the data. Dr. Macarena Siri recorded and analyzed Fourier-Transform Infrared (FTIR-ATR) spectroscopy data of protein condensates. Tsu Wang Sun prepared large unilamellar vesicles for UV–Vis spectroscopy and analyzed UV-Vis spectroscopy data. Dr. habil. PD Rumiana Dimova and Prof. Dr. Reinhard Lipowsky developed the theoretical interpretation. Dr. Agustin Mangiarotti and Mina Aleksanyan wrote the manuscript with contributions from all authors.

The original article including the supporting information is included on the following pages and available online at:

https://doi.org/10.1002/advs.202304336

Press release at: https://www.mpikg.mpg.de/6820099/shaping-cells-with-light?c=132305

RESEARCH ARTICLE

ADVANCED SCIENCE Open Access

www.advancedscience.com

Photoswitchable Endocytosis of Biomolecular Condensates in Giant Vesicles

*Agustín Mangiarotti, Mina Aleksanyan, Macarena Siri, Tsu-Wang Sun, Reinhard Lipowsky, and Rumiana Dimova**

Interactions between membranes and biomolecular condensates can give rise to complex phenomena such as wetting transitions, mutual remodeling, and endocytosis. In this study, light-triggered manipulation of condensate engulfment is demonstrated using giant vesicles containing photoswitchable lipids. UV irradiation increases the membrane area, which can be stored in nanotubes. When in contact with a condensate droplet, the UV light triggers rapid condensate endocytosis, which can be reverted by blue light. The affinity of the protein-rich condensates to the membrane and the reversibility of the engulfment processes is quantified from confocal microscopy images. The degree of photo-induced engulfment, whether partial or complete, depends on the vesicle excess area and the relative sizes of vesicles and condensates. Theoretical estimates suggest that utilizing the light-induced excess area to increase the vesicle-condensate adhesion interface is energetically more favorable than the energy gain from folding the membrane into invaginations and tubes. The overall findings demonstrate that membrane-condensate interactions can be easily and quickly modulated via light, providing a versatile system for building platforms to control cellular events and design intelligent drug delivery systems for cell repair.

1. Introduction

Biomolecular condensates are specialized, membraneless cellular compartments formed through the dynamic and reversible assembly of proteins, nucleic acids, and other biomacromolecules within the cytoplasm or nucleus of a cell.[1] They are involved in a wide range of cellular processes including gene transcription and translation,[2] signal transduction,[3] stress response,[4] protein quality control,[5] and cell division.[6] Lately, condensate-membrane interactions have been shown to be crucial for the formation of tight junctions,[7] transport of stress granules,[8] stabilization of membrane damage by stress granules,[9] signal transduction in T-cells,[3] and endocytosis.[10] The associated morphologies are governed by membrane-wetting transitions[11] that can be tuned via changes in the salinity of the milieu or the membrane composition.[11,12] In vitro studies have demonstrated that condensate endocytosis can occur when sufficient membrane area is available.[11,12] Furthermore, coacervates of various compositions can be completely engulfed by lipid vesicles by altering the membrane charge and increasing the strength of droplet-membrane interaction.[12] This compartmentalization provided by condensate-membrane assemblies is crucial for cell function, highlighting the roles of condensates and their potential applications in artificial cells and biomolecular transport across membranes.[13] Recent studies have demonstrated the potential of complex coacervates, composed of oligo-arginine and RNA, to penetrate phospholipid bilayers and enter liposomes,[14] suggesting their utility for therapeutic purposes in biotechnology by serving as effective drug delivery platforms in living cells. The burgeoning field of synthetic cell construction, with a focus on coacervate droplets as both membrane-free compartments and crowded cytosol-like environments, is already demonstrating their potential applications in assembling integrated synthetic cells capable of mimicking various life-inspired functions.[15]

Introducing biocompatible molecular photoswitches into such bio-systems provides additional leverage for fast and reversible manipulation of cellular processes through light.[16] Here, we construct a photoswitchable biomimetic system for condensate endocytosis using giant unilamellar vesicles (GUVs) and glycinin protein condensates.

Giant vesicles are cell-sized, biomembrane compartments with an increasingly broad spectrum of applications.[17] UV exposure of GUVs composed of 1-palmitoyl-2-oleoyl-glycero-3-phosphocholine (POPC) and photoswitchable azobenzene

A. Mangiarotti, M. Aleksanyan, M. Siri, T.-W. Sun, R. Lipowsky, R. Dimova
Max Planck Institute of Colloids and Interfaces
Science Park Golm, 14476 Potsdam, Germany
E-mail: rumiana.dimova@mpikg.mpg.de

M. Aleksanyan
Institute for Chemistry and Biochemistry
Free University of Berlin
Takustraße 3, 14195 Berlin, Germany

M. Siri
Max Planck Queensland Centre
Science Park Golm, 14476 Potsdam, Germany

The ORCID identification number(s) for the author(s) of this article can be found under https://doi.org/10.1002/advs.202309864

DOI: 10.1002/advs.202309864

phospholipid analog (azo-PC) can trigger a reversible increase in membrane area upon *trans*-to-*cis* isomerization.[18] Azo-PC is a commercially available photolipid with a well-characterized synthetic route.[19] The effects of light on the material and electrical properties of azo-PC-containing GUVs have been already extensively characterized.[18–20] The precise membrane area increase resulting from the isomerization of azo-PC has recently been measured from GUV electrodeformation and the results were found consistent with molecular dynamics simulations.[18]

Glycinin is a storage protein from the soybean that constitutes a robust model for protein condensation[21] with well-characterized phase diagrams at different conditions.[21] Membrane wetting of this protein and other condensate systems have been shown to lead to remodeling events[11,22] and changes in membrane lipid packing and hydration.[23]

Recently, Lu et al.[12] provided evidence of the engulfment of complex coacervates into GUVs by modulating the charges of the membrane and the condensates. However, in this approach, endocytosis relies on the available access area of the GUVs, presumably achieved via deflation, which is a slow passive process that can take even up to an hour.[12] In contrast, manipulating the vesicle excess area with light offers control, faster response, and reversibility.[16] Here, we employed azo-PC containing GUVs and glycinin condensates to provide a versatile, biocompatible and fast platform for tuning condensate-membrane interactions via light. To our knowledge, this is the first study demonstrating that light can finely manipulate protein-lipid interactions, leading to the endocytosis of protein condensates in an instantaneous and reversible manner. By carefully characterizing the light-triggered endocytosis of condensates, we aimed to propose promising, bio-inspired, and simple photolipid-doped cell models and liposomal drug carriers, offering potential therapeutic applications for addressing cellular disorders.

2. Results and Discussion

2.1. Reversible Partial and Complete Engulfment of Protein Condensates Under the Influence of Light

When the photoswitchable azo-PC lipids are exposed to UV-light (365 nm), *trans*-to-*cis* photo-isomerization occurs[24] (**Figure 1a**), which effectively increases the area per molecule and the total vesicle area accordingly[18] (Figure 1b). Photoisomerization in membranes containing 50 mol% azo-PC results in a substantial area increase of ~18%.[18] We prepared POPC:azo-PC (1:1 molar ratio) GUVs labeled with 0.1 mol% ATTO-647N-DOPE and observed them with confocal microscopy. Under UV light, the GUVs grow in size and the generated excess membrane area quickly transforms into internal nanotubes (Figure 1b,c). This process can be reversed by blue irradiation (450 nm), Movie S1 (Supporting Information). The formation of nanotubes is caused by the buffer asymmetry across the GUV membrane (sucrose solution inside and isotonic sodium chloride solution outside) resulting in high negative spontaneous curvature stabilizing the tubes.[25] The sodium chloride solution was required for condensate formation (see the Experimental section for details), while the internal sucrose solution osmotically stabilizes the GUV ensuring volume conservation.

To probe whether condensate-membrane interactions can be tuned by light, we placed the vesicles in contact with glycinin condensates formed at 150 mM NaCl and labeled with the water-soluble dye Sulforhodamine B (SRB). Upon adhesion, the condensates deform the GUV membrane (**Figure 2**), as previously shown.[11] Under UV irradiation, the *trans*-to-*cis* photoisomerization of azo-PC results in fast membrane expansion accompanied by increasing adhesion zone. We observed two outcomes depending on the relative sizes of the interacting vesicle and condensate (Figure 2). For larger condensates, with a radius (R_{cond}) comparable to or exceeding the vesicle radius (R_{GUV}), the generated excess membrane is consumed to partially engulf the droplet, see Figure 2a,b, and Movie S2 (Supporting Information). For smaller condensates ($R_{GUV}>>R_{cond}$), the UV-induced excess area of the GUV allows complete engulfment, i.e. endocytosis of the condensate (Figure 2c,d and Movie S3, Supporting Information). Images of the membrane channel and the 3D projection show that the condensate is fully enclosed by the membrane, confirming endocytosis (Figure S1, Supporting Information). Note that to allow reversibility of endocytosis, the membrane adhering to the droplet must be connected to the mother vesicle by a closed (nanometric) membrane neck.[26] This membrane neck can be subsequently cleaved via scaffolding proteins[27,28] or low density of membrane-bound proteins inducing large spontaneous curvature that generates a constriction force.[29]

In addition, a single GUV can engulf multiple condensates, as shown in Figure S2a (Supporting Information). However, this case requires more available membrane area, and the adhesion of multiple condensates might increase the membrane tension,[12,30] reducing the likelihood of the engulfment of many droplets.

As shown in Figure 2, both, the complete and partial engulfment processes can be quickly reversed by blue light exposure, see Figures S2–S4 and Movies S4–S8 (Supporting Information) for more examples including large-field images. We emphasize that the protein structure remains unaltered after UV irradiation as demonstrated by Fourier-transform infrared spectroscopy (Figure S5, Table S1 in Supporting Information, and Experimental section), indicating that the observed changes in membrane-condensate affinity are solely due to the light-induced changes in the membrane. We also conducted control experiments involving the exposure of pure POPC GUVs to UV and blue light irradiation for similar or longer durations and monitored their interactions with glycinin condensates under UV and blue light (Figure S6, Supporting Information). The applied irradiation conditions did not lead to any changes in the membrane response or GUV morphology (Figure S6a–d, Supporting Information), as previously demonstrated.[18] Additionally, they did not induce any alterations in the protein-lipid interactions (Figure S6e–h, Supporting Information).

2.2. Quantifying the Condensate Affinity to the Membrane From the System Geometry

In the case of the partial engulfment of condensates by GUVs, the contact angle between the membrane and the condensate (Figure 2a,b) changes, suggesting altered affinity. Note that

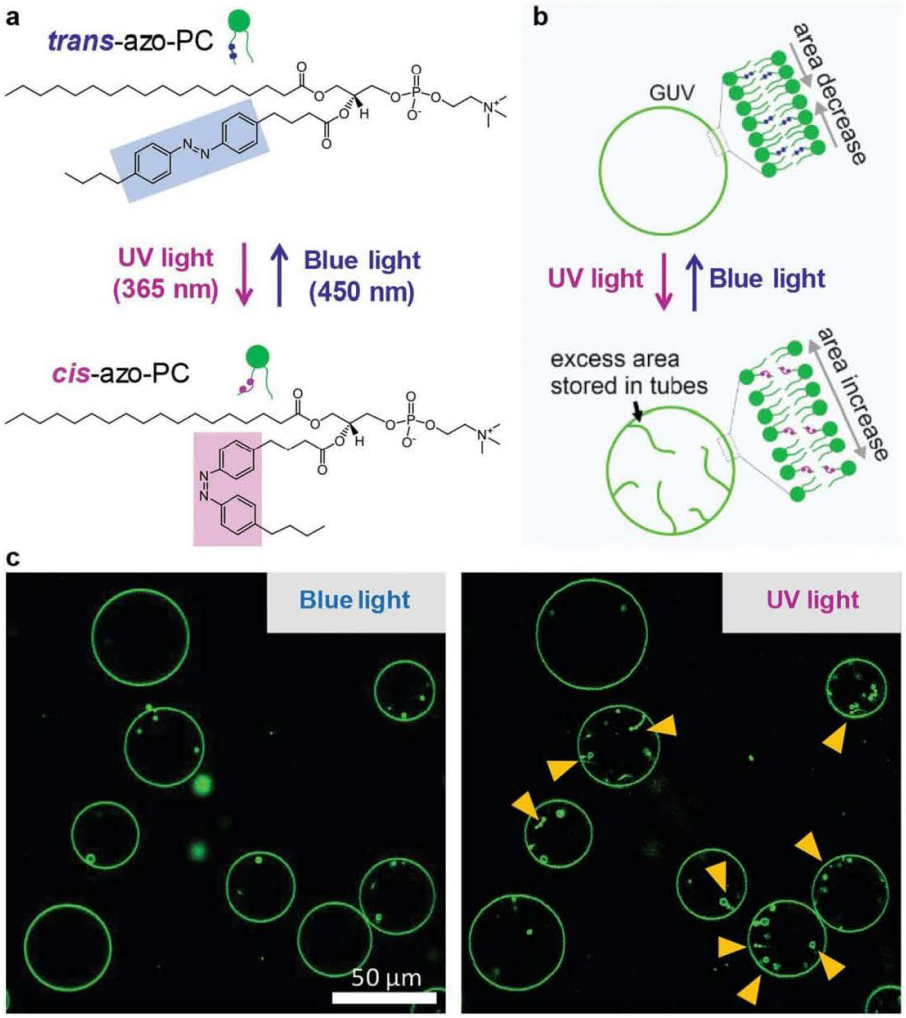

Figure 1. Irradiation of membranes doped with photoswitchable azo-PC causes reversible area increase and morphological changes in GUVs. a) Molecular structures of *cis* and *trans* azo-PC photoswitchable isomers. b) Schematic illustration of the reversible membrane area changes in GUVs under UV and blue light. The excess area generated under UV irradiation can be stored in nanotubes. c) Confocal cross-sections showing membrane area change of POPC:azo-PC (1:1) GUVs labeled with 0.1 mol% Atto-647N-DOPE upon *trans-cis* photoisomerization and extensive nanotube formation in the GUV lumen (arrowheads); the right image shows the vesicle response after 1 s of UV light irradiation, Movie S1 (Supporting Information).

measuring only this apparent contact angle may provide an inaccurate understanding of the interaction. Assessing it solely from confocal cross-sections where either the condensate center or the vesicle centers are not in the plane of the image (out of focus) results in an incorrect system geometry description.[11] To obtain accurate information, it is crucial that the rotational axis of symmetry of the vesicle-droplet system lies in the image plane of the projected image. This often necessitates the acquisition and reorientation of a 3D image of the vesicle and droplet., see e.g.[11]

The changes in the affinity of the condensate to the membrane can be precisely quantified by measuring the geometric factor $\Phi = (\sin\theta_e - \sin\theta_c)/\sin\theta_i$, which is obtained from the apparent (measured by light microscopy) contact angles facing the external phase, θ_e, the vesicle lumen, θ_i, and the condensate interior, θ_c. Note that while the membrane shape appears to have a kink at the three-phase contact line, the detailed structure of this kink corresponds to a highly curved membrane segment that is resolvable only with super-resolution microscopy.[31]

The geometric factor is a dimensionless quantity reflecting the tensions in the system, namely the interfacial tension Σ_{ce} and the two mechanical tensions of the membrane segments in contact with the external phase, Σ^m_{ie}, and with the condensate, Σ^m_{ic} (see details in **Figure 3**a). It can adopt values between -1, corresponding to complete wetting and spreading of the condensate on the membrane surface, and 1 corresponding to no wetting where both vesicles and condensate remain spherical. The intermediate values, $-1 < \Phi < 1$, reflect the case of partial wetting. While the contact angles reflect the specific geometry of a vesicle-condensate couple and can exhibit broad variations in the sample, the geometric factor is a material property of

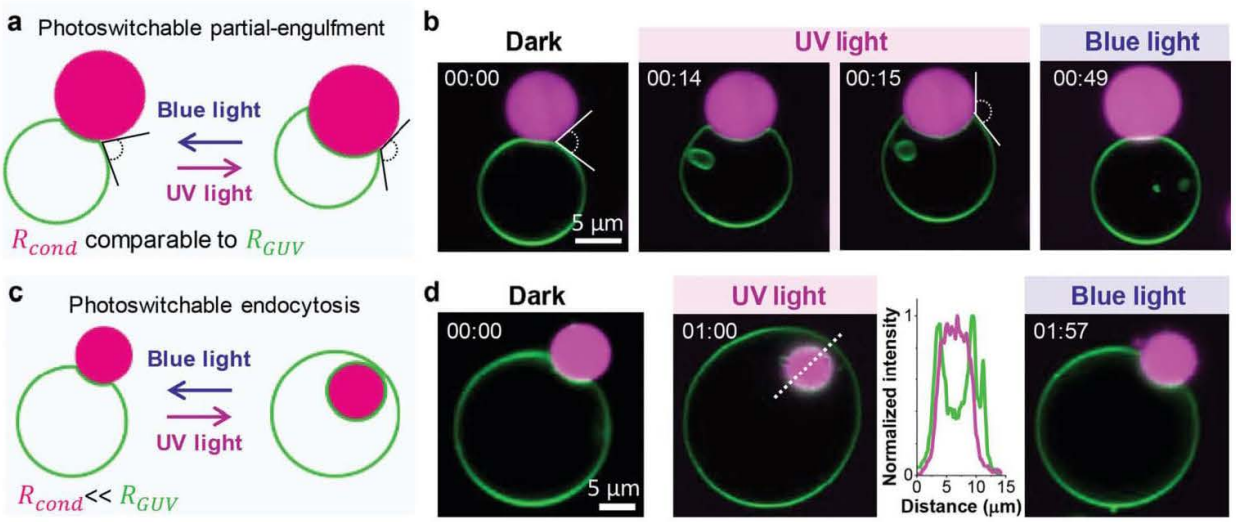

Figure 2. Light-induced engulfment of condensates. a,b) Condensates with sizes comparable to that of the GUV experience reversible partial engulfment (schematic and confocal cross-sections) mediated by UV/blue irradiation. The time stamps (mm:ss) correspond to the time after starting the recording; the UV light was switched on at 14 s and changed to blue light at 49 s (Movie S2 Supporting Information for time-lapse recording of this GUV-condensate couple). The contact angle between the condensate and the membrane changes upon photoisomerization as highlighted. c,d) For smaller condensates, photoisomerization leading to sufficient excess area leads to complete engulfment, which is reversible; the UV light was switched on at 6 s and changed to blue light at 1 min 47 s (Movie S3, Supporting Information). The intensity profile corresponds to the white dashed line shown in the second image in d) showing the position of the condensate (magenta) wrapped by the membrane (green).

the condensate-membrane system.[11] It has been theoretically derived[26,32] (as reviewed[30]) and supported by experimental data on condensate-vesicle systems.[11,22,31] Indeed, because the geometric factor is a material property, it is constant over the whole population of vesicle-condensate pairs. It reflects the wetting affinity and is independent of condensate-vesicle geometry as well as droplet and vesicle sizes and vesicle excess area.[11]

Figure 3b shows that the geometric factor for pure POPC and POPC:azo-PC membranes in the *trans* state are similar, but *trans*-to-*cis* photo-isomerization alters it. The data indicate that the

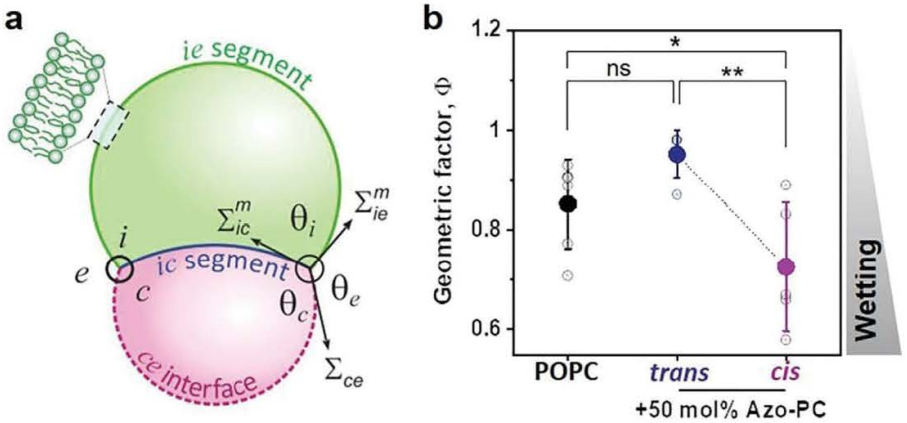

Figure 3. System geometry and contact angles used to determine the geometric factor, which shows increased wetting affinity upon *trans*-to-*cis* isomerization. a) For partial wetting morphologies of condensate-membrane systems, the contact interface between the condensate (magenta) and the membrane (green) partitions the membrane into the *ie* and *ic* segments, with the contact angles $\theta_i + \theta_e + \theta_c = 360°$. The interfacial tension Σ_{ce} and the mechanical tensions Σ^m_{ic} and Σ^m_{ie} within the two membrane segments are balanced, see.[11,30] b) Experimental data for the geometric factor $\Phi = (\sin\theta_e - \sin\theta_c)/\sin\theta_i$ for pure POPC GUVs or POPC:azo-PC 1:1 GUVs in contact with glycinin condensates at 150 mM NaCl. Individual values are shown as open circles and the solid symbols and lines indicate the mean and standard deviation, n = 5 per condition. The geometric factor reaches the maximum value of $\Phi = +1$ for complete dewetting (no interaction between the condensate and the vesicle) and partial wetting for lower values. The drop in Φ for the *trans*-to-*cis* isomerization of the azo-PC lipids indicates that the affinity between the condensates and the membrane is increasing. The vesicle-condensate couples were irradiated with UV light for 15 s before imaging for contact angle measurement. The statistical analysis was performed with One-way ANOVA and Tukey post-test analysis ($p < 0.0001$, **** | $p < 0.001$, *** | $p < 0.01$, ** | $p < 0.05$, * | ns = non-significant).

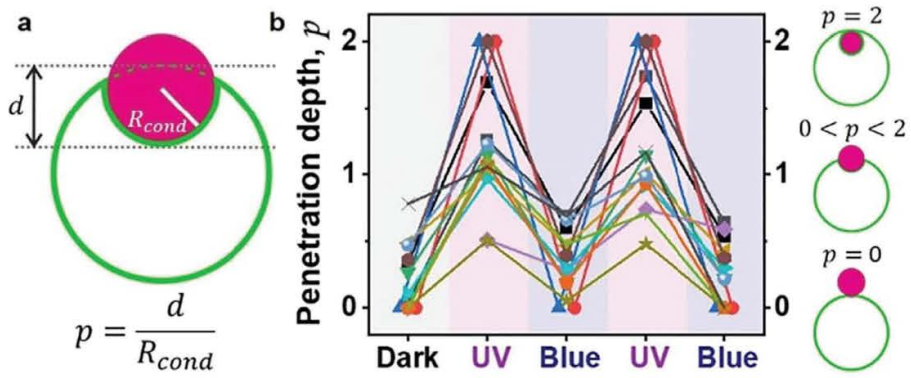

Figure 4. Reversible endocytosis. a) Sketch showing the measured parameters for calculating the rescaled penetration depth, p. b) The penetration depth of condensates into vesicles, p, is fully reversible for multiple photoswitching cycles (up to six cycles were tested, each consisting of approximately 20 s irradiation with UV and 20 s irradiation with blue light). Each symbol represents a single vesicle-condensate pair and the data is measured from a single cross section.

condensate-membrane affinity increases upon *trans*-to-*cis* photoisomerization of azo-PC.

2.3. Light-Triggered Condensate Engulfment and Reversibility Kinetics

Next, we assessed the light-triggered endocytosis and partial engulfment over multiple cycles of UV and blue light irradiation. To quantify the light-induced engulfment and release of the protein condensates from GUVs containing 50 mol % azo-PC, the degree of the penetration of the protein condensates in the vesicles (penetration depth, p) was calculated. For this, we used confocal cross-sections at different levels perpendicular to the optical axis (z-axis) within the sample exposed to UV and blue illumination for two photo-switching cycles. The definition of p is based on the study of Dietrich et al.,[33] which addresses the adhesion dynamics of spherical solid particles to lipid vesicles and reflects the distance d from the estimated outer rim of the vesicle to its interface with the particle (**Figure 4a**). This distance rescaled by the particle radius yields p. Ideally, the distance d and the condensate radius should be measured along the axis of rotation of the system, which may not always align with the focal plane of observations unless the vesicle and condensate have similar radii and their equators are in focus. To precisely measure d in our system, acquiring z-stacks for 3D imaging would be necessary to determine the correct projection along the rotational axis. However, generating a z-stack can take a few minutes, and the sample would need to be irradiated during that time. Therefore, we directly used confocal cross-sections to determine p, which may introduce some scatter in the data as the correct axis of rotation is not determined. Nevertheless, for investigating kinetics at shorter times and the reversibility of engulfment, we use the penetration depth determined from a single confocal cross-section at an intermediate height, roughly reflecting the sizes of the GUV and the condensate.

Figure 4b shows data for the penetration depth where $p \cong 2$ corresponds to endocytosis and $0 < p < 2$ reflects partial engulfment, see the Experimental section. The value of p also depends on the initial excess area and relative condensate-vesicle sizes. The penetration depth and the GUV-to-condensate area under UV irradiation show an inverse correlation characterized by a Pearson coefficient of –0.57, Figure S7 (Supporting Information). The penetration depth alternates with photoswitching cycles of UV and blue light and is fully reversible. Both light-triggered partial and complete engulfment processes are characterized by fast kinetics in the milliseconds (*cis*-to-*trans*) to a few seconds range (*trans*-to-*cis*), see **Figure 5**. This is consistent with the notion that the *trans* state is more stable. However, we emphasize that this dynamic behavior may vary depending on the light intensity (specified in the Experimental section). Furthermore, the time response of changes in vesicle area and condensate engulfment does not necessarily reflect the kinetics of the photoswitch isomerization but rather relates to the timescales involved in membrane reorganization, deformation, hydrodynamic contributions, and potential relative displacement of the GUV and/or condensate. In any case, the light-triggered kinetics observed here are faster than passive engulfment, which can take from seconds to minutes, or even hours depending on the particular condensate-vesicle system.[12]

2.4. Recruiting Excess Membrane Area for Condensate Adhesion is Energetically More Favorable than Membrane Tubulation

As shown in Figure 1, the excess vesicle area generated by the *trans*-to-*cis* photoisomerization of azo-PC can be stored in tubes. When in contact with a condensate, this excess area goes to the membrane-condensate interface enabling partial or complete endocytosis of the condensate (Figures 2 and 5). However, we observed that nanotube formation can also take place during and after the engulfment of condensates. We questioned whether all area generated by *trans*-to-*cis* photoisomerization is transferred to the condensate interface. This required precise determination of the UV-induced area increase, which we assessed from electrodeformation of GUVs[34] in the absence of condensates. The vesicles were exposed to an alternating current (AC) field to pull out membrane fluctuations and induce elliptical deformation.[35]

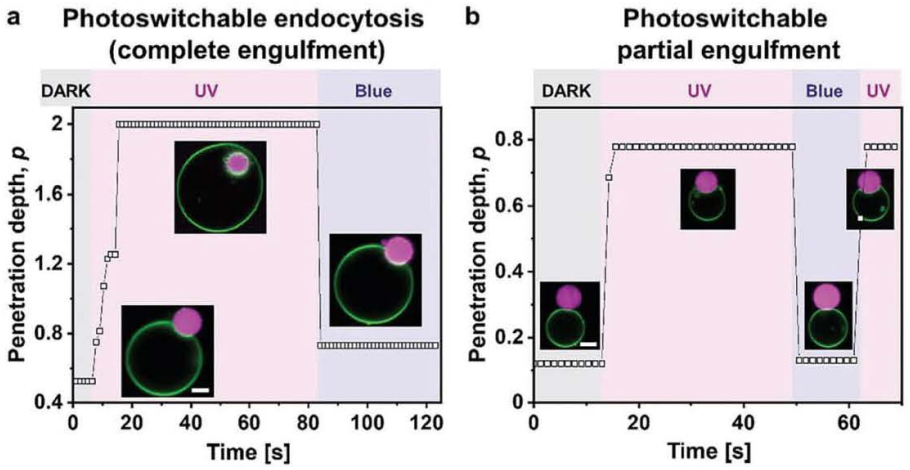

Figure 5. Penetration depth, p vs time showing the kinetics of photoswitchable endocytosis a) and b) partial-engulfment. Scale bars are 5 µm. The response of the GUV-condensate system to *trans*-to-*cis* photoisomerization is completed in 2–9 s, while the response to *cis*-to-*trans* photoisomerization occurs at times faster than the frame rate of the image acquisition (below 650 milliseconds). The values of p in each data point are estimated from a single frame, and the mismatch between the dark and blue penetration depths in panel (a) is due to the vesicle going out of focus during recording.

This allows the precise measure of the total vesicle area from its geometry, see the Experimental section. Subtracting this initial membrane area from the membrane area under the influence of both UV light and AC field yields a UV-induced area increase of 18±2%, (Figures S8–S10, Supporting Information), which is in good agreement with reported data for slightly different solution conditions.[18]

We then compared this expected absolute area increase for individual vesicles wetted by a condensate with the change in apparent area of the vesicles measured directly from the microscopy images as the area sum of the bare vesicle membrane segment and the membrane segment in contact with the condensate (i.e. excluding the area of possible tubular structures), see **Figure 6**. Provided all UV-induced excess area is consumed to expand the membrane-condensate interface, the data should fall on a line described by $y = x$. However, many data points are distributed above this line, indicating that the excess area does not only accumulate at the membrane-condensate interface but is also stored in membrane nanotubes.

High salt and sugar concentrations are known to modify the membrane structure and properties.[25,36] Under high salt/sugar asymmetry across the vesicle membrane, ion adsorption to the outer leaflet produces negative membrane spontaneous curvature, which stabilizes inward tubes.[25] Note that in the absence of this salt asymmetry, UV irradiation only produces large membrane fluctuations in the GUVs but no tube formation, Figure S12 (Supporting Information). Thus, the total area increase due to UV irradiation of the vesicles (as plotted in Figure 6) represents the sum of the outer spherical vesicle membrane and the membrane area stored in tubes.

We also compared this area change to the change in the area of the membrane segment wetted by the condensate before and after UV illumination (Figure S11, Supporting Information). Similar trend was observed. The observations imply that nanotube formation competes with transferring the excess area to the membrane-condensate interface and that the final morphology could depend on the initial geometry of the vesicle-condensate pair (note that the preparation method leads to vesicles with different area-to-volume ratios).

Next, we theoretically estimated the energetic gain of transferring the excess area to the vesicle-condensate interface and compared it to that arising from the formation of nanotubes. To estimate the energy gain arising from tubulation, we consider a cylindrical tube of area ΔA stabilized by membrane spontaneous curvature m. The tube is characterized by a radius $R_{tu} \cong \frac{1}{2m}$. The gain of bending energy, ΔE_{be} associated with the transfer of the

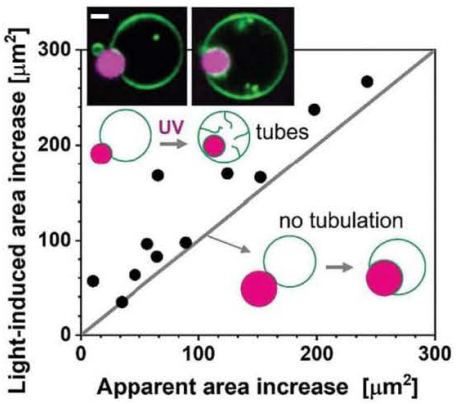

Figure 6. Light-induced area increase as expected from electrodeformation experiments (Figures S9–S11, Supporting Information) versus apparent area increase (area of the spherical segments of the bare and wetted membrane excluding tubes) for POPC:Azo-PC 1:1 GUVs in contact with condensate droplets. The system was irradiated with UV light for 10–20 s. Data fall at the $y = x$ gray line when all the excess area is transferred to the membrane-condensate contact area, as shown in the lower sketches. Data lying above this line correspond to vesicles in which part of the excess area is stored in nanotubes (upper sketch and example images; scale bar 5 µm). Each point corresponds to an individual vesicle-condensate pair.

membrane area ΔA from the weakly curved mother vesicle to the nanotube is given by

$$\Delta E_{be} = -2\kappa m^2 \Delta A < 0 \quad (1)$$

where κ is the membrane bending rigidity. For membranes asymmetrically exposed to sugar and sodium chloride solutions as studied here, $m \approx 9\ \mu m^{-1}$ as measured.[25] The bending rigidity for POPC membranes containing 50 mol% of azo-PC is $\kappa \approx 10\ k_B T$,[18] where $k_B T = 4.1\times10^{-21}$ J is the thermal energy. The excess area ΔA available for tube formation is simply the difference between the light-induced area change A_{li} and the apparent area A_{app} plotted in Figure 6, where we see that $\Delta A = A_{li} - A_{app}$ ranges between 0 and roughly 160 μm^2. Taking 80 μm^2 as a mean value of ΔA, we obtain for the bending energy gain $\Delta E_{be} \approx -1.3\times10^5\ k_B T$.

As long as the *ce* interface of the droplet (see Figure 3a) is not completely covered by the vesicle membrane, the photo-induced excess area ΔA can be alternatively used to increase the contact area between droplet and membrane. The adhesion energy per unit area is given by $\Phi\Sigma_{ce}\Delta A$ with $\Phi = 0.75$ when the membrane is exposed to UV light and the azo-PC lipids attain their *cis*-conformation (Figure 3b). As we cover the area ΔA of the droplet surface, we reduce its interfacial free energy by $\Sigma_{ce}\Delta A$. Therefore, the gain in adhesion energy is equal to

$$\Delta E_{ad} = (\phi - 1)\,\Sigma_{ce}\Delta A = -0.25\Sigma_{ce}\Delta A \quad (2)$$

where the numerical value $\Phi = 0.75$ for *cis*-azo-PC has been used in the second equality. The interfacial tension has the value $\Sigma_{ce} \approx 0.5$ mN m^{-1}[11] which implies $\Delta E_{ad} = -2.4\times10^6\ k_B T$ for $\Delta A = 80\ \mu m^2$. Comparing the gain ΔE_{ad} in adhesion energy with the gain $\Delta E_{be} \approx -1.3\times10^5\ k_B T$ in bending energy as caused by tubulation, we conclude that the gain in adhesion energy exceeds the gain in bending energy by more than one order of magnitude. As a consequence, the vesicle membrane will continue to spread over the droplet until this droplet is completely engulfed. Any additional excess area created by the light-induced isomerization will be stored in membrane nanotubes. Indeed, a subsequent inspection of the vesicle-condensate images demonstrated that data points in Figure 6 located above the line with slope 1 correspond to vesicles where the condensates are completely engulfed and the remaining excess area engages in the formation of nanotubes (see confocal images in the inset).

3. Conclusions

In summary, our work shows that light can be used as a facile, inexpensive, and sustainable tool for efficiently tuning the membrane-condensate interactions in a fast and reversible manner. By using GUVs containing the azo-PC photolipid as minimalistic artificial cells, we effectively generated and characterized light-induced membrane-condensate wetting transitions leading to fast reversible endocytosis (within a few seconds) over multiple photoswitching cycles. By combining theoretical studies with experimental observations, we have elucidated the interaction mechanisms between protein condensates and lipid membranes leading to engulfment and membrane morphology changes. The application of these results could be extended to different condensate systems and membrane compositions, provided that there is partial wetting between the condensate and the vesicles. The photoswitchable system presented here provides a promising platform for the development of synthetic cells and versatile drug delivery systems with applications in photo-pharmacology.

4. Experimental Section

Materials: The phospholipids 1-stearoyl-2-[(E)-4-(4-((4-butylphenyl) diazenyl)phenyl)butanoyl]-sn-glycero-3-phosphocholine (azo-PC) and 1-palmitoyl-2-oleoyl-sn-glycero-3-phosphocholine (POPC) were purchased from Avanti Polar Lipids, Alabaster, AL, USA. The purity of azo-PC as indicated by the producer was >99%. The synthesis and characterization of the molecule were reported in[19,37] and the UV/Vis spectrum of azo-PC was reported in[19,38] and is displayed in Figure S9d (Supporting Information), see also[39] for effect of membrane composition on the spectra. The lipid 1,2-dioleoyl-sn-glycero-3-phosphoethanolamine labeled with Atto 647N (Atto-647N-DOPE) was obtained from ATTO-TEC GmbH, Siegen, Germany. Sucrose, glucose, and sodium chloride (NaCl) were purchased from Merck, Germany. The fluorescent dye Sulforhodamine B (SRB) was obtained from ThermoFisher Scientific, Massachusetts, USA. Bovine serum albumin (BSA) was purchased from Merck, Germany. Stock solutions of the phospholipids and the dye-conjugated lipid were prepared in chloroform solution to a concentration of 4 mM and stored at -20 °C until usage. Indium-tin oxide (ITO)-coated glass plates were purchased from PGO GmbH, Iserlohn, Germany. An Agilent 33220A 20 MHz Function/Arbitrary Waveform Generator from Agilent Technologies, USA was used for GUVs electroformation. The microscopic observations were done either with commercially available Eppendorf electrofusion chambers (Germany) or homemade chambers assembled from 22 × 40 and 22 × 22 mm^2 cover slides purchased from Knittel Glass (Germany). Cover slides were rinsed with ethanol and distilled water and then passivated with a 2 mg mL^{-1} BSA solution. An Osmomat 3000 osmometer (Gonotec GmbH, Berlin, Germany) was used to measure solutions osmolarities.

All commercially available chemicals and solvents were used without further purification. In order to prevent any dust or dirt, all the glassware was rinsed with ethanol and chloroform, and then dried under an inert atmosphere before usage.

Vesicle Preparation: Giant unilamellar vesicles were prepared at room temperature (23° C) by the electroformation method.[17] An equimolar solution of azo-PC and POPC including 0.1 mol% Atto-647N-DOPE was prepared in chloroform to a final concentration of 4 mM. In order to create a thin lipid film, 14 µL of this lipid solution was first spread on a pair of electrically conductive, ITO-coated glass plates and then the majority of the chloroform was evaporated by exposing the plates to a stream of N_2. For the removal of solvent traces, the plates were also subsequently placed under a vacuum for two hours. A chamber was assembled using a rectangular Teflon spacer of 2 mm thickness sandwiched between the ITO-glass plates. The chamber was filled with a solution of 300 mM (300 mOsmol kg^{-1}) sucrose to hydrate the lipid film. Electroswelling was induced by applying an AC field at 10 Hz frequency with a 1.6 V (peak to peak) amplitude for 1 h in the dark. GUVs were then transferred to light-protective glass vials for storage at room temperature and used the same day.

For the GUV electrodeformation studies, GUVs were swelled in a 100 mM sucrose and 0.5 mM NaCl solution and then were 8-fold diluted in a 105 mM glucose solution. The presence of a small amount of salt ensures higher conductivity of the internal solution compared to the external one, resulting in prolate deformation of the GUVs under the AC field.[35] The control experiments of azo-PC GUVs in low sugar concentrations and in the absence of any salts in the external GUV medium were performed by harvesting GUVs in 100 mM sucrose solution and 1:1 dilution into 105 mM glucose solution for the confocal microscopy observations.

Large unilamellar vesicles (LUVs) used for UV–Vis spectroscopy were prepared as follows. The azo-PC solution in chloroform (10 mg mL^{-1}) was dried in a glass vial under a stream of nitrogen and subsequently placed

in a desiccator for 2 h. Water was then added to the vial to achieve a final lipid concentration of 1.5 mM. Multilamellar vesicles were produced through three freeze-thaw cycles, involving immersion in liquid nitrogen and incubation in a 60 °C metal block, followed by vortexing. The multilamellar vesicles were extruded through a 100 nm polycarbonate membrane (Whatman Nuclepore Track-Etched Membranes, Merck, Germany) using an Avanti MiniExtruder (Avanti Polar Lipids, USA) for a total of 21 times to obtain LUVs.

Protein Purification and Condensate Formation: Glycinin was purified as described by Chen et al.[21] Briefly, defatted soy flour was dispersed 15-fold in water by weight and adjusted to pH 7.5 with 2 M NaOH. After centrifugation at 9000×g for 30 min at 4 °C, dry sodium bisulfite was added to the supernatant (0.98 g L^{-1}). The pH of the solution was adjusted to 6.4 with 2 M HCl, and the obtained turbid dispersion was kept at 4 °C overnight. Next, the dispersion was centrifuged at 6500 × g for 30 min at 4 °C. The glycinin-rich precipitate was dispersed 5-fold in water, and the pH was adjusted to 7. The glycinin solution was then dialyzed against Millipore water for two days at 4 °C and then freeze-dried to acquire the final product with a purity of 97.5%.[21]

To form the condensates, a 20 mg mL^{-1} glycinin solution at pH 7 was freshly prepared in ultrapure water and filtered with 0.45 µm filters to remove any insoluble materials. Then, the desired volume of the glycinin solution was mixed with the same volume of a 300 mM NaCl solution to achieve a solution with final concentrations of 10 mg mL^{-1} glycinin and 150 mM NaCl. The condensates were labeled by including 10 µM SRB dye prior to condensate formation.

Condensate-Vesicle Suspensions: First, the vesicle suspension was diluted 1:10 in a 150 mM NaCl solution. Then, the condensate suspension was diluted 1:4 and added to the vesicle suspension at 15% v/v (corresponding to a final protein concentration of 0.4 mg mL^{-1}). After gently mixing the vesicle-condensate suspension, an aliquot of 10 µL was placed on a coverslip for confocal microscopy, and a chamber was formed using a round spacer and closed with a coverslip.

Confocal Microscopy Imaging and Irradiation Conditions: UV-induced morphological changes of azo-PC GUVs as well as the engulfment of protein condensates into GUVs were monitored through a Leica TCS SP8 scanning confocal microscope (Wetzlar, Germany) using either a 40× (0.60 NA) air or 63× (1.2 NA) water immersion objectives. The pinhole size during the experiment was set to 1 AU (Airy unit) and the scanning speed was 400 Hz in bidirectional mode. Time-lapse imaging was performed at a frame rate of 650 ms per frame. SRB was excited with a 561 nm laser and the emission signal was collected with HyD (hybrid) detector in the 573–626 nm range. Atto-647N-DOPE was excited with a HeNe 633nm laser and the emission signal was collected with a HyD detector in the range 645–785 nm. In order to induce *trans*-to-*cis* photoisomerization of azo-PC in the GUVs, an external UV LED (365 nm wavelength; "UV light") with a maximum power intensity of 20 mW cm^{-2} (Roschwege, Germany) was attached to the condenser of the confocal microscope. The reversed azo-PC photoisomerization (*cis*-to-*trans*) was generated by simultaneously using 458 and 476 nm lasers at 50% intensity ("blue light"), respectively corresponding to 0.40 and 0.67 mW cm^{-2} measured in line-scanning mode and at the position of the sample using a LaserCheck power meter (Coherent, USA). Under the conditions of UV/blue light intensities used in our experiments the isomerization, as assessed from vesicle deformation response, is fully reversible over multiple cycles and within the experimental sensitivity range, as shown earlier[18] and confirmed here (Figure S9d,e, Supporting Information). Considering that experimentally measured membrane area changes were found very consistent with simulations,[18] it is tempting to speculate that the azo-PC molecules in the membrane undergo complete *trans-cis* conversion. Even though assessing the precise degree of conversion was not crucial for the experiments reported here, confirming this speculation for full photoconversion with additional experimental techniques would be advantageous.

Phase Contrast Microscopy Imaging and Irradiation Conditions: Electrodeformation of azo-PC GUVs was monitored under phase contrast mode of an inverted Axio Observer D1 microscope (Zeiss, Germany), equipped with a Ph2 40x (NA 0.6) objective. Images were acquired with an ORCA R2 CCD camera (Hamamatsu, Japan). The GUVs were placed either in an Eppendorf electrofusion chamber or a homemade chamber with approximate thicknesses of 8 or 1 mm, respectively; Figure S8 (Supporting Information). To induce UV irradiation, the light from the HBO 100W mercury lamp was used in epi-illumination mode and was collected through a 365 nm DAPI filter. For blue irradiation, the light from the mercury lamp was applied through a 470/40 nm filter. The irradiation power of the HBO lamp was measured with the LaserCheck power meter at the position of the sample and recorded as 60 mW cm^{-2} for the UV filter and 26 mW cm^{-2} for the blue filter.

Penetration Depth Analysis and Irradiation: The penetration depth of the protein condensate into GUV, *p*, reflects the degree of insertion of the droplet inside the vesicle and is calculated as:

$$p = \frac{d}{R_{\text{cond}}} \tag{3}$$

where R_{cond} and d are defined in Figure 4a. For each interacting condensate-GUV pair, d was measured from confocal screenshots using the Fiji software at 3 illumination conditions. In the initial illumination condition, "dark", the 561 and 633 nm lasers were used to only excite the fluorescent dyes labeling the condensate and the membrane. In addition to these two lasers, an external UV LED at 365 nm was used to promote the *trans*-to-*cis* isomerization of azo-PC, and this condition was referred to as "UV-light". Switching off the UV LED was followed by the immediate exposure of the sample to 458 and 476 nm lasers, which was referred to as "blue-light". Then, the measured d and R_{cond} values were used in Equation 3 to calculate the p values at the three conditions (dark, UV, blue) for 2 photo-switching cycles. Origin Pro was used for plotting the penetration depth values from 15 protein condensates interacting with 8 GUVs (Figure 4b).

Fourier-Transform Infrared (FTIR-ATR) Spectroscopy: Spectra were recorded on an infrared microscope AIM-90000 (SHIMADZU, Germany) equipped with an ATR objective. First, a 3 µL aliquot of each sample was spread on glass slides and dried until a film formed with N_2. A second aliquot was spread on glass slides and irradiated for 10–20 s with the above-mentioned UV LED, before drying it with N_2 until a film was formed. The ATR objective was placed pressuring the sample to acquire the protein spectra. Measurements consisted of an average of 64 scans recorded at 25 °C with a nominal resolution of 4 cm^{-1}. The spectra were processed using Kinetic software developed by Dr. Erik Goormaghtigh of the Structure and Function of Membrane Biology Laboratory (Université Libre de Bruxelles, Belgium).[40] The spectra were analyzed in the amide I' region of the protein (1700 and 1600cm^{-1}). The spectra were deconvoluted using the Lorentzian deconvolution factor with a full width at the half maximum (FWHM) of 30 cm^{-1} and a Gaussian apodization factor with a FWHM of 16.66 cm^{-1} to obtain a line narrowing factor $K = 1.8$. Band assignment was performed using the deconvoluted and second derivative spectra of each sample in the amide *I'* region. These were the initial parameters for an iterative least square curve fit of the original IR band ($K = 1$) using mixed Gaussian–Lorentzian bands. The bounds for the peak positions of each identified individual component were within ±2 cm^{-1} of the initial value. The FWHM input values are described in detail in Table S1 (Supporting Information). FTIR-ATR spectra and analysis of the secondary structure content of glycinin condensates before and after the UV illumination are demonstrated in Figure S5 (Supporting Information).

Vesicle Electrodeformation: Electrodeformation experiments to determine the membrane area changes associated with azo-PC isomerization were performed using both, a Leica TCS SP8 scanning confocal microscope (Wetzlar, Germany) equipped with an HC PL FLUOTAR L 40x (0.60 NA) objective, and an inverted microscope in phase contrast mode Axio Observer D1 (Zeiss, Germany) equipped with a PH2 40x (0.6 NA) objective and an ORCA R2 CCD camera (Hamamatsu, Japan). GUVs were observed in a commercial Eppendorf electrofusion chamber (Eppendorf, Germany) or a home-made chamber (Figure S8, Supporting Information) to compare the effect of chamber thickness on the penetration of UV-light through the sample and observation of light-induced changes on the vesicles in the sample. The Eppendorf chamber (Figure S8a, Supporting Information) contains two parallel cylindrical platinum electrodes 92 µm in

radius, located 500 µm apart from each other. There the GUVs were exposed to an AC field (1 MHz, 5 V peak-to-peak amplitude), as previously described.[35,41] The homemade chamber was assembled on a 22 × 40 mm^2 glass cover slide with a pair of parallel copper strips (3M, Cergy-Pontoise, France) located 1 mm apart from each other (Figure S8b, Supporting Information). Small Parafilm pieces were attached to the glass slide 10 mm apart from each other to seal the ends and form a closed compartment. An aliquot of 50 µL GUV solution 1:1 diluted in 105 mM glucose buffer was added in the spacing between the copper tapes and a 22 × 22 mm^2 cover slide was placed on top of the solution.

Contrary to the Eppendorf chamber, the thickness of the homemade chamber was comparable to the one used for the rest of the microscopy experiments. However, the homemade chamber could not be used together with the external UV LED on the confocal microscope due to safety reasons associated with the strong reflection of the UV light from the copper tapes to the user. By repeating the electrodeformation experiments with both chambers under a phase contrast microscope, which did not require the attachment of an external UV LED, we could rule out the effect of chamber thickness on the penetration of UV light into the sample (Figure S10c, Supporting Information).

The copper tape electrodes were connected to Agilent 33220A 20 MHz Function/Arbitrary Waveform Generator (Agilent Technologies, USA) as shown in Figure S8 (Supporting Information). The voltage and frequency of the electric field were set to 10 V (peak to peak) and 1 MHz, respectively.

Before the electric field application, a typical, tensionless GUV adopts a quasi-spherical morphology and displays visual membrane fluctuations through microscopy observations. In the vesicle electrodeformation method, a mild AC field was used to pull out the excess vesicle area stored in membrane fluctuations and tubes by deforming the vesicles into ellipsoidal shapes[42] thus providing an accurate and direct assessment of the total membrane area. The area of an ellipsoidal vesicle is:

$$A = 2\pi b\left(b + a\frac{\sin^{-1}\varepsilon}{\varepsilon}\right) \quad (4)$$

Here, a and b are the vesicle semi-axes along and perpendicular to the applied electric field, while ϵ denotes ellipticity: $\epsilon^2 = 1 - (b/a)^2$.

After recording the area increase of GUVs under AC field, they were next illuminated with UV light, while the AC field was also still switched on, and further area increase of the vesicles was recorded for 40–50 s at an acquisition speed of 8 frames per second (fps), Figure S9 (Supporting Information). Subtracting the initial vesicle area in the absence of UV light (but with electric field on), A_i, from the vesicle area under UV light, A_{UV}, yields the percentage of relative area increase as $\frac{A_{UV}-A_i}{A_{UV}} \times 100\%$ related to the *trans*-to-*cis* photoisomerization of azo-PC.

The length of the vesicle semi-axes was measured from the recorded vesicle images using Fiji software. Between 10 and 15 GUVs were analyzed from three separate sets of experiments for each condition to generate statistics. The corresponding plots in Figures S9 and S10 (Supporting Information) are prepared with Origin Pro. The statistical significance of the vesicle area changes from different microscopy techniques and chamber conditions was tested with the one-way analysis of variance (ANOVA) and t-test (p-values for null hypothesis were found as 0.76 and 0.082, respectively).

Since the majority of observations in this manuscript rely on confocal microscopy imaging performed in a thinner home-made chamber, electrodeformation calculations were also performed through confocal images focused on the equatorial trajectories of the vesicles sampled on the home-made chamber with the same thickness dimensions as in the rest of the experiments. Because confocal images display information from a single focal plane, any potential experimental error or deviation was checked carefully and the accuracy of the confocal experiments to obtain the precise maximum projection of the vesicles for area increase calculations was compared to the results from phase contrast microscopy (Figure S10c, Supporting Information). Similarly, effects from differences in the chamber thickness potentially affecting the UV irradiation through the GUV sample were also examined (Figure S10c, Supporting Information).

Analysis of Changes in the Apparent Light-Induced and Adhesion Areas: In order to check the relation between the UV-induced area increase of GUVs and the increase in the membrane area adhered to the protein condensates, the interaction of GUVs and protein condensates were monitored first in the absence and then in the presence of UV light under confocal microscopy. Subtracting the initial vesicle area in the absence of UV irradiation from the vesicle area under UV illumination allowed to deduce the apparent area increase of azo-PC GUVs interacting with the protein condensates. The observed area increase was associated with the *trans*-to-*cis* photoisomerization of the azo-PC molecules. The area increase of the spherical segments was defined as an 'apparent area increase' and further compared to the expected area increase as assessed by the electrodeformation method.

Statistics of the plots in Figure 6 in the main text and Figure S11 (Supporting Information) were generated with 11 data points for ten pairs of GUV-condensate systems in which each vesicle interacted with only one condensate. To calculate the areas of the bare membrane segment and the one in contact with the condensate, spherical cap geometry was assumed. All plots were generated through Origin Pro software.

In order to probe the correlation of the size differences between the interacting GUV and condensate to the distribution of the adhered area changes in the above-mentioned plots, the ratio of the condensate-to-GUV area $\frac{R_{cond}^2}{R_{GUV}^2}$ was measured and the resulting values were displayed above each data point in Figure S11 (Supporting Information). No correlation was detected between this ratio and the distribution of data points in Figure S11 (Supporting Information).

UV–Vis Spectroscopy: Absorbance spectra were recorded in a Specord 210 Plus UV–Vis spectrophotometer (Analytik Jena, Germany) using a 1 cm path quartz cuvette (Hellma Analytics, Germany). The slit was set to 1 nm and the scanning speed to 20 nm s^{-1}. The blank solution (water) was subtracted from all curves. The LUV samples, diluted to a concentration of 30 µM, were irradiated using either fiber-coupled LED blue light at 450 nm (Doric, Canada) with a maximum intensity of 55 mW cm^{-2} or the same external UV LED used for the microscopy measurements. Irradiation for 1 min was applied to generate LUVs in either *trans* or *cis* states.

Statistical Analysis: Individual points shown in the graphics correspond to individual vesicle-condensate pairs unless stated otherwise. Where indicated, results were analyzed using One-way ANOVA, t-test, Tukey post-test, and Pearson correlation coefficient analysis ($p < 0.0001$, **** | $p < 0.001$, *** | $p < 0.01$, ** | $p < 0.05$, * | n.s. = non-significant). Statistical analysis and data processing were performed with the Origin Pro software (Originlab corporation). All microscopy images shown were representative of at least three independent experiments. Details for the statistical analysis were further described in the corresponding plots in the main text and Supporting Information.

Supporting Information

Supporting Information is available from the Wiley Online Library or from the author.

Acknowledgements

A.M. acknowledges support from the Alexander von Humboldt Foundation. M.A. acknowledges funding from the International Max Planck Research School on Multiscale Bio-systems. The authors would like to acknowledge Dr. Nannan Chen for providing the purified protein, and Fucsia Crea, Nicky Tam, and Joachim Heberle for fruitful discussions. This work was supported by Germany's Excellence Strategy, EXC 2008/1 (UniSysCat), Grant 390540038.

Conflict of Interest

The authors declare no conflict of interest.

Author Contributions

A.M. and M.A. contributed equally to this work. R.D. designed the project. A.M., M.A., M.S., and T-W.S. performed the experiments and analyzed the data. R. L. and R.D. developed the theoretical interpretation. All authors wrote and edited the manuscript.

Data Availability Statement

The data that support the findings of this study are available from the corresponding author upon reasonable request.

Keywords

endocytosis, giant vesicles, membrane morphology, photoswitchable lipids, protein-rich condensates, wetting

Received: December 15, 2023
Revised: March 14, 2024
Published online: April 6, 2024

[1] a) S. F. Banani, H. O. Lee, A. A. Hyman, M. K. Rosen, *Nat. Rev. Mol. Cell Biol.* **2017**, *18*, 285; b) C. P. Brangwynne, C. R. Eckmann, D. S. Courson, A. Rybarska, C. Hoege, J. Gharakhani, F. Jülicher, A. A. Hyman, *Science* **2009**, *324*, 1729.
[2] a) F., M. Boisvert, S. van Koningsbruggen, J. Navascués, A. I. Lamond, *Nat. Rev. Mol. Cell Biol.* **2007**, *8*, 574; b) T. Hirose, K. Ninomiya, S. Nakagawa, T. Yamazaki, *Nat. Rev. Mol. Cell Biol.* **2023**, *24*, 288.
[3] X. Su, J. A. Ditlev, E. Hui, W. Xing, S. Banjade, J. Okrut, D. S. King, J. Taunton, M. K. Rosen, R. D. Vale, *Science* **2016**, *352*, 595.
[4] D. S. W. Protter, R. Parker, *Trends Cell Biol.* **2016**, *26*, 668.
[5] L. Lei, Z. Wu, K. F. Winklhofer, *Matrix Biol.* **2021**, *100–101*, 9.
[6] B. Ramm, D. Schumacher, A. Harms, T. Heermann, P. Klos, F. Müller, P. Schwille, L. Søgaard-Andersen, *Nat. Commun.* **2023**, *14*, 3825.
[7] O. Beutel, R. Maraspini, K. Pombo-García, C. Martin-Lemaitre, A. Honigmann, *Cell* **2019**, *179*, 923.
[8] Y., C. Liao, M. S. Fernandopulle, G. Wang, H. Choi, L. Hao, C. M. Drerup, R. Patel, S. Qamar, J. Nixon-Abell, Y. Shen, W. Meadows, M. Vendruscolo, T. P. J. Knowles, M. Nelson, M. A. Czekalska, G. Musteikyte, M. A. Gachechiladze, C. A. Stephens, H. A. Pasolli, L. R. Forrest, P. St George-Hyslop, J. Lippincott-Schwartz, M. E. Ward, *Cell* **2019**, *179*, 147.
[9] C. Bussi, A. Mangiarotti, C. Vanhille-Campos, B. Aylan, E. Pellegrino, N. Athanasiadi, A. Fearns, A. Rodgers, T. M. Franzmann, A. Šarić, R. Dimova, M. G. Gutierrez, *Nature* **2023**, *623*, 1062.
[10] a) L., P. Bergeron-Sandoval, S. Kumar, K. Heris Hossein, L. A. Chang Catherine, E. Cornell Caitlin, L. Keller Sarah, P. François, G. Hendricks Adam, J. Ehrlicher Allen, V. Pappu Rohit, W. Michnick Stephen, *Proc. Natl. Acad. Sci. USA* **2021**, *118*, e2113789118; b) K. J. Day, G. Kago, L. Wang, J. B. Richter, C. C. Hayden, E. M. Lafer, J. C. Stachowiak, *Nat. Cell Biol.* **2021**, *23*, 366.
[11] a) Y. Li, R. Lipowsky, R. Dimova, *J. Am. Chem. Soc.* **2008**, *130*, 12252; b) A. Mangiarotti, N. Chen, Z. Zhao, R. Lipowsky, R. Dimova, *Nature Commun* **2023**, *14*, 2809.
[12] T. Lu, S. Liese, L. Schoenmakers, C. A. Weber, H. Suzuki, W. T. S. Huck, E. Spruijt, *J. Am. Chem. Soc.* **2022**, *144*, 13451.
[13] T. Lu, S. Javed, C. Bonfio, E. Spruijt, *Small Methods* **2023**, *7*, 2300294.
[14] T. Lu, X. Hu, M. H. I. van Haren, E. Spruijt, W. T. S. Huck, *Small* **2023**, *19*, 2303138.
[15] Z. Lin, T. Beneyton, J., C. Baret, N. Martin, *Small Methods* **2023**, *7*, 2300496.
[16] a) A. Goulet-Hanssens, F. Eisenreich, S. Hecht, *Adv. Mater.* **2020**, *32*, 1905966; b) J. Simon, M. Schwalm, J. Morstein, D. Trauner, A. Jasanoff, *Nat. Biomed. Eng.* **2023**, *7*, 313; c) J. Morstein, M. Kol, A. J. E. Novak, S. Feng, S. Khayyo, K. Hinnah, N. Li-Purcell, G. Pan, B. M. Williams, H. Riezman, G. E. Atilla-Gokcumen, J. C. M. Holthuis, D. Trauner, *ACS Chem. Biol.* **2021**, *16*, 452.
[17] a) R. Dimova, C. Marques, *The Giant Vesicle Book*, Taylor & Francis Group, Boca Raton **2019**; b) R. Dimova, *Annu. Rev. Biophys.* **2019**, *48*, 93; c) T. Toyota, Y. Zhang, *Micromachines* **2022**, *13*, 644; d) Y. Li, S. Liu, W. Xu, K. Wang, F. He, J. Liu, *Sensors & Diagnostics* **2023**, *2*, 806; e) R. Dimova, S. Aranda, N. Bezlyepkina, V. Nikolov, K. A. Riske, R. Lipowsky, *J. Phys.: Condens. Matter* **2006**, *18*, S1151.
[18] M. Aleksanyan, A. Grafmüller, F. Crea, V. N. Georgiev, N. Yandrapalli, S. Block, J. Heberle, R. Dimova, *Adv. Sci.* **2023**, *10*, 2304336.
[19] a) J. A. Frank, D. A. Yushchenko, D. J. Hodson, N. Lipstein, J. Nagpal, G. A. Rutter, J. S. Rhee, A. Gottschalk, N. Brose, C. Schultz, D. Trauner, *Nat. Chem. Biol.* **2016**, *12*, 755; b) C. Pernpeintner, J. A. Frank, P. Urban, C. R. Roeske, S. D. Pritzl, D. Trauner, T. Lohmüller, *Langmuir* **2017**, *33*, 4083.
[20] a) P. Urban, S. D. Pritzl, D. B. Konrad, J. A. Frank, C. Pernpeintner, C. R. Roeske, D. Trauner, T. Lohmüller, *Langmuir* **2018**, *34*, 13368; b) M. Doroudgar, J. Morstein, J. Becker-Baldus, D. Trauner, C. Glaubitz, *J. Am. Chem. Soc.* **2021**, *143*, 9515; c) J. Morstein, A. C. Impastato, D. Trauner, *ChemBioChem* **2021**, *22*, 73.
[21] a) N. Chen, Z. Zhao, Y. Wang, R. Dimova, *ACS Macro Lett.* **2020**, *9*, 1844; b) N. Chen, M. Zhao, T. Nicolai, C. Chassenieux, *Biomacromolecules* **2017**, *18*, 2064.
[22] A. Mangiarotti, R. Dimova, *Annu. Rev. Biophys.* **2024**, *53*, 319.
[23] A. Mangiarotti, M. Siri, N. W. Tam, Z. Zhao, L. Malacrida, R. Dimova, *Nat. Commun.* **2023**, *14*, 6081.
[24] a) H. M. D. Bandara, S. C. Burdette, *Chem. Soc. Rev.* **2012**, *41*, 1809; b) M. Gao, D. Kwaria, Y. Norikane, Y. Yue, *Natural Sciences* **2023**, *3*, e220020.
[25] M. Karimi, J. Steinkühler, D. Roy, R. Dasgupta, R. Lipowsky, R. Dimova, *Nano Lett.* **2018**, *18*, 7816.
[26] R. Lipowsky, *J. Phys. Chem. B* **2018**, *122*, 3572.
[27] a) A. Roux, K. Uyhazi, A. Frost, P. De Camilli, *Nature* **2006**, *441*, 528; b) M. Simunovic, J., B. Manneville, H., F. Renard, E. Evergren, K. Raghunathan, D. Bhatia, A. K. Kenworthy, G. A. Voth, J. Prost, H. T. McMahon, L. Johannes, P. Bassereau, A. Callan-Jones, *Cell* **2017**, *170*, 172.
[28] Y. Avalos-Padilla, V. N. Georgiev, E. Ewins, T. Robinson, E. Orozco, R. Lipowsky, R. Dimova, *IScience* **2023**, *26*, 105765.
[29] a) R. Ghosh, V. Satarifard, R. Lipowsky, *Nat. Commun.* **2023**, *14*, 615; b) J. Steinkühler, R. L. Knorr, Z. Zhao, T. Bhatia, S. M. Bartelt, S. Wegner, R. Dimova, R. Lipowsky, *Nature Commun* **2020**, *11*, 905.
[30] R. Lipowsky, *Membranes* **2023**, *13*, 223.
[31] Z. Zhao, D. Roy, J. Steinkühler, T. Robinson, R. Lipowsky, R. Dimova, *Adv. Mater.* **2022**, *34*, 2106633.
[32] a) H. Kusumaatmaja, Y. Li, R. Dimova, R. Lipowsky, *Phys. Rev. Lett.* **2009**, *103*, 238103; b) R. Lipowsky, in *The Giant Vesicle Book* (Eds.: R. Dimova, C. Marques), Taylor & Francis Group, Boca Raton **2019**, pp. 73–168; c) *Faraday Discuss.* **2013**, *161*, 305.
[33] C. Dietrich, M. I. Angelova, B. Pouligny, *J. Phys. II* **1997**, *7*, 1651.
[34] a) K. A. Riske, T. P. Sudbrack, N. L. Archilha, A. F. Uchoa, A. P. Schroder, C. M. Marques, M. S. Baptista, R. Itri, *Biophys. J.* **2009**, *97*, 1362; b) M. Aleksanyan, H. A. Faizi, M., A. Kirmpaki, P. M. Vlahovska, K. A. Riske, R. Dimova, *Adv. Phys.: X* **2023**, *8*, 2125342; c) V. N. Georgiev, A. Grafmüller, D. Bléger, S. Hecht, S. Kunstmann, S. Barbirz, R. Lipowsky, R. Dimova, *Adv. Sci.* **2018**, *5*, 1800432.
[35] S. Aranda, K. A. Riske, R. Lipowsky, R. Dimova, *Biophys. J.* **2008**, *95*, L19.
[36] a) H. D. Andersen, C. Wang, L. Arleth, G. H. Peters, P. Westh, *Proc. Natl. Acad. Sci. USA* **2011**, *108*, 1874; b) A. Catte, M. Girych,

M. Javanainen, C. Loison, J. Melcr, M. S. Miettinen, L. Monticelli, J. Määttä, V. S. Oganesyan, O. H. S. Ollila, J. Tynkkynen, S. Vilov, *Phys. Chem. Chem. Phys.* **2016**, *18*, 32560.

[37] J. A. Frank, Dissertation, LMU Munich, **2017**.

[38] F. Crea, A. Vorkas, A. Redlich, R. Cruz, C. Shi, D. Trauner, A. Lange, R. Schlesinger, J. Heberle, *Front. Mol. Biosci.* **2022**, *9*, 905306.

[39] A. Manafirad, C. A. Menendez, G. R. Perez-Lemus, S. Thayumanavan, J. J. de Pablo, A. D. Dinsmore, *Langmuir* **2023**, *39*, 15932.

[40] a) E. Goormaghtigh, V. Cabiaux, J., M. Ruysschaert, *Eur. J. Biochem.* **1990**, *193*, 409; b) G. Long, Y. Ji, H. Pan, Z. Sun, Y. Li, G. Qin, *Int. J. Food Prop.* **2015**, *18*, 763.

[41] K. A. Riske, T. P. Sudbrack, N. L. Archilha, A. F. Uchoa, A. P. Schroder, C. M. Marques, M. S. Baptista, R. Itri, *Biophys. J.* **2009**, *97*, 1362.

[42] R. Dimova, K. A. Riske, S. Aranda, N. Bezlyepkina, R. L. Knorr, R. Lipowsky, *Soft Matter* **2007**, *3*, 817.

Open Access

Supporting Information

for *Adv. Sci.*, DOI 10.1002/advs.202309864

Photoswitchable Endocytosis of Biomolecular Condensates in Giant Vesicles

*Agustín Mangiarotti, Mina Aleksanyan, Macarena Siri, Tsu-Wang Sun, Reinhard Lipowsky and Rumiana Dimova**

Supporting Information

Photoswitchable Endocytosis of Biomolecular Condensates in Giant Vesicles

Agustín Mangiarotti[1‡], Mina Aleksanyan[1,2‡], Macarena Siri[1,3], Tsu-Wang Sun[1], Reinhard Lipowsky[1] and Rumiana Dimova[1*]

[1] *Max Planck Institute of Colloids and Interfaces, Science Park Golm, 14476 Potsdam, Germany*

[2] *Institute for Chemistry and Biochemistry, Free University of Berlin, Takustraße 3, 14195 Berlin, Germany*

[3] *Max Planck Queensland Centre, Science Park Golm, 14476 Potsdam, Germany*

[‡]Authors contributed equally.

[*]Address for correspondence: Rumiana.Dimova@mpikg.mpg.de

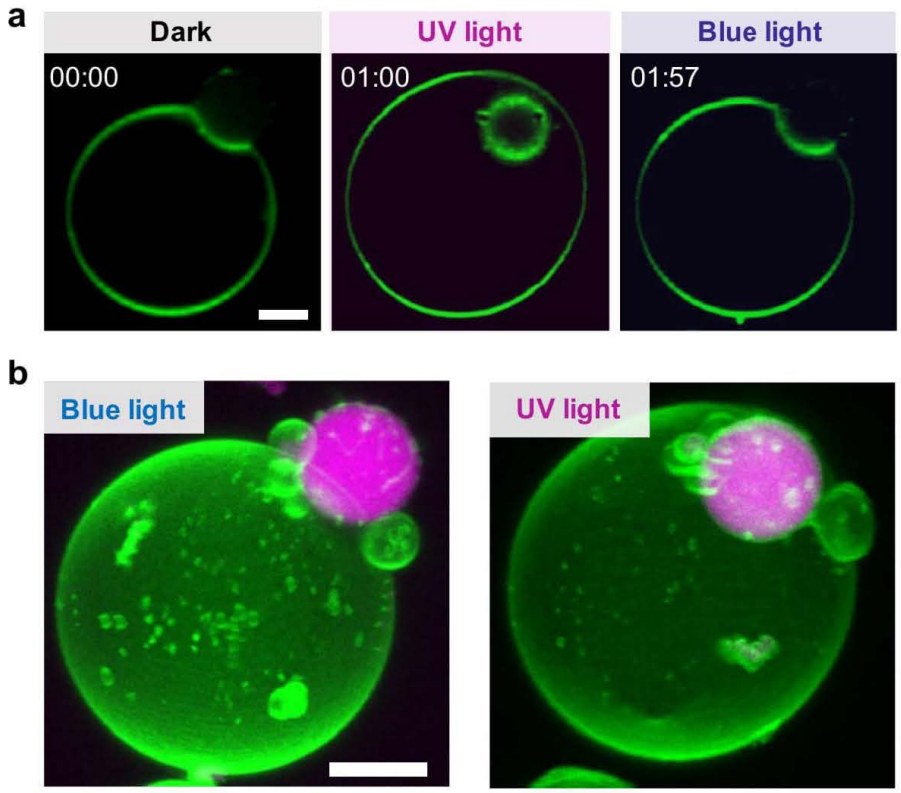

Figure S1. (a) Membrane channel and (b) 3D confocal projection for the vesicle shown in Figure 2b under blue and UV light as indicated. Note that the centers of the condensate droplet and the vesicle are not always in focus. Thus, contrary to 3D projections, confocal cross-sections do not always show properly the area increase and degree of engulfment upon isomerization. The time stamps (mm:ss) correspond to the time after starting the recording. Scale bars are 5 μm.

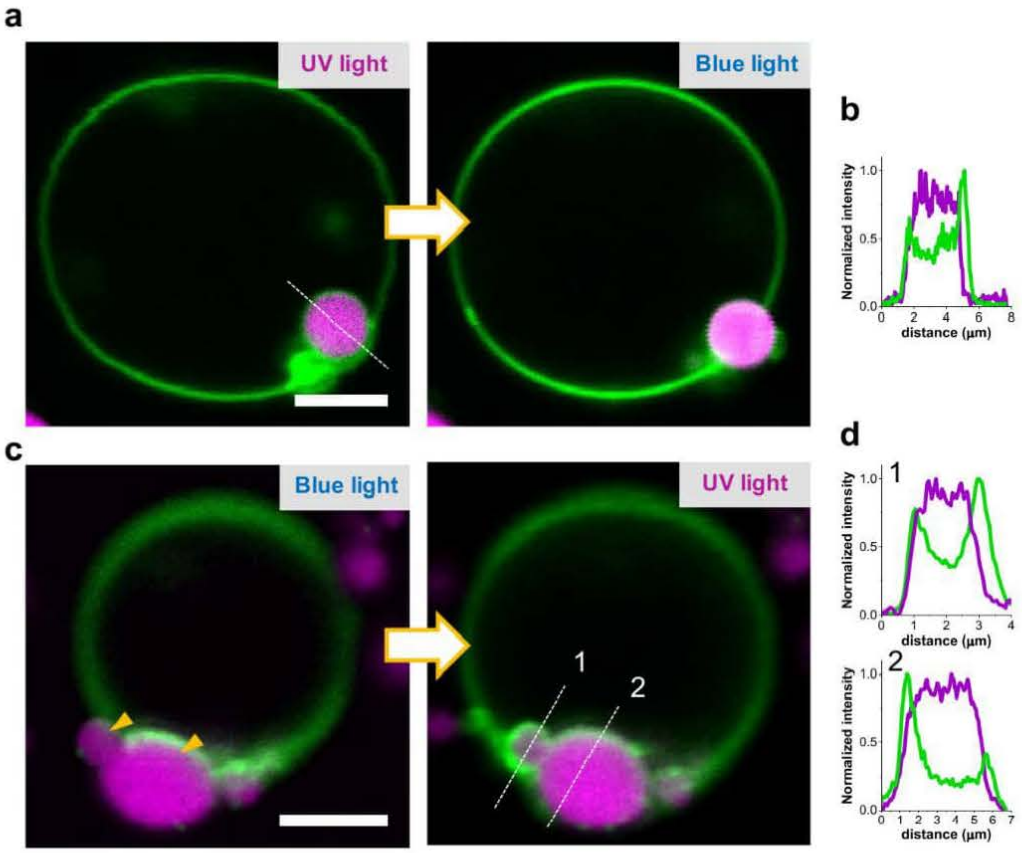

Figure S2. Confocal microscopy images showing examples of photoswitchable endocytosis. GUVs composed of equimolar POPC and azo-PC and labelled with 0.1 mol% Atto-647N-DOPE. Glycinin condensates are labelled with 10 μM SRB. (a) The completely engulfed condensate is released after blue light exposure; see Movie S5 for duration of irradiation. (b) Intensity profiles (green – membrane, magenta – condensate) for the dashed line shown in (a) demonstrate that the droplet is fully wrapped by the membrane evidenced by the two peaks in the green profile. (c) The condensates indicated by the yellow arrows become engulfed after 1 s UV light exposure; see Movie S6 for duration of irradiation. (d) Intensity profiles for the dashed lines shown in (c). Scale bars are 5 μm. Further examples for complete engulfment are found in Fig S4.

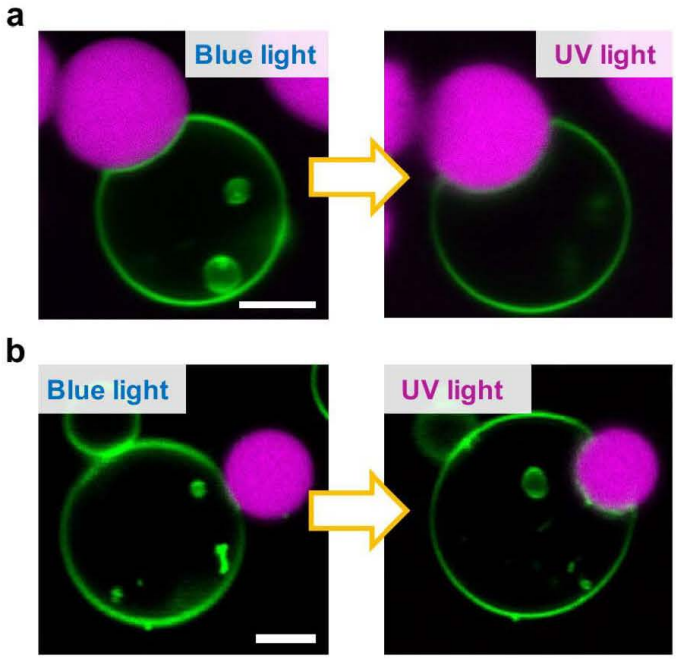

Figure S3. (a-b) Confocal microscopy images showing examples of photoswitchable partial-engulfment, see Movies S7 and S8 for duration of irradiation. GUVs composed of equimolar POPC and azo-PC and labelled with 0.1 mol% Atto-647N-DOPE. Glycinin condensates are labelled with 10 µM SRB. Scale bars are 5 µm.

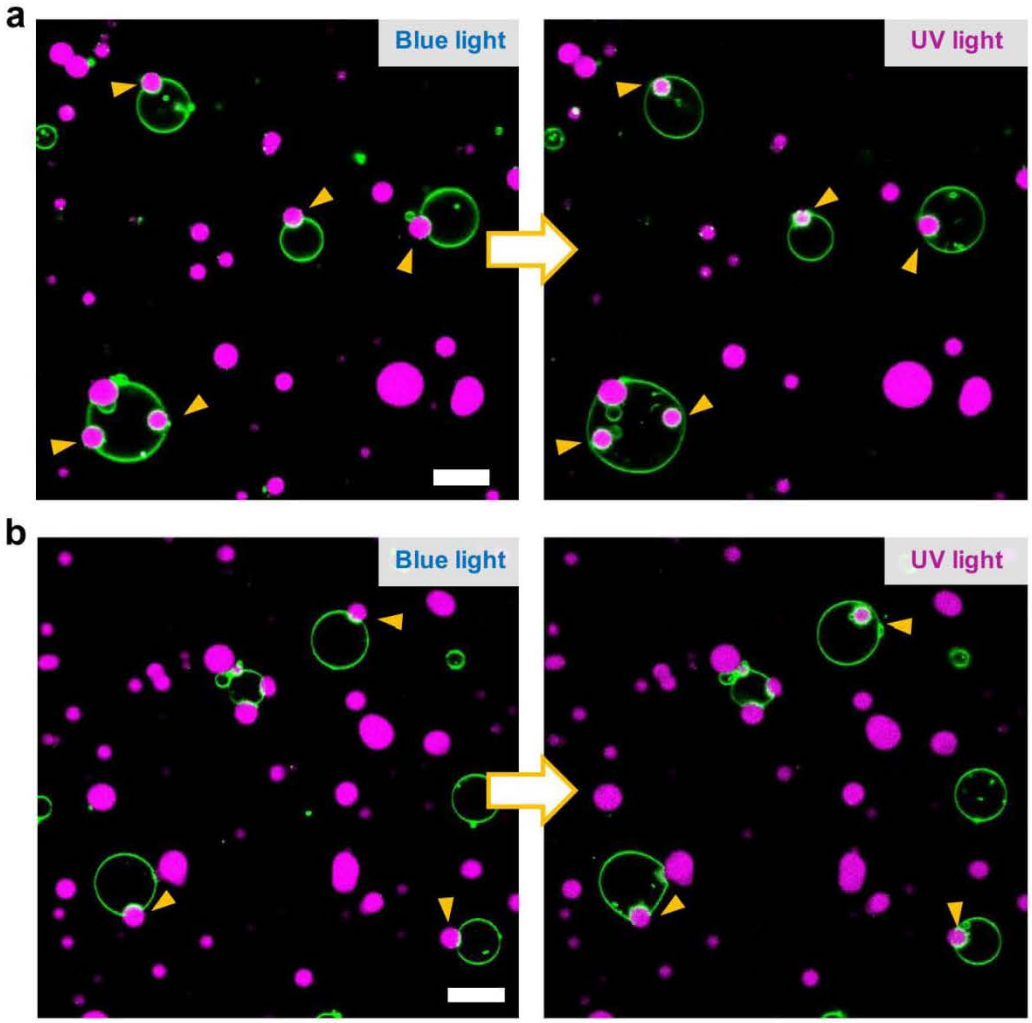

Figure S4. Confocal fluorescence full field images taken under UV/blue light exposure as indicated (see Movie S4 for duration of irradiation). The GUVs are composed of equimolar POPC and azo-PC and labelled with 0.1 mol% Atto-647N-DOPE. The glycinin condensates are labelled with 10 μM SRB. The yellow arrowheads point to the reversibly engulfed condensates, whether partially or fully. Scale bars are 20 μm.

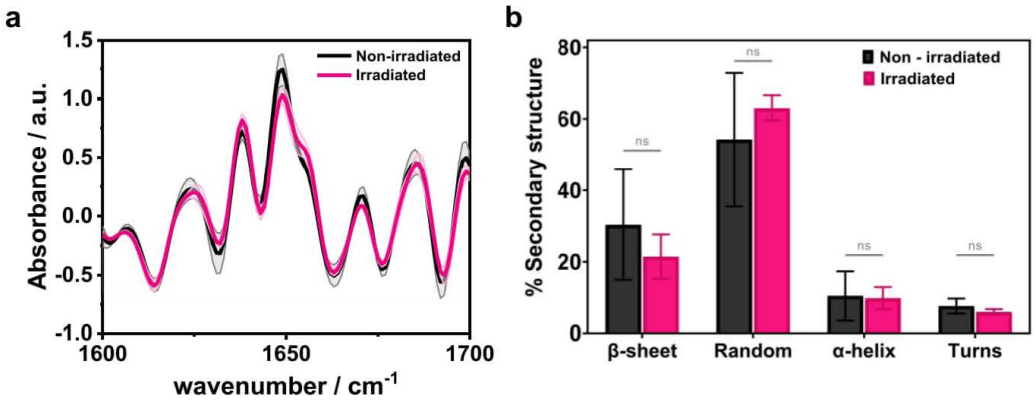

Figure S5. FTIR-ATR analysis of the secondary structure content of glycinin condensates before and after irradiation with UV-light. **a.** Second derivative of glycinin condensates at 150 mM NaCl before and after irradiation with UV-light for 60 seconds (note that much shorter irradiation times were used in the vesicle-condensate studies). **b.** Percent of secondary structure change before and after irradiation with UV-light. There are no significant differences between the irradiated and non-irradiated samples.

Table S1. Full width at half maximum (FWHM) input values in cm^{-1} and their physically plausible ranges expected for each type of secondary structure as measured with ATR-FTIR.[1]

Secondary structure component		FWHM input (cm^{-1})	Lower limit (cm^{-1})	Upper limit (cm^{-1})
β-sheet	*High wavenumber component (1670 – 1680)*	9	8	11
	Low wavenumber component (1610 – 1640)	22	11	33
Random (1640 – 1650)		55	50	60
α-helix (1650 – 1660)		20	5	30
Turns (1660 – 1670; 1680 – 1700)		20	5	30

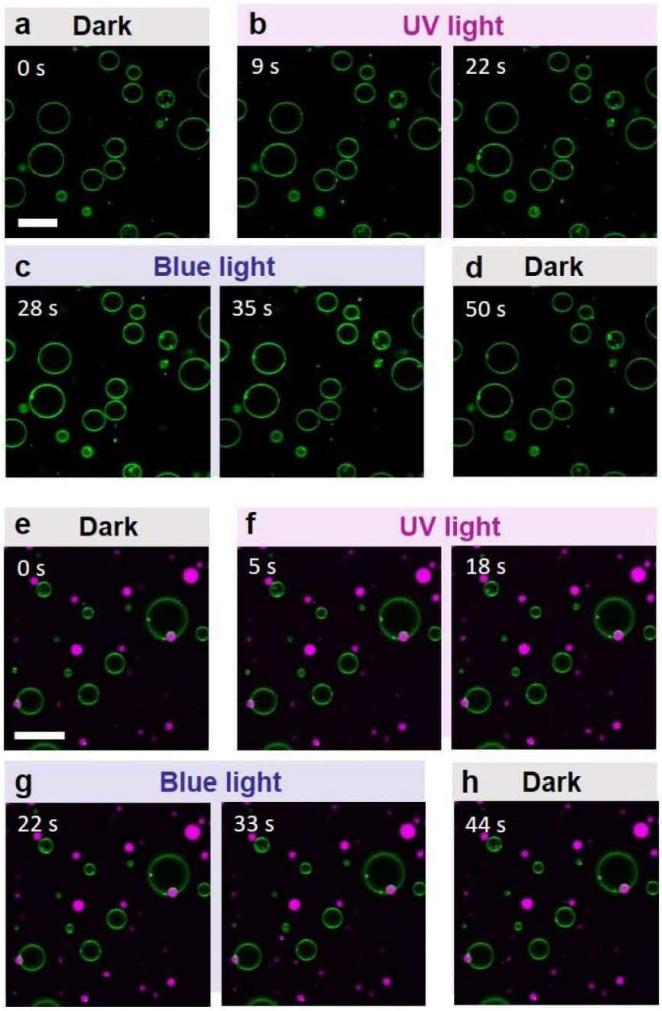

Figure S6. Control experiments with pure POPC GUVs (labelled with 0.1 mol% Atto-647N-DOPE, green) in different irradiation conditions in the absence (a-d) and presence (e-h) of glycinin condensate (labelled with 10 μM SRB, magenta) demonstrating that UV and blue light irradiation do not induce any alterations in the GUV morphology and the protein-lipid interactions. The GUVs were exposed to UV and blue irradiation in (b, f) and (c, g), respectively. Initial illumination conditions of GUVs in the absence of extra UV or blue irradiation are stated as 'dark' in (a, e, d. h). The time stamps show the time in seconds after initiating acquisition. The UV light was turned on at 8 s in (a-d) and 5 s in (e-h), switched to blue at 27 s in (a-d) and 21 s in (e-h). The scale bars in (a) and (e) correspond to 40 μm. Exposing pure POPC GUVs to UV and blue illumination do not induce any changes in the morphology and the membrane area increase of the vesicles.

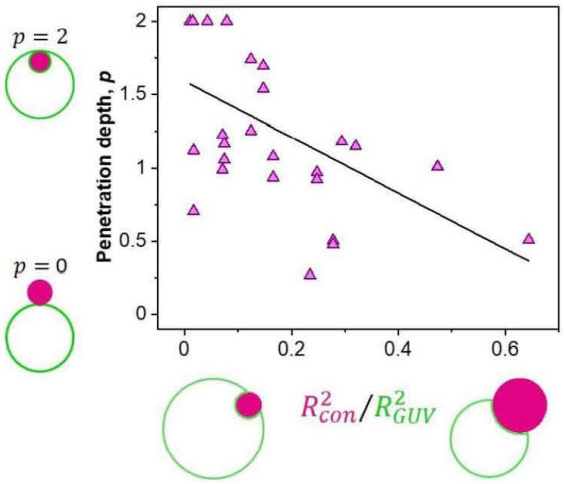

Figure S7. The excess area created upon UV irradiation in larger vesicles leads to higher penetration depth values and smaller condensates penetrate deeper. Alternatively, the larger the condensate is, the more membrane area is required to engulf it and as a result the penetration depth is smaller. To illustrate this, we plot the penetration depth, *p,* versus the area ratio of the condensate to GUV. The cartoons illustrate various scenarios. The graph displays all penetration depth data under UV light shown in Figure 4 in the main text as a function of the area ratio, $\frac{R^2_{cond}}{R^2_{GUV}}$. The scatter in the data are due to fact that the measurements were done using single confocal cross sections rather than 3D scans that would provide projections for the correct determination of the penetration depth and vesicle and condensate radii as explained in the manuscript. The two sets of data (n = 30) are linearly correlated with Pearson correlation coefficient of –0.57 (the solid line is a guide to the eye). Two-tailed test of significance was used and the correlation is significant at the 0.05 level as assessed with Origin Pro software. These results demonstrate that the penetration depth values of protein condensates in GUVs under UV irradiation have a statistically significant correlation to $\frac{R^2_{cond}}{R^2_{GUV}}$, i.e. the increase in excess area resulting from UV irradiation in larger vesicles results in greater penetration depth values, allowing smaller condensates to penetrate more deeply.

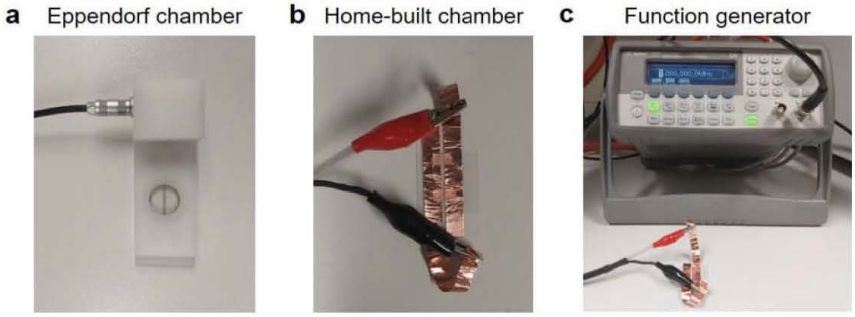

Figure S8: Pictures of electrodeformation chambers before being mounted on a microscope: (a) Eppendorf electrofusion chamber and (b) home-built chamber for electrodeformation assembled from two coverslips sandwiching copper-tape electrodes and parafilm strips. (c) Function generator to apply AC field to induce electrodeformation of GUVs. The two different chambers were used to compare the effects of sample thickness because of concerns regarding the penetration of the UV light.

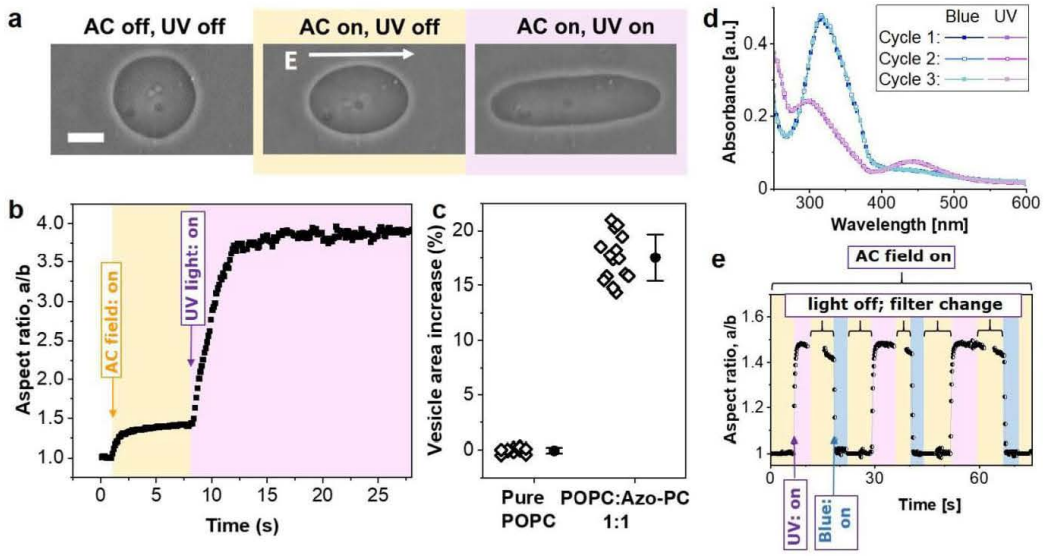

Figure S9: (a) Phase contrast images of a GUV composed of POPC:azo-PC (1:1) in AC field and UV irradiation, as indicated. The arrow indicates the direction of the field. The vesicle was first exposed to an AC field (5 kV m^{-1} and 1 MHz) to pull out thermal fluctuations and deform them into a prolate ellipsoid with semi-axes a and b. Then, while keeping the AC field on, UV irradiation (365 nm) was initiated. Scale bar is 10 µm. (b) Electrodeformation analysis of the GUV in (a). (c) Quantification of the UV-induced area increase of POPC and POPC:azo-PC (1:1) GUVs via vesicle electrodeformation. 10-15 GUVs per condition were analyzed from 3 separate sets of experiments. Each open diamond represents the result of single GUV analysis while the solid circles and line bars are mean values and standard errors. Azo-PC containing GUVs showed ~18±2% of area increase under UV illumination. (d) UV/Vis spectra of large unilamellar vesicles made of azo-PC either in *cis* or *trans* state. Multiple irradiation cycles result in overlapping spectra suggesting full reversibility. For clarity, every 5 data point of the spectra in the 2nd and 3rd cycle are displayed. (e) Area increase as a result of azo-PC photoswitching is fully reversible as shown for the degree of deformation under UV and blue light (as indicated in the correspondingly shaded regions for the first cycle) for a vesicle containing 10 mol% azo-PC; data reproduced from [2]. The GUV is continuously exposed to AC-field (5 kV.m-1 and 1 MHz).

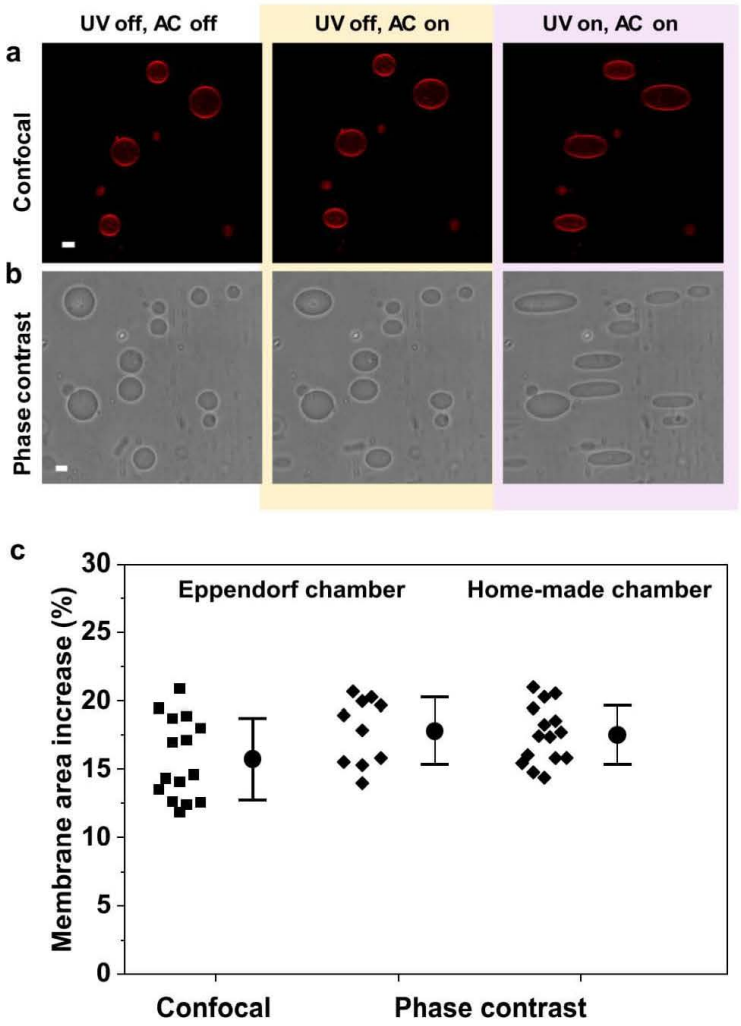

Figure S10. (a) Confocal and (b) phase contrast images of 50 mol% azo-PC containing GUVs during electrodeformation analysis. Initial state of GUVs before the exposure to AC field and UV light is demonstrated on the left panels. The middle panels show the morphology of GUVs in AC field only. In the right panel, GUVs are exposed to UV illumination as well as AC field. In order to monitor vesicles in confocal microscopy, GUVs are labelled with 0.1 mol% Atto-647N-DOPE. The scale bars are 10 μm. Quantification of light-induced membrane area under confocal and phase contrast microscopy based on vesicle electrodeformation. (c) The deformation of the vesicles in AC-field and UV light are measured through the changes in the vesicle aspect ratio. Membrane area of the GUVs are calculated through the area of the ellipsoid. By subtracting the initial membrane area in AC field from the membrane area under the influence of both UV light and AC field, we could obtain the UV induced area increase in the membrane. In addition to different microscopes, the effects of usage of Eppendorf and home-made chambers are also compared. Based on the ANOVA and T-tests (p-values are 0.76 and 0.082, respectively), the differences between different methods are not significant. Each filled square and diamond symbol represents the analysis of a single GUV while filled circles and line bars are the mean values and standard deviation. The average area increase of vesicles under UV illumination shows no dependence on the microscope mode or the used experimental chamber.

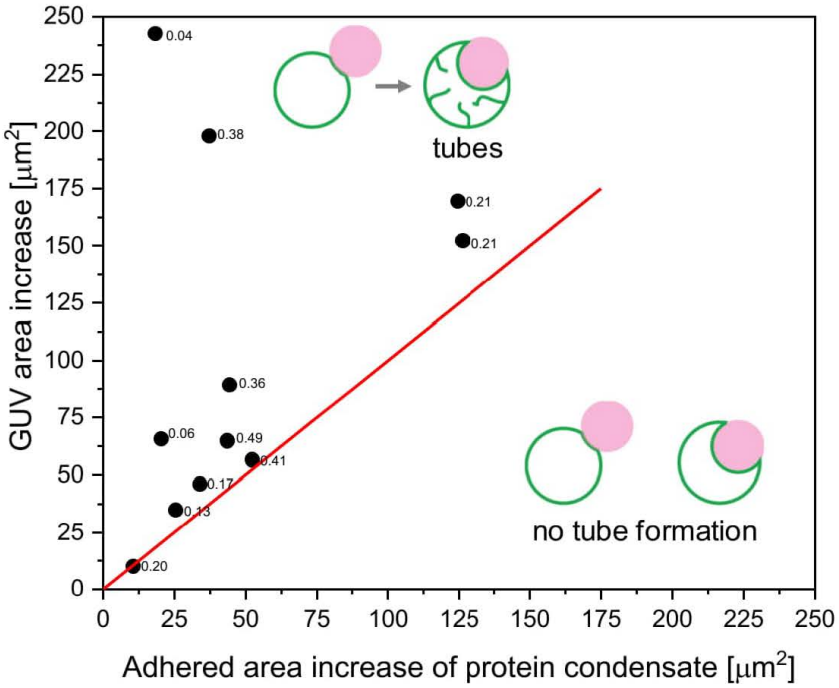

Figure S11. UV-induced GUV area increase versus adhered area increase of the glycinin condensates. GUVs composed of 1:1 POPC:Azo-PC and labelled with 0.1 mol% Atto-647N-DOPE. The adhered area changes detected through confocal screenshots in the absence and presence of UV irradiation were measured through Fiji software. The calculations were based on the spherical cap geometries. Each filled square is an individual data point generated from the pair of interacting GUV-condensate system in which a single vesicle interacted with a single condensate. The quadratic proportionality of the radius of the interacting condensate to the radius of the GUV, $\frac{R_{cond}^2}{R_{GUV}^2}$, were indicated on top of the each datapoint. Red line corresponds to the y=x line representing the data points when all the excess area accumulates on the membrane-condensate interface. The data points are distributed above the y=x line and their distribution does not show any dependence on $\frac{R_{cond}^2}{R_{GUV}^2}$, thus revealing that the adhesion changes are not correlated to size differences of the interacting GUV-protein condensate pairs and that not all UV-induced excess area accumulates at the GUV-condensate interface.

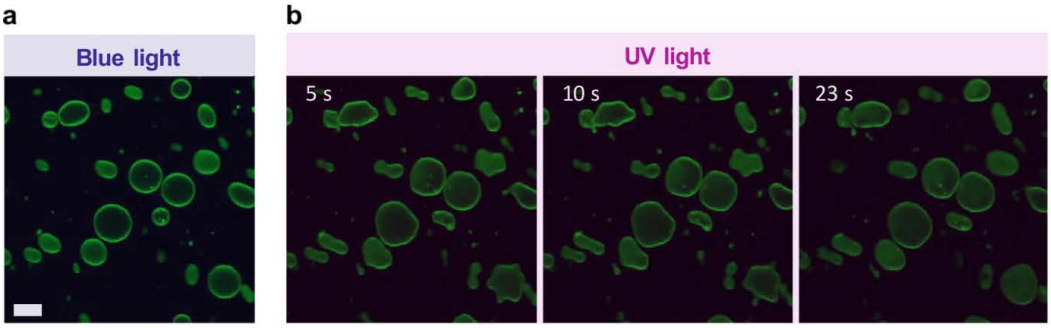

Figure S12. Blue (a) and UV (b) light induced shape transformations of 50 mol% azo-PC containing GUVs in low concentrations of sugar solution and in the absence of any salt asymmetry between internal and external GUV media. GUVs labeled with 0.1 mol% Atto-647N-DOPE were grown in 100 mM sucrose solution and 1:1 diluted to 105 mM glucose solution in absence of any salts. Upon UV irradiation (365 nm), the GUVs underwent complex shape transformations over time which were distinct from the internal tubulation events observed in the presence of high salt asymmetry like in Figure 1c in the main text. The time stamps of changing UV-induced morphological transitions of GUVs are shown in the upper part of the images. The scale bar is same for all these confocal images and corresponds to 10 µm.

Movie Captions

Movie S1: GUVs composed of POPC:Azo-PC 1:1 and labelled with 0.1 mol% Atto-647N-DOPE were sequentially exposed to UV and blue light. The time stamps show the time in seconds after initiating acquisition and switching on the UV and blue light is indicated on the corresponding images. The scale bar is 50 µm.

Movie S2: Photo-switchable partial engulfment of a condensate under UV and blue light as indicated on the upper part of the video. The GUV is composed of POPC:Azo-PC 1:1 and labelled with 0.1 mol% Atto-647N-DOPE and the glycinin condensate was labelled with 10 µM SRB. The time stamps show the time in seconds after initiating acquisition and switching on the UV and blue light is indicated on the corresponding images. The scale bar is 5 µm.

Movie S3: Photo-switchable endocytosis of a condensate. The GUV composed of POPC:Azo-PC 1:1 and labelled with 0.1 mol% Atto-647N-DOPE in contact with the glycinin condensate (labelled with 10 10 µM SRB) was sequentially exposed to UV and blue light as indicated on the upper part of the video. The time stamps show the time in seconds after initiating acquisition. The scale bar is 5 µm.

Movie S4: Large field confocal image showing several examples of complete and partial condensate engulfment. The GUVs composed of POPC:Azo-PC 1:1 and labelled with 0.1 mol% Atto-647N-DOPE in contact with the glycinin condensate (labelled with 10 10 µM SRB) were sequentially exposed to UV and blue light as indicated in the corresponding frame of the video. The time stamps show the time in seconds after initiating acquisition. The scale bar is 20 µm.

Movie S5: Release of a completely engulfed condensate in blue light. The GUV composed of POPC:Azo-PC 1:1 and labelled with 0.1 mol% Atto-647N-DOPE were sequentially exposed to UV and blue light. Glycinin condensate was labelled with 10 µM SRB. The time stamps show the time in seconds after initiating acquisition. The periods of irradiation of the sample are indicated on the upper part of the video. The scale bar is 5 µm.

Movie S6: Engulfment of multiple condensates in UV light. The GUV composed of POPC:Azo-PC 1:1 and labelled with 0.1 mol% Atto-647N-DOPE was exposed to UV light. Glycinin condensates were labelled with 10 µM SRB. The time stamps show the time in seconds after initiating acquisition. The periods of irradiation of the sample are indicated on the upper part of the video. The scale bar is 5 µm. The video was processed with LAS X and Fiji software.

Movie S7: Condensate partial engulfment when exposed to UV light, displaying a large change in the contact angle between the condensate and the membrane. The GUV composed of POPC:Azo-PC 1:1 and labelled with 0.1 mol% Atto-647N-DOPE was exposed to UV light. Glycinin condensate was labelled with 10 µM SRB. The time stamps show the time in seconds after initiating acquisition. The periods of irradiation of the sample are indicated on the upper part of the video. The scale bar is 5 µm.

Movie S8: Condensate partial engulfment in UV light. The GUV composed of POPC:Azo-PC 1:1 and labelled with 0.1 mol% Atto-647N-DOPE was exposed to UV light. Glycinin condensate was labelled with 10 µM SRB. The time stamps show the time in seconds after initiating acquisition. The periods of irradiation of the sample are indicated on the upper part of the video. The scale bar is 5 µm.

References

[1] a) E. Goormaghtigh, V. Cabiaux, J.-M. Ruysschaert, *European Journal of Biochemistry* **1990**, *193* (2), 409; b) G. Long, Y. Ji, H. Pan, Z. Sun, Y. Li, G. Qin, *International Journal of Food Properties* **2015**, *18* (4), 763.

[2] M. Aleksanyan, A. Grafmüller, F. Crea, V. N. Georgiev, N. Yandrapalli, S. Block, J. Heberle, R. Dimova, *Adv. Sci.* **2023**, *10* (31), 2304336.

5 Light-induced gating of the mechanosensitive ion channel of large conductance in giant unilamellar vesicles

Summary of results from preliminary experiments serving as a proof of principle for the MscL reconstitution and gating. Some parts of this chapter will be used in a future publication.

Contribution

Dr. Naresh Yandrapalli trained Mina Aleksanyan in protein labeling and reconstitution. Antreas Vorkas performed expression and purification of the MACH-MscL and hist-MscL constructs as well as sodium dodecyl sulfate-polyacrylamide gel electrophoresis (SDS-PAGE) of the labeled MACH-MscL by Mina Aleksanyan. Mina Aleksanyan performed all other experiments (labeling, purification and analysis of labeling efficiency of MACH-MscL, preparation of GUVs, reconstitution of MscL into GUVs and microscopic analysis, investigation of photoactivation of reconstituted MscL by sulforhodamine permeation) and analyzed all data with input from Dr. Naresh Yandrapalli. Mina Aleksanyan wrote this manuscript and prepared all figures.

5.1 Abstract

Mechanosensation, regulated by mechanosensitive ion channels in cells, influences various cellular processes and cell vitality. Dysfunctions or mutations in these channels can lead to severe disorders. Strategies to modulate the gating activity of these channels may have a therapeutic potential to overcome the related diseases. Here, we have established a light-triggered, artificial biomimetic system with giant unilamellar vesicles (GUVs) composed of an azobenzene-phosphatidylcholine (azo-PC) photolipid and a bacterial mechanosensitive channel of large conductance (MscL). By modulating membrane properties and tension through the photoisomerization of azo-PC under UV/blue illumination, we aimed to photoactivate MscL and trigger the opening of the channel through light. Our preliminary studies allowed us to develop a novel protocol to directly reconstitute MscL into azo-PC GUVs in the presence of a trace amount of a mild detergent, n-dodecyl-β-D-maltoside. The amount of detergent was found to play an important role in the reconstitution process, destabilizing the GUVs and maintaining the folding of MscL. Labeling MscL with Atto 647 maleimide dye enabled us to monitor the kinetics of the reconstitution process via confocal microscopy and determine the optimal conditions for MscL reconstitution. To confirm the initial conformation of MscL reconstituted in the GUVs and to test the light-induced gating activity, a sulforhodamine probe was employed. Our preliminary results illustrated that most of the MscL remained in the closed state in the GUV membrane after the reconstitution. UV/blue illumination led GUVs to open the channel and permeate the sulforhodamine molecules into the GUV interior through the light-controlled gating of the MscL. Our preliminary findings revealed the possibility of modulation of mechanosensitive ion channels by light.

5.2 Introduction

The ability of cells to sense and respond to mechanical stimuli such as osmotic pressure, temperature and pH by directly transmitting them into the cell interior or by converting them into chemical signals is essential for maintaining the cellular homeostasis and viability (Eyckmans et al., 2011; Tyler, 2012). Mechanosensation initiates multiple signaling pathways of mechanotransduction and plays an important role in the activation of a wide range of biological processes such as gene expression mechanisms (Gordon et al., 2015), cell growth (Mammoto et al., 2013), division, migration, adhesion (Paluch et al., 2015), trafficking (Alvarez and Smutny, 2022), tissue morphogenesis (Heisenberg and Bellaïche, 2013) as well as complex inflammatory and pathological cascades (Hannezo and Heisenberg, 2019). In the membrane of bacteria, archaea and eukaryotic cells, mechanosensation is achieved by mechanosensitive ion channels which are pore-forming transmembrane proteins regulating heat, osmotic pressure and the flow of the ions and small molecules across an otherwise impermeable membrane (Pivetti et al., 2003; Haswell et al., 2011). In eukaryotes, mechanosensitive ion channels are also involved in hearing, balance, touch, vision, taste and pain sensation (Gu and Gu, 2014). Dysfunction or mutation of mechanosensitive ion channels can lead to the lysis of cells, physiological, neuronal, secretion and vision disorders (Dworakowska and Dołowy, 2000). Effective strategies to control the gating activity of mechanosensitive ion channels can contribute to the repair of anomalies of these ion channels thus allowing the treatment of related diseases.

In this study, the activity of mechanosensitive ion channels is targeted to be controlled by light. The application of light in biotechnology offers unique advantages as an environmentally-friendly, fast and inexpensive tool to induce mechanical forces (Goulet-Hanssens et al., 2020). Here, we employed POPC as one of the most abundant phospholipids of animal cells (Alberts et al., 2015) and photoresponsive lipid analog of it, azo-PC, as well as a bacterial mechanosensitive ion channel of large conductance (MscL) to construct a photoswitchable biomimetic platform to control transmembrane transport through GUVs. GUVs are regarded as minimalist cells because they retain the essential lipid bilayer structure of plasma membrane and have cell-sized dimensions (Peter Walde, 2019). In our photoswitchable biomimetic platform, we also embedded bacterial MscL as a model protein because it is one of the widely studied mechanosensitive ion channels (Martinac et al., 1987; Haswell et al., 2011). MscL is a homo-pentameric, pore-forming, transmembrane protein translating the mechanical stresses at the bacterial membrane into an electrophysiological response (Sawada et al., 2012). Optimized protocols make it practical to express and purify MscL from *E. coli* with reasonable yields (Martinac et al., 2010). Its crystal structure has already been resolved (Sukharev et al., 2001), allowing the prediction of the molecular interactions with the lipid bilayer (Gullingsrud et

al., 2001). The main domains of MscL consist of an amphipathic α-helix (S1) situated along the cytoplasmic membrane; two transmembrane domains named as TM1 on the pore constriction side and TM2 facing the lipid bilayer; a periplasmic loop; a linker as well as a cytoplasmic α-helical bundle (Pivetti et al., 2003; Balleza and Gómez-Lagunas, 2009). When the MscL channel is in the closed state, the TM1 domains form a narrow pore constriction with a diameter of 2-4 Å (Cruickshank et al., 1997; Mukherjee et al., 2014). However, increasing membrane tension dramatically affects the structure of the embedded MscL on the bilayer and corkscrew movement in the TM1 domains triggers the opening of a larger pore with a diameter of 30 Å (Cruickshank et al., 1997; Mukherjee et al., 2014) (see Figure 5.1). MscL has a large conductance (3nS) (Sukharev et al., 1993) and a non-selective ion channel (Corry and Martinac, 2008) permeating both large molecules as well as ions in its open state thus making it possible to monitor the transfer of a wide range of molecules to test its potential applications in drug delivery.

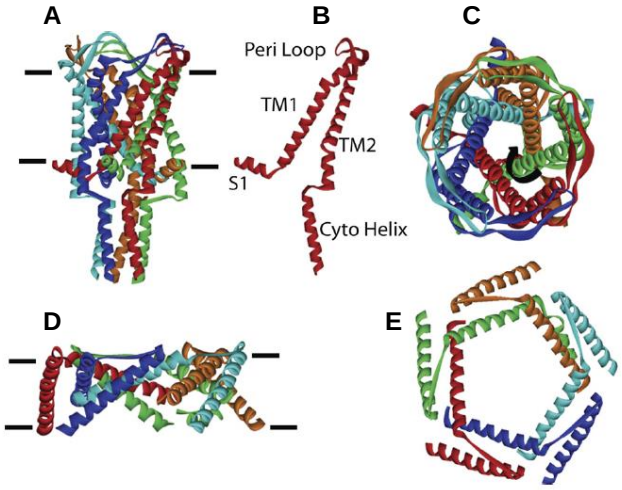

Figure 5.1. A resolved crystal structure of *Mycobacterium tuberculosis* MscL (MscL-Tb). (A) A side view of MscL-Tb across the plane of the membrane. The approximate covered area of the membrane is illustrated as black horizontal lines. (B) A single subunit of MscL. 'S1' is the N-terminal amphipathic α-helix that lies along the cytoplasmic membrane, 'TM1' and 'TM2' are the transmembrane domains, a 'Peri Loop' is the periplasmic loop, and 'Cyto Helix' corresponds to the cytoplasmic helical bundle. (C) The top view of MscL-TB from the periplasmic side of the membrane. The thick black arrow near the green subunit highlights the corkscrew movement of TM1 that occurs throughout the gating process. (D) and (E) are the side and top views of MscL-TB in the open state, respectively. This figure is adapted from (Booth Ian and Blount, 2012).

MscL has been extensively investigated throughout the literature to gain insight into mechanosensitive gating processes and to mimic mechanotransduction pathways in cells (Martinac et al., 1990; Moe and Blount, 2005; Jeon and Voth, 2008; Teng et al., 2015). The structure and composition of the lipids (Martinac et al., 1990; Moe and Blount, 2005; Balleza, 2012; Ridone et al., 2018), lateral packing and organization (Perozo et al., 2002; Balleza, 2012; Nomura et al., 2012) within

the membrane, in which MscL is embedded, are the key regulators of the channel activity. Changes in the material properties of the membrane such as bilayer thickness (Balleza, 2012), membrane spontaneous curvature(Mukherjee et al., 2014) and membrane compressibility modulus (Xue et al., 2020) dramatically affect the function of MscL, alter the kinetics and efficiency/probability of the gating. When the hydrophobic thickness of the lipid bilayer and of the TM domain of the integrated protein are different, hydrophobic mismatch may occur and then the membrane lipids or proteins undergo spatial arrangements to adjust the mismatch (McIntosh and Simon, 2006; Andersen and Koeppe, 2007). If the TM segment of the protein is longer than the thickness of the lipid bilayer, the protein can endure tilted morphologies and the α-helix can reduce its apolar length (Kandasamy and Larson, 2006). Shorter TM segments compared to the lipid bilayer thickness, however, can lead to the local constriction of the lipid bilayer and extension of the side chains of the charged or polar amino acid residues in the TM domain along the perpendicular direction to the membrane bilayer thus exposing their hydrophilic portions more to the hydrophobic tails of the lipid molecules (Chamberlain et al., 2004; Kandasamy and Larson, 2006). This process is referred to as 'snorkeling effect' of transmembrane proteins (Kandasamy and Larson, 2006). TM tilting, membrane snorkeling of charged or polar residues as well as electrostatic interactions at the lipid-water interface are the key mechanisms triggering the protein-lipid interactions thus modulating the function and gating process of MscL channels (Balleza, 2012).

Liposome-based biomimetic platforms (Sukharev, 2002; Battle et al., 2009; Martinac et al., 2010; Hindley et al., 2019) have enabled a novel design of MscL-reconstituted artificial cells to modulate the activity of protein channels. The studies attempting to characterize the channel efflux, as well as structural transformations of MscL during the gating activity have relied extensively on electrophysiology (Corry et al., 2010; Mukherjee et al., 2014), fluorescence (van den Bogaart et al., 2007; Powl et al., 2008; Corry et al., 2010; Mukherjee et al., 2014) and other spectroscopy (Corry et al., 2010; Mukherjee et al., 2014; Yilmaz et al., 2015) techniques and have employed indirect means of opening the channel or gating the lateral pressure. Martinac et al. (Martinac et al., 1990), Perozo et al. (Perozo et al., 2002) and Corry et al. (Corry et al., 2010) have inserted various amphipaths into one of the leaflets of the MscL-containing liposomes asymmetrically to modify the lateral pressure of the membrane and trigger the opening of the channel. However, these strategies do not have good control over the amount of inserted amphipaths into the bilayer leaflet. Furthermore, it is unclear whether the amphipaths are homogeneously distributed in the membrane and between the liposomes in the sample. Van den Bogaart et al. (van den Bogaart et al., 2007) and Hindley et al. (Hindley et al., 2019) have engineered a cysteine residue of MscL at the constriction site of the pore

(G22C), labeled with [2-(triethylammonium)ethyl]methanethiosulfonate bromide to induce electrostatic and hydrophobic forces to activate the channel (Yoshimura et al., 2001) to its open state. Then, they compared liposomes with incorporated G22C mutant to liposomes containing the wild-type MscL. However, they could not monitor the transition of MscL from closed to open state. The studies of van den Bogaart and coworkers (van den Bogaart et al., 2007) also implemented the patch clamping technique to check the function of MscL, which is technically a challenging approach requiring the assessment of the curvature of the membrane patch to allow the calculation of membrane tension from the applied pressure. Kocer et al. (Koçer et al., 2005; Koçer et al., 2007) designed a photoswitchable MscL by attaching small photoswitchable molecules to the cysteine residue of MscL at the constriction site of the pore. They reconstituted this mutant MscL into LUVs and probed the activation of the channel through efflux of a self-quenching fluorescent dye, calcein, by analyzing the changes in the fluorescence intensity. The whole protocol of Kocer and coworkers includes synthesis of light-responsive molecules, MscL isolation and its chemical labeling, reconstitution of MscL into artificial membranes, its analysis at the single-molecule level and its application in liposomal delivery. This protocol is laborious and requires 4 days (Koçer et al., 2005; Koçer et al., 2007) of work to reach the final studies with MscL reconstituted liposomes. In addition, LUVs are smaller than cells and have a higher surface-to-volume ratio. The preparation protocols for LUVs typically result in membranes that are under stress and do not provide control over membrane tension. The high membrane tension and curvature of LUVs may alter the behavior of mechanosensitive ion channels and affect the interpretation of the mechanosensation process in cellular systems. By reconstituting MscL into photoswitchable GUVs, our aim was to modify membrane tension on demand through the usage of UV and blue illumination. This approach allows us to monitor the complete gating process of MscL, including its transition from the closed to open state, in cell-sized dimensions through optical imaging and characterization techniques.

Since we have already investigated the effects of azo-PC photoisomerization on the material properties of GUVs in the absence of MscL in our previous studies (Aleksanyan et al., 2023b), we could gain information on how *trans*-to-*cis* photoisomerization of azo-PC increases the membrane area, softens the bilayer, weakens the interleaflet interactions and reduces the membrane capacitance and dielectric values of the bilayer with increasing fractions of the *cis* azo-PC in the membrane. These initial characterization studies with azo-PC GUVs were necessary to design effective strategies for protein reconstitution and to establish a good control over the transport of macromolecules through the light-induced gating of MscL. Our results illustrated that 50 mol% and higher azo-PC content of the GUVs resulted in large membrane deformations and complex shape transformations which also led to slow

shape response to UV irradiation (see Chapter 3 for the membrane area increase values and the response time). The photoresponse of GUVs containing lower fractions of azo-PC was faster in the absence of any membrane budding events (Aleksanyan et al., 2023b). These data suggested that up to 25 mol% of azo-PC would be sufficient to modulate the membrane tension of MscL-incorporated GUVs for inducing the gating activity of ion channels without causing GUVs to undergo complex shape transformations.

In this part of the project, a novel protocol to reconstitute bacterial MscL into photoswitchable azo-PC GUVs was developed and the possibility of light-induced gating of ion channels was tested. To confirm the protein reconstitution process through optical microscopy, MscL in monomeric form was labeled with Atto 647 maleimide before GUV incorporation. Permeation of water-soluble, sulforhodamine dye into the vesicle interior under the exposure of UV and blue light enabled us to check the functionality of the reconstituted MscL. Our results demonstrated that sulforhodamine can successfully pass through the light-induced opening of MscL, which resulted from the photoisomerization of azo-PC in the bilayer. These preliminary results demonstrated that light can also be used as an effective trigger to mimic the complete mechanosensation process and gating activity of MscL channel by modulating the material properties of azo-PC GUVs thus leading to the transport of small molecules across MscL.

5.3 Materials and methods

5.3.1 Labeling of MscL with Atto 647 maleimide and its purification

This protocol was developed from the previously reported protocols (Alexiev et al., 1994; Heberle et al., 1994). 1.6 mg of Tris(2-carboxyethyl)phosphine hydrochloride (TCEP), (Sigma Aldrich, St. Louis, USA) was dissolved in 5 mL of 0.02% w/v n-dodecyl-β-D-maltoside (DDM), (Avanti Polar Lipids, Alabaster, AL) and Phosphate Buffered Saline (PBS) solution (ThermoFisher Scientific, Waltham, USA). The pH of the solution was adjusted to 7. The buffer solution was degassed in a desiccator for 30 minutes to suppress the foam from the surfactant. 450 µL of TCEP buffer was then mixed with 50 µL of 100 µM of MACH-tagged MscL (obtained from a collaborator, Antreas Vorkas at the Department of Physics, Genetic Biophysics, Freie Universität Berlin, Berlin, Germany) and incubated for 20 minutes in the presence of inert gas (N_2) to reduce the disulfide bonds in the cysteine. An increase in the number of free thiol groups of the protein increases the labeling efficiency of maleimide-conjugated dye in the next step.(Winther and Thorpe, 2014) An aliquot of 20 µL of 2.3 mM Atto 647 maleimide (Sigma Aldrich, St. Louis, USA) dissolved in Dimethyl sulfoxide (DMSO), (ThermoFisher Scientific, Waltham, USA) was then added drop by drop into 500 µL of MscL mixture containing TCEP buffer and incubated at 4 ^{o}C overnight. The excess amount of dye was removed either through PD-10 desalting

columns packed with Sephadex G-25 resin (Cytiva™, Marlborough, United States) or ultracentrifugation via Eppendorf microcentrifuge 5417 C (12045 x g at 4 °C, 5 repeats for 4 minutes) (Marshall Scientific, New Hampshire, United States) with Amicon ultracentrifugal filter units (10000 MWCO) (Merck, Darmstadt, Germany). Purification of the labeled protein was analyzed through BioTek Epoch Microplate Spectrophotometer (Fisher Scientific, Waltham, United States) and sodium dodecyl sulfate-polyacrylamide gel electrophoresis (SDS-PAGE). Purified labeled proteins were stored at – 80 °C in aliquots and thawed just before usage. For the spectrophotometer, 2 µL of each solution was placed on the pedestal of the machine and absorbance values were obtained automatically via Gen5.209 software. Then, the measured absorbance values were converted to concentration by using the following equation of the Beer-Lambert Law:

$$A = \varepsilon\, c\, L \tag{1}$$

where A and ε correspond to the absorbance and molar extinction coefficient of the sample, respectively. L is the path length of the light and equal to 1 cm. Then, c is the concentration of the sample in mg/mL units. For each sample, absorbance values were collected at both 280 nm (for protein) and 647 nm (for Atto 647 maleimide). The amino acid sequence of MACH-MscL according to https://www.uniprot.org/ is MACH MSIIKEFREF AMRGNVVDLA VGVIIGAAFG KIVSSLVADI IMPPLGLLIG GIDFKQFAVT LRDAQGDIPA VVMHYGVFIQ NVFDFLIVAF AIFMAIKLIN KLNRKKEEPA AAPAPTKEEV LLTEIRDLLK EQNNRS. By loading these sequences at https://web.expasy.org/cgi-bin/protparam/ (Gasteiger et al., 2005), we obtained the molar extinction coefficient, ε_{MscL}, as 1490 M^{-1} cm^{-1} for MACH-MscL. The molar extinction coefficient for Atto 647 maleimide, ε_{dye}, was found 1.2 x 10^5 M^{-1} cm^{-1} from manufacturer documentation. The molarity of the protein, M_{MscL}, was calculated through the following equation:

$$M_{MscL} = \left(\frac{A_{280} - (A_{max}\, CF)}{\varepsilon_{MscL}}\right) DF \tag{2}$$

In this equation, A_{280} is the absorbance of MscL at 280 nm while A_{max} is the absorbance of Atto 647 maleimide dye measured at wavelength maximum at 647 nm. CF corresponds to the correction factor to eliminate the contribution of the dye at 280 nm and it is 0.03, which is obtained from manufacturer documentation. DF is the dilution factor in case the sample is diluted before the absorbance measurements. Samples were not diluted during our assessments. Then, we calculated the degree of labeling, DL, by:

$$DL = \left(\frac{A_{280}}{\varepsilon_{dye}\, M_{MscL}}\right) DF\ 100 \tag{3}$$

5.3.2 Preparation of GUVs

GUVs were grown in 307 mM (307 mosmol/kg) sucrose using the electroformation method (Matthias Garten, 2019) from 4 mM solution of 1-palmitoyl-2-oleoyl-sn-glycero-3-phosphocholine (POPC) and 0 – 25 mol% 1-stearoyl-2-[(E)-4-(4-((4-butylphenyl)diazenyl)phenyl)butanoyl]-sn-glycero-3-phosphocholine (azo-PC) in chloroform. Both of the lipids were purchased as chloroform solutions from Avanti Polar Lipids, Alabaster, AL. For fluorescence imaging of vesicles, 0.1 mol% 1,1'-Dioctadecyl-3,3,3',3'-Tetramethylindocarbocyanine perchlorate (DiLC18) (Invitrogen™, Waltham, United States) or 1,2-Dioleoyl-sn-glycero-3-phosphoethanolamine labeled with Atto 647N (Atto-647N-DOPE) (Avanti Polar Lipids, Alabaster, United States) was added to the lipid solution. A thin film was formed with 8 µL of this lipid solution on a pair of electrically conductive indium-tin-oxide (ITO) coated glass plates (PGO GmbH, Iserlohn, Germany). In order to evaporate the chloroform, glass plates were exposed to a stream of N_2 and then located under a vacuum for two hours. Then, a Teflon spacer of 2 mm thickness was placed between the ITO-glass plates to form a chamber. For the hydration of the lipid film, the chamber was filled with 1.8 mL of 307 mM (307 mosmol/kg) solution of sucrose (Sigma Aldrich, St. Louis, USA). Hydrated lipids were then electroswelled by a sinusoidal AC electric field at 10 Hz frequency with a 1.6 V_{pp} (peak to peak) amplitude for 1 hour in the dark at room temperature. Electric field was generated through Agilent 33220A function generator (Agilent Scientific Instruments, United States). GUVs were then transferred to a light-protective glass vial for storage at room temperature and used the same day. For the microscopy observations, GUVs were further diluted in 310 mM (310 mosmol/kg) glucose solution (Merck, Darmstadt, Germany) and corresponding buffers. The osmolarity values of the solutions were adjusted with an osmometer (Osmomat 3000, Gonotec GmbH, Germany).

5.3.3 Reconstitution of MscL into GUVs and microscopy observations

This protocol was developed from the previously reported protocol of Dezi and coworkers (Dezi et al., 2013). A 5 fold-diluted GUV solution (in 310 mM Glucose) was mixed in 10 : 1 ratio with labeled MscL solution (containing PBS buffer and 0.00068% w/v DDM, pH 7) to reach 150 nM MscL concentration in the final volume of the solution. Various concentrations of DDM (0.05 – 0.00125% w/v) and MscL (50 – 200 nM) were compared to find the optimum concentrations of each for efficient reconstitution (Here and all the rest of the manuscript, MscL refers to the homopentameric structure of the protein and the calculations about the concentration of MscL were performed accordingly. The molecular weight of the monomeric unit of MscL was assumed as 15 kDa as it is previously reported by Sukharev and coworkers (Sukharev et al., 1999).). Biobeads SM-2 Resin (BIO-RAD, California, United States) were added to the final mixture to remove the detergent, DDM, according to the manufacturer's

guidelines (Spack et al., 1986). After 20 minutes of incubation, the solution was removed from the adsorbent with a pipette and transferred to Bovine Serum Albumin (BSA) (Merck, Darmstadt, Germany) coated 96-well plates (Corning, New York, USA) for confocal microscopy observations. In order to coat the surface of the microtiter plates and prevent the adhesion and bursting of the vesicles, 2 mg/mL of BSA was dissolved in water, incubated on the surface of the microtiter plates for 15 minutes and then rinsed with Milli-Q water.

MscL incorporation of GUVs was monitored via Leica TCS SP8 confocal microscope (Wetzlar, Germany) with either 40 x (1.3 NA) oil or 63 x (1.2 NA) water immersion objectives. The red dye DiLC18 on the membrane was excited with a diode-pumped solid-state laser at 561 nm and the emission was detected in the range 565 − 620 nm. The far-red dye, Atto 647 maleimide, was excited with a HeNe 633 nm laser and the signal was collected in the range of 645-705 nm. The sequential mode of image acquisition was activated to minimize cross-talk. Images were recorded with 512 x 512 pixels and scanned with 600 Hz speed in the bidirectional mode with two-line averages. Image analyses were performed through Leica LASX software (Jena, Germany) and ImageJ (NIH, USA).

5.3.4 Probing the functionality of MscL and microscopy observations

To monitor the light-induced activity of reconstituted MscL in GUVs, a mixture of labeled and unlabeled MscL (1:4 ratio) was added to GUV media. In these experiments, GUVs were composed of 25 mol% azo-PC and 75 mol% POPC (They did not contain any DILC18 dye.). An aliquot of 4 µL of 1.378 µM Hist-tagged MscL, 1 µL of 5.55 µM of MACH-tagged MscL and 5 µL of 310 mM glucose solution (pretreated in Biobeads for 10 minutes) were incubated in 100 µL of 1:4 diluted GUV solution and 310 mM Glucose solution for 20 minutes. A 5 µL of 220 µM Sulforhodamine B (Thermo Fischer Scientific, Waltham, USA) was further added to the MscL reconstituted GUV solution in a BSA coated microtiter plate. The permeation process of GUVs during the sulforhodamine B incubation was directly monitored just after the addition of Sulforhodamine B under the confocal microscope over 30 minutes. Then GUVs were exposed to UV light for 1 minute and afterwards the sulforhodamine permeation of GUVs was further monitored under blue and red light for 30 minutes. Observations were performed under a Leica TCS SP8 confocal microscope (Wetzlar, Germany) with either 40 x (1.3 NA) oil or 63 x (1.2 NA) water immersion objectives. Water soluble, red dye, Sulforhodamine B was excited with a diode-pumped solid-state laser at 561 nm and the emission was detected in the range of 571 − 620 nm. The far-red dye, Atto 647 maleimide, was excited with a HeNe 633 nm laser and the signal was collected in the range 645-705 nm. The sequential mode of image acquisition was activated to minimize cross-talk. A 365 nm UV-LED (maximum output power intensity of 20 mW cm^{-2}, Roschwege, Germany) was attached to the condenser of the confocal microscope to generate UV

illumination. The blue light was generated through a 458 nm laser line. Images were recorded with 512 x 512 pixels and scanned with 600 Hz speed in the bidirectional mode with two-line averages. Image analyses were performed through Leica LASX software (Jena, Germany) and ImageJ (NIH, USA). Permeation plot was generated through Origin Pro software. The statistical significance of the plotted permeation graph was tested with the two-sample t-test (*p*-values were found less than 0.05).

5.4 Results and Discussion

5.4.1 Detergent-mediated direct incorporation of solubilized MscL into GUVs and optimization of the reconstitution protocol

MscL reconstitution was achieved through the detergent-mediated direct insertion of solubilized MscL into preformed GUVs. This method begins with the preparation of a detergent-solubilized form of the protein of interest (Dezi et al., 2013). The preformed GUVs are then incubated with this protein-detergent mixture under controlled conditions, allowing the detergent to be gradually removed, typically by dilution or adsorption onto polystyrene beads. This removal of detergent facilitates the spontaneous insertion of the protein into the GUV membrane, effectively reconstituting the protein in a functional membrane environment. An advantageous feature of this method is that it promotes the unidirectional incorporation of the transmembrane proteins into the membranes (Dezi et al., 2013; Matthias Garten, 2019). In this incorporation, the most hydrophobic domain of the protein is predicted to be integrated into the lipid bilayer, while the hydrophilic domain is located outward toward the vesicle exterior (Dezi et al., 2013; Matthias Garten, 2019). First step of the protocol is the preparation of the 25 mol% azo-PC containing GUVs in sucrose by electroformation method. Then, the sucrose concentration in the growth solution was chosen to match the osmolarity of the buffer in which MscL was solubilized. The presence of sucrose and other sugar molecules in the media is also known to stabilize the protein folding (Lee and Timasheff, 1981; Arakawa and Timasheff, 1982; Allison et al., 1999). One of the most important steps of this protein reconstitution method was the optimization of the concentration of the detergent in the final GUV media. In order to destabilize the GUV bilayer during the reconstitution of MscL, we have used DDM which is regarded as a sugar-based milder detergent in terms of solubilizing and stabilizing the membrane proteins without denaturing them (Vanaken et al., 1986; Dezi et al., 2013; Matthias Garten, 2019).

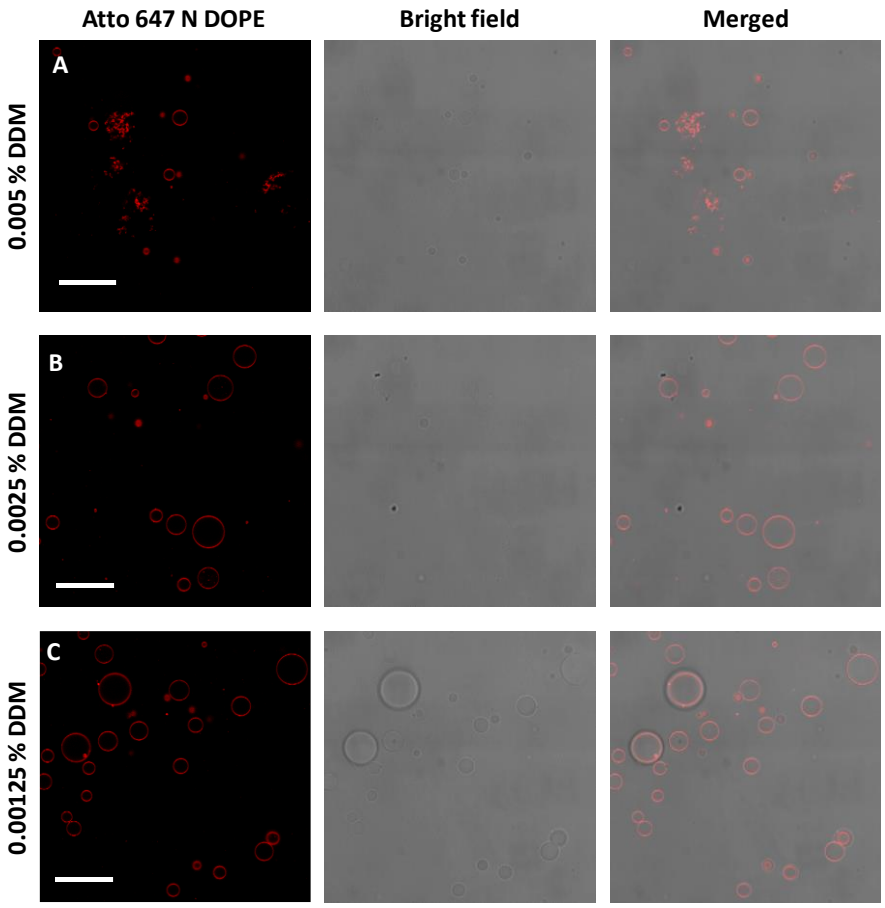

Figure 5.2. Optimization of DDM amount in GUV media for MscL reconstitution. GUVs composed of 25 mol% azo-PC, 75 mol% POPC and labeled with 0.1 mol% Atto 647 N DOPE (indicated as red signal). GUVs harvested in 307 mM sucrose were 1:1 diluted in 310 mM Glucose. The new GUV solution was then 1:1 diluted in PBS buffer and (A) 0.005% w/v DDM, (B) 0.0025% w/v DDM and (C) 0.00125% w/v DDM. Each panel provides with the confocal microscopy images of GUVs in corresponding buffer conditions. Final concentrations of DDM in each GUV medium are indicated on the left corner of each panel. The scale bars represent 50 µm.

DDM has a relatively low critical micelle concentration (CMC) of 0.17 mM, so it can solubilize the hydrophobic molecules and form micelles at lower concentrations (Vanaken et al., 1986). During the reconstitution of MscL into GUVs, the DDM amount should be slightly above the CMC in order to prevent the aggregation of the protein (Moraes et al., 2014). When DDM concentration is above the CMC, micellar and monomeric forms of DDM are in equilibrium. With a lower CMC, a lower amount of detergent will be necessary to preserve the folding of MscL during the reconstitution process, thus making it easier to remove the excess DDM from the MscL reconstituted vesicles afterward (Vanaken et al., 1986; Moraes et al., 2014). Another advantage of choosing low DDM concentration is that they will not solubilize the vesicle membrane (i.e. dissolve the vesicles). Additionally, sugar-based detergents are known to produce a lower background fluorescence thus minimizing the detergent interference in any further fluorescence-based characterization studies (Vanaken et al., 1986; Moraes

et al., 2014). So, the amount of DDM in the media should be low enough to destabilize the bilayer for the insertion of MscL as well as preserving the native structure of MscL without causing any bursting of the vesicles as well as denaturing of MscL. In this respect, the morphology of GUVs was directly compared for 0.01 to 0.00125% w/v DDM-containing media (see Figure 5.2) under confocal microscopy. Having 0.005 and higher % w/v DDM in the solution caused either partial or full bursting of GUVs and resulted in the formation of lipid aggregates (see Figure 5.2A). All the GUVs having a diameter larger than 10 µm lost their sharp vesicle contrast coming from the refractive index differences between the sugar solutions in the vesicle interior and exterior. So, the vesicles became permeated, which indicates the GUV leakage and destabilization. The same trend of vesicle permeation was also observed in GUV media containing 0.0025% w/v DDM while in 0.00125% w/v DDM-containing media, 70 – 80% of the GUVs retained their sharp contrast and only 20 – 30% of the GUVs showed a permeation due to the surfactant destabilization (see Figure 5.2B, C). So, having 0.00125% w/v and lower concentrations of DDM in the GUV media will be sufficient to prevent the bursting of vesicles during the protein reconstitution. In the next step, while labeling the protein with a dye and purifying the free dye, we also adjusted the amount of DDM in the final solution accordingly.

5.4.2 Labeling MscL with a dye and monitoring the reconstitution process through confocal microscopy

In order to monitor the reconstitution of MscL into GUVs, the MACH-MscL construct was labeled through Atto 647 maleimide. Free dye was removed by a size exclusion column and ultracentrifugation. The purity of the final solution including labeled protein was analyzed with SDS-PAGE under UV illumination (see Figure 5.3A). Samples 1 and 2 were identical and composed of PBS buffer with TCEP and 0.02% w/v DDM. Sample 3 was the solution of the labeled MACH-MscL construct before the purification steps whereas samples 4 and 5 were identical and contained the solution of the labeled MACH-MscL construct after the purification. Samples 6 and 7 were identical and contained the free dye solution. The single peak in samples 4 and 5 corresponding to the labeled MACH-MscL construct demonstrated the purity of the final solution.

To verify the labeling efficiency of the protocol, all the samples were also analyzed with a spectrophotometer which could measure the absorbance of protein and Atto 647 maleimide and then correlated these values with their concentration based on Beer-Lambert law (see equation 1). The maximum absorbance of MACH-MscL was measured at 280 nm and found as 0.022. However, the dye could also absorb at 280 nm, so a correction factor was introduced when calculating the molarity of MscL (see equation 2) in order to eliminate the contribution of the dye at 280 nm. This parameter was obtained as 0.03 from the manufacturer documentation. The maximum absorbance of Atto 647

maleimide at 647 nm was measured as 0.0041. Putting all these values in equation 2 led us to the molarity of MscL being 6.49 x 10^{-6} M. Then, we calculated the degree of labeling by applying equation 3. Our results suggested that 29% of MscL in the monomeric unit was labeled with Atto 647 maleimide dye. Considering the homopentameric assembly of MscL as a transmembrane protein, we expected a labeling efficiency of 145% for a homopentameric unit. The next step was to reconstitute this labeled protein on 25 mol% azo-PC containing GUVs (the rest of the lipid composition was POPC) and to confirm the reconstitution by monitoring the fluorescence of this labeled MACH-MscL in the 633 nm laser line via confocal microscopy.

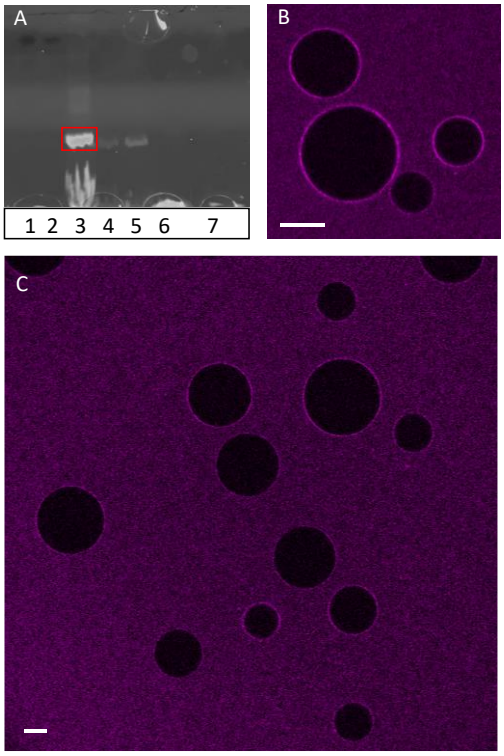

Figure 5.3. Monitoring the reconstitution of MACH-MscL into 25 mol% azo-PC containing GUVs via Atto 647 maleimide dye. Assessment of the purity of labeled-MACH-MscL with SDS-PAGE (A). Samples 1 and 2 were the identical blank solutions that only contained the buffers in which MscL was dissolved. They only contained PBS buffer with TCEP and 0.02% w/v DDM. Sample 3 was the solution of labeled-MACH-MscL before the purification steps which also contained free Atto 647 maleimide. Samples 4 and 5 were identical and contained the labeled MACH-MscL solution after the purification steps in which free dye was removed through the size exclusion column and ultracentrifugation. Samples 6 and 7 were identical and only contained Atto 647 maleimide solution. The peak coming from the labeled MACH-MscL (in sample 3) was highlighted with a red rectangle. Confocal screenshot of MscL-reconstituted GUVs after 10 minutes (B) and 20 minutes (C) of incubation. GUVs were composed of 25 mol% azo-PC and 75 mol% POPC. The concentration of labeled-MACH-MscL was 150 nM of the final solution. The incorporation of MACH-MscL into the GUV membrane was detected from the fluorescence signal (shown as magenta) of the label of the protein, Atto 647 maleimide dye. The scale bars are 10 µm.

The labeled MACH-MscL was directly injected on to the BSA-coated microtiter plate containing 25 mol% azo-PC GUVs and the incubation process of labeled MscL in GUV media was directly monitored under a confocal microscope. The effect of MscL amount on the reconstitution process was investigated by the addition of various concentrations of labeled MACH-MscL ranging from 50 – 200 nM in the final GUV media. Among the others, 150 nM and higher concentrations of protein showed a higher yield of reconstitution. In the case of the addition of 150 nM labeled MACH-MscL to the GUV media, a strong signal of Atto 647 maleimide was already detected on some of the GUVs after 10 minutes of incubation (see Figure 5.3B) while all of the GUVs showed a dye signal after 20 minutes of incubation (see Figure 5.3C). These results indicated a successful reconstitution of labeled MACH-MscL into GUVs. Our protocol offers an improved time efficiency compared to the previously published MscL reconstitution protocol of Mukherjee et al. (Mukherjee et al., 2014) for GUVs. Since the protocol of Mukherjee et al. (Mukherjee et al., 2014) obtains the GUVs from proteo-liposomes through the dehydration/rehydration techniques, additional steps to incorporate MscL to LUVs are required. These initial steps prolong the overall preparation process in comparison to our protocol. Battle et al. (Battle et al., 2009) directly reconstituted MscL into GUVs earlier through a 6-hour protocol by using a sucrose solution as the rehydration medium. However, GUVs generated through this protocol (Battle et al., 2009) exhibited a lot of defects including multilamellar vesicles, various fused structures, buds and aggregates. In comparison to the protocol of Battle et al. (Battle et al., 2009), our protocol enabled us to obtain defect-free GUVs.

5.4.3 Monitoring Sulforhodamine B permeation of MscL incorporated GUVs to test the conformation and functionality of MscL in the bilayer by using confocal microscopy

After the reconstitution of MscL into the GUV membrane, we next investigated the conformation of the protein in the bilayer, i.e. whether the reconstituted MscL stayed in the membrane in an open or a closed state. In these experiments, the reconstitution process was performed both with MACH-tagged MscL as well as a mixture of MACH and Hist-tagged MscL in a 1 to 4 ratio to compare if any effects coming from the presence of additional MACH residue on the labeled MscL or not. By combining a small fraction of MACH-tagged MscL with hist-tagged MscL during the reconstitution process, we could still monitor the incorporation of MscL through the fluorescence signal of the labeled dye on MACH-tagged MscL. However, most of the protein population would be in native-like, dye-free conformation in the bilayer. This approach would allow us to make a comparison between a native-like MscL and a mutant construct of it.

To interrogate the conformational state of reconstituted MscL in the GUV bilayer, a small, water-soluble, membrane-impermeable dye, namely sulforhodamine, was added to the GUV media

after the incorporation of MscL into the GUV membrane. In the case of an intact membrane in which MscL is in a closed state, sulforhodamine dye cannot cross the membrane and reach the vesicle interior, so the inner solution of the GUV preserves the dark appearance in confocal cross sections. If MscL endures an open conformation and forms a transmembrane pore, the presence of a pore in membrane results in an exchange of solutions between GUV interior and exterior. The pore diameter of MscL is approximately 3 nm, and the size of the sulforhodamine dye is small enough to pass through this opening when MscL is in its open state. Given that sulforhodamine dye is smaller than a POPC lipid, which has a reported area of 68.3 ± 1.5 Å² (0.683 ± 0.015 nm²)(Kucerka et al., 2005), the dye should be able to permeate through the MscL channel during gating.

To probe the state of MscL, sulforhodamine was introduced to GUV media after the confirmation of MscL reconstitution. The permeation process of GUVs was monitored for 30 minutes (see Figure 5.4A). In order to quantify the membrane leakage after the reconstitution of MscL, the ratio between the fluorescence intensities of GUV interior and exterior ($\frac{F_{in}}{F_{out}}$) was calculated as permeation index by assessing a circular region of interest (ROI) of nominal radius of 2 µm for 70-180 GUVs. When MscL was incorporated into the GUV membrane, a small fraction (below 25%) of GUVs showed some degree of permeation, but the majority of the GUV population retained dark contrast, indicating that most of MscL remained in a closed state in the membrane after reconstitution (see Figure 5.4D). When vesicles with pure MACH-MscL incorporated were compared to vesicles with the reconstituted mixture of Hist-MscL and MACH-MscL, the permeation indices of GUVs in these two conditions showed statistically different results based on a two-sample t-test (*p*-value was found to be 0.0006). The mean value of the permeation index of pure MACH-MscL incorporated GUVs was 0.33 whereas the reconstitution with Hist-MscL and MACH-MscL containing mixture lowered the mean of permeation index of GUVs to 0.25. The increased permeation of the GUV population containing MACH-MscL reconstituted vesicles may indicate that MACH-MscL incorporated vesicles are more prone to defects. However, since the majority of the MscL-reconstituted GUVs remained non-permeated in both conditions, we proceeded with the next step to test the light-induced gating activity of MscL by using a sulforhodamine probe.

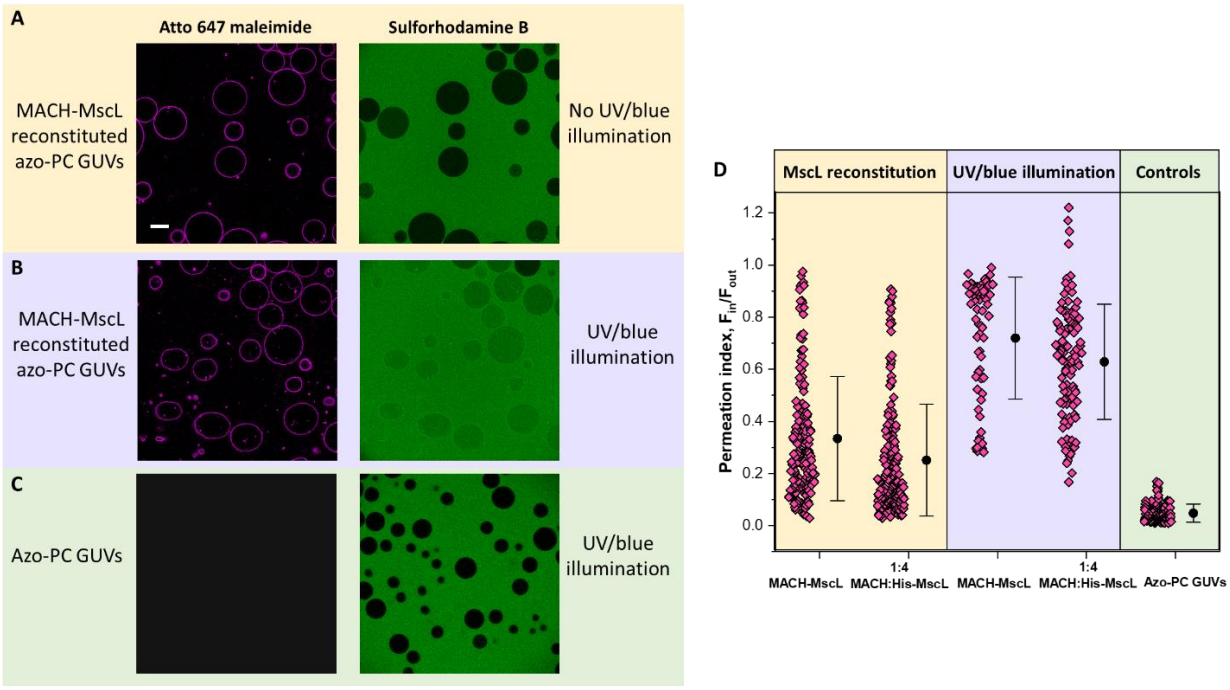

Figure 5.4. Testing the functionality of reconstituted MscL in the GUV bilayer via sulforhodamine probe under UV/blue illumination. Screenshots of MACH-MscL incorporated azo-PC GUVs 30 minutes after the reconstitution (A), MACH-MscL incorporated azo-PC GUVs after exposing to 1 minute of UV illumination and then to the blue light for 30 minutes (B), the repetition of the same experimental design in (B) in the absence of MACH-MscL just with 25 mol% azo-PC including GUVs (C). The left column indicates the fluorescence signal of labeled MACH-MscL and the magenta color corresponds to Atto 647 maleimide while the right column shows the sulforhodamine entry into GUVs in case of MscL opening under UV/blue illumination. The scale bar is 20 µm. Quantification of GUV leakage through fluorescence intensity analysis. (D) Each pink-filled diamond symbol corresponds to a measurement on a single GUV. Mean and standard deviation values are shown on the right side.

After confirming the incorporation of MscL in the GUV bilayer in a closed conformation, another important question was to check whether or not a reconstituted MscL retains the functionality and switches on/off with the differences in membrane tension or not. In our experimental design, light was used to modulate the membrane tension of the MscL-incorporated GUVs. First, GUVs containing reconstituted MscL were subjected to UV light for a minute while the external solution of the GUVs contained sulforhodamine dye. These GUVs were observed in confocal microscopy for 30 minutes, but no permeation was detected. However, when these GUVs were further exposed to blue light after a minute of UV exposure, all GUVs permeated within 30 minutes. The mean of the permeation index increased to 0.72 for pure MACH labeled MscL incorporated GUVs while it was 0.63 for the reconstitution with Hist-MscL and MACH-MscL mixture (see Figure 5.4B, D). In parallel, control experiments were performed with 25 mol% azo-PC containing GUVs diluted in PBS and DDM-containing solution in the absence of any MscL to check whether the salt and detergent concentration play a role in the permeation of GUVs. In these control experiments, the inside of GUVs

retained the dark contrast over time and did not show any remarkable permeation (see Figure 5.4C). The mean permeation index for 25 mol% azo-PC GUVs under UV/blue irradiation was found as 0.05. So, all these preliminary results illustrated that the permeation of GUVs under UV/blue illumination was associated with the reconstituted MscL constructs. Thus, the successful gating activity of MscL was monitored through the permeation of the sulforhodamine molecules to the vesicle interior under confocal microscopy. Our preliminary results with GUVs are consistent with the findings of Crea et al. (Crea et al., 2022) on MscL-inserted nanodiscs revealing that light can effectively regulate the activation of mechanosensitive ion channels.

5.5 Conclusions and outlook

The capacity of cells to perceive and react to mechanical stimuli via mechanosensitive ion channels is pivotal in preserving vital cellular processes while malfunctions of these channels can result in diverse disorders. In the studies presented here, we aimed to manipulate the activity of mechanosensitive ion channels by utilizing light with a photoswitchable biomimetic platform composed of azo-PC and bacterial MscL. Our preliminary results helped us to develop a novel, straightforward protocol to reconstitute bacterial MscL into azo-PC GUVs and then we tested the possibility of light-induced gating of these ion channels. Our studies illustrated that the concentration of detergent in the final GUV solution should be 0.00125% w/v or less to prevent the bursting or solubilization of the vesicles during protein reconstitution. In order to monitor the reconstitution process in microscopy, a MACH residue was introduced in MscL and it was labeled with Atto 647 maleimide dye. After the purification of the labeled protein by PD-10 column and ultracentrifugation, the labeling efficiency was assessed through SDS-PAGE and absorbance measurements via spectrophotometer. The degree of labeling was found to be 29% in the monomeric unit of MscL. Then, various concentrations of this labeled protein were reconstituted into 25 mol% azo-PC containing GUVs and the incorporation was confirmed through fluorescence monitoring with confocal microscopy. A 150 nM and higher concentrations of MscL showed a higher yield of reconstitution. The fluorescence signal of labeled MscL for this concentration was observed 10 minutes after the protein incubation in GUV media. Lastly, the conformation and gating activity of the reconstituted protein was assessed via a sulforhodamine probe. The majority of MscL was found to remain in the closed state in the membrane after the reconstitution and our preliminary results also suggest that MscL can be gated and converted to its open state by UV/blue illumination.

Future studies should focus on a more comprehensive characterization of the MscL reconstitution process into GUVs and the light-induced gating events on MscL-incorporated GUVs. Firstly, one should probe whether the amount of the reconstituted MscL is homogeneously distributed

across vesicles in the sample. The fluorescence of individual GUV membranes should be quantified and related to the amount of MscL. For these quantification experiments, reference GUVs would be prepared from the known fractions of lipids conjugated with the same fluorophore as the fluorescently labeled MACH-MscL construct. By analyzing the fluorescence intensity values of these reference GUVs containing various fractions of dye-conjugated lipids, we would plot a calibration curve as a function of the fraction of dye. Then, the fluorescence intensity values of the GUVs containing the same fluorophore-labeled MACH-MscL construct would be analyzed. The intensity values would be assigned in the calibration curve to derive the fraction of the dye on the labeled MACH-MscL construct thus deciding the degree of reconstitution of the labeled MACH-MscL in the GUVs. In order to decide the degree of the assembly of the monomeric units of MscL to homopentamers, protein surface coverage and diffusion properties of proteins should be analyzed through fluorescence correlation spectroscopy (FCS) and fluorescence recovery after photobleaching (FRAP) under confocal microscopy.

FCS analyzes the fluorescence intensity fluctuations in a certain volume of the sample defined by a tightly focused laser beam. The fluorescence intensity patterns show a variety, depending on the number or the fluorescence quantum yield of molecules passing through the detection volume (Petersen et al., 1993; Berland et al., 1996). The time-dependent fluorescence intensity can be analyzed in terms of the temporal autocorrelation which provides information about diffusivity of the molecules in the sample. The initial amplitude of the autocorrelation function is inversely proportional to the number of molecules in the detection volume.(Petersen et al., 1993; Berland et al., 1996) So, monomeric proteins should show more fluctuating patterns in the fluorescence spectra and a single exponential decay in the autocorrelation curve while proteins with multimeric units exhibit broader patterns in fluctuation spectroscopy and a multi-exponential decay in the autocorrelation curve.

FRAP, on the other hand, analyzes the photobleaching and recovery process of the fluorescent molecules within the selected area of the sample thus obtaining the diffusion coefficient and mobility parameters of molecules by using mathematical modeling (Ishikawa-Ankerhold et al., 2012). After monitoring the initial fluorescence intensity of the fluorescently labeled MscL in the membrane, they would be then photobleached within the selected area by exposing the area to intense illumination leading to the extinction of the fluorophores. The extinction of the fluorophore would appear as a dark spot in the observed area. Then, the diffusion process of fluorescent molecules from the surroundings to exchange the photobleached ones is monitored over time showing recovery of the signal (Ishikawa-Ankerhold et al., 2012). Monomeric proteins exhibit a faster recovery of fluorescence compared to larger assemblies (Ishikawa-Ankerhold et al., 2012) and this dependence could be explored as a function of overall MscL intensity (concentration) reconstituted in the GUV. If the degree

of MscL reconstitution would be found low after the evaluation of the results of all the above-mentioned techniques deliberately, more protein reconstitution protocols in the literature (Matthias Garten, 2019) could be explored.

After finding the optimal reconstitution protocol with a well-quantified MscL amount in the GUV system, the next step could be a comprehensive investigation of the gating process of MscL by light. It would be interesting to explore the role of membrane tension in the opening process of the channel. Micropipette aspiration technique could be employed to identify the optimal membrane tension conditions to trigger the gating activity of MscL under UV and blue irradiation. This technique allows for the modulation of the membrane tension of a vesicle externally with a micropipette, representing a single-vesicle assay. Another approach could involve modifying the osmotic pressure of the GUVs by changing the solute concentration inside and outside the vesicles. In this respect, tension modulation via osmotic stress could be conducted as a bulk assay. Alternatively, microfluidic devices could be also utilized. In this technique, vesicles are individually trapped in microfluidic chips, and solution exchange enables the assessment of the gating process under various osmolarities. In all these above-mentioned approaches, the GUV external solution should also contain sulforhodamine B dye to monitor membrane permeation during the tension application. Control experiments should also be performed with photoswitchable GUVs in the absence of MscL to confirm vesicles do not permeate in the absence of MscL. To check the reverse gating of MscL from GUV interior to exterior, MscL reconstituted GUVs grown in sulforhodamine-containing solution could also be loaded in microfluidic channels and flushed with sulforhodamine-free, hypotonic solution. The rinsing step will cause the GUV exterior solution to appear dark under a confocal microscope while the solution in the GUV interior preserves the red fluorescence. During this process, GUVs will also be subjected to UV illumination to retain the *cis* conformation of azo-PC. The MscL channel should then open upon exposure to the blue light. The exchange of solutions between the GUV interior and exterior should result in the loss of the strong fluorescence signal in the GUV interior due to sulforhodamine permeation. Additionally, the kinetics of the permeation of sulforhodamine dye across the membrane could be investigated as an indirect method to correlate with the kinetics of the MscL channel opening. This approach would enable us to identify the effects of the duration and intensity of applied illumination conditions on the gating activity of MscL. If all these planned experiments lead to a successful gating of MscL, this new biomimetic tool could be further tested for potential applications in photopharmacology to manipulate the mechanosensitive ion channels for the transport of small drugs into cells via light.

6 General discussion and future directions

My doctoral project has aimed to establish a well-characterized photoswitchable biomimetic platform using GUVs to modulate the morphology and mechanical/electrical properties of the membrane via light, and in addition to regulate the transport of molecules in/out of the designed light-triggered bio-system. In order to provide an optical control of the biomimetic system, the GUV membrane contained azo-PC, a commercially available synthetic analog of one of the most abundant phospholipids in animal cells (Barbour et al., 1999). Being a photo-responsive molecule that undergoes reversible isomerization under UV and blue light, azo-PC reconstituted in the lipid membrane imparted light-responsive properties to the vesicle membrane. Modification of the material properties of photoswitchable GUVs under the exposure to UV or blue irradiation also induced changes in the lipid-protein interactions and enabled the reversible engulfment of glycinin condensates by azo-PC GUVs. Similarly, reconstitution of MscL into these photoswitchable GUV systems led to light-induced gating of the ion channels and permeation of sulforhodamine into the GUV interior. Both of these successful results obtained from the studies with azo-PC containing photoswitchable biomimetic platforms provide a promising background to develop them further as smart biomaterials in cell-repair mechanisms (Morstein et al., 2021; Mukhopadhyay et al., 2022). This section of the thesis summarizes the key findings of each part, compares them with the previous and recent studies in membrane biochemistry, highlights the contributions of this thesis to the existing research, suggests further aspects to investigate, discusses current limitations in the research area, and proposes potential strategies to overcome the limitations.

6.1 Comparison of our results on characterizing *trans* and *cis* azo-PC vesicles with recently published studies

Our research with various fractions of azo-PC containing membranes illustrated that light can effectively induce reversible changes in membrane properties and morphology with a fast response time (in the range of a few milliseconds), highlighting the potential for designing a photoswitchable biomimetic system with azo-PC photoisomerization to precisely regulate membrane properties for further applications in biotechnology (Aleksanyan et al., 2023b). Although the light-controlled deformations of azo-PC vesicles were first reported by Pernpeintner et al. (Pernpeintner et al., 2017), our meticulous studies exploring membranes containing various fractions of azo-PC and employing a comprehensive set of experimental and computational methods. Our results revealed that the previously reported characterization techniques did not accurately report several aspects. Specifically, the maximum extent of light-induced membrane area changes was previously underestimated and the mechanical properties of azo-PC-doped membranes were inaccurately estimated. Our

electrodeformation experiments on giant vesicles combined with MD simulations demonstrated that the *trans*-to-*cis* isomerization of the azo-PC membrane resulted in a larger area increase on the membrane compared to the values reported by Pernpeintner et al. (Pernpeintner et al., 2017). The latter were collected on LUVs using indirect measurements with dynamic light scattering. Similarly, the same research group reported very conflicting bending rigidity values for *cis* and *trans* azo-PC giant vesicles using optical tweezers in one study (Pernpeintner et al., 2017) (which resulted in values 131 k_BT for *cis* azo-PC GUVs and 2433 k_BT for *trans* azo-PC GUVs) and micropipette aspiration in another study from the same group (Urban et al., 2018) (which resulted in values 1.6 k_BT for *cis* azo-PC GUVs and 7.5 k_BT for *trans* azo-PC GUVs). Both micropipette aspiration and optical tweezers techniques are challenging and require caution (Dimova, 2014; Aleksanyan et al., 2023a). Laser intensity fluctuations, detector noise and the trap stiffness (force per unit displacement) should be carefully calibrated in order to the minimize the possible errors (Elisa Parra-Ortiz, 2019; Gheorghe Cojoc, 2019). For the micropipette aspiration method, the aspiration pressure, suction force and micropipette dimensions (inner diameter of the micropipette and its shape) should also be calibrated to obtain uniform deformation of the vesicles (Elisa Parra-Ortiz, 2019). Since micropipettes are made up of glass material and glass can reflect roughly ~ 60% of the UV light (Serrano and Moreno, 2020), the intensity of the UV light reaching the vesicle portion aspirated in the capillary may be lower than the actual applied intensity, resulting in less effective *trans*-to-*cis* photoisomerization of azo-PC in the membrane thus reducing the extent of membrane expansion and resulting in misleading measurements of the membrane bending rigidity. Additionally, the optical tweezers experiments assume a simple spherical geometry to derive the membrane bending rigidity (Gheorghe Cojoc, 2019). However, the photoisomerization of azo-PC can result in membrane shape transformations, such as the formation of small buds and tubes which are difficult to detect optically, especially with transmitted light or epifluorescence as used in the above studies. If these buds and tubes are not adsorbed back by the vesicle during the measurement time, any irregular shapes can lead to misleading results with these techniques.

To address the above difficulties, in my studies I employed fluctuation spectroscopy on giant vesicles to deduce the light-induced changes in the membrane bending rigidity. This method has been well established and employed for different membrane compositions (Dimova, 2014; Aleksanyan et al., 2023a). With fluctuation spectroscopy, we detected a 10-fold softening of the membrane under *trans*-to-*cis* photoisomerization of azo-PC. As recently reported by Manafirad et al. (Manafirad et al., 2023), it is also important to note here that the power intensity of the applied illumination conditions also plays a significant role in the observed degree of deformations and modifications in the material properties of the membrane.

Our research also represents the first comprehensive investigation of the electrochemical response of azo-PC membranes. For the first time we were able to deduce and reported the specific membrane capacitance and dielectric constant values for azo-PC vesicles. For this we employing a vesicle electrodeformation approach where at constant field strength we varied the field frequency (Salipante et al., 2012; Vitkova et al., 2018; Aleksanyan et al., 2023a). With this technique, one determines the frequency at which the vesicles undergo prolate-to-oblate transition. We found that membranes doped with azo-PC in the *trans* state have an increased ability to store electrical charges. The high electrical charge storage capacity of the *trans* azo-PC membrane is of particular interest for biomedical applications, since biomaterials with high electrical charge storage capacity are known to be used in the design of biosensors, smart drug delivery systems, and in tissue engineering for electrical stimulation of neurons to promote nerve regeneration and functional recovery (Olvera and Monaghan, 2021; Pinto et al., 2022). Recently, Basetto Jr et al. (Bassetto et al., 2024) also highlighted the importance of light-induced changes in membrane capacitance on the activation of ion channels in cells. By increasing the membrane capacitance of cells upon incubation with a photolipid and exposing them to UV illumination, the authors were able to depolarize optocapacitive currents leading to the opening of the voltage-gated sodium channels in the cells.

All the above mentioned-biophysical characterization techniques to understand and quantitatively characterize light-triggered changes in the morphology and membrane properties of azo-PC doped vesicles are straightforward and practical to employ in any moderately equipped laboratory. They also allow gaining insights into the membrane properties of newly designed biomimetic systems. One example for a work I have contributed to includes dendrimersomes, the mechanical properties of which were characterized in a collaboration with the lab of Cesar Rodriguez-Emmenegger (Joseph et al., 2022). Furthermore, Erkan-Candag and coworkers (Erkan-Candag et al., 2022) collaborated with us to implement the vesicle electrodeformation technique to understand the photoactivation and thermal relaxation kinetics of azobenzene containing photoswitchable diacylglycerol analogs. Results on GUVs doped with these molecules were compared to patch clamp data of HEK293 cells to understand the behavior of a membrane channel in the presence of photoswitches. The obtained light-triggered morphological changes of GUVs containing photolipids under the influence of UV and blue light corresponded well with the light induced channel activation/deactivation recordings in the HEK293 cells. However, the response of one of the photoswitchable diacylglycerol derivatives containing azobenzene molecules in both of the acyl chains, which is named as OptoDArG, showed a different thermal relaxation kinetics in the lipid bilayer and cells when UV light was switched off and the sample was left in the dark. The *cis* isomer of OptoDArG in the GUV bilayer (the rest of the bilayer was composed of POPC lipid) remained stable in

the dark while it showed a faster thermal relaxation in HEK293 cells as assessed with patch clamp experiments. Erkan-Candag and coworkers related these two distinct results to the interaction of OptoDArG with the short transient receptor potential channel 3 (TRPC3) protein in HEK293 cells (Erkan-Candag et al., 2022).

6.2 Effects of azo-PC photoisomerization on the interaction between vesicles and protein condensates

In the second part of my thesis, we investigated how exposure of azo-PC doped vesicles to UV and blue irradiation can modify the lipid-protein interactions between protein condensates and induce a partial or complete engulfment of protein condensates in azo-PC vesicles; the results were reported in an article where I share first-author contributions (Mangiarotti et al., 2024). The effect of light and photoswitchable lipids on manipulating lipid-protein interactions has been previously compared by Socrier et al. (Socrier and Steinem, 2023), and the effects of photoswitching on the domain rearrangement and protein organization in various membrane models containing photolipids were extensively reviewed. Pfefferman et al. (Pfeffermann et al., 2021) showed that light-triggered changes in the physicochemical properties of photoswitchable planar lipid bilayers can affect the channel activity of a transmembrane peptide, gramicidin A. However, to the best of our knowledge, our studies provide for the first time in the literature photomanipulated interactions between membranes and protein-rich condensates and the photoswitchable endocytosis of condensates into vesicles. Protein condensates in cells are dynamic, phase separated, membraneless organelles controlling cellular processes, including gene regulation, signaling, and stress response thus studying them is quite important for understanding cellular organization (Qian et al., 2022; Harrington et al., 2024). In our work, we investigated *in* vitro reconstituted condensates of the glycinin which is a plant storage protein promoting vacuole membrane remodelling. By exposing azo-PC GUVs to the UV irradiation, vesicles increased the membrane area and promoted a rapid endocytosis of condensates, while blue illumination was shown to reverse the process. The degree of engulfment, i.e. whether it is partial or complete engulfment, was found to depend on the relative sizes of the interacting condensate and vesicle. Our results show that *trans*-to-*cis* photoisomerization of azo-PC not only induces excess membrane area in the GUVs, but also increases the membrane affinity for the protein condensates. However, the light-induced excess area does not only accumulate at the membrane-condensate interface, but is also stored in the membrane nanotubes. By combining our experimental results from vesicle electrodeformation and optical microscopy with theoretical estimates comparing the bending and adhesion energy contributions, we found out that utilizing the light-induced excess area at the vesicle-condensate adhesion interface is energetically more favorable than the energy gain to fold the

membrane into invaginations and tubes. Overall, our findings display azo-PC vesicles as a photomanipulated, versatile platform allowing control over vesicle-condensate interactions with the potential to regulate cellular events and design light-responsive biomimetic drug delivery systems. The detailed examination of the light-induced modulation of more complex biosystems offer a foundation for future research aimed at developing innovative therapeutic strategies and further bioengineering applications.

6.3 Activation of the MscL channel in GUVs via azo-PC photoisomerization

In the third part of my thesis, we tested the possibility of modulating the membrane properties and tension with photoswitchable lipids to control the activity of the mechanosensitive ion channel, MscL. Since GUVs are minimalist model membranes, their membrane tension is simply related to the area-to-volume ratio of the vesicles (Lipowsky, 2019). We hypothesized that by increasing/decreasing the membrane area of the vesicles through the photoisomerization of azo-PC under UV/blue light, we could modify the membrane tension thus gating MscL. In order to change the area-to-volume ratio of lipid vesicles, various external stimuli such as temperature gradients (Käs and Sackmann, 1991; Döbereiner et al., 1993), osmotic pressure (Yanagisawa et al., 2008; Oglecka et al., 2012), electric fields (Dimova et al., 2007; Peterlin, 2010; Aleksanyan et al., 2023a) or pH modifications (Khalifat et al., 2008) have been used throughout the literature. Assessing the membrane tension of vesicles in the presence of the above-mentioned external stimuli remains challenging, a limited number of methods are available in the literature. Among others, the micropipette aspiration method is one of the most accurate techniques to determine the membrane tension when it is performed carefully (Elisa Parra-Ortiz, 2019). Recently, Shendrik et al. (Shendrik et al., 2023) combined micropipette aspiration of GUVs with optically trapped membrane-coated beads to modify membrane tension and control the membrane fusion processes. In our studies, by introducing photoswitchable lipid components, we provided a practical, optical platform of changing membrane tension of GUVs via UV and blue light. The reconstitution process of MscL into vesicles was mediated by the addition of 0.00125% w/v DDM surfactant to the GUV media. Successful MscL reconstitution was confirmed through the observation of a strong signal of the labelled MscL under the confocal microscopy 10 minutes after incubation of 150 nM and higher concentrations of labelled MscL in the GUV external medium. After the incorporation of MscL into the GUV membrane, the majority of the GUV population preserved the dark contrast inside the GUVs, indicating non-permeation by a water-soluble probe (sulforhodamine). Thus, the majority of the vesicles remained with intact membrane after the reconstitution process. However, in comparison to native like Hist-MscL reconstituted GUVs, MACH-MscL incorporated vesicles (used only to label MscL and monitor MscL reconstitution via optical microscopy) were prone

to more defects. Lastly, the exposure of the MscL-reconstituted GUVs to UV and blue light showed light-driven permeation of the sulforhodamine molecules into the GUV interior media and thus allowed monitoring of the light-triggered gating activity of MscL. Although future studies are necessary to more comprehensively characterize the reconstitution of MscL and its light-triggered gating activity in GUVs, our preliminary studies illustrated that reconstitution of MscL in GUVs and light-triggered opening of the channel are feasible. Thus, MscL can be photoactivated under the influence of UV and blue irradiation in the presence of azo-PC lipids in the vesicles.

6.4 Future applications of azo-PC photoisomerization in light-triggered cell-like systems and bioprocesses

The integration of light-responsive azo-PC lipid into the design of synthetic cell-like vesicles was presented here as a novel approach to dynamically modulate the behavior and properties of vesicles via light. All of the above-mentioned projects involving azo-PC-containing biomembranes clearly demonstrate that leveraging azo-PC photoswitches in cell-like simplistic vesicles, and exposing them to UV and blue light, can precisely modify the morphology, material and electrical properties of these vesicles as well as their interactions with other biomacromolecules. Thus, our approaches provide effective control over the transport of substances in and out of the vesicles. Our studies reveal promising results for broader implications of light and photolipid containing cell-like simplified biomembrane models in biotechnology to further design highly responsive and adaptable bio-inspired materials in synthetic biology to address membrane defects in cellular processes and induce cell-repair. In particular, our results demonstrate a significant application potential of light in drug delivery systems, where the ability of light to reversibly modulate membrane permeability and vesicle morphology can enhance targeted delivery and release mechanisms (Morstein et al., 2021). The potential to harness light as a non-invasive, reversible, and precise control mechanism opens up exciting possibilities for future research in biotechnology, including the development of synthetic cells that can interact with natural biological systems in various ways such as in the modulation of neurons (Xiong et al., 2023) or in the design of light-triggered wearable biosensors for healthcare monitoring (Mukhopadhyay et al., 2022). In the context of synthetic biology, our findings can contribute to the development of a light-triggered, bio-inspired, versatile toolkit for engineering life-like systems that can perform specific functions in medical and industrial applications to treat disease-related cellular damage and dysfunction. In addition, the knowledge gained from our studies on the membrane mechanics and electrochemical properties of azo-PC containing vesicles promotes the development of next-generation of light-responsive smart biomaterials that can also mimic complex biological functions more closely to provide a better understanding about cellular mechanisms.

6.5 From photoswitchable membrane models to photoswitchable cells

In order to further develop medical and industrial applications of these light-triggered minimalistic synthetic cells and membranes, more comprehensive research with more complex biomembrane models, cells and tissues is needed to bridge the gap between in vitro studies and in vivo applications. In this respect, a preprint by Jiménez-Rojo and coworkers (Jiménez-Rojo et al., 2022) shows recently initiated more complex studies by exogenously introducing a synthetic fatty acid with an azobenzene photoswitch into various adherent and suspension cell lines. They named this photoswitch as FAAzo4 and monitored the effects of FAAzo4 incorporation and photoisomerization on cell properties and cellular processes. The investigated cell lines are listed as H358, HEK293T, MDA-MB-231, HCT116, K562, MCF7, MV-4-11, RS4;11, U2OS and HeLa cells. Loading of these cells with FAAzo4 led to the generation of the various chain lengths of photoswitchable azobenzene phosphatidylcholine analogs (v-azo-PC) in the cells. The amount of FAAzo4 metabolization and v-azo-PC generation showed a variance depending on the cell type but v-azo-PC lipids were found to be mainly located in the membrane of the endoplasmic reticulum (ER) of the cells. They found out that the photoisomerization of v-azo-PC affects the membrane fluidity of the ER and regulates the protein export mechanisms from the ER. This novel optical approach of metabolizing FAAzo4 into the ER membrane of cells as v-azo-PC to manipulate the membrane fluidity of the ER and control protein secretion processes in cells through v-azo-PC photoisomerization represents a unique application of these photoswitchable azo-benzene lipid analogs in cell biology (Jiménez-Rojo et al., 2022). This study provides evidence for the efficiency of light as a non-invasive input signal to provide a high spatiotemporal control over the protein secretion processes in the ER, but it does not indicate the effect of metabolized FAAzo4 on the function and membrane properties of other organelles of each cell.

Cells as the fundamental subunit of life (Szostak et al., 2001) are very dynamic and complex entities to thoroughly capture the effects of the incorporated photoswitch. They constantly interact with their environment, neighboring cells, and the extracellular matrix. These interactions involve signaling pathways, molecular cascades, and feedback loops, making the study of cellular behavior intricate (Ji, 2012; Bertolaso, 2022). In their dynamic nature, they can grow, divide, differentiate, respond and easily adapt to various stimuli. Within a single cell, a variety of organelles as subcellular compartments and an array of proteins, lipids, nucleic acids and metabolites perform specialized functions. Understanding their interactions with each other or individual roles and responses in the presence of any stimuli during the cellular events remains challenging in this dynamic organization of cells (Szostak et al., 2001; Bertolaso, 2022). In this respect, giant plasma membrane vesicles (GPMVs) or blebs can be implemented in future studies to simplify the complexity of cells while serving as an

intermediate membrane model between cells and GUVs to mimic the biological processes (Chan and Boxer, 2007; Levental and Levental, 2015; Li et al., 2023).

By integrating azo-PC photoswitches into GPMVs, future studies will bring more insights into the optical manipulation of biological processes and complement up-to-date data *in vitro* before empowering further *in vivo* applications. GPMVs are micron-sized, cell-derived vesicles that preserve the plasma membrane content of the parent cell, including both lipids and proteins (Baumgart et al., 2007; Levental and Levental, 2015). Their lipid composition is nearly identical to that of the parent cell, while membrane proteins in GPMVs also retain the correct orientation in the parent cell (Bauer et al., 2009; Chen et al., 2010; Sezgin et al., 2012; Levental and Levental, 2015; Zhao et al., 2016). They are devoid of cellular organelles and energy-mediated pathways of the cell (Levental and Levental, 2015; Levental and Veatch, 2016) but are filled with cytoplasm (Levental and Levental, 2015). When GPMVs are fluorescently labeled, their dye partitioning can reveal phase heterogeneity of the membrane at sub-physiological temperatures (below the miscibility transition temperature) (Baumgart et al., 2007). With all these additional features, GPMVs provide a more realistic representation of the cellular membrane in cell biomimetics in comparison to GUVs (Chan and Boxer, 2007; Levental and Levental, 2015; Li et al., 2023) and can provide further insights into optical manipulation of biological processes via azo-PC photoswitches.

6.6 Current limitations of using azo-PC photoswitches in cell studies and potential strategies to overcome them

While transferring our *in vitro* studies towards *in vivo*, exposure of cells and tissues to UV light may also be a challenge for biotechnology applications in the future. The usage of UV illumination for the photoswitching of *trans*-to-*cis* azo-PC confines the applications of these molecules and corresponding materials in medical treatment practices because UV light poorly penetrates into cells and tissues (Cheong et al., 1990; D'Orazio et al., 2013). Additionally, the intensity of the applied UV light on the cells and tissues should be comprehensively examined in terms of cell and tissue viability because it may even be a phototoxic to cells in a dose-dependent manner (Cheong et al., 1990; Banerjee et al., 2005). In this respect, coupling bioelectronic devices into our optical manipulation approach with azo-PC containing bio-inspired materials may offer additional advantages and enable more precise control over the biological processes. Designing implantable biosensors from azo-PC containing hybrid materials and integrating these optically modified hybrid materials into personalized bioelectronic devices can enhance the spatiotemporal resolution and signal acquisition efficiency of our studies for broader applications in the future. Another strategy to overcome the challenges of exposing cells and tissues to UV irradiation can be to involve red-shifted photolipids in the medical applications of our

studies. A recently developed tetra-ortho-chloro azobenzene-substituted phosphatidylcholine (red-azo-PC) (Pritzl et al., 2022) can undergo a *trans*-to-*cis* photoconversion in red light (≥ 630 nm), which can penetrate into cells and tissues (Stolik et al., 2000). Photoisomerization of red-azo-PC is also found to modify the fluidity and stiffness of the photolipid membranes similarly as it is reported in our studies for azo-PC membrane models (Pritzl et al., 2022). Thus, in order to overcome the limitations of azo-PC biosystems in biotechnology applications, a red-azo-PC substitute can also be further developed and employed in future studies.

In addition, the integration of azo-PC-containing bioinspired materials into cells and tissues and their irradiation with various light intensities and wavelengths also require further investigation with respect to cytotoxicity and long-term adverse effects *in vivo*. The long-term stability, biocompatibility and potential adverse effects of azo-PC containing materials on cells and tissues should be carefully evaluated in future studies in medical research and photopharmacology. Preclinical data on the safety and efficacy of the targeted drug provide the basis for clinical trials (Collins et al., 1990; Kimmelman and Henderson, 2016). The development of azo-PC containing biomaterials for biotechnology applications should follow the specific guidelines for clinical trials and comply with the health and safety requirements of the relevant national and international regulatory agencies (such as the Federal Institute for Drugs and Medical Devices in Germany and the European Medicines Agency for the drug administrations in Europe) to ensure the validity of the new material in clinical research (Sekar et al., 2021). During clinical trials, the pharmacokinetics, pharmacodynamics and dose-response relationship of the emerging material should be carefully evaluated and all the data and long-term effects should be meticulously monitored and reported by including studies with diverse patient groups (such as pediatric, elderly) (Tonkens, 2005). Inclusion/exclusion criteria for the studied population and demographic details should be transparently defined and the dosing of the applied drug candidate should be clearly described during the clinical studies (Tonkens, 2005). The production of the approved azo-PC containing biomaterial for biotechnology applications should follow the regulations of 'Good Manufacturing Practices' (World-Health-Organization(WHO), 2007) addressing product segregation, label reconciliation, confirmatory testing, and quality control requirements to ensure enhanced productivity, profitability, and risk mitigation.

In conclusion, our studies on photoswitchable GUVs through azo-PC photoisomerization demonstrate that these light-triggered biomimetic platforms enable precise control of cellular processes and molecular interactions. They show promising potential for broadening future studies and exploring their biotechnology applications. Once the current limitations of azo-PC photoisomerization in cells are overcome, this technology could significantly enhance targeted drug delivery, biosensing, and the development of dynamic, light-responsive biomaterials.

References

Chapters 3 to 4 each have their own list of references from the presented manuscripts. References listed here are for the rest of the thesis, namely, from Chapters 1, 5 and 6.

Agliarulo I, Parashuraman S (2022) Golgi Apparatus Regulates Plasma Membrane Composition and Function. Cells 11.

Akbarzadeh A, Rezaei-Sadabady R, Davaran S, Joo SW, Zarghami N, Hanifehpour Y, Samiei M, Kouhi M, Nejati-Koshki K (2013) Liposome: classification, preparation, and applications. Nanoscale Res Lett 8:102.

Albers RW, Siegel GJ, Xie Z-J (2012) Membrane transport. In: Basic neurochemistry, pp 40-62: Elsevier.

Alberts B, Johnson A, Lewis J, Morgan D, Raff MC, Roberts K, Walter P, Wilson JH, Hunt T, Alberts B (2015) Molecular biology of the cell / Bruce Alberts, Alexander Johnson, Julian Lewis, David Morgan, Martin Raff, Keith Roberts, Peter Walter ; with problems by John Wilson, Tim Hunt, Sixth edition. Edition. New York, NY: Garland Science, Taylor and Francis Group.

Alberts B JA, Lewis J, et al. (2002) Molecular Biology of the Cell, 4th Edition Edition. New York: Garland: Science.

Aleksanyan M, Faizi HA, Kirmpaki MA, Vlahovska PM, Riske KA, Dimova R (2023a) Assessing membrane material properties from the response of giant unilamellar vesicles to electric fields. Adv Phys X 8.

Aleksanyan M, Grafmüller A, Crea F, Georgiev VN, Yandrapalli N, Block S, Heberle J, Dimova R (2023b) Photomanipulation of Minimal Synthetic Cells: Area Increase, Softening, and Interleaflet Coupling of Membrane Models Doped with Azobenzene-Lipid Photoswitches. Adv Sci (Weinh) 10:e2304336.

Alexiev U, Marti T, Heyn MP, Khorana HG, Scherrer P (1994) Surface charge of bacteriorhodopsin detected with covalently bound pH indicators at selected extracellular and cytoplasmic sites. Biochemistry 33:298-306.

Allison SD, Chang B, Randolph TW, Carpenter JF (1999) Hydrogen bonding between sugar and protein is responsible for inhibition of dehydration-induced protein unfolding. Arch Biochem Biophys 365:289-298.

Alvarez Y, Smutny M (2022) Emerging Role of Mechanical Forces in Cell Fate Acquisition. Frontiers in Cell and Developmental Biology 10.

Andersen OS, Koeppe RE, 2nd (2007) Bilayer thickness and membrane protein function: an energetic perspective. Annu Rev Biophys Biomol Struct 36:107-130.

Arakawa T, Timasheff SN (1982) Stabilization of protein structure by sugars. Biochemistry 21:6536-6544.

Aranda S, Riske KA, Lipowsky R, Dimova R (2008) Morphological transitions of vesicles induced by alternating electric fields. Biophys J 95:L19-21.

Bagatolli LA (2019) Application of optical microscopy techniques on giant unilamellar vesicles. In: The Giant Vesicle Book, 1st Edition (Dimova R, Marques C, eds). Boca Raton: Taylor & Francis Group, LLC.

Bagatolli LA, Needham D (2014) Quantitative optical microscopy and micromanipulation studies on the lipid bilayer membranes of giant unilamellar vesicles. Chemistry and Physics of Lipids 181:99-120.

Balleza D (2012) Mechanical properties of lipid bilayers and regulation of mechanosensitive function: from biological to biomimetic channels. Channels (Austin) 6:220-233.

Balleza D, Gómez-Lagunas F (2009) Conserved motifs in mechanosensitive channels MscL and MscS. European Biophysics Journal 38:1013-1027.

Banani SF, Lee HO, Hyman AA, Rosen MK (2017) Biomolecular condensates: organizers of cellular biochemistry. Nature Reviews Molecular Cell Biology 18:285-298.

Banerjee G, Gupta N, Kapoor A, Raman G (2005) UV induced bystander signaling leading to apoptosis. Cancer Letters 223:275-284.
Barbour SE, Kapur A, Deal CL (1999) Regulation of phosphatidylcholine homeostasis by calcium-independent phospholipase A2. Biochim Biophys Acta 1439:77-88.
Bassetto CAZ, Pfeffermann J, Yadav R, Strassgschwandtner S, Glasnov T, Bezanilla F, Pohl P (2024) Photolipid excitation triggers depolarizing optocapacitive currents and action potentials. Nature Communications 15:1139.
Battle AR, Petrov E, Pal P, Martinac B (2009) Rapid and improved reconstitution of bacterial mechanosensitive ion channel proteins MscS and MscL into liposomes using a modified sucrose method. FEBS Lett 583:407-412.
Bauer B, Davidson M, Orwar O (2009) Proteomic analysis of plasma membrane vesicles. Angew Chem Int Ed Engl 48:1656-1659.
Baumgart T, Hammond AT, Sengupta P, Hess ST, Holowka DA, Baird BA, Webb WW (2007) Large-scale fluid/fluid phase separation of proteins and lipids in giant plasma membrane vesicles. Proceedings of the National Academy of Sciences 104:3165-3170.
Bechinger B (2019) Supported Lipid Bilayers. In: Encyclopedia of Biophysics (Roberts G, Watts A, eds), pp 1-8. Berlin, Heidelberg: Springer Berlin Heidelberg.
Beharry AA, Woolley GA (2011) Azobenzene photoswitches for biomolecules. Chemical Society Reviews 40:4422-4437.
Berland KM, So PT, Chen Y, Mantulin WW, Gratton E (1996) Scanning two-photon fluctuation correlation spectroscopy: particle counting measurements for detection of molecular aggregation. Biophys J 71:410-420.
Bertolaso M (2022) Understanding Complexity in Life Sciences. In: Environmental Alteration Leads to Human Disease : A Planetary Health Approach (Ingegnoli V, Lombardo F, La Torre G, eds), pp 1-13. Cham: Springer International Publishing.
Bikle D, Adams J, Christakos S (2018) Vitamin D: Production, Metabolism, Action, and Clinical Requirements. In, pp 230-240.
Billman GE (2020) Homeostasis: The Underappreciated and Far Too Often Ignored Central Organizing Principle of Physiology. Frontiers in Physiology 11.
Boelke J, Hecht S (2019) Designing Molecular Photoswitches for Soft Materials Applications. Advanced Optical Materials 7:1900404.
Booth Ian R, Blount P (2012) The MscS and MscL Families of Mechanosensitive Channels Act as Microbial Emergency Release Valves. Journal of Bacteriology 194:4802-4809.
Brémaud E, Favard C, Muriaux D (2022) Deciphering the Assembly of Enveloped Viruses Using Model Lipid Membranes. Membranes (Basel) 12.
Breton M, Amirkavei M, Mir LM (2015) Optimization of the Electroformation of Giant Unilamellar Vesicles (GUVs) with Unsaturated Phospholipids. J Membr Biol 248:827-835.
Brezesinski G, Möhwald H (2003) Langmuir monolayers to study interactions at model membrane surfaces. Advances in Colloid and Interface Science 100-102:563-584.
Casares D, Escribá PV, Rosselló CA (2019) Membrane Lipid Composition: Effect on Membrane and Organelle Structure, Function and Compartmentalization and Therapeutic Avenues. Int J Mol Sci 20.
Castellana ET, Cremer PS (2006) Solid supported lipid bilayers: From biophysical studies to sensor design. Surf Sci Rep 61:429-444.
Chamberlain AK, Lee Y, Kim S, Bowie JU (2004) Snorkeling Preferences Foster an Amino Acid Composition Bias in Transmembrane Helices. Journal of Molecular Biology 339:471-479.
Chan YH, Boxer SG (2007) Model membrane systems and their applications. Curr Opin Chem Biol 11:581-587.
Chen L, Novicky L, Merzlyakov M, Hristov T, Hristova K (2010) Measuring the Energetics of Membrane Protein Dimerization in Mammalian Membranes. Journal of the American Chemical Society 132:3628-3635.

Cheong WF, Prahl SA, Welch AJ (1990) A review of the optical properties of biological tissues. IEEE Journal of Quantum Electronics 26:2166-2185.
Cheppali SK, Dharan R, Sorkin R (2022) Forces of Change: Optical Tweezers in Membrane Remodeling Studies. The Journal of Membrane Biology 255:677-690.
Christie JM (2007) Phototropin blue-light receptors. Annu Rev Plant Biol 58:21-45.
Collins JM, Grieshaber CK, Chabner BA (1990) Pharmacologically Guided Phase I Clinical Trials Based Upon Preclinical Drug Development. JNCI: Journal of the National Cancer Institute 82:1321-1326.
Cooper GM, Adams K (2022) The cell: a molecular approach: Oxford University Press.
Corry B, Martinac B (2008) Bacterial mechanosensitive channels: Experiment and theory. Biochimica et Biophysica Acta (BBA) - Biomembranes 1778:1859-1870.
Corry B, Hurst AC, Pal P, Nomura T, Rigby P, Martinac B (2010) An improved open-channel structure of MscL determined from FRET confocal microscopy and simulation. J Gen Physiol 136:483-494.
Crea F, Vorkas A, Redlich A, Cruz R, Shi C, Trauner D, Lange A, Schlesinger R, Heberle J (2022) Photoactivation of a Mechanosensitive Channel. Frontiers in Molecular Biosciences 9.
Cruickshank CC, Minchin RF, Le Dain AC, Martinac B (1997) Estimation of the pore size of the large-conductance mechanosensitive ion channel of Escherichia coli. Biophys J 73:1925-1931.
D'Orazio J, Jarrett S, Amaro-Ortiz A, Scott T (2013) UV radiation and the skin. Int J Mol Sci 14:12222-12248.
Dahm R, van Marle J, Quinlan RA, Prescott AR, Vrensen GF (2011) Homeostasis in the vertebrate lens: mechanisms of solute exchange. Philos Trans R Soc Lond B Biol Sci 366:1265-1277.
Dao TPT, Fauquignon M, Fernandes F, Ibarboure E, Vax A, Prieto M, Le Meins JF (2017) Membrane properties of giant polymer and lipid vesicles obtained by electroformation and pva gel-assisted hydration methods. Colloids and Surfaces A: Physicochemical and Engineering Aspects 533:347-353.
Deng Y, Long G, Zhang Y, Zhao W, Zhou G, Feringa BL, Chen J (2024) Photo-responsive functional materials based on light-driven molecular motors. Light: Science & Applications 13:63.
Dezi M, Di Cicco A, Bassereau P, Lévy D (2013) Detergent-mediated incorporation of transmembrane proteins in giant unilamellar vesicles with controlled physiological contents. Proceedings of the National Academy of Sciences 110:7276-7281.
Dias AR, Minas Da Piedade ME, Martinho Simões JA, Simoni JA, Teixeira C, Diogo HP, Meng-Yan Y, Pilcher G (1992) Enthalpies of formation of cis-azobenzene and trans-azobenzene. The Journal of Chemical Thermodynamics 24:439-447.
Dias C, Nylandsted J (2021) Plasma membrane integrity in health and disease: significance and therapeutic potential. Cell Discov 7:4.
Dimova R (2014) Recent developments in the field of bending rigidity measurements on membranes. Advances in Colloid and Interface Science 208:225-234.
Dimova R (2019) Giant Vesicles and Their Use in Assays for Assessing Membrane Phase State, Curvature, Mechanics, and Electrical Properties. Annu Rev Biophys 48:93-119.
Dimova R, Riske KA, Aranda S, Bezlyepkina N, Knorr RL, Lipowsky R (2007) Giant vesicles in electric fields. Soft Matter 3:817-827.
Dimova R, Bezlyepkina N, Jordö MD, Knorr RL, Riske KA, Staykova M, Vlahovska PM, Yamamoto T, Yang P, Lipowsky R (2009) Vesicles in electric fields: Some novel aspects of membrane behavior. Soft Matter 5:3201-3212.
Diogo MLG, Campos TM, Fonseca ESR, Pavani C, Horliana A, Fernandes KPS, Bussadori SK, Fantin F, Leite DPV, Yamamoto Â TA, Navarro RS, Motta LJ (2021) Effect of Blue Light on Acne Vulgaris: A Systematic Review. Sensors (Basel) 21.
Döbereiner HG, Käs J, Noppl D, Sprenger I, Sackmann E (1993) Budding and fission of vesicles. Biophysical Journal 65:1396-1403.

Dube H, Aprahamian I, Tamaoki N (2019) Photoresponsive Molecular Switches and Machines. ChemPhotoChem 3:266-267.
Dworakowska B, Dołowy K (2000) Ion channels-related diseases. Acta Biochim Pol 47:685-703.
Edidin M (2003) Lipids on the frontier: a century of cell-membrane bilayers. Nature Reviews Molecular Cell Biology 4:414-418.
Elani Y, Trantidou T, Wylie D, Dekker L, Polizzi K, Law RV, Ces O (2018) Constructing vesicle-based artificial cells with embedded living cells as organelle-like modules. Scientific Reports 8:4564.
Elisa Parra-Ortiz DN (2019) Mechanic assays of synthetic lipid membranes based on micropipette aspiration In: The Giant Vesicle Book. Boca Raton: Taylor & Francis Group, LLC.
Elmets CA et al. (2019) Joint American Academy of Dermatology-National Psoriasis Foundation guidelines of care for the management and treatment of psoriasis with phototherapy. J Am Acad Dermatol 81:775-804.
Erkan-Candag H, Krivic D, Gsell MAF, Aleksanyan M, Stockner T, Dimova R, Tiapko O, Groschner K (2022) Characterization of DAG Binding to TRPC Channels by Target-Dependent cis-trans Isomerization of OptoDArG. Biomolecules 12.
Ernits M, Reinsalu O, Yandrapalli N, Kopanchuk S, Moradpur-Tari E, Sanka I, Scheler O, Rinken A, Kurg R, Kyritsakis A, Linko V, Zadin V (2024) Microfluidic production, stability and loading of synthetic giant unilamellar vesicles. Scientific Reports 14:14071.
Eyckmans J, Boudou T, Yu X, Chen CS (2011) A hitchhiker's guide to mechanobiology. Dev Cell 21:35-47.
Faizi HA, Reeves CJ, Georgiev VN, Vlahovska PM, Dimova R (2020) Fluctuation spectroscopy of giant unilamellar vesicles using confocal and phase contrast microscopy. Soft Matter 16:8996-9001.
Falcone S, Cocucci E, Podini P, Kirchhausen T, Clementi E, Meldolesi J (2006) Macropinocytosis: regulated coordination of endocytic and exocytic membrane traffic events. Journal of Cell Science 119:4758-4769.
Ford J (2013) Red blood cell morphology. Int J Lab Hematol 35:351-357.
Frank JA, Franquelim HG, Schwille P, Trauner D (2016) Optical Control of Lipid Rafts with Photoswitchable Ceramides. Journal of the American Chemical Society 138:12981-12986.
Galluzzi L, Yamazaki T, Kroemer G (2018) Linking cellular stress responses to systemic homeostasis. Nat Rev Mol Cell Biol 19:731-745.
Gasteiger E, Hoogland C, Gattiker A, Duvaud Se, Wilkins MR, Appel RD, Bairoch A (2005) Protein Identification and Analysis Tools on the ExPASy Server. In: The Proteomics Protocols Handbook (Walker JM, ed), pp 571-607. Totowa, NJ: Humana Press.
Gheorghe Cojoc AG, Ulysse Delabre, and Jochen Guck (2019) Manipulation and biophysical characterization of giant unilamellar vesicles with an optical stretcher. In: The Giant Vesicle Book (Dimova R, Marques C, eds). Boca Raton: Taylor & Francis Group, LLC.
Gordon Wendy R, Zimmerman B, He L, Miles Laura J, Huang J, Tiyanont K, McArthur Debbie G, Aster Jon C, Perrimon N, Loparo Joseph J, Blacklow Stephen C (2015) Mechanical Allostery: Evidence for a Force Requirement in the Proteolytic Activation of Notch. Developmental Cell 33:729-736.
Goulet-Hanssens A, Eisenreich F, Hecht S (2020) Enlightening Materials with Photoswitches. Advanced Materials 32:1905966.
Gracià RS, Bezlyepkina N, Knorr RL, Lipowsky R, Dimova R (2010) Effect of cholesterol on the rigidity of saturated and unsaturated membranes: fluctuation and electrodeformation analysis of giant vesicles. Soft Matter 6:1472-1482.
Groves J (2007) Supported Lipid Bilayers as Mimics for Cell Surfaces and as Tools in Biotechnology. In: BioMEMS and Biomedical Nanotechnology: Volume III Therapeutic Micro/Nanotechnology (Ferrari M, Desai T, Bhatia S, eds), pp 305-323. Boston, MA: Springer US.

Groza R, Schmidt KV, Müller PM, Ronchi P, Schlack-Leigers C, Neu U, Puchkov D, Dimova R, Matthaeus C, Taraska J, Weikl TR, Ewers H (2024) Adhesion energy controls lipid binding-mediated endocytosis. Nature Communications 15:2767.
Gu Y, Gu C (2014) Physiological and pathological functions of mechanosensitive ion channels. Mol Neurobiol 50:339-347.
Gullingsrud J, Kosztin D, Schulten K (2001) Structural Determinants of MscL Gating Studied by Molecular Dynamics Simulations. Biophysical Journal 80:2074-2081.
Hannezo E, Heisenberg C-P (2019) Mechanochemical Feedback Loops in Development and Disease. Cell 178:12-25.
Harrington MJ, Mezzenga R, Miserez A (2024) Fluid protein condensates for bio-inspired applications. Nature Reviews Bioengineering 2:260-278.
Hartrampf N, Leitao SM, Winter N, Toombs-Ruane H, Frank JA, Schwille P, Trauner D, Franquelim HG (2023) Structural diversity of photoswitchable sphingolipids for optodynamic control of lipid microdomains. Biophysical Journal 122:2325-2341.
Harvey JW (1997) Chapter 7 - The Erythrocyte: Physiology, Metabolism, and Biochemical Disorders. In: Clinical Biochemistry of Domestic Animals (Fifth Edition) (Kaneko JJ, Harvey JW, Bruss ML, eds), pp 157-203. San Diego: Academic Press.
Haswell ES, Phillips R, Rees DC (2011) Mechanosensitive channels: what can they do and how do they do it? Structure 19:1356-1369.
Heberle J, Riesle J, Thiedemann G, Oesterhelt D, Dencher NA (1994) Proton migration along the membrane surface and retarded surface to bulk transfer. Nature 370:379-382.
Heisenberg CP, Bellaïche Y (2013) Forces in tissue morphogenesis and patterning. Cell 153:948-962.
Helfrich W (1974) Deformation of Lipid Bilayer Spheres by Electric Fields. Zeitschrift für Naturforschung C 29:182-183.
Henne WM (2021) Organelle homeostasis principles: How organelle quality control and inter-organelle crosstalk promote cell survival. Dev Cell 56:878-880.
Hindley JW, Zheleva DG, Elani Y, Charalambous K, Barter LMC, Booth PJ, Bevan CL, Law RV, Ces O (2019) Building a synthetic mechanosensitive signaling pathway in compartmentalized artificial cells. Proc Natl Acad Sci U S A 116:16711-16716.
Höglinger D, Nadler A, Schultz C (2014) Caged lipids as tools for investigating cellular signaling. Biochimica et Biophysica Acta (BBA) - Molecular and Cell Biology of Lipids 1841:1085-1096.
Höglsperger F, Betz T, Ravoo BJ (2022) Reversible Photoresponsive Modulation of Osmotic Pressure via Macromolecular Host–Guest Interaction. ACS Macro Letters 11:537-542.
Horger KS, Estes DJ, Capone R, Mayer M (2009) Films of Agarose Enable Rapid Formation of Giant Liposomes in Solutions of Physiologic Ionic Strength. Journal of the American Chemical Society 131:1810-1819.
Irie M (2000) Diarylethenes for Memories and Switches. Chemical Reviews 100:1685-1716.
Ishikawa-Ankerhold HC, Ankerhold R, Drummen GP (2012) Advanced fluorescence microscopy techniques--FRAP, FLIP, FLAP, FRET and FLIM. Molecules 17:4047-4132.
Jeon J, Voth GA (2008) Gating of the Mechanosensitive Channel Protein MscL: The Interplay of Membrane and Protein. Biophysical Journal 94:3497-3511.
Ji S (2012) Why Is the Cell So Complex? In: Molecular Theory of the Living Cell: Concepts, Molecular Mechanisms, and Biomedical Applications (Ji S, ed), pp 585-598. New York, NY: Springer New York.
Jiménez-Rojo N, Feng S, Morstein J, Pritzl SD, Harayama T, Asaro A, Vepřek NA, Arp CJ, Reynders M, Novak AJE, Kanshin E, Ueberheide B, Lohmüller T, Riezman H, Trauner D (2022) Optical Control of Membrane Fluidity Modulates Protein Secretion. bioRxiv:2022.2002.2014.480333.
Jones P, Maragó O, Volpe G (2015) Optical tweezers: Cambridge University Press Cambridge.
Joseph A, Wagner AM, Garay-Sarmiento M, Aleksanyan M, Haraszti T, Söder D, Georgiev VN, Dimova R, Percec V, Rodriguez-Emmenegger C (2022) Zwitterionic Dendrimersomes: A Closer Xenobiotic Mimic of Cell Membranes. Advanced Materials 34:2206288.

Kaksonen M, Roux A (2018) Mechanisms of clathrin-mediated endocytosis. Nature Reviews Molecular Cell Biology 19:313-326.
Kandasamy SK, Larson RG (2006) Molecular Dynamics Simulations of Model Trans-Membrane Peptides in Lipid Bilayers: A Systematic Investigation of Hydrophobic Mismatch. Biophysical Journal 90:2326-2343.
Karamdad K, Law RV, Seddon JM, Brooks NJ, Ces O (2015) Preparation and mechanical characterisation of giant unilamellar vesicles by a microfluidic method. Lab on a Chip 15:557-562.
Karimi M, Steinkühler J, Roy D, Dasgupta R, Lipowsky R, Dimova R (2018) Asymmetric Ionic Conditions Generate Large Membrane Curvatures. Nano Lett 18:7816-7821.
Käs J, Sackmann E (1991) Shape transitions and shape stability of giant phospholipid vesicles in pure water induced by area-to-volume changes. Biophysical Journal 60:825-844.
Khalifat N, Puff N, Bonneau S, Fournier J-B, Angelova MI (2008) Membrane Deformation under Local pH Gradient: Mimicking Mitochondrial Cristae Dynamics. Biophysical Journal 95:4924-4933.
Kimmelman J, Henderson V (2016) Assessing risk/benefit for trials using preclinical evidence: a proposal. J Med Ethics 42:50-53.
Klajn R (2014) Spiropyran-based dynamic materials. Chemical Society Reviews 43:148-184.
Kloda A, Petrov E, Meyer GR, Nguyen T, Hurst AC, Hool L, Martinac B (2008) Mechanosensitive channel of large conductance. Int J Biochem Cell Biol 40:164-169.
Kluge C, Pöhnl M, Böckmann RA (2022) Spontaneous local membrane curvature induced by transmembrane proteins. Biophys J 121:671-683.
Koçer A, Walko M, Feringa BL (2007) Synthesis and utilization of reversible and irreversible light-activated nanovalves derived from the channel protein MscL. Nat Protoc 2:1426-1437.
Koçer A, Walko M, Meijberg W, Feringa BL (2005) A Light-Actuated Nanovalve Derived from a Channel Protein. Science 309:755-758.
Kowaltowski AJ, Menezes-Filho SL, Assali EA, Gonçalves IG, Cabral-Costa JV, Abreu P, Miller N, Nolasco P, Laurindo FRM, Bruni-Cardoso A, Shirihai OS (2019) Mitochondrial morphology regulates organellar Ca2+ uptake and changes cellular Ca2+ homeostasis. The FASEB Journal 33:13176-13188.
Kucerka N, Tristram-Nagle S, Nagle JF (2005) Structure of fully hydrated fluid phase lipid bilayers with monounsaturated chains. J Membr Biol 208:193-202.
Lee AG (2011) Biological membranes: the importance of molecular detail. Trends in Biochemical Sciences 36:493-500.
Lee H-M, Larson DR, Lawrence DS (2009) Illuminating the Chemistry of Life: Design, Synthesis, and Applications of “Caged” and Related Photoresponsive Compounds. ACS Chemical Biology 4:409-427.
Lee JC, Timasheff SN (1981) The stabilization of proteins by sucrose. Journal of Biological Chemistry 256:7193-7201.
Levental I, Veatch S (2016) The Continuing Mystery of Lipid Rafts. J Mol Biol 428:4749-4764.
Levental KR, Levental I (2015) Giant plasma membrane vesicles: models for understanding membrane organization. Curr Top Membr 75:25-57.
Li C, Qian T, He R, Wan C, Liu Y, Yu H (2021) Endoplasmic Reticulum-Plasma Membrane Contact Sites: Regulators, Mechanisms, and Physiological Functions. Front Cell Dev Biol 9:627700.
Li J, Li G, Wang H, Wang Deng X (2011) Phytochrome signaling mechanisms. Arabidopsis Book 9:e0148.
Li Y, Liu S, Xu W, Wang K, He F, Liu J (2023) Formation of giant plasma membrane vesicles for biological and medical applications: a review. Sensors & Diagnostics 2:806-814.
Lichtenegger M, Tiapko O, Svobodova B, Stockner T, Glasnov TN, Schreibmayer W, Platzer D, de la Cruz GG, Krenn S, Schober R, Shrestha N, Schindl R, Romanin C, Groschner K (2018) An optically controlled probe identifies lipid-gating fenestrations within the TRPC3 channel. Nature Chemical Biology 14:396-404.

Lichtman JW, Conchello J-A (2005) Fluorescence microscopy. Nature Methods 2:910-919.
Lin C, Todo T (2005) The cryptochromes. Genome Biol 6:220.
Lind TK, Cárdenas M (2016) Understanding the formation of supported lipid bilayers via vesicle fusion—A case that exemplifies the need for the complementary method approach (Review). Biointerphases 11.
Lipowsky R (2019) Understanding giant vesicles: A theoretical perspective. In: The Giant Vesicle Book (Dimova R, Marques C, eds): CRC Press, Taylor & Francis Group.
Lira RB, Dimova R, Riske KA (2014) Giant unilamellar vesicles formed by hybrid films of agarose and lipids display altered mechanical properties. Biophys J 107:1609-1619.
Lira RB, Leomil FSC, Melo RJ, Riske KA, Dimova R (2021) To Close or to Collapse: The Role of Charges on Membrane Stability upon Pore Formation. Advanced Science 8:2004068.
López-García P, Moreira D (2015) Open Questions on the Origin of Eukaryotes. Trends in Ecology & Evolution 30:697-708.
López Mora N, Hansen JS, Gao Y, Ronald AA, Kieltyka R, Malmstadt N, Kros A (2014) Preparation of size tunable giant vesicles from cross-linked dextran(ethylene glycol) hydrogels. Chemical Communications 50:1953-1955.
Lorent JH, Levental KR, Ganesan L, Rivera-Longsworth G, Sezgin E, Doktorova M, Lyman E, Levental I (2020) Plasma membranes are asymmetric in lipid unsaturation, packing and protein shape. Nature Chemical Biology 16:644-652.
Lynch M, Conery JS (2003) The origins of genome complexity. science 302:1401-1404.
Mammoto T, Mammoto A, Ingber DE (2013) Mechanobiology and developmental control. Annu Rev Cell Dev Biol 29:27-61.
Manafirad A, Menendez CA, Perez-Lemus GR, Thayumanavan S, de Pablo JJ, Dinsmore AD (2023) Structural and Mechanical Response of Two-Component Photoswitchable Lipid Bilayer Vesicles. Langmuir 39:15932-15941.
Mangiarotti A, Aleksanyan M, Siri M, Sun TW, Lipowsky R, Dimova R (2024) Photoswitchable Endocytosis of Biomolecular Condensates in Giant Vesicles. Adv Sci (Weinh):e2309864.
Marsh M, McMahon HT (1999) The structural era of endocytosis. Science 285:215-220.
Martinac B (2012) Mechanosensitive ion channels: an evolutionary and scientific tour de force in mechanobiology. Channels (Austin) 6:211-213.
Martinac B, Adler J, Kung C (1990) Mechanosensitive ion channels of E. coli activated by amphipaths. Nature 348:261-263.
Martinac B, Buechner M, Delcour AH, Adler J, Kung C (1987) Pressure-sensitive ion channel in Escherichia coli. Proceedings of the National Academy of Sciences 84:2297-2301.
Martinac B, Rohde PR, Battle AR, Petrov E, Pal P, Foo AF, Vásquez V, Huynh T, Kloda A (2010) Studying mechanosensitive ion channels using liposomes. Methods Mol Biol 606:31-53.
Marturano V, Ambrogi V, Bandeira NAG, Tylkowski B, Giamberini M, Cerruti P (2017) Modeling of Azobenzene-Based Compounds. Physical Sciences Reviews 2.
Matosevic S, Paegel BM (2011) Stepwise synthesis of giant unilamellar vesicles on a microfluidic assembly line. J Am Chem Soc 133:2798-2800.
Matthias Garten DL, and Patricia Bassereau (2019) Protein reconstitution in giant vesicles. In: The Giant Vesicle Book (Dimova R, Marques C, eds): CRC Press, Taylor & Francis Group.
McIntosh TJ, Simon SA (2006) Roles of bilayer material properties in function and distribution of membrane proteins. Annual Review of Biophysics and Biomolecular Structure 35:177-198.
Meier O, Boucke K, Hammer SV, Keller S, Stidwill RP, Hemmi S, Greber UF (2002) Adenovirus triggers macropinocytosis and endosomal leakage together with its clathrin-mediated uptake. J Cell Biol 158:1119-1131.
Mesarec L, Góźdź W, Iglič A, Kralj-Iglič V, Virga EG, Kralj S (2019) Normal red blood cells' shape stabilized by membrane's in-plane ordering. Scientific Reports 9:19742.
Moe P, Blount P (2005) Assessment of Potential Stimuli for Mechano-Dependent Gating of MscL: Effects of Pressure, Tension, and Lipid Headgroups. Biochemistry 44:12239-12244.

Moga A, Yandrapalli N, Dimova R, Robinson T (2019) Optimization of the Inverted Emulsion Method for High-Yield Production of Biomimetic Giant Unilamellar Vesicles. ChemBioChem 20:2674-2682.
Moghimi SM (2016) Liposomes. In: Encyclopedia of Nanotechnology (Bhushan B, ed), pp 1802-1808. Dordrecht: Springer Netherlands.
Molday RS, Moritz OL (2015) Photoreceptors at a glance. J Cell Sci 128:4039-4045.
Montoya-Navarrete AL, Guerrero-Barrera AL, Quezada-Tristán T, Valdivia-Flores AG, Cano-Rábano MJ (2022) Red blood cells morphology and morphometry in adult, senior, and geriatricians dogs by optical and scanning electron microscopy. Front Vet Sci 9:998438.
Moradi S, Nowroozi A, Shahlaei M (2019) Shedding light on the structural properties of lipid bilayers using molecular dynamics simulation: a review study. RSC Advances 9:4644-4658.
Moraes I, Evans G, Sanchez-Weatherby J, Newstead S, Stewart PD (2014) Membrane protein structure determination - the next generation. Biochim Biophys Acta 1838:78-87.
Morstein J, Impastato AC, Trauner D (2021) Photoswitchable Lipids. ChemBioChem 22:73-83.
Mueller P, Chien TF, Rudy B (1983) Formation and properties of cell-size lipid bilayer vesicles. Biophys J 44:375-381.
Mukherjee N, Jose MD, Birkner JP, Walko M, Ingólfsson HI, Dimitrova A, Arnarez C, Marrink SJ, Koçer A (2014) The activation mode of the mechanosensitive ion channel, MscL, by lysophosphatidylcholine differs from tension-induced gating. Faseb j 28:4292-4302.
Mukhopadhyay TK, Morstein J, Trauner D (2022) Photopharmacological control of cell signaling with photoswitchable lipids. Curr Opin Pharmacol 63:102202.
Musters AH, Mashayekhi S, Harvey J, Axon E, Lax SJ, Flohr C, Drucker AM, Gerbens L, Ferguson J, Ibbotson S, et al. (2021) Phototherapy for atopic eczema. Cochrane Database of Systematic Reviews.
Nelson N, Yocum CF (2006) Structure and function of photosystems I and II. Annu Rev Plant Biol 57:521-565.
Nomura T, Cranfield CG, Deplazes E, Owen DM, Macmillan A, Battle AR, Constantine M, Sokabe M, Martinac B (2012) Differential effects of lipids and lyso-lipids on the mechanosensitivity of the mechanosensitive channels MscL and MscS. Proceedings of the National Academy of Sciences 109:8770-8775.
Oglecka K, Sanborn J, Parikh AN, Kraut RS (2012) Osmotic Gradients Induce Bio-Reminiscent Morphological Transformations in Giant Unilamellar Vesicles. Frontiers in Physiology 3.
Olvera D, Monaghan MG (2021) Electroactive material-based biosensors for detection and drug delivery. Advanced Drug Delivery Reviews 170:396-424.
Pabst G, Keller S (2024) Exploring membrane asymmetry and its effects on membrane proteins. Trends in Biochemical Sciences 49:333-345.
Paluch EK, Nelson CM, Biais N, Fabry B, Moeller J, Pruitt BL, Wollnik C, Kudryasheva G, Rehfeldt F, Federle W (2015) Mechanotransduction: use the force(s). BMC Biology 13:47.
Panda S, Hogenesch JB, Kay SA (2002) Circadian rhythms from flies to human. Nature 417:329-335.
Pawley J (2013) Handbook of Biological Confocal Microscopy: Springer US.
Pelkmans L, Helenius A (2002) Endocytosis via caveolae. Traffic 3:311-320.
Pernpeintner C, Frank JA, Urban P, Roeske CR, Pritzl SD, Trauner D, Lohmüller T (2017) Light-Controlled Membrane Mechanics and Shape Transitions of Photoswitchable Lipid Vesicles. Langmuir 33:4083-4089.
Perozo E, Kloda A, Cortes DM, Martinac B (2002) Physical principles underlying the transduction of bilayer deformation forces during mechanosensitive channel gating. Nature Structural Biology 9:696-703.
Perrier DL, Rems L, Boukany PE (2017) Lipid vesicles in pulsed electric fields: Fundamental principles of the membrane response and its biomedical applications. Advances in Colloid and Interface Science 249:248-271.

Peter Walde PS, Carlos M. Marques, Rumiana Dimova (2019) Preparation methods for giant unilamellar vesicles In: The Giant Vesicle Book, 1st Edition. Boca Raton: Taylor & Francis Group, LLC.
Peterlin P (2010) Frequency-dependent electrodeformation of giant phospholipid vesicles in AC electric field. Journal of Biological Physics 36:339-354.
Petersen NO, Höddelius PL, Wiseman PW, Seger O, Magnusson KE (1993) Quantitation of membrane receptor distributions by image correlation spectroscopy: concept and application. Biophys J 65:1135-1146.
Pfeffermann J, Eicher B, Boytsov D, Hannesschlaeger C, Galimzyanov TR, Glasnov TN, Pabst G, Akimov SA, Pohl P (2021) Photoswitching of model ion channels in lipid bilayers. Journal of Photochemistry and Photobiology B: Biology 224:112320.
Pinto BI, Bassetto CAZ, Jr., Bezanilla F (2022) Optocapacitance: physical basis and its application. Biophys Rev 14:569-577.
Pivetti CD, Yen M-R, Miller S, Busch W, Tseng Y-H, Booth IR, Milton H. Saier (2003) Two Families of Mechanosensitive Channel Proteins. Microbiology and Molecular Biology Reviews 67:66-85.
Portet T, Dimova R (2010) A new method for measuring edge tensions and stability of lipid bilayers: effect of membrane composition. Biophys J 99:3264-3273.
Powl AM, East JM, Lee AG (2008) Anionic phospholipids affect the rate and extent of flux through the mechanosensitive channel of large conductance MscL. Biochemistry 47:4317-4328.
Pritzl SD, Konrad DB, Ober MF, Richter AF, Frank JA, Nickel B, Trauner D, Lohmüller T (2022) Optical Membrane Control with Red Light Enabled by Red-Shifted Photolipids. Langmuir 38:385-393.
Qian Z-G, Huang S-C, Xia X-X (2022) Synthetic protein condensates for cellular and metabolic engineering. Nature Chemical Biology 18:1330-1340.
Reeves JP, Dowben RM (1969) Formation and properties of thin-walled phospholipid vesicles. J Cell Physiol 73:49-60.
Rideau E, Dimova R, Schwille P, Wurm FR, Landfester K (2018) Liposomes and polymersomes: a comparative review towards cell mimicking. Chemical Society Reviews 47:8572-8610.
Ridone P, Grage SL, Patkunarajah A, Battle AR, Ulrich AS, Martinac B (2018) "Force-from-lipids" gating of mechanosensitive channels modulated by PUFAs. J Mech Behav Biomed Mater 79:158-167.
Riske KA, Dimova R (2005) Electro-deformation and poration of giant vesicles viewed with high temporal resolution. Biophys J 88:1143-1155.
Riske KA, Dimova R (2006) Electric pulses induce cylindrical deformations on giant vesicles in salt solutions. Biophys J 91:1778-1786.
Robinson T (2019) Microfluidic Handling and Analysis of Giant Vesicles for Use as Artificial Cells: A Review. Advanced Biosystems 3:1800318.
Rosales C, Uribe-Querol E (2017) Phagocytosis: A Fundamental Process in Immunity. Biomed Res Int 2017:9042851.
Saiz L (2017) Insights into Signaling and the Functional Complexity of Biological Membranes. The Journal of Membrane Biology 250:335-336.
Salipante PF, Knorr RL, Dimova R, Vlahovska PM (2012) Electrodeformation method for measuring the capacitance of bilayer membranes. Soft Matter 8:3810-3816.
Sapp K, Aleksanyan M, Kerr K, Dimova R, Sodt A (2023) Kinetic relaxation of giant vesicles validates diffusional softening in a binary lipid mixture. Physical Review E 107:054403.
Sarkis J, Vié V (2020) Biomimetic Models to Investigate Membrane Biophysics Affecting Lipid–Protein Interaction. Frontiers in Bioengineering and Biotechnology 8.
Sawada Y, Murase M, Sokabe M (2012) The gating mechanism of the bacterial mechanosensitive channel MscL revealed by molecular dynamics simulations: from tension sensing to channel opening. Channels 6:317-331.
Schultz SG (1980) Basic principles of membrane transport. United States: Cambridge University Press,Cambridge, MA.

Schwendener RA (2007) Liposomes in Biology and Medicine. In: Bio-Applications of Nanoparticles (Chan WCW, ed), pp 117-128. New York, NY: Springer New York.
Sekar MP, Budharaju H, Zennifer A, Sethuraman S, Vermeulen N, Sundaramurthi D, Kalaskar DM (2021) Current standards and ethical landscape of engineered tissues-3D bioprinting perspective. J Tissue Eng 12:20417314211027677.
Serrano M-A, Moreno JC (2020) Spectral transmission of solar radiation by plastic and glass materials. Journal of Photochemistry and Photobiology B: Biology 208:111894.
Sezgin E, Kaiser HJ, Baumgart T, Schwille P, Simons K, Levental I (2012) Elucidating membrane structure and protein behavior using giant plasma membrane vesicles. Nat Protoc 7:1042-1051.
Shendrik P, Golani G, Dharan R, Schwarz US, Sorkin R (2023) Membrane Tension Inhibits Lipid Mixing by Increasing the Hemifusion Stalk Energy. ACS Nano 17:18942-18951.
Shimanouchi T, Umakoshi H, Kuboi R (2009) Kinetic Study on Giant Vesicle Formation with Electroformation Method. Langmuir 25:4835-4840.
Socrier L, Steinem C (2023) Photo-Lipids: Light-Sensitive Nano-Switches to Control Membrane Properties. ChemPlusChem 88:e202300203.
Spack EG, Jr., Packard B, Wier ML, Edidin M (1986) Hydrophobic adsorption chromatography to reduce nonspecific staining by rhodamine-labeled antibodies. Anal Biochem 158:233-237.
Sprovieri P, Martino G (2018) The role of the carbohydrates in plasmatic membrane. Physiol Res 67:1-11.
Stamatialis DF, Papenburg BJ, Gironés M, Saiful S, Bettahalli SNM, Schmitmeier S, Wessling M (2008) Medical applications of membranes: Drug delivery, artificial organs and tissue engineering. Journal of Membrane Science 308:1-34.
Stefaniu C, Brezesinski G, Möhwald H (2014) Langmuir monolayers as models to study processes at membrane surfaces. Advances in Colloid and Interface Science 208:197-213.
Steinkühler J, De Tillieux P, Knorr RL, Lipowsky R, Dimova R (2018) Charged giant unilamellar vesicles prepared by electroformation exhibit nanotubes and transbilayer lipid asymmetry. Scientific Reports 8:11838.
Stolik S, Delgado JA, Pérez A, Anasagasti L (2000) Measurement of the penetration depths of red and near infrared light in human “ex vivo” tissues. Journal of Photochemistry and Photobiology B: Biology 57:90-93.
Sukharev S (2002) Purification of the small mechanosensitive channel of Escherichia coli (MscS): the subunit structure, conduction, and gating characteristics in liposomes. Biophys J 83:290-298.
Sukharev S, Betanzos M, Chiang C-S, Guy HR (2001) The gating mechanism of the large mechanosensitive channel MscL. Nature 409:720-724.
Sukharev SI, Schroeder MJ, McCaslin DR (1999) Stoichiometry of the Large Conductance Bacterial Mechanosensitive Channel of E. coli. A Biochemical Study. The Journal of Membrane Biology 171:183-193.
Sukharev SI, Martinac B, Arshavsky VY, Kung C (1993) Two types of mechanosensitive channels in the Escherichia coli cell envelope: solubilization and functional reconstitution. Biophys J 65:177-183.
Szoka F, Papahadjopoulos D (1980) Comparative Properties and Methods of Preparation of Lipid Vesicles (Liposomes). Annual Review of Biophysics 9:467-508.
Szostak JW (2017) The Origin of Life on Earth and the Design of Alternative Life Forms. Molecular Frontiers Journal 01:121-131.
Szostak JW, Bartel DP, Luisi PL (2001) Synthesizing life. Nature 409:387-390.
Teng J, Loukin S, Anishkin A, Kung C (2015) The force-from-lipid (FFL) principle of mechanosensitivity, at large and in elements. Pflügers Archiv - European Journal of Physiology 467:27-37.
Terman M, Terman JS (2005) Light therapy for seasonal and nonseasonal depression: efficacy, protocol, safety, and side effects. CNS Spectr 10:647-663; quiz 672.
Tonkens R (2005) An overview of the drug development process. Physician Exec 31:48-52.

Träuble H, Grell E (1971) Carriers and specificity in membranes. IV. Model vesicles and membranes. The formation of asymmetrical spherical lecithin vesicles. Neurosciences Research Program bulletin 9:373-380.
Tyler WJ (2012) The mechanobiology of brain function. Nature Reviews Neuroscience 13:867-878.
Urban P, Pritzl SD, Konrad DB, Frank JA, Pernpeintner C, Roeske CR, Trauner D, Lohmüller T (2018) Light-Controlled Lipid Interaction and Membrane Organization in Photolipid Bilayer Vesicles. Langmuir 34:13368-13374.
van den Bogaart G, Krasnikov V, Poolman B (2007) Dual-color fluorescence-burst analysis to probe protein efflux through the mechanosensitive channel MscL. Biophys J 92:1233-1240.
van Meer G, Voelker DR, Feigenson GW (2008) Membrane lipids: where they are and how they behave. Nat Rev Mol Cell Biol 9:112-124.
Vanaken T, Foxall-Vanaken S, Castleman S, Ferguson-Miller S (1986) [3] Alkyl glycoside detergents: Synthesis and applications to the study of membrane proteins. In: Methods in Enzymology, pp 27-35: Academic Press.
Vasconcelos-Cardoso M, Batista-Almeida D, Rios-Barros LV, Castro-Gomes T, Girao H (2022) Cellular and molecular mechanisms underlying plasma membrane functionality and integrity. Journal of Cell Science 135.
Vellai T, Vida G (1999) The origin of eukaryotes: the difference between prokaryotic and eukaryotic cells. Proc Biol Sci 266:1571-1577.
Vitkova V, Mitkova D, Antonova K, Popkirov G, Dimova R (2018) Sucrose solutions alter the electric capacitance and dielectric permittivity of lipid bilayers. Colloids and Surfaces A: Physicochemical and Engineering Aspects 557:51-57.
Vlahovska PM, Gracià RS, Aranda-Espinoza S, Dimova R (2009) Electrohydrodynamic Model of Vesicle Deformation in Alternating Electric Fields. Biophysical Journal 96:4789-4803.
Walde P, Cosentino K, Engel H, Stano P (2010) Giant vesicles: preparations and applications. Chembiochem 11:848-865.
Wang E, Rodrigues M (2022) An update and review of narrowband ultraviolet B phototherapy for vitiligo. Dermatological Reviews 3:326-335.
Wang G, Zhang J (2012) Photoresponsive molecular switches for biotechnology. Journal of Photochemistry and Photobiology C: Photochemistry Reviews 13:299-309.
Wang Y, Kumar A, Jin H, Zhang Y (2021) Single-molecule manipulation of macromolecules on GUV or SUV membranes using optical tweezers. Biophysical Journal 120:5454-5465.
Weinberger A, Tsai FC, Koenderink GH, Schmidt TF, Itri R, Meier W, Schmatko T, Schröder A, Marques C (2013) Gel-assisted formation of giant unilamellar vesicles. Biophys J 105:154-164.
Winther JR, Thorpe C (2014) Quantification of thiols and disulfides. Biochimica et Biophysica Acta (BBA) - General Subjects 1840:838-846.
Woolfson DN, Bromley EHC (2011) Synthetic Biology: A bit of rebranding, or something new and inspiring? The Biochemist 33:19-25.
World-Health-Organization(WHO) (2007) Quality Assurance of Pharmaceuticals: A Compendium of Guidelines and Related Materials. Good manufacturing practices and inspection: World Health Organization.
Wu L-G, Hamid E, Shin W, Chiang H-C (2014) Exocytosis and Endocytosis: Modes, Functions, and Coupling Mechanisms*. Annual Review of Physiology 76:301-331.
Xiong H, Alberto KA, Youn J, Taura J, Morstein J, Li X, Wang Y, Trauner D, Slesinger PA, Nielsen SO, Qin Z (2023) Optical control of neuronal activities with photoswitchable nanovesicles. Nano Research 16:1033-1041.
Xu C, Hu S, Chen X (2016) Artificial cells: from basic science to applications. Mater Today (Kidlington) 19:516-532.

Xue F, Cox CD, Bavi N, Rohde PR, Nakayama Y, Martinac B (2020) Membrane stiffness is one of the key determinants of E. coli MscS channel mechanosensitivity. Biochimica et Biophysica Acta (BBA) - Biomembranes 1862:183203.
Yamamoto T, Aranda-Espinoza S, Dimova R, Lipowsky R (2010) Stability of spherical vesicles in electric fields. Langmuir 26:12390-12407.
Yanagisawa M, Imai M, Taniguchi T (2008) Shape Deformation of Ternary Vesicles Coupled with Phase Separation. Physical Review Letters 100:148102.
Yandrapalli N, Robinson T (2019) Ultra-high capacity microfluidic trapping of giant vesicles for high-throughput membrane studies. Lab on a Chip 19:626-633.
Yang NJ, Hinner MJ (2015) Getting across the cell membrane: an overview for small molecules, peptides, and proteins. Methods Mol Biol 1266:29-53.
Yeagle PL (1985) Cholesterol and the cell membrane. Biochimica et Biophysica Acta (BBA) - Reviews on Biomembranes 822:267-287.
Yilmaz D, Dimitrova AI, Walko M, Kocer A (2015) Study of light-induced MscL gating by EPR spectroscopy. European Biophysics Journal 44:557-565.
Yoshimura K, Batiza A, Kung C (2001) Chemically charging the pore constriction opens the mechanosensitive channel MscL. Biophys J 80:2198-2206.
Zernike F (1955) How I discovered phase contrast. Science 121:345-349.
Zhao C, Busch DJ, Vershel CP, Stachowiak JC (2016) Multifunctional Transmembrane Protein Ligands for Cell-Specific Targeting of Plasma Membrane-Derived Vesicles. Small 12:3837-3848.